



Carbon dioxide (CO₂) Valorization by Mineral Storage and Abiotic Hydrocarbons Generation

Kanchana Kularatne

► To cite this version:

Kanchana Kularatne. Carbon dioxide (CO₂) Valorization by Mineral Storage and Abiotic Hydrocarbons Generation. Geochemistry. IFP Energies Nouvelles, Rueil Malmaison, 2018. English. NNT : . tel-02312280

HAL Id: tel-02312280

<https://hal.science/tel-02312280>

Submitted on 11 Oct 2019

HAL is a multi-disciplinary open access archive for the deposit and dissemination of scientific research documents, whether they are published or not. The documents may come from teaching and research institutions in France or abroad, or from public or private research centers.

L'archive ouverte pluridisciplinaire **HAL**, est destinée au dépôt et à la diffusion de documents scientifiques de niveau recherche, publiés ou non, émanant des établissements d'enseignement et de recherche français ou étrangers, des laboratoires publics ou privés.

UNIVERSITÉ SORBONNE PARIS CITÉ



Thèse préparée
à l'INSTITUT DU PHYSIQUE DU GLOBE DE PARIS
École doctorale STEP'UP-ED N°560
IPGP - Équipe Géochimie des Isotopes Stables
et
à l'IFP ENERGIES NOUVELLES
Rueil Malmaison- Équipe Géofluides et roches (R163)

Carbon dioxide (CO₂) Valorization by Mineral Storage and Abiotic Hydrocarbons Generation

Par
Kanchana Kularatne

Présentée et soutenue publiquement le
12 Juin 2018

Thèse de doctorat de Sciences de la Terre et de l'environnement
Dirigée par Isabelle Martinez

Devant un jury composé de :

Truche Laurent	Rapporteur
Professeur (ISTerre, Grenoble)	
Andreani Muriel	Rapporteur
Maître de conférences (Laboratoire Géologie de Lyon)	
Menez Bénédicte	Présidente de Jury
Professeur (Université Paris Diderot, IPGP)	
Monnin Christophe	Membre
Director CNRS (Géosciences Environment Toulouse)	
Vitale-Brovarone Alberto	Membre
Chercheur CNRS (IMPMC, Paris)	
Sissmann Olivier	Co-encadrant
Ingénieur (IFPEN, Rueil Malmaison)	
Martinez Isabelle	Directrice de thèse
Maître de conférences (Université Paris Diderot, IPGP)	

To my Mom.

Acknowledgement

I sincerely thank my PhD supervisors, Isabelle Martinez and Olivier Sissmann, for accepting me for this project and introducing me to fluid-rock interactions. In particular, I thank Olivier, for all his support to commence my work at IFPEN as a foreign student. It has been an honor to be his first PhD student. I appreciate all his contributions of time, ideas and immense for making this work productive and stimulating. I thank Isabelle for continuously encouraging me with fruitful discussions. I am always grateful to both of you!

I am thankful to members of my PhD jury, Laurent Truche and Muriel Andreani for accepting to review the thesis manuscript, and Bénédicte Menez, Christophe Monnin and Alberto Vitale-Brovarone for accepting to read the thesis manuscript and to participate in my thesis defense.

I am grateful to IFP Energies Nouvelles (IFPEN) for funding my PhD project. I am thankful to Jean-Marc Lombard, Olga Vizika-Kavvadias and Andreas Ehinger for the administrative support.

I thank Fabrice Brunet, Sylvan Bernard, Virgile Rouchon, Bruno Garcia, Valerie Beaumont, François Guyot, for constructive discussions on this project and accepting to be in my thesis committees.

I cannot forget the immense support that I received from IFPEN and IPGP for my experimental and analytical work. I owe a debt of gratitude to Michel Chardin for kindly showing me the instrumentation of hydrothermal batch reactors and for helping with fluid sampling. I am also thankful to Sonia Noirez, who taught me the gas chromatography technique and supported me in gas analyses. I am also in debt to Helene Vermesse, Clemence Le Gallo, Isabelle Boboune and Patience Ekambas for their support in gas analysis at different stages. I am grateful to Eric Kohler, Julien Labaume, Joel Lopes de Azavedo, Daniel Pillot and Fanny Lutz for their assistance in mineralogical analysis. I also thank Jerome, Herman, Pascal and Said for all the technical support. I thank Louise Sylvie, Meriam Jehl, Amel Krochane, who deserves credit for providing much needed assistance with administrative tasks and keeping the work running smoothly. Thank you Pauline, Sylvia, Maria, Violine, Guillaume, Samir, Marc, Valerie, Sylvie Sarasagopalan and all the amazing people I met IFPEN. I thank Carine Chaduteau, Stephane Borensztajn, Laure Cordier, Julie Carlut for their great support in element analysis, SEM, ICP AES analysis and magnetic measurements conducted at IPGP.

My sincere gratitude goes to my professors at the Department of Geology, University of Peradeniya, Sri Lanka for introducing me to Geology and encouraging me to peruse research in Geology. I am also thankful to BGI, Bayreuth, Germany for introducing me to experimental Geoscience. I sincerely thank Hans Keppler, Andreas Audétat, Nobuyoshi Miyajima, and Tiziana Boffa-Ballaran for training me to conduct experimental techniques in high pressure and high temperature geochemistry. This journey would not be possible without you.

I thank all the doctoral students at IFPEN and at IPGP for sharing a good time together during the past 3 years, 7 months and 9 days. Thanks Erica, Xavier, Jianning, Anabel, Hamza, Sebastian, Imane, Aurelian, Damaris, Anouk, Richard, Nico, Vasilis, Virgini, Clair, Christa, Julia, Isabelle, Laura (the volcanologist), Lucas, Thomas, Caroline, Pierre, Lambert, David, Amandine, Malorie, Amorie, Sarah, Guillame and Virginia, Viviana, Andreina, Chizu and Jan for the spirit of motivation, coffees, good beers and amazing moments! Although far away, thank you Corrinne, Elisabetta, Anna Cernok, Thiwanka, Dickson and my friends in Sri Lanka, for stay connected across the globe.

I am grateful to my all my family, my mom, dad, my sisters and grandpa for encouraging me and keeping me warm even though from far away.

09/05/2018, Vincennes

Résumé

Cette étude a porté sur la production d'hydrogène, le stockage de CO₂ et la production d'hydrocarbures abiotiques dus aux interactions gaz-eau-roche lors d'expériences hydrothermales. La première partie du manuscrit présente la séquestration de CO₂ et la production de H₂ simultanées lors de la réaction de résidus miniers de Nouvelle-Calédonie avec de l'eau saturée en CO₂ à 473 K < T < 573 K et 15 MPa < PCO₂ < 30 MPa. Les résultats montrent que les meilleures conditions pour ces deux réactions sont 523 K < T < 540 K à 30 MPa, où 320.5g de CO₂ sont capturés sous forme de magnésite riche en fer ((Mg,Fe)CO₃), et où 0.57g de H₂ par kilogramme de résidu minier sont produits. En outre, en considérant la production annuelle de résidus miniers et d'émissions de CO₂ en Nouvelle-Calédonie, la méthode proposée permettrait de potentiellement capturer ~90 % des émissions totales de CO₂. De plus, la production de H₂ pourrait contribuer à hauteur de 10% de la consommation énergétique annuelle. L'étude avancée des produits secondaires et leurs interfaces mineral-eau à l'échelle nanométrique nous indique que les réactions ont lieu en dissolvant les résidus miniers puis en précipitant de la magnésite riche en fer, des minéraux argileux smectites (nontronite, vermiculite), des traces d'oxydes de fer et de silice amorphe. Bien que les phyllosilicates et la silice amorphe pourraient potentiellement agir comme des films de passivation réduisant la cinétique de dissolution et par conséquent le stockage de CO₂ et la production de H₂, nos expériences montrent que la réactivité des résidus miniers de Nouvelle-Calédonie peut être réduite par la présence de verre. La seconde partie du manuscrit présente l'interaction entre le CO₂ dissout et le H₂ pendant la synthèse d'hydrocarbures abiotiques, notamment la réaction de Fischer-Tropsch (FTT) en présence de deux catalyseurs potentiels que l'on trouve dans les systèmes naturels : la sphalerite (ZnS) et la marcasite (FeS₂). Les expériences ont été conduites à 573 K et 30 MPa dans des capsules en or placées dans un autoclave. L'hydrogène nécessaire à la réaction provient par l'oxydation-Fe²⁺ des minéraux tels que l'olivine (Mg_{1.80}Fe_{0.2}SiO₄), la fayalite (Fe₂SiO₄) et la chlorite riche en fer ou chamosite (6Fe₅Al(AlSi₃)O₁₀(OH)₈). La production de méthane (CH₄) lors des expériences est d'un ordre de grandeur supérieur à ce qui a été rapporté dans la littérature lorsque de la magnetite et de la chromite ont été utilisées comme catalyseur, et est du même ordre de grandeur que lors de l'utilisation des catalyseurs pentlandite et alliages Fe-Ni. En revanche, le faible taux de conversion de carbone inorganique en carbone organique et la distribution Shulz-Flory des alcanes C1-C4 nous montrent que la sphalerite et la marcasite ne catalysent pas explicitement la réaction FTT d'hydrocarbures dans les conditions des expériences.

Mots clés: séquestration CO₂, hydrogène, méthane, interaction eau-roche, résidus miniers de Nouvelle-Calédonie.

Abstract

This study examined hydrogen production, CO₂ storage and abiotic hydrocarbon generation during gas-water-rock interactions by conducting hydrothermal experiments. The first part of this manuscript presents the simultaneous CO₂ sequestration and hydrogen production by reacting New Caledonian mine tailings with CO₂ saturated water at 473 K <T< 573 K and 15 MPa <PCO₂< 30 MPa. The results showed that the best conditions for both these reactions were 523 K <T<540 K at 30 MPa, capturing 320.5 g of CO₂ in the form of iron-rich magnesite ((Mg,Fe)CO₃), and producing 0.57 g of H₂ per 1 kg of mine tailings. In addition, considering the annual mine tailings production and the annual CO₂ emission in New Caledonia, the proposed method could potentially capture ~90 % of New Caledonia's CO₂ emissions. In addition, the H₂ produced by this method could offset ~10 % of New-Caledonia's annual electrical consumption. Further investigation of secondary products and their mineral-water interfaces at nanometer scale indicated that the reactions were taken place by dissolving mine tailings followed by precipitation of iron rich magnesite, smectite group clay minerals (nontronite, vermiculite), traces of iron oxides and amorphous silica. Although, the phyllosilicates and amorphous silica could potentially act as passivating layers, slowing down the dissolution kinetics and consequently limiting the CO₂ storage and H₂ production capacities, our experiments demonstrated that the reactivity of New Caledonian mine tailings could also be lowered by the presence of glass. The second part of this manuscript presents the interaction of dissolved CO₂ and H₂ during the synthesis of "abiotic" hydrocarbons, via Fischer-Tropsch type (FTT) synthesis in the presence of two potential catalysts found in natural systems; sphalerite (ZnS) and marcasite (FeS₂). The experiments were conducted at 573 K and 30 MPa in gold capsules heated and pressurize in autoclaves. Hydrogen necessary for the reaction was provided by Fe²⁺ oxidation of minerals such as olivine (Mg_{1.80}Fe_{0.2}SiO₄), fayalite (Fe₂SiO₄) and Fe-rich chlorite or chamosite (6Fe₅Al(AlSi₃)O₁₀(OH)₈). Methane (CH₄) produced in our experiments was one order of magnitude higher than those reported in previous studies when magnetite and iron oxide-chromite were used as catalysts for CH₄ production, and in the same order of magnitude as pentlandite and Fe-Ni alloy catalysts. However, the small conversion rates of inorganic carbon into organic carbon as well as the Schulz-Flory distribution of C1-C4 alkanes demonstrated that sphalerite and marcasite do not explicitly catalyze the FTT synthesis of hydrocarbons under the conditions of these experiments.

Key words: CO₂ sequestration, hydrogen, methane, water-rock interactions, New Caledonian mine tailings

Table of contents

1. Introduction

General introduction	2
1.1 Carbon dioxide (CO ₂) sequestration in minerals	2
1.1.1 Atmospheric CO ₂ budget	2
1.1.2 Impacts of increasing CO ₂ in atmosphere	4
1.1.3 CO ₂ sequestration efforts	6
1.1.4 CO ₂ sequestration by minerals	7
1.1.5 Ex-situ CO ₂ sequestration by olivine	10
1.1.6 Ex-situ CO ₂ sequestration by mine tailings	16
1.2 Hydrogen production from Fe-rich minerals	19
1.3 Abiotic hydrocarbons.	21
1.3.1 Distinguish biotic Vs. abiotic hydrocarbons	21
1.3.2 Natural occurrences of abiotic hydrocarbons	25
1.3.3 Laboratory simulation of abiotic hydrocarbon production: the role of mineral catalysts	28
1.4 Problematic	33

2. Materials and methods

2.1 Section I- Experimental investigation of simultaneous ex-situ carbon dioxide sequestration and hydrogen production from New Caledonian mine tailings	36
2.1.1 General introduction	37
2.1.2 Characterization of mine tailings	40
2.1.3 Preparation of starting materials	45
2.1.4 High pressure and high temperature experiments	46
2.1.5 Gas sampling and gas chromatography analysis	49
2.1.6 Liquid sampling and ICP-AES analysis	55
2.1.7 Solid product analysis	57
2.1.8 Thermodynamic modeling	62
2.2 Section II – Experimental investigation of catalytic potential of sphalerite and marcasite for abiotic hydrocarbon generation	64
2.2.1 General introduction	64
2.2.2 Starting materials	64
2.2.3 Preparation of gold capsules	65
2.2.4 High pressure high temperature experiments	66
2.2.5 Analysis of gas phase	66
2.2.6 Analysis of Liquid phase	72
2.2.7 Thermodynamic modeling of dissolved organic compounds	75

3. Simultaneous ex-situ CO₂ mineral sequestration and hydrogen production from olivine-bearing mine tailings

Abstract	77
3.1 Introduction	78
3.2 Materials and methods	80
3.2.1 Starting materials	80
2.2.2 High pressure and high temperature experiments	82

3.2.3	Sampling and analytical methods	83
3.3	Results	86
3.3.1	Secondary products	86
3.3.2	Carbonate yield	88
3.3.3	Hydrogen production	89
3.3.4	H ₂ production estimated by Fe(III)/Fe(II) analysis	91
3.4	Discussion	92
3.4.1	Preferential dissolution of olivine within mine tailings at 473-573 K and 15-30 MPa	92
3.4.2	Reaction path and formation of secondary Mg-silicates	92
3.4.3	Fe-rich magnesite precipitation and hydrogen production	93
3.4.4	Carbonation and hydrogen production from mine tailings vs. other slags	95
3.4.5	Implications for CO ₂ sequestration and hydrogen production in New Caledonian mining sites and other Ni mining sites	96
3.5	Conclusions	98

4. Water-rock interactions during simultaneous ex-situ CO₂ mineral sequestration and hydrogen production from New Caledonian mine tailings

Abstract	100
4.1 Introduction	101
4.2 Materials and methods	102
4.2.1 Starting materials	102
4.2.2 Experimental and analytical methods	103
4.2.3 Thermodynamic modeling	105
4.3 Results	107
4.3.1 Short duration experiments	107
4.3.2 Long duration experiments	109
4.3.2.1 Chemistry of aqueous solutions	109
4.3.2.2 Hydrothermal production of hydrogen	115
4.3.2.3 Hydrocarbons production	115
4.3.2.4 Precipitation of magnesite and other secondary phyllosilicates	123
4.4 Discussion	131
4.4.1 Reactivity of mine tailings vs. olivine	131
4.4.1.1 Effect of crystal structure on dissolution rate	132
4.4.1.2 Effect of secondary phases on dissolution rate	133
4.4.2 Mine tailings carbonation and hydrogen production	134
4.4.3 Methane production	139
4.5 Conclusions	139

5. Laboratory simulation of abiotic hydrocarbon production: investigating the role of iron and zinc sulfides

Abstract	142
5.1 Introduction	143
5.2 Materials and methods	145
5.2.1 Starting materials	145
5.2.2 High pressure and high temperature experiments	146
5.2.3 Gas extraction and analysis	146

5.2.4	Estimation of carbon contamination	149
5.2.5	Schulz-Flory distribution	149
5.2.6	Solid product analysis	150
5.2.7	Liquid analysis	150
5.2.8	Thermodynamic modeling	153
5.3	Results	154
5.3.1	Production of gaseous hydrocarbons at 300°C and 30 MPa	154
5.3.2	Solid products	158
5.3.3	HPLC analysis for dissolved organic compounds	164
5.3.4	NMR analysis for dissolved organic compounds	169
5.4	Discussion	171
5.4.1	Reaction paths predicted by thermodynamic modeling	171
5.4.1.1	Olivine system	171
5.4.1.2	Fayalite system	176
5.4.1.3	Chlorite system	181
5.4.1.3	Summary of reaction paths predicted by thermodynamic modeling	182
5.4.2	Summary of thermodynamic modelling and experimental data	186
5.4.2.1	Hydrogen production	186
5.4.2.2	Far-from-equilibrium methane production	187
5.4.2.3	Formation of carbon-rich solid phases	187
5.4.3	Experimental production of C1-C4 hydrocarbons and catalysis by sphalerite and marcasite	192
5.5	Conclusions	197
6. Conclusions and perspectives		
6.1	Conclusions	199
6.2	Perspectives	201
References		203
Appendices		
Appendix I		220
Appendix II		233
Appendix III		241
Appendix IV		246

Chapter 1

Introduction

General introduction

Gas-water-rock interactions are key processes to understand large number of geochemical processes occurring on the Earth. Few common examples include the weathering of minerals at the Earth's surface, formation of ore deposits, magmatic process in the Earth's crust and mantle. Among these interactions, this thesis focuses on the H_2 - CO_2 - H_2O -mineral interactions in mafic and ultramafic systems in the hydrothermal context. In nature, for instance, deep-sea hydrothermal systems are one such natural system where important H_2 - CO_2 - H_2O -mineral interactions take place. The aim of this thesis is to study three significant reactions occurring in mafic and ultramafic systems at high pressure and high temperature conditions relevant to hydrothermal conditions. The first reaction concerns the hydrogen production by redox reaction between Fe(II) contained in mafic minerals and sea water. This reaction often occurs during the serpentinization reaction, when minerals become hydrated. The second reaction consists in carbonate precipitation which occurs through the reaction of divalent cations in mafic minerals with dissolved- CO_2 . Finally, abiotic methane generation by Fischer-Tropsch Type (FTT) synthesis occurs through the reaction of hydrogen with dissolved inorganic carbon species (or intermediates such as fatty acids), and is accelerated in the presence of suitable minerals which could act as potential catalysts. Two first two natural reactions have become an inspiration for two major, present day industrial applications in the energy industry. Firstly, hydrogen production by reacting Fe(II)-rich minerals or mine wastes with water is being now investigated as a low cost, alternate method of industrial hydrogen production, compared to the traditional steam methane reforming which is economically extremely costly. Secondly, the reactions of carbonate mineralization during weathering have been extensively studied to develop geological CO_2 sequestration methods, as a CO_2 mitigation strategy for industrial CO_2 emissions. In contrast to the above two reactions which were inspired by the natural processes, the abiotic hydrocarbon production in the hydrothermal systems whose mechanism has not yet been constrained well, is currently being attributed to the industrial process of methane production: the Fischer-Tropsch synthesis.

This chapter includes the background and bibliographic review for these three topics which make the basement for this work. In the first part, the mineral sequestration for CO_2 storage will be addressed. Secondly, a brief review of hydrogen production using iron rich minerals will be provided. Third, the abiotic hydrocarbons in nature and experimental simulations of abiotic hydrocarbons will be discussed. The problematic and the structure of the thesis will be presented at the end of this chapter.

1.1 Carbon dioxide (CO_2) sequestration in minerals

1.1.1 Atmospheric CO_2 budget

The Earth's atmosphere is the smallest carbon reservoir which contains ~800 Gt C of carbon of the global carbon cycle (Figure 1-1). It consists of 78.09% nitrogen (N_2), 20.95% oxygen (O_2), 0.93% argon (Ar) and only 0.04% carbon dioxide (CO_2) by volume. Even

though, it occupies less than one percent ($<1\%$) of the Earth's atmosphere, CO_2 is a major contributor to greenhouse effect, that warms the Earth's surface and thus makes the Earth a habitable planet. When the Sun's energy reaches the Earth's atmosphere, some of it is reflected back to space and the rest of the energy is absorbed by the land, ocean surface heating the Earth, and radiating heat back into the space. This energy is absorbed and re-radiated by greenhouse gases, namely, water vapor (30-70 %), carbon dioxide (9-26 %), and other gases that account for less than 10% (methane, nitrous oxide, ozone, chlorofluorocarbons). The absorbed energy warms the atmosphere and sustains the life, by maintaining the Earth's temperature at around 33°C warmer than it would otherwise be.

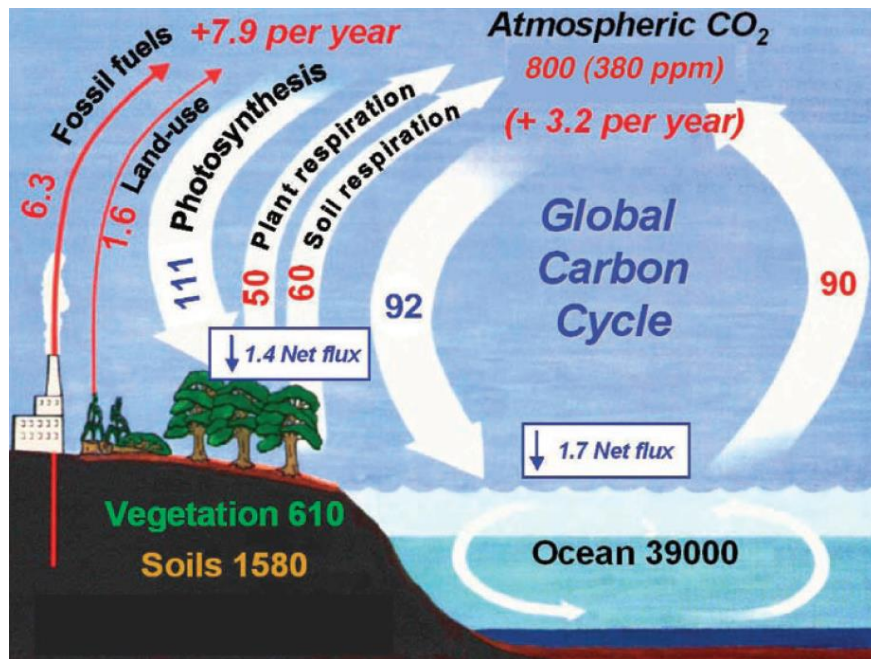


Figure 1-1. Schematic diagram of the simplified global carbon cycle. The amount carbon in reservoirs and carbon fluxes are reported in gigatons of carbon per year (GT C/year). Source: (Oelkers and Cole, 2008).

CO_2 was added to the Earth's atmosphere during the early history of the Earth via degassing from volcanism, together with nitrogen and other inert gases, ca.3.5 billion years ago. Since then the natural balancing of CO_2 concentration occurred as cycles of increments-decrements due to addition and removal of CO_2 by various natural processes (Figure 1-2). After photosynthesis emerged on the Earth, it became the major process of pumping CO_2 , where it is permanently converted into carbohydrates inside photosynthetic life forms within the oceans and the terrestrial biosphere. Even though the rates are slow, CO_2 is also consumed for geological reactions of rock weathering. CO_2 enters the atmosphere through various processes such as the respiration of all life forms, volcanic eruptions, and other geological processes such as metamorphism. Then, throughout Earth's history, atmospheric CO_2 concentration varied as cycles of increments-decrements, maintaining the balance between natural CO_2 releasing processes, and the CO_2 -consuming geochemical processes, such as weathering of silicates and burial of organic matter in sedimentary rocks.

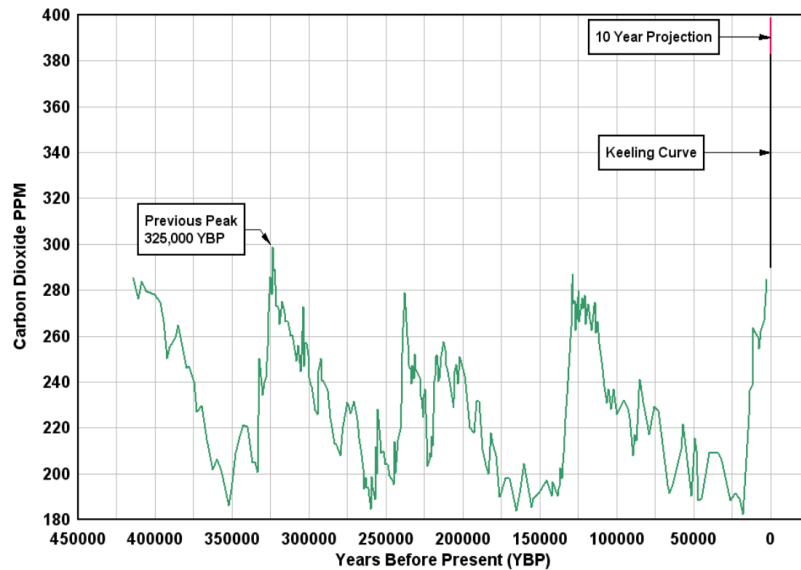


Figure 1-2. The natural balancing of CO₂ concentration shown by cycles of increments-decrements (source: planetforlife (2017), and also reported in (Marini, 2006)). The curve in green was drawn based on data taken from carbon dioxide concentration in the air bubbles trapped in the Vostok Antarctic ice core (Barnola et al., 2003) and references therein. The curve in black is the Keeling curve, which is the measurement of ongoing changes in CO₂ concentration. The increments in CO₂ represent the CO₂ released into the atmosphere through natural processes such as Earth's degassing, including diagenesis, metamorphism, magmatism and mantle degassing. The decrements are due to the natural processes which remove CO₂ from the atmosphere, such as weathering of silicates and burial of organic matter in sedimentary rocks.

1.1.2 Impacts of increasing CO₂ in atmosphere

Due to the extensive usage of fossil fuels after the industrial revolution in the 19th century, CO₂ concentration in the atmosphere increased drastically. This gradual increase of atmospheric CO₂ concentration since 1958 until present day is clearly shown in Figure 1-3a. Between year 2000 and 2005, global CO₂ emissions from burning fossil fuels averaged 26.4 Gt CO₂ yr⁻¹, at or above the highest rates predicted by IPCC (Intergovernmental Panel on Climate Change). Globally, the use of fossil fuels such as, coal, oil and gas, accounts for 82% of the energy consumption in year 2012 (IPCC, Intergovernmental Panel on Climatic Change). In addition, the amount of CO₂ emitted by fossil fuel combustion accounts for 65% of global greenhouse gas emissions, causing global warming, one of the major environmental issues ahead of 21st century (Edenhofer et al., 2014). Figure 1-3b clearly shows the existence of this correlation between the atmospheric CO₂ levels and the global temperature, which emphasizes that the annual rise of temperature has been increased from 0.54 °C/year in 1960 to 3.05 °C/year in 2015, as a result of global warming. Increasing temperature eventually causes many environmental complications, such as, rising sea levels in response to glacial melting, ocean acidification, decrease in ocean thermohaline circulation, and threatening global ecosystems (Oelkers and Cole, 2008, and references therein), that need to be

answered. The world political leaders recently agreed to maintain the global temperature rise well below 2 °C above pre-industrial levels and to pursue efforts to limit the temperature increase even further to less than 1.5 °C, in the Paris agreement, COP 21 (IEA, 2015). Achieving the goals of the Paris agreement requires a substantial and sustained reduction in the net flow of CO₂ into the atmosphere. This necessitates the rapid and extensive employment of low-emission technologies and mitigation options (Snæbjörnsdóttir et al., 2017), where CO₂ capture and storage methods expected to be the most reliable solution to control CO₂ emissions.

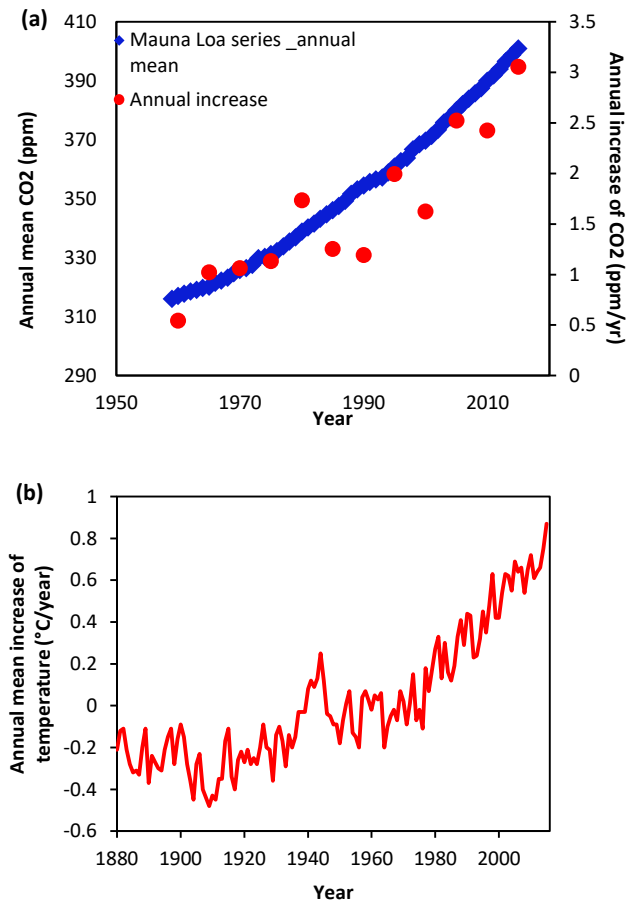


Figure 1-3. Increase of global atmospheric CO₂ correlates with the global rise in temperature. (a) The evolution of atmospheric CO₂ from 1958 until present (blue trend) and annual increase of CO₂ concentration (measured in ppm) per year (in red); data from direct measurements of atmospheric CO₂ at the Mauna Loa station, in Hawaii. Note that the maximum level reached in 2015 (400.83 ppm) and the maximum increase rate is also recorded in 2015 (3.05 ppm/year). Figure constructed based on the data obtained from US Government's Earth System Research Laboratory, Global Monitoring Division (OKFN, 2016); (b) The increase of mean annual temperature (°C/ year) monitored from 1888 to 2015. Plotted by Land-Ocean Temperature Index, LOTI, data set obtained from NASA web page (NASA, 2016).

1.1.3 CO₂ sequestration efforts

In an attempt to reduce or at least to stabilize the increase of atmospheric CO₂ content, thereby reducing the risk of global climate change, the international community has considered various options, such as the “geological sequestration of CO₂” (Oelkers, 2005), which means the injection of CO₂ into deep geological formations. Geological sequestration involves three main processes; capturing CO₂, transporting CO₂, and placing CO₂ in geological formations for semi-permanent or permanent storage. CO₂ is compressed up to ~100 bar in order to transport in pipe lines and then bring to its supercritical state (supercritical point of CO₂: 304.25 K and 7.39 MPa), with a lower density (0.469 g/cm³) than water, if necessary. Either gaseous or supercritical CO₂ is injected into geological formation by means of injection wells. Three major types of CO₂ storage have been proposed: hydrodynamic trapping, solubility trapping and mineral sequestration.

Hydrodynamic trapping: This method, also termed as physical trapping by Matter and Kelemen (2009), involves injection of CO₂ gas or supercritical CO₂ into porous formations such as, sedimentary basins, depleted oil reservoirs and non-economic coal beds, overlaid by low permeable or impermeable cap rocks such as shale or salt deposits. The impermeable caps rocks prevent leaking CO₂ back to the surface during the upwards migration, due to its buoyancy since CO₂ is less dense than water.

Solubility trapping: This method involves the injection of captured CO₂ into aquifers in the form of bicarbonate and carbonate ions and also into the ocean, at depths >1000 m, and allow the CO₂ to dissolve in deep waters.

Mineral sequestration of CO₂: This technique involves conversion of CO₂ into stable solid forms via precipitating into secondary carbonates after dissolution of primary silicates (Mg, Ca, or Fe bearing mafic/ultramafic minerals) upon injection of CO₂ into deep aquifers, or in CO₂ storage plants. The idea of trapping CO₂ sequestration in silicates was first proposed by Seifritz (1990), followed by Lackner et al., (1995) who put the foundation for today’s research efforts. This technique can be applied in-situ when storage occurs into basic or ultrabasic rocks and their aquifers; but also ex-situ in dedicated power plants with accelerated reaction rates.

The stability of different CO₂ storage methods in terms of storage time vs. the quantity of CO₂ that can be stored by each method is shown in Figure 1-4. The figure also shows the stability of carbon stored in natural reservoirs such as leaf litter, woody biomass, ocean (uptake capacities for carbonic acid and neutralized carbonic acid), and CO₂ injected for enhanced oil recovery. This diagram clearly indicates that compared to the other two methods, mineral sequestration is remarkable, because (i) it’s a permanent CO₂ fixation method, since CO₂ is fixed in the form of solid carbonates (eg. CaCO₃, MgCO₃, FeCO₃ and their solid solutions) which are stable over long periods of time, and (ii) compared to hydrodynamic or solubility trapping, it induces no risk of returning CO₂ back to the atmosphere, providing a promising method of CO₂ storage which also opens the opportunity to number of fundamental and applied research projects.

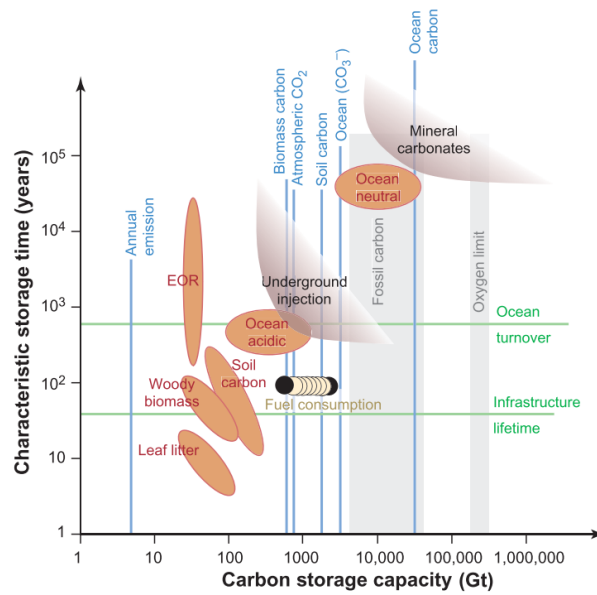
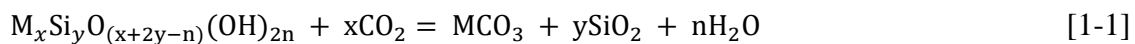


Figure 1-4. Estimated storage capacities and times for various sequestration methods (Lackner, 2003). The “fossil carbon” range includes at its upper end methane hydrates from the ocean floor. The “oxygen limit” is the amount of fossil carbon that would use up all oxygen available in air for its combustion. Carbon consumption for the 21st century ranges from 600 Gt (current consumption held constant) to 2400 Gt. “Ocean acidic” and “ocean neutral” are the ocean’s uptake capacities for carbonic acid and neutralized carbonic acid, respectively. The upper limits of capacity or lifetime for underground injection and mineral carbonates are not well constrained. EOR stands for enhanced oil recovery.

As mentioned in the general introduction, we have attempted to use the ex-situ CO₂ sequestration using an olivine bearing mine tailings material. The geochemical and mineralogical aspects of this topic and a bibliographic review on previous experimental works on this topic will be further discussed in the following sections.

1.1.4 CO₂ sequestration by minerals

Carbon dioxide (CO₂) sequestration by minerals (or mineral trapping) is the conversion of dissolved CO₂ into stable carbonates (eg. FeCO₃, MgCO₃ or CaCO₃ or their solid solutions), by reacting with Fe²⁺, Mg²⁺ and Ca²⁺ rich-minerals (Seifritz, 1990; Lackner et al., 1995; Perkins and Gunter, 1995; Oelkers, 2005). This technique is based on the natural process of carbonate precipitation during the alteration of rocks. A peridotite which has been naturally altered into magnesite, dolomite, travertine and listvanite has been shown in Figure 1-5. A generalized equation for CO₂ storage in minerals is given by equation [1-1];



where (M²⁺) represents a divalent cation such as, Fe²⁺, Mg²⁺ and Ca²⁺ in a silicate mineral and MCO₃ thus represent the carbonate of corresponding element M. Accordingly, we can

write the carbonation of olivine, a common and efficient mineral for carbonation, as given by equation [1-2];

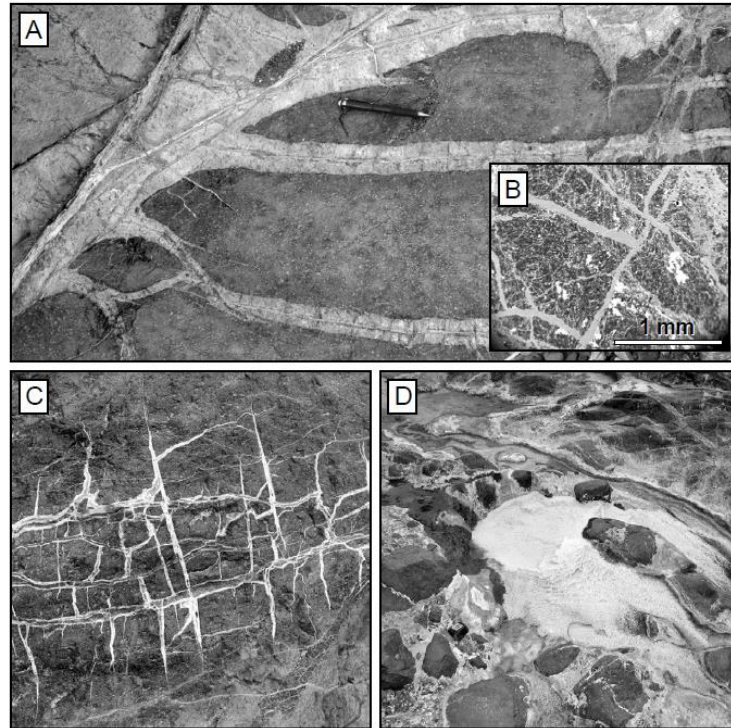
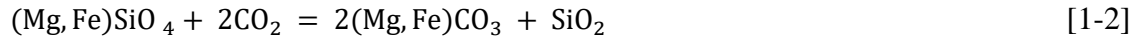


Figure 1-5. Carbonate mineralization during natural alteration of peridotite (from Power et al., 2013) (a) light colored soapstone (talc + dolomite) has partially replaced darker, partially serpentinized peridotite (b) listvenite [magnesite (grey) + quartz (light grey veins) + chromite (bright white)] replacing peridotite (c) white magnesite veins in darker partially serpentinized peridotite (d) travertine terrace growing at outlet of a peridotite-hosted alkaline spring.

Carbonate minerals are thermodynamically stable over geologic timescales, and as a result, sequestration by this method minimizes the risk of later leakage back to the atmosphere. The process can be called either *in-situ*, i.e. injection of CO_2 into geological formations or *ex-situ*, i.e. CO_2 storage plant in which crushed rock is reacted with dissolved CO_2 .

In-situ CO_2 sequestration: The in-situ process has developed more recently and differs from conventional geological storage in that supercritical CO_2 mixed with brine is injected underground under optimized conditions which are meant to accelerate the natural process of mineral carbonation. The in-situ mineralization may be far more effective in basalt or ultramafic rock (e.g. McGrail et al. 2006; Matter et al. 2007), which are rich in divalent cations and poor in silica (Oelkers et al., 2008). A typical basalt contains 7–10 wt% Ca, 5–6 wt% Mg and 7–10 wt% Fe, and these metals are readily liberated by reaction with CO_2 -rich water. For example, Columbia river basalts, Siberian basalts and Iceland basalts serve large volumes for in-situ CO_2 sequestration. More locations of continental basalts which could potentially serve as in-situ CO_2 storage sites are shown in Figure 1-6.

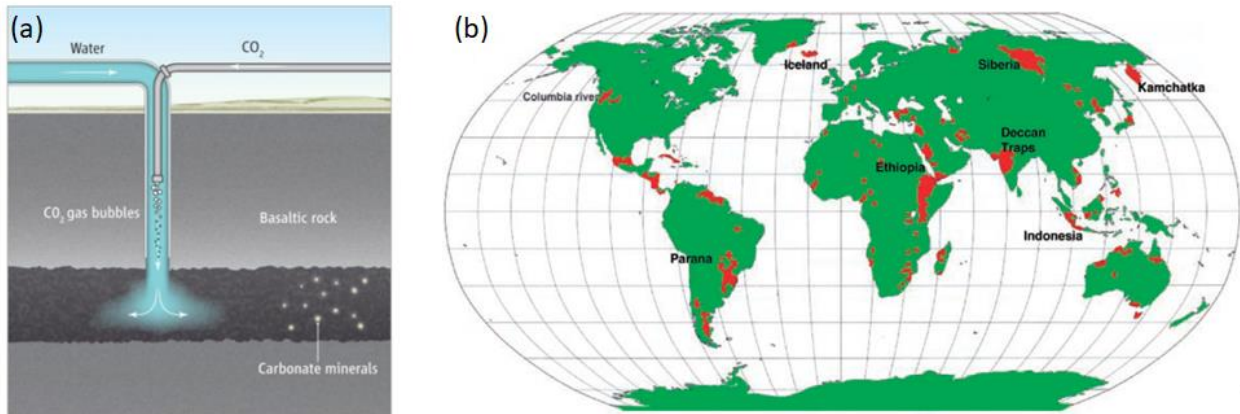


Figure 1-6. In-situ CO₂ storage (a) CO₂ is dissolved into water during its injection into porous basaltic rocks (Snæbjörnsdóttir et al., 2014) (b) Locations of continental basalts that could serve as in situ mineral carbonation sites (Oelkers et al., 2008)

Ex-situ CO₂ sequestration: The ex-situ process refers to mineral carbonation in a chemical plant under controlled temperature and pressure conditions (Figure 1-7). Numerous experimental studies have been focused on evaluating the potential of ex-situ CO₂ sequestration in various mafic/ultramafic minerals and rocks: for example basalt (Assayag et al., 2009; Matter and Kelemen, 2009; Sissmann et al., 2014), olivine (Andreani et al., 2009; Garcia et al., 2010; Guyot et al., 2011a; Saldi et al., 2013), wollastonite (Daval et al., 2009), pyroxene (Dufaud et al., 2009), serpentines (Dufaud et al., 2009), and brucite (Zhao et al., 2010). Figure 1-8 shows the standard reaction Gibbs free energies for carbonation of some of the above mentioned silicate minerals, where those with a negative ΔG are more favorable for carbonation over those with a positive ΔG . Although wollastonite (CaSiO₃) (-pyroxene mineral) exhibit the lowest ΔG , olivine is more abundant in nature in mafic and ultramafic environments (eg. basalt, peridotites). It is also one of the fastest dissolving Mg-silicate (Guyot et al., 2011). Therefore, among the minerals rich in divalent Ca, Mg or Fe, olivine is considered the most favorable for carbonation. This ex-situ CO₂ sequestration conducted in this study focuses on mine tailings rich in olivine.

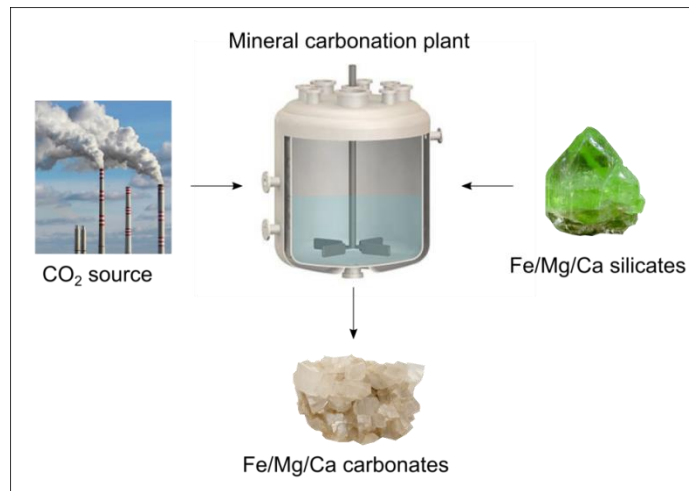


Figure 1-7. Schematic showing the material fluxes in ex-situ CO₂ storage plant

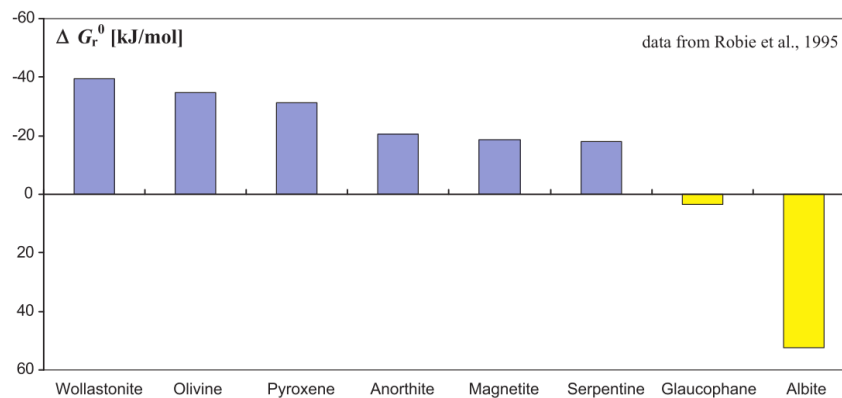


Figure 1-8. Standard Gibbs free energies for the carbonation reaction of different silicate minerals. Minerals containing divalent carbonate forming cations are thermodynamically more prone to favour that reaction. A favourable reaction is indicated by a negative standard Gibbs free energy (Guyot et al., 2011).

1.1.5 Ex-situ CO₂ sequestration by olivine

Olivine has been extensively studied in laboratories at different pressure, temperature, and pH to understand the rates and mechanisms of its carbonation. In principle, the ex-situ aqueous mineral CO₂ sequestration is experimentally performed by reacting the powdered olivine (or olivine bearing rock depending upon the studies), either with a NaHCO₃ solution or water saturated with gaseous CO₂. In the latter case, dissolution of CO₂ into water will take place reaching the following equilibria;

Gaseous CO₂ dissolves in water producing aqueous CO₂;



The aqueous CO₂ reacts with water producing carbonic acid;

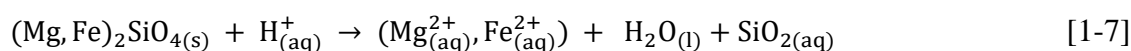


In the solution, depending on pH conditions, carbonic acid dissociates as follows;

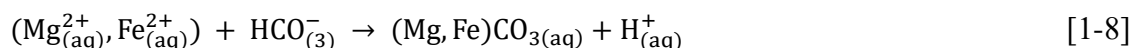


The carbonation process of olivine consists of two steps (i) dissolution of olivine due to the acidification of the fluid after CO₂ injection releasing divalent cations into the solution and, (ii) precipitation of solid carbonates (eg. Oelkers and Schott, 1995 and 2005; Guyot et al., 2011) as shown by the equations [1-7] and [1-8];

Dissolution of olivine:



Precipitation of carbonates:



The overall reaction of olivine carbonation reaction results by the combination of equation [1-7] and [1-8] and was mentioned above [1-2].

The dissolution of olivine has been shown to be the rate limiting step of the overall carbonation process (Daval et al., 2011; Sissmann et al., 2013). Several experimental studies report the kinetics of olivine dissolution at ambient conditions up to those relevant to the in-situ CO₂ sequestration conditions. These data are summarized in Figure 1-9. This figure shows that, at a given pH, the olivine dissolution rate increases with increasing temperature, and for a given temperature, decreases as a function of increasing pH.

Only few studies have focused on the kinetics of olivine dissolution (equation [1-7]) at high temperature (Malvoisin et al., 2012) and at high pCO₂ (Hänchen et al., 2006; Prigiobbe et al., 2009). A systematic review on olivine dissolution kinetics can be found in (Rimstidt et al., 2012). In summary, the results of these studies indicate that olivine dissolution rate increases as a function of (i) temperature, (ii) increasing pCO₂, (iii) concentration of salts in the solution (NaCl), and (iv) decreasing pH. These studies also suggest that Mg is released faster than Si at acidic pH, whereas the opposite is observed at basic pH (Kaszuba et al., 2013). The authors also discuss that stoichiometric release of Mg, Si occurs at pH=6, but also at any pH only if steady state dissolution rate is reached. Olivine dissolution is enhanced by adding organic additives such as citric acids and oxalic acids which are polydentate ligands, by ligand promoted dissolution. The study by Prigiobbe and Mazzotti (2011) showed that for pH =1 to 7 and temperature ranging from 90 <T>120 °C, citrate and oxalate promotes the olivine dissolution. Finally, the presence of aluminum also increases the olivine dissolution rate via Al-Si complexation, at hydrothermal conditions

(Andreani et al., 2012). However, at room temperature Al seems to have no effect on dissolution rate of olivine (Chen and Brantley, 2000).

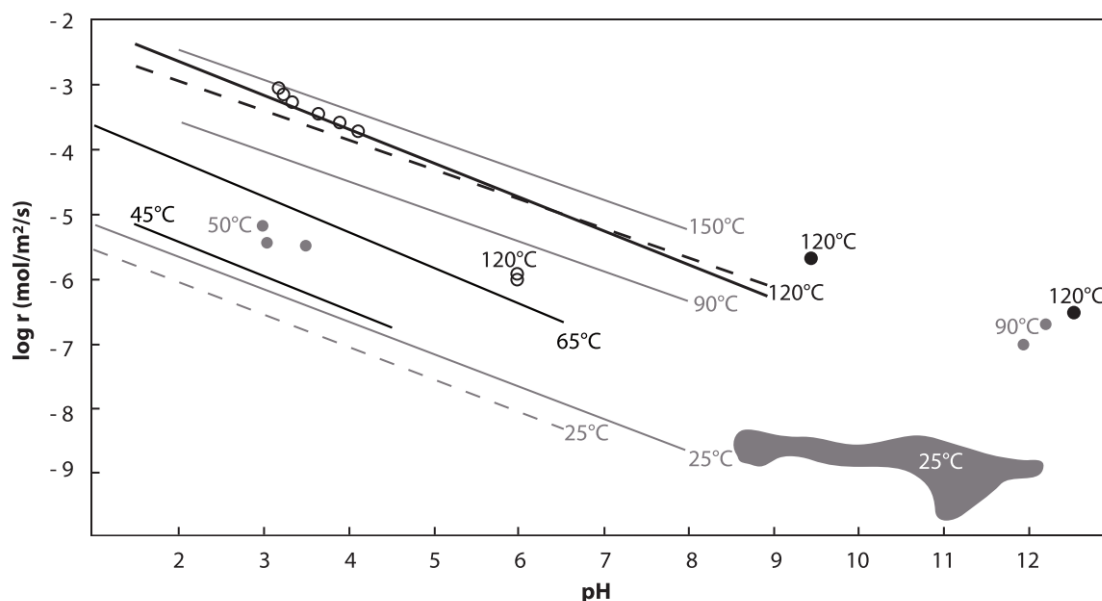


Figure 1-9. Experimental dissolution rates (r) of olivine as a function of pH at 25 °C showing that the rate of olivine dissolution increases as a function of temperature and decreases as a function of increasing pH, from Kaszuba et al. (2013). Dotted line: data from Blum and Lasaga, 1988; Wogelius and Walther, 1991; line and grey area: data from Pokrovsky and Schott, 2000), at 45 °C (data from Rosso and Rimstidt, 2000), at 50 °C (dots: data from Wang and Giammar, 2013), at 65 °C (data from Wogelius and Walther, 1991; Chen and Brantley, 2000), at 90 °C (data from Hänchen et al., 2006), at 120 °C (data from Hänchen et al., 2006: without CO₂ (dotted line and dots), with CO₂ (open circles); line: data from Prigiobbe et al., 2009), and at 150 °C (data from Hänchen et al., 2006).

In general, the second step, carbonate precipitation (equation [1-7]) is much faster than olivine dissolution (Kaszuba et al., 2013), and it occurs when the solution is supersaturated with respect to the carbonate mineral. For Mg-rich carbonates, however, carbonate precipitation is limited by the nucleation process that requires a critical saturation index. In that case, even though the solution reach the supersaturation (Giammar et al., 2005), magnesite does not precipitate. The presence of iron is known to accelerate the precipitation of Mg carbonates even under low degree of supersaturation by promoting the fast precipitating Mg-Fe carbonate solid solutions, which nucleates faster than pure Mg-carbonate (Saldi et al., 2013).

The entire process of olivine carbonation has been studied experimentally using batch reactors in order to study the optimum conditions for CO₂ storage, and to examine the effect of secondary phases on the dissolution rate of primary silicates and the rate of entire carbonation process. An experimental study conducted by (Giammar et al., 2005), on carbonation of olivine (Fo89) at low temperatures such as 30 °C and 95 °C, and at low pCO₂

such as 1 and 100 bar, (inducing acidic pH conditions), showed that olivine dissolution rate increases as a function of temperature and $p\text{CO}_2$. However, carbonation reaction did not occur at these experimental conditions following the dissolution of forsterite, even though the thermodynamic conditions were favorable for magnesite saturation. The author concluded that the precipitation of magnesite is kinetically hindered and supersaturated conditions may persist without magnesite precipitation.

A more recent experimental study by Gerdemann et al. (2007) showed that olivine can be completely transformed into carbonates within few hours (<6hrs) (Figure 1-10). According to the experimental conditions of the above study, olivine carbonation was highest under alkaline conditions (pH~8) where CO_3^{2-} is dominant, whereas olivine dissolution is known to be inhibited under such conditions (Hanchen et al., 2006). The optimum carbonation conditions for olivine, identified by the authors are 15 MPa $p\text{CO}_2$, 185 °C, using a 0.64 molar NaHCO_3 , and 1 molar NaCl, at which the extent of carbonation, (i.e. the degree of stoichiometric conversion of the silicate to the carbonate), became maximum leveling to a value slightly above 80%. This means that the optimum extent of carbonation is obtained by increasing both the alkalinity and the salinity of the aqueous solution. The alkalinity and salinity at the optimum conditions has to be a compromise between (i) promoting magnesite precipitation (which is favored at high pH), and (ii) not lowering too much the dissolution of olivine (favored at low pH) (Daval et al., 2011; O'Connor et al., 2002). Moreover, the experimental results (Gerdemann et al., 2007) also showed the dependence of the carbonation rate on temperature and $p\text{CO}_2$ (Figure 1-9). Figure 1-11a shows the effect of increase of temperature from room temperature to 250 °C on the extent of reaction. According to this figure, the carbonation reaction is extremely slow or non-existing at the temperatures below 90 °C for olivine carbonation due to slow reaction kinetics, and at temperatures higher than 90°C, the reaction rate increases until 185 °C, which is the optimum temperature for carbonation. As the temperature exceeds 185 °C the reaction rate decreases, but the reasons for such decrease at higher temperatures is not straightforward. However, it could be due to the competition between carbonation and serpentinization reactions, as suggested by the results reported in Dufaud et al. (2009) and King et al. (2010). Figure 1-11b shows the effect of $p\text{CO}_2$ on the rate of carbonation, and it demonstrates that the rate of olivine carbonation increases as a function of $p\text{CO}_2$. The overall carbonation process of Mg-rich olivine close to forsterite (Mg_2SiO_4) composition, has been also addressed by several authors (Bearat et al., 2006; Chen et al., 2006; Dufaud et al., 2009; Jarvis et al., 2009; King et al., 2010; O'Connor et al., 2002), whose results agree with the first order results obtained by Gerdemann et al. (2007) and Giammar et al. (2005).

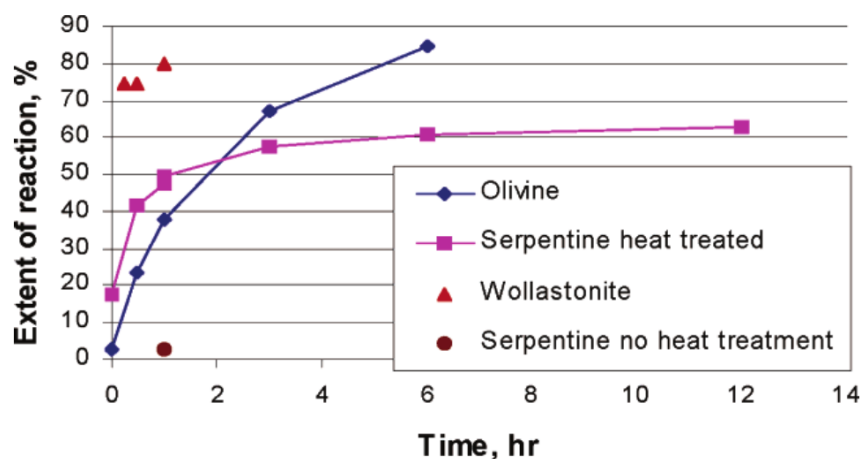


Figure 1-10. Extent of carbonation reaction as a function of time, for experiments conducted at 15 MPa $p\text{CO}_2$, 185 °C, using a 0.64 molar NaHCO_3 /1 molar NaCl solution (Gerdemann et al., 2004).

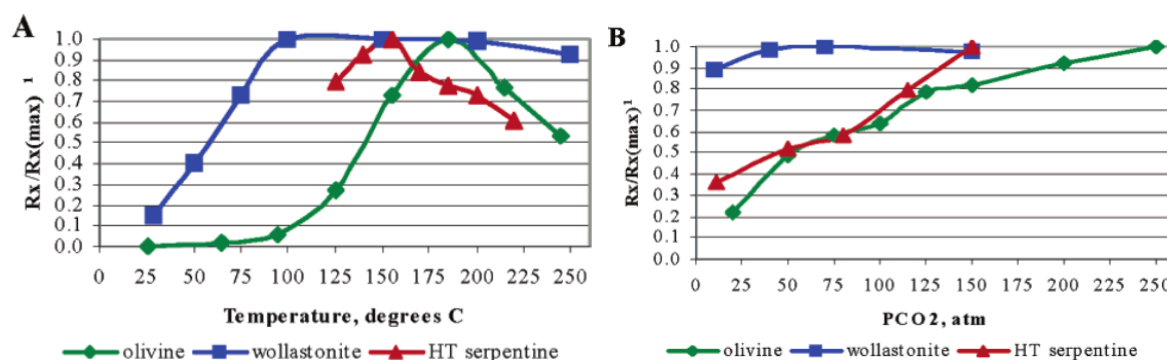


Figure 1-11. variation of normalized reaction rate of carbonation as a function of (a) temperature (b) $p\text{CO}_2$ (Gerdemann et al., 2004).

At temperatures below ~200 °C, the rates of carbonation of silicates can be slowed down by the formation of secondary amorphous silica layers which can passivate the primary mineral surface (Figure 1-12a). A possible mechanism of formation of porous amorphous silica layer has been discussed by (Hellmann et al., 2012), and is shown in Figure 1-12b. This mechanism involves: (i) dissolution at a single reaction front in a thin fluid film in contact with the pristine mineral lattice. All constituent atoms are released to the fluid film at the same stoichiometric rate from the crystal lattice, irrespective of the pH, with no diffusion control and no preferential leaching; (ii) surface layers are formed by the contemporaneous precipitation of a distinct porous amorphous phase; (iii) precipitation of amorphous silica (i.e. acid to circum-neutral pH) occurs even when the bulk solution is under-saturated, which could be attributed to the properties of thin fluid films in contact with mineral surfaces (the dielectric constant of water is different than in bulk fluid). However, this mechanism only explains the formation of amorphous silica with a permeable structure, which does not have a passivating effect, allowing the transfer of ions either ways, a different mechanism must induce passivation within those layers.

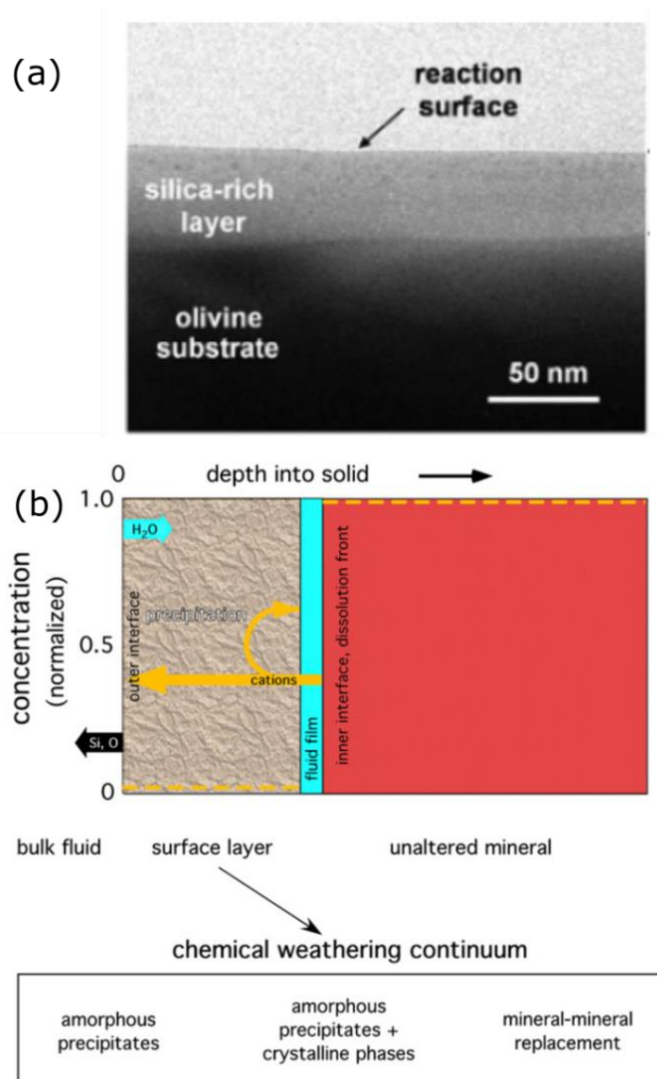


Figure 1-12. (a) Amorphous silica layer formed on olivine substrate (Bearat et al., 2006); (b) Coupled interfacial dissolution–precipitation mechanism proposed by (Hellmann et al., 2012), a formation mechanism of amorphous silica layer during the dissolution of olivine. Supersaturation may occur in the interfacial fluid film, while the bulk remains undersaturated.

The formation of amorphous silica layers with passivating behavior has also been observed by Daval et al. (2011), in a study on coupled weathering–carbonation reactions on olivine. According to this study, amorphous silica layers (20–40 nm) that presumably formed on the olivine surface by dissolution–precipitation became passivating with increasing reaction progress, due to an internal densification process. The authors clearly evidenced a decrease in olivine dissolution rate due to the precipitation of passivating amorphous silica layer. (Putnis, 2009) states that as long as the porous precipitate is in contact with an aqueous solution, its microstructure will continue to evolve with time via dissolution–precipitation reactions, and it is possible that these pores could be closed by precipitation of other mineral phases from the solution. Later, (Sissmann et al., 2013) experimentally showed the formation

of an iron rich silica layer during carbonation of olivine at 120 °C and $p\text{CO}_2 = 280$ bar. At oxidizing conditions, Fe(III) incorporation into amorphous silica layer, or precipitation of Fe(III) clogging the pores of the silica layer acted as a protective layer slowing down the olivine dissolution (Figure 1-13b). However, reducing conditions leads to break down this protective layer, re-initiating olivine dissolution. The authors also pointed out that iron rich phyllosilicate formed at their high temperature experiment (170 °C/ $p\text{CO}_2 = 280$ bar), has less affected the dissolution of olivine than the iron rich silica layer. Formation of porous and non-porous amorphous silica layers have been observed by Daval et al. (2009) during the carbonation of wollastonite (Figure 1-13a).

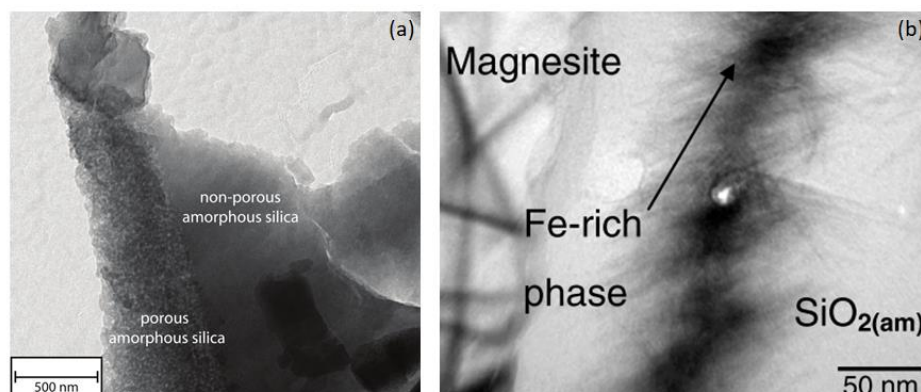


Figure 1-13. (a) Porous and non-porous amorphous silica layers formed during carbonation of wollastonite (Daval et al., 2009). The pores of the non-porous layer are presumably filled with nanometer-sized calcite minerals therefore; it is likely that the transport of Ca-rich aqueous fluids between the wollastonite reaction front and the bulk solution has been occurred; (b) Fe-rich phases located within the $\text{SiO}_{2(\text{am})}$ layer formed during olivine carbonation at 120 °C/ $p\text{CO}_2=280$ bar (Sissmann et al., 2013), potentially inducing the passivation effect.

1.1.6 Ex-situ CO_2 sequestration by mine tailings

Industrial wastes containing Mg and Ca-silicates, oxides and hydroxides are potential feedstocks for ex-situ CO_2 sequestration (Renforth et al. 2011, Bobicki et al., 2012). The key advantages of ex-situ carbonation of mine wastes over natural minerals include low cost and proximity to point sources of CO_2 (Huntzinger et al. 2009b; Gunning et al. 2010; Renforth et al. 2011; Bobicki et al. 2012). Industrial wastes such as steel slags, cement wastes, waste ashes, alkaline paper wastes and mining and mineral processing wastes have shown different degrees and variety of carbonation precipitation (Bobicki et al., 2012). These industrial wastes contribute to offset CO_2 emissions in different scales as shown in Figure 1-14. Among them, mine tailings represents ~17% of CO_2 stabilization of all the technologies available, as shown in Figure 1-15. Mine tailings produced by mafic and ultramafic-hosted ore deposits are rich in Mg-silicate and-hydroxide minerals, such as olivine, pyroxene, serpentine, forsterite, and brucite, in which CO_2 is precipitated as Mg-carbonates. Specially, those containing olivine are interesting since olivine is one of the most suitable mineral for

carbonation (section 1.1.4). At low temperatures ($<100\text{ }^{\circ}\text{C}$), mostly during the passive carbonation of these mine tailings at near surface conditions, hydrated Mg-carbonates such as nesquehite ($\text{MgCO}_3 \cdot 3\text{H}_2\text{O}$), lansfordite ($\text{MgCO}_3 \cdot 5\text{H}_2\text{O}$), hydromagnesite $\text{Mg}_5(\text{CO}_3)_4(\text{OH})_2 \cdot 4\text{H}_2\text{O}$ and dypingite ($\text{Mg}_5(\text{CO}_3)_4(\text{OH})_2 \cdot 5\text{H}_2\text{O}$), are precipitated. However, at high temperature ($100^{\circ}\text{C} - 300^{\circ}\text{C}$) engineered systems, magnesite (MgCO_3) is the most stable Mg-carbonate resulted from the ex-situ CO_2 sequestration.

Mine tailings with passive carbonation rates of $\sim 10^{-4}$ to 10^{-2} t CO_2 /t tailings/yr has shown to offset $>100\%$ industry specific CO_2 emissions, (Power et al., 2013; Wilson et al. 2009a,b, 2011; Bea et al. 2012; Pronost et al. 2012; Harrison et al. 2013). Mine tailings carbonation can be allelerated by increasing surface area by crushing, heat treatment, and applying high T and high $p\text{CO}_2$, and addition of organic ligands (Bobicki et al., 2012; Harrison et al., 2013; Power et al., 2013; Wilson et al., 2014). For instance, Harrison et al. (2013) documented an acceleration of ~ 240 times over passive rates of brucite carbonation in alkaline slurry by supplying gas similar in composition to flue gas (Power et al., 2013). In certain industries, carbonation of provides an opportunity to “close the loop” on CO_2 emissions (Power et al., 2013).

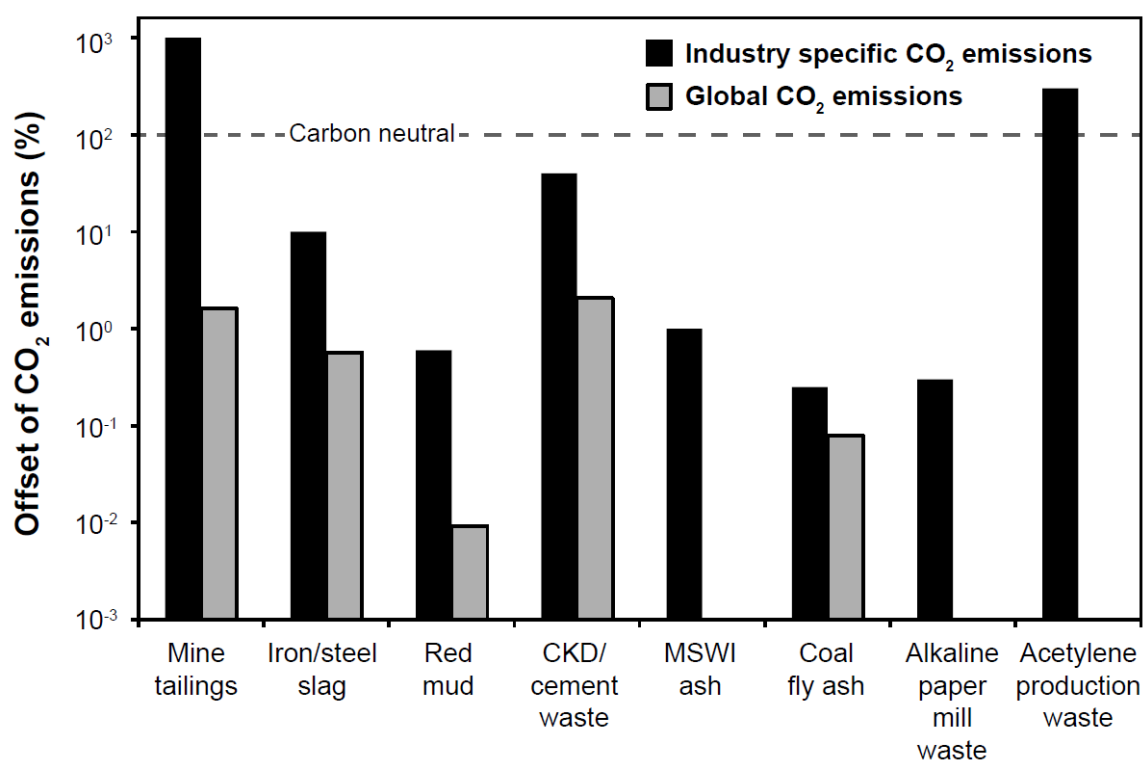


Figure 1-14. Percent offset of CO_2 emissions for specific industries and global annual emissions provided via carbonation of various industrial waste materials, from Power et al. (2013). CKD = cement kiln dust; MSWI = municipal solid waste incinerator. As mentioned by the author, the data were insufficient to calculate the offset of total annual global CO_2 emissions provided via carbonation of MSWI ash, acetylene production, and alkaline paper mill waste.

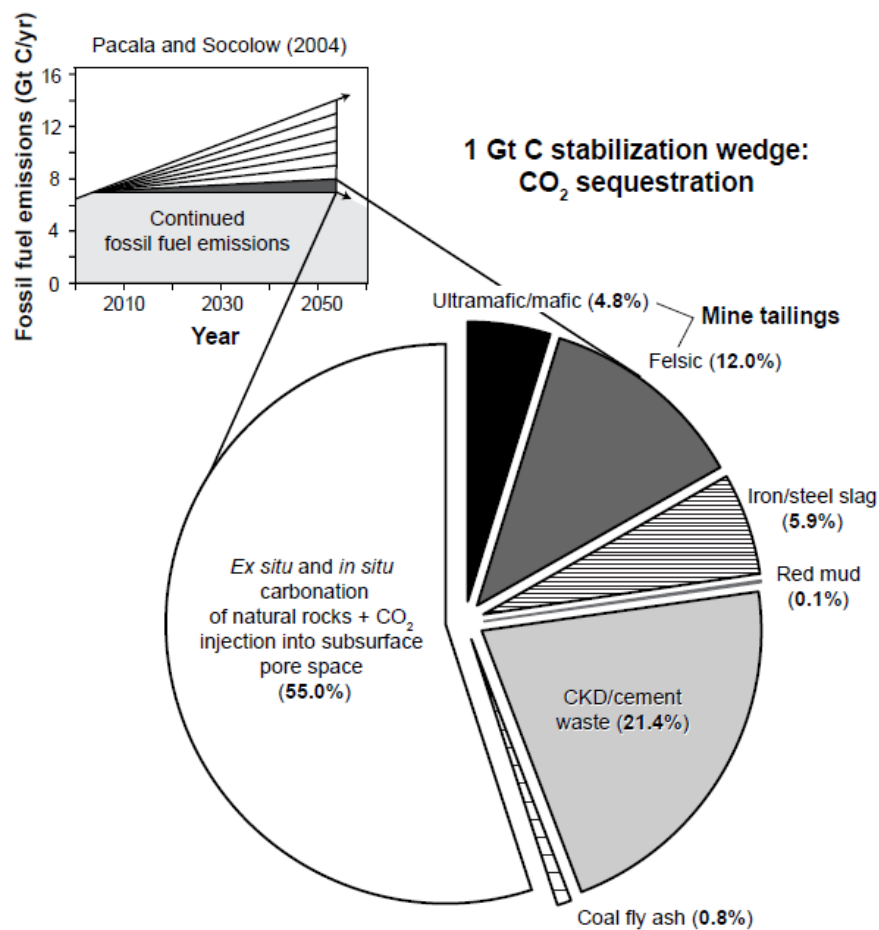


Figure 1-15. Contribution of different carbon sequestration technologies towards a 1 Gt C/yr “stabilization wedge” (I. M. Power et al., 2013). “CKD” is the abbreviation for cement kiln dust.

1.2 Hydrogen production from Fe-rich minerals

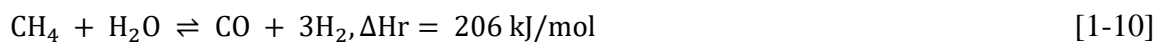
Large quantities of hydrogen is naturally produced by the serpentinization of oceanic lithospheric mantle particularly along the slow spreading ridges (Cannat et al., 2013, 1992; 2002; Früh-Green et al., 2004; Klein et al., 2009). Fluids ranging from pH~3 (at high temperatures) to 12 (at low temperatures), with high hydrogen, therefore highly reducing, and methane concentrations, make these systems one of the most extreme environments on Earth and provide energy to deep oceanic biosphere (Klein et al., 2009 and references therein). Hydrogen is produced when H₂O oxidizes the Fe²⁺ in primary minerals such as olivine [(Mg,Fe)₂SiO₄] in the oceanic lithosphere. The equation for olivine serpentinization [1-13] and more details are given in section 1.3.2 below. Experimental and theoretical studies on serpentinization of olivine lead to following important points (1) high hydrogen concentrations are associated with low aSiO₂ (Allen and Seyfried, 2003; Berndt et al., 1996; Katayama et al., 2010; McCollom and Bach, 2009; Wetzell and Shock, 2002); (2) iron distribution among serpentine, magnetite and brucite play a key role in quantification of hydrogen (Klein et al., 2009; Marcaillou et al., 2011); (3) olivine dissolution is the rate limiting process and could be enhanced by, increasing the reactive surface area of olivine, high temperatures and addition of aluminum (Al) (Andreani et al., 2012; Malvoisin et al., 2012; McCollom et al., 2016).

Today, hydrogen (H₂) has become an important energy vector which produces highest specific energy (~120 MJ/kg) after radioactive substances upon its combustion, producing steam as the only bi-product (eq. 1-9).



Owing to these two properties, hydrogen has enormous industrial applications. Hydrogen is used mainly used in the space industry as the rocket engine fuel, since 1 kg of hydrogen contains 3 times more energy than 1 kg of gasoline. Secondly, hydrogen is used to produce electrical energy by fuel cell technology (eg. conversion of chemical potential energy into electrical energy), mainly used to produce electricity directly onboard in electrical vehicles. Third major industrial application of hydrogen is the clean transportation by “zero emission vehicles” since hydrogen combustion does not produce greenhouse gases. Hydrogen is also used for the industrial production of ammonia (NH₃) by Haber process, production of methanol (CH₃OH) and certain pharmaceuticals.

Currently, hydrogen is produced by “steam methane reforming” where methane is reacted with steam at high temperature (700 – 1100 °C) and in the presence of a metal-based catalyst (nickel), according to the equation below (eq. 1-10).



This method is catalyst-based, fossil fuel dependent and high temperature process making it a costly industry (Marbán and Valdés-Solís, 2007). As a result, alternate methods for hydrogen production have drawn the attention of scientific research. Some alternate

methods currently being investigated are; (i) fermentation, where biomass is converted into sugar-rich feedstocks that can be fermented to produce hydrogen (Balat and Kirtay, 2010; Nath and Das, 2003; Ni et al., 2006; Parthasarathy and Narayanan, 2014; Tanksale et al., 2010); (ii) splitting water, either by electrolysis, photochemical methods, photo-electrochemical methods, photo-biological methods (by using microbes, such as green algae, which consume water in the presence of sunlight, producing hydrogen as a byproduct,) or by using high temperature produced by nuclear reactors or solar concentrators (Chen et al., 2010; Han et al., 2007; Ismail and Bahnemann, 2014; Matsuoka et al., 2007; Nann et al., 2010). Once produced, hydrogen can be stored either as a compressed gas, a refrigerated liquefied gas, a cryo-compressed gas or in hydrides (Barthelemy et al., 2017).

More recently, inspired by the natural hydrogen production by interaction of ocean floor rocks and hot water at the mid oceanic ridges, a new method has been investigated (Malvoisin et al., 2013). In the ocean floor, Fe(II) in olivine and pyroxenes in the basaltic oceanic crust is oxidized into Fe(III) in magnetite, while reducing water into hydrogen, during the serpentinization reaction. The method describes the hydrogen production by treating iron rich minerals with water at hydrothermal conditions, according to the equation [1-11] given below.

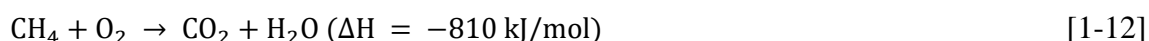


Malvoisin et al. (2013) showed that high purity hydrogen could be produced by reacting a basic oxygen furnace steel slag (BOF), which contained iron in the form of 2.7 wt.% Fe(0), 20.58 wt.% FeO and 3.16 wt.% Fe₂O₃ respectively. The reaction of steel slag with pure water at 250 °C and 50 MPa produced approximately 5 nL of H₂ per kg of slag within 3 days of reaction. A recent study by Crouzet et al. (2017), experimentally demonstrated the production of hydrogen by reacting pure FeO, which has a much simple chemistry than the steel slag. The experiments were conducted at 200 -300 °C, under acidic pH conditions obtained by two organic acids (acetic and oxalic acid), and HCl. The authors showed that the production of H₂ is much more efficient under acidic conditions, and that acetic acid was much more efficient than both oxalic and HCl acid. It is proposed that it increases the efficiency of hydrogen production by ligand promoted dissolution of FeO. However, it was also shown that the positive kinetic effect of mild acetic acid solutions over H₂ yield evidenced on FeO does not apply directly to steel slags which buffer the pH to high values due to the presence of large amounts of CaO.

These two studies demonstrate the possibility of producing hydrogen by reacting Fe bearing minerals with water at temperatures >200 °C, much lower temperatures compares to steam methane reforming. The study by (Crouzet et al., 2017), serves as a model for any mineral, steel slag or mine waste containing Fe(II), but it also shows that the ligand promoted dissolution could not be applicable to those containing Ca, which buffers the mild acidity. Consequently, differences in chemical compositions could result in different mechanisms and efficiencies of hydrogen production by this method.

1.3 Abiotic hydrocarbons

Hydrocarbons (HC) are compounds containing only carbon and hydrogen, which could exist either as acyclic (aliphatic) hydrocarbons (ex. methane, ethane, propane), or as cyclic (aromatic) hydrocarbons (ex. benzene, toluene). Hydrocarbons are known to generate naturally in sedimentary basins through the process of diagenesis of organic materials, resulting into petroleum (heavy HC in liquid form, C₅₊) or natural gases (light HC gas form, C₁-C₄), which play an important role as present day primary sources of energy. These are combustible fuels, which accounts for 85.5% of world's energy consumption by 2016 (Petroleum, 2016). For example, the combustion of one mole of methane yields 810 kJ of energy as shown in the equation below;



The origin of hydrocarbons can be two fold; biotic or abiotic. Biotic hydrocarbons are those produced by degradation of organic matter by microbes at low temperature (biogenic), or by thermal decomposition of high molecular weight organic matter such as kerogen or oil (thermogenic) (Etiope and Sherwood Lollar, 2013). Most of the hydrocarbons exploited today are biotic hydrocarbons. The abiotic hydrocarbons are those formed by non-organic reactions, which does not involve organic material at all. These are known to occur in trace amounts (ppbv and ppmv) in geological fluids (Capaccioni et al., 2004; Fiebig et al., 2007). Some of the reactions by which abiotic methane is formed are summarized in table 1-1, obtained from Etiope and Sherwood Lollar (2013). The production mechanisms of abiotic hydrocarbons can be divided in to two main classes: the high temperature magmatic reactions (500 °C < T < 1500 °C) and the low temperature water-rock reactions (400°C < T). However, up to about 90 vol.% of abiotic hydrocarbons are known to generate through low temperature water-rock interactions occurring in Precambrian crystalline shields and serpentinized ultramafic rocks in submarine peridotite-hosted hydrothermal systems, continental ophiolites and peridotite massifs (Etiope et al., 2011; Etiope and Schoell, 2014; Etiope and Sherwood Lollar, 2013; Lollar et al., 2008; Shuai et al., 2018).

1.3.1 Distinguish biotic Vs. abiotic hydrocarbons

a. Carbon-deuterium (CD) diagram

Biotic and abiotic hydrocarbons are hardly distinguished from each other; a tentative issue is to use their isotopic composition: $\delta^{13}\text{C}$ (a measure of the ratio of stable isotopes $^{13}\text{C}/^{12}\text{C}$) and δD (a measure of the ratio of stable isotopes $^2\text{H}/^1\text{H}$) (Figure 1-16a). Although empirical, the plot of $\delta^{13}\text{C}$ vs. δD or carbon-deuterium diagram (CD diagram), provides a first order evaluation for the origin of hydrocarbons (Tissot and Welte, 1984; Whiticar, 1999). A recently updated CD diagram by Etiope and Sherwood Lollar (2013) is shown in Figure 1-16b and simplified in Figure 1-16a. Important points on this diagram as summarized by (Etiope and Sherwood Lollar, 2013) are:

1. $\delta^{13}\text{C}$ and δD values of abiotic CH₄ vary in a wide range

2. It partly overlaps with both the microbial and thermogenic fields
3. Abiotic data are distinguished from biotic gas fields by an overall shift toward more ^{13}C - and D-enriched values.
4. ^{13}C - ^2H enriched (“heavy” abiotic CH_4) values are obtained in the high temperature volcanic-hydrothermal systems, and in the serpentinized ultra- mafic rocks of Lost City, Chimaera, Zambales, Semail, and Genova.
5. ^{13}C -D depleted (“light” abiotic CH_4) appears to be more closely associated with gases found in the Precambrian crystalline igneous rocks of South Africa, Canada and Scandinavia, and in the present-day serpentinization seeps of Poison Bay (New Zealand), Othrys (Greece) and Happa (Japan).

The $\delta^{13}\text{C}$ and δD of ^{13}C - and ^2H - enriched abiotic CH_4 vary between $\delta^{13}\text{C} > -20\text{‰}$ and $\delta\text{D} > -200\text{‰}$, whereas, those with $\delta^{13}\text{C}$ and δD of ^{13}C - and ^2H - depleted abiotic methane ranges between $\delta^{13}\text{C} -30$ and -47‰ and $\delta\text{D} < -200\text{‰}$ (Etiope and Sherwood Lollar, 2013). However, as mentioned earlier, this method is a first order method to distinguish biotic and abiotic hydrocarbons.

b. Methane clumped isotopes

As described earlier, distinguishing abiotic gas from biotic gas is sometimes challenging because their isotopic and molecular composition may overlap. The clumped-isotope analysis on hydrocarbons (methane clumped isotopes) is a new tool in the process of developing to identify the origin of hydrocarbons. “Clumped isotopes” refers to molecules with two or more rare, generally heavy isotopes (Eiler, 2013, 2007). For CH_4 , this refers to ^{13}C and one or more D substitutions in the same molecule. The principle of clumped isotope technique rely on the fact that, in a population of CH_4 that are in isotopic equilibrium with each other, the abundance of multiply substituted isotopologues relative to a random distribution is a function of temperature (Stolper et al., 2014b; Wang et al., 2015; Webb and Miller, 2014). Therefore the methane clumped isotope technique allows to be used as a geothermometer to construct the formation temperature of methane, and hence an indirect additional line of evidence regarding methane origin (Etiope and Sherwood Lollar, 2013; Stolper et al., 2014a; Wang et al., 2015). Besides the robust differentiation between microbially produced CH_4 formed at temperatures $< 80^\circ\text{C}$ and magmatic CH_4 produced by abiotic organic synthesis at a high temperature hydrothermal vent may be possible by this method, Etiope and Sherwood Lollar (2013) highlighted that there can be certain overlaps even in the methane clumped isotope approach of distinguishing the methane origin, due to the processes such as low temperature methanogenesis via diagenesis of organic matter, versus microbial CH_4 production by thermophiles, or abiotic CH_4 synthesis via low temperature-water rock reactions in continental ultramafic rocks.

Table 1-1. Chemical reactions by which the abiotic methane forms (summarized from Etiope and Sherwood Lollar (2013))

Process	T (°C)	Main reactions
Primordial	-	Extra-terrestrial methane synthesis
Metal carbide hydrolysis/ hydrogenation (in mantle)	500 – 1500	$\text{Al}_3\text{C}_3 + 12\text{H}_2\text{O} = 3\text{CH}_4 + 4\text{Al}(\text{OH})_3$
Reduction of CO, CO ₂ and carbonates with H ₂ O (in mantle)	500 – 1500	$\text{Fe}_3\text{C} + 4\text{H}^+ = 3\text{Fe} + \text{CH}_4$ $8\text{FeO} + 3\text{CaCO}_3 + 2\text{H}_2\text{O} = 4\text{Fe}_2\text{O}_3 + \text{CaO} + \text{CH}_4$
Respeciation of C-O-H fluids (eg. Magma cooling)	<500 – 600	$\text{CO}_2 + 4\text{H}_2\text{O} = \text{CH}_4 + \text{O}_2$
Post magmatic reactions	400-500	$\text{CO}_2 + 4\text{H}_2\text{O} = \text{CH}_4 + \text{O}_2$ $8\text{FeO} + 2\text{H}_2\text{O} + \text{CO}_2 = 4\text{Fe}_2\text{O}_3 + \text{CH}_4$ $2\text{C} + \text{H}_2\text{O} = \text{CO}_2 + \text{CH}_4$
Carbonate-graphite metamorphism	<400	$\text{Mg}_3\text{Si}_4\text{O}_{10}(\text{OH})_2 + 3\text{CaCO}_3 + 6\text{C} + 5\text{H}_2\text{O} = 3\text{CaMg}(\text{CO}_3)_2 + 4\text{SiO}_2 + 3\text{CH}_4$
Iron carbonate decomposition	300	$3\text{FeCO}_3 + w\text{H}_2\text{O} = \text{Fe}_3\text{O}_4 + x\text{CO}_2 + y\text{CO} + z\text{H}_2 + \text{HCs}$
Thermal decomposition of carbonate and direct reduction to CH ₄		$\text{CaCO}_3 + 4\text{H}_2 = \text{CH}_4 + \text{Ca}(\text{OH})_2 + \text{H}_2\text{O}$ $\text{MgCO}_3 + 4\text{H}_2 = \text{CH}_4 + \text{Mg}(\text{OH})_2$ $\text{FeCO}_3 + 5\text{H}_2 = \text{CH}_4 + \text{FeO} + \text{H}_2\text{O}$
Uncatalyzed aqueous CO ₂ reduction	150-300	Variable reactions with CO ₂ , CO, HCOOH, NaHCO ₃ , NaHCOO and H ₂
Fischer-Tropsch type reactions:	25-500	
Sabatier reaction		$\text{CO}_2 + 4\text{H}_2 = \text{CH}_4 + 2\text{H}_2\text{O}$
Reverse water gas shift+FT		$\text{CO}_2 + 4\text{H}_2 = \text{CO} + 2\text{H}_2\text{O}$ $\text{CO} + 3\text{H}_2 = \text{CH}_4 + 2\text{H}_2\text{O}$
In aqueous solutions:		$\text{CO}_3^{2-} + 4\text{H}_2 = \text{CH}_4 + \text{H}_2\text{O} + 2\text{OH}^-$

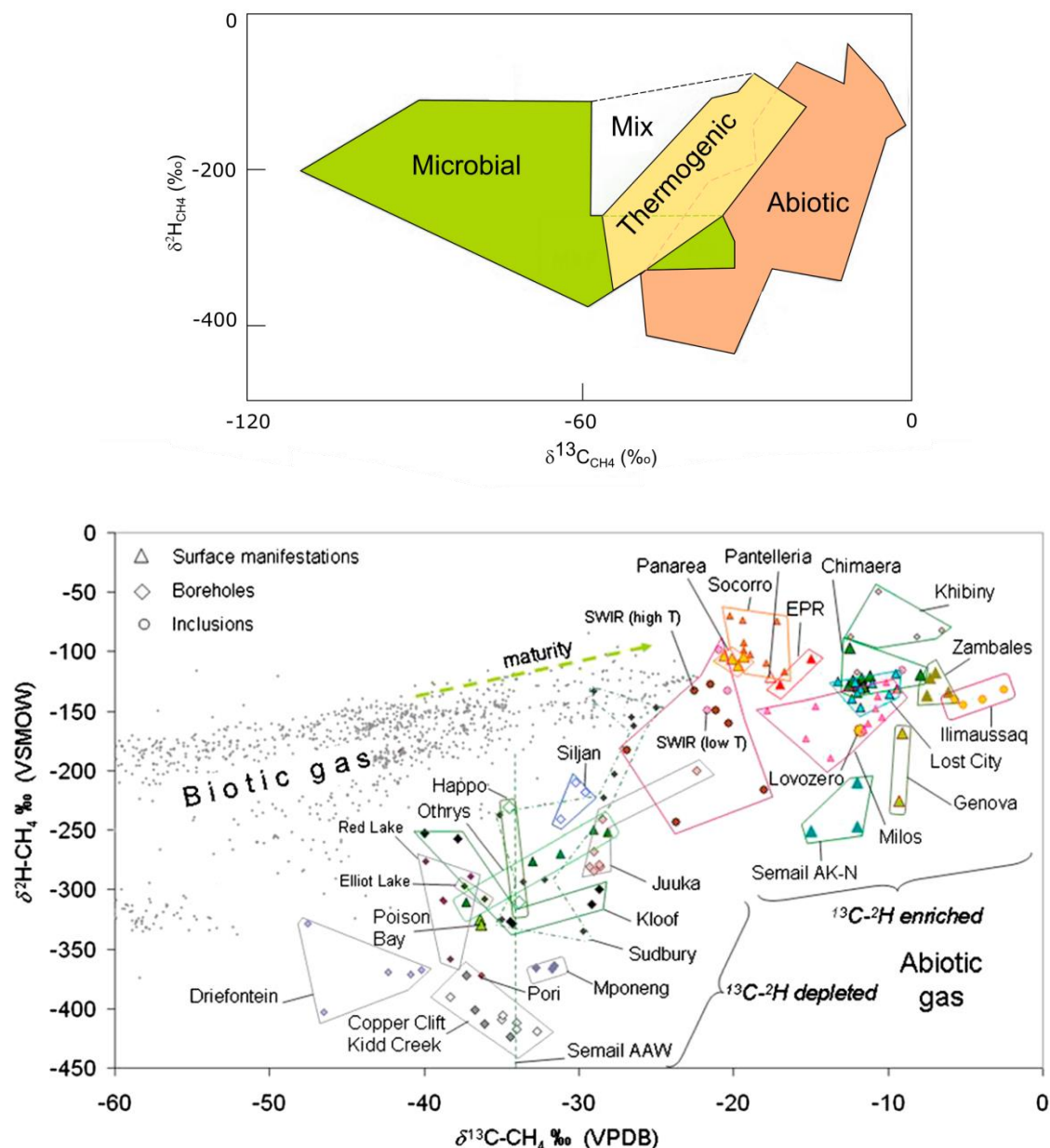
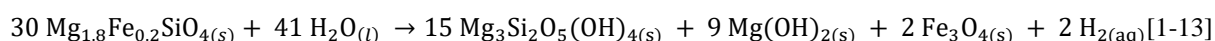


Figure 1-16. $\delta^{13}\text{C}$ vs. $\delta^2\text{H}$ for CH_4 , (a) for microbial, thermogenic and abiogenic gases [modified from (Etiope, 2015) page 6]; (b) for actual gas samples which are considered to have a dominant abiogenic component (Etiope and Sherwood Lollar, 2013). The samples are from various geological settings (1) surface manifestations in serpentinized ultramafic rocks; (2) boreholes in deep Precambrian shield crystalline rocks; (3) fluid inclusions in crystalline intrusions; and (4) volcanic and high temperature hydrothermal systems.

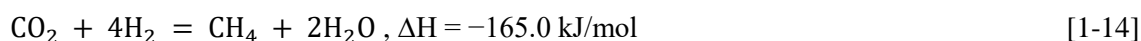
1.3.2 Natural occurrences of abiotic hydrocarbons

In nature, abiotic hydrocarbons occur in various settings such as mid oceanic hydrothermal systems, volcanic and geothermal systems, sedimentary basins, Precambrian crystalline basement as shown in Figure 1-17, where abiotic hydrocarbon could be generated through magmatic or gas-water-rock interactions (Etiope and Sherwood Lollar, 2013) as discussed above (table 1-2). Among the various settings, hydrothermal vents in mid-oceanic ridges are of special interest since it is believed that early forms of life originated in such systems. Hydrothermal vents are the result of sea water circulation through fractures in oceanic crust created due to the extension during spreading the oceanic crust. Close to ridge axis, cold sea water is heated while it penetrates through the oceanic crust, thus dissolving minerals. As this hot fluid rises back to the surface, it cools down and precipitates specially the metal sulfides forming chimneys through which the hot (90 -350 °C) mineral-rich fluids are venting (Figure 1-18).

Fluids rich in molecular hydrogen and hydrocarbons have been widely documented in hydrothermal systems along mid-oceanic ridges, such as Rainbow hydrothermal field, Lost city, Logatchev, Ashedze (Charlou et al., 2013; J L Charlou et al., 2002; Konn et al., 2009; Petrova et al., 2009; Giora Proskurowski et al., 2008; Schmidt et al., 2007; Von Damm, 2001), (Figure 1-19). The compositions of fluids venting from the major hydrothermal fields along the mid-Atlantic ridge are given in table 1-1. High concentrations of hydrogen (7.8-26.5 mmol/L), CO₂ (3.7-17 mmol/L), methane (0.8-2.6 mmol/L) and small concentrations of ethane, propane and butane were reported. It is admitted that the large flux of H₂ results from the intense serpentinization of olivine present in peridotitic rocks from the oceanic lithosphere, which is the major geochemical process known to release significant amounts of hydrogen. The serpentinization of olivine (Fo90) can be written as follows;

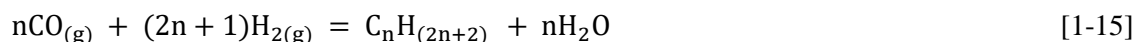


The production of H₂ in this reaction creates highly reducing conditions, sufficiently favorable for reduction of inorganic carbon into methane and other light hydrocarbons with an abiotic origin. However, the mechanism of conversion of inorganic carbon into reduced carbon species is not clear until today, but the Sabatier or Fischer-Tropsch type synthesis are thought to be the most plausible reactions for the formation of abiotic hydrocarbons on the Earth (Charlou et al., 2002; Giuseppe Etiope et al., 2011; Foustoukos and Seyfried., 2004; Horita and Berndt, 1999; Mccollom and Seewald, 2007; Proskurowski et al., 2008; Szatmari, 1989), equations [1-14 and 1-15]. The Sabatier reaction involves the reaction of gaseous hydrogen with carbon dioxide at elevated temperatures (optimally 300–400 °C) and pressures in the presence of a catalyst (eg. nickel, Ni) to produce methane and water as shown by equation 1-13.



In contrast, the Fischer-Tropsch reaction involves the reaction of gaseous hydrogen with carbon monoxide (CO), typically at temperatures of 150–300 °C and pressures of one to

several tens of atmospheres, in the presence of metal catalysts (eg. Ruthenium, Ru) to produce simple alkanes and water as given by the equation 1-14.



Both the Sabatier reaction and Fischer-Tropsch reaction are gas-phase reactions, extensively used in industry to synthesize hydrocarbons. For both reactions, synthetic catalysts based on iron (Fe), nickel (Ni), cobalt (Co) and ruthenium (Ru) are used. However, recent experimental studies have demonstrated that CO_2 dissolved in water can be converted to CH_4 and other hydrocarbons in the presence of ultramafic rocks under reducing hydrothermal conditions; suggesting that natural minerals with transition metals can catalyze the formation of abiogenic CH_4 . The next section includes a bibliographic review on some experimental works simulating abiogenic hydrocarbons synthesis under hydrothermal conditions, emphasizing the role of natural minerals as catalysts for Fischer-Tropsch type (FTT) synthesis of abiogenic hydrocarbons.

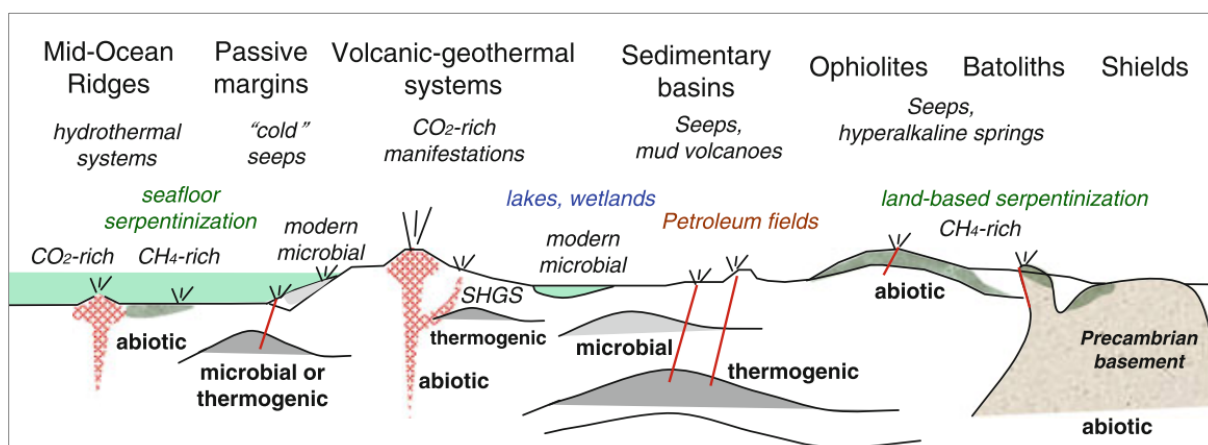


Figure 1-17. The various geological environments for methane production on Earth (Etiope, 2015)

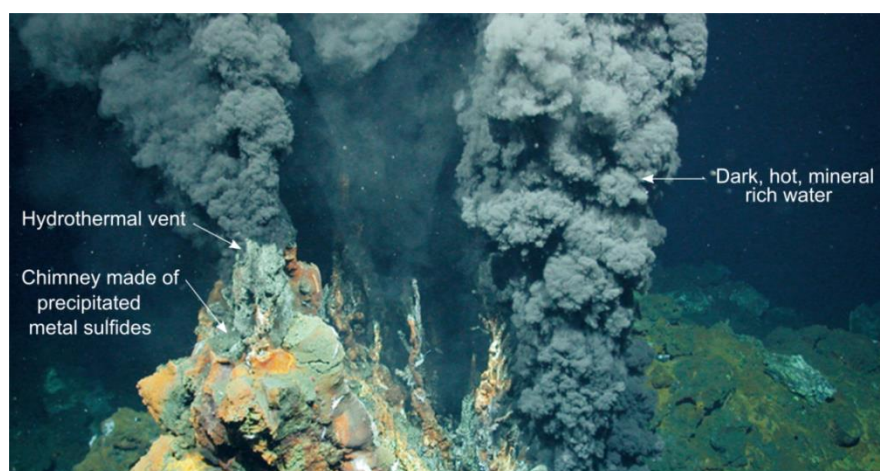


Figure 1-18. Hydrothermal vents in the deep sea mid-oceanic ridge system (Copyright: World Ocean Review)

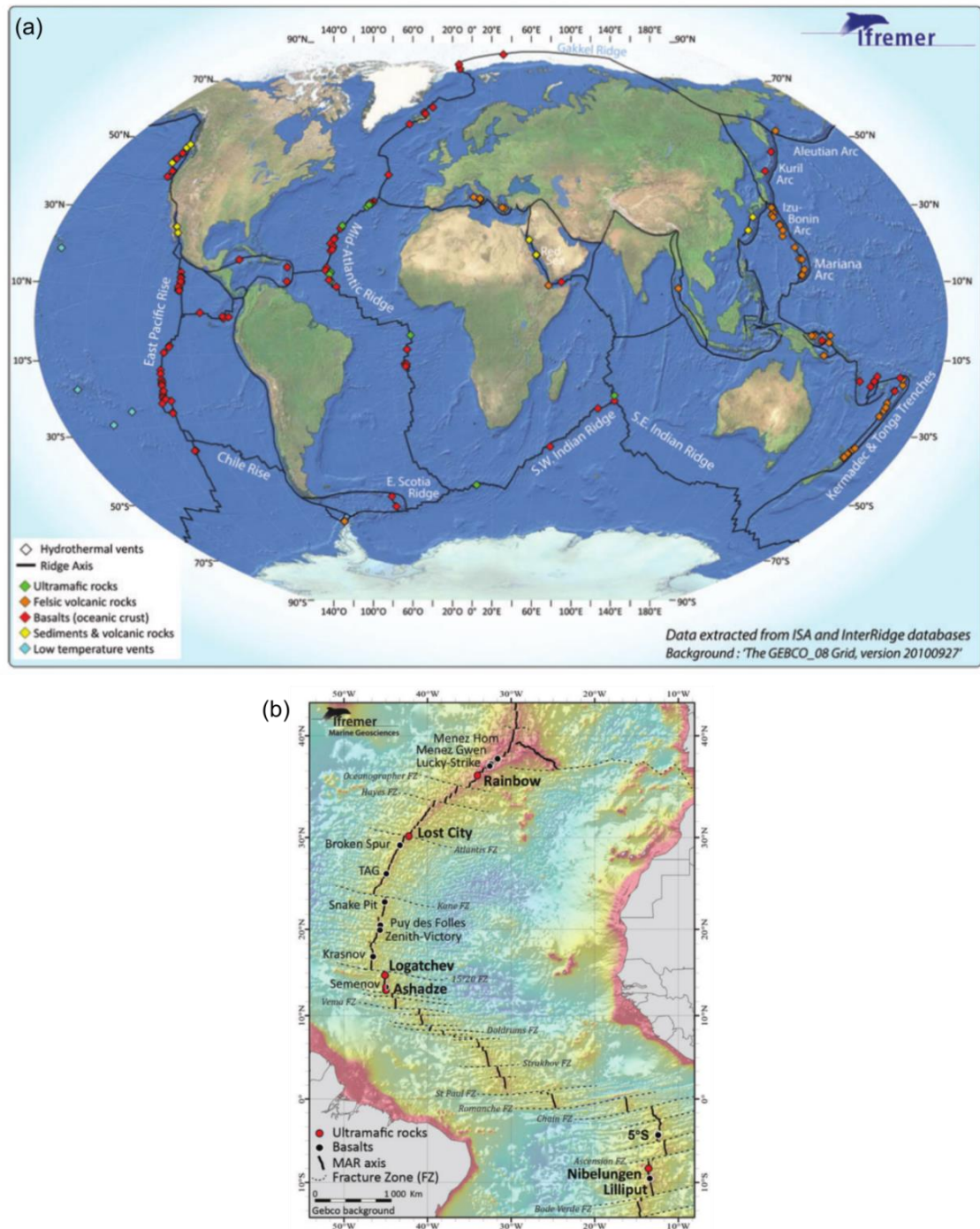


Figure 1-19. (a) The MOR system showing the presently known and sampled hydrothermal sites (b) TheMAR axis between 10°S and 45°N showing the known hydrothermal vent fields. Black circles represent basalt-hosted hydrothermal fields. Red circles represent ultramafic-hosted vent fields (Konn et al., 2015).

Table 1-2. Composition of fluids sampled from mid-Atlantic ridge hydrothermal fields (from Konn et al., 2015).

Element	Lost city 30°07'N	Rainbow 36°14'N	Logatchev 1 14°45'N	Logatchev 2 14°45'N	Ashadze 1 12°58'N	Ashadze 2 12°59'N
T (°C) max	94	365	359	320	372	>296
pH	12.1	3	3.9	4.2	3.1	4.1
Total gas volume (mL/kg)	211	813	525	527	687	776
H ₂ (mmol/L)	7.8	12.9	12.5	11.1	19	26.5
CO ₂ (mmol/L)	-	17	4.4	6.2	3.7	nd
CH ₄ (mmol/L)	0.9	1.65	2.6	1.2	1.2	0.8
C ₂ H ₆ (μmol/L)	0.67	0.83	0.77	0.19	0.17	5.7
C ₃ H ₈ (μmol/L)	0.07	0.046	0.024	0.011	0.02	0.21

1.3.3 Laboratory simulation of abiotic hydrocarbon production: the role of mineral catalysts

Number of experiments on abiotic hydrocarbon generation have been conducted at P/T conditions relevant to serpentinization at mid-oceanic ridges (Berndt et al., 1996; Berndt et al., 1996; Fu et al., 2007; Horita and Berndt, 1999; McCollom and Seewald, 2001; Fu et al., 2008). These studies focus on production of abiotic methane and light hydrocarbons catalyzed by minerals precipitated in the sea floor hydrothermal vent environment or closely associated to serpentinization; for instance, magnetite (Fe₃O₄), awaruite (Fe₃Ni), chromite or hydrothermally precipitated Fe-Ni alloys. More details on the catalytic reduction of carbon into hydrocarbons, and related thermodynamic and kinetic constraints will be further discussed below.

1.3.3.1 Thermodynamic and kinetic control on abiotic methane formation

The speciation of carbon at the upper mantle to crustal P/T and fO_2 conditions depicts that CO₂ is thermodynamically more stable over methane. For example, pristine magmatic-derived fluids, such as magmatic volatiles trapped in vesicles within seafloor basalts, are characterized by very high CO₂/CH₄ ratios (Kelley, 1996; Mathez, 1984; Pineau and Javoy, 1983). On the other hand, the oxidizing conditions at Earth's surface ensure that CO₂ and bicarbonate (HCO₃⁻), are the predominant forms of dissolved carbon in seawater, in fracture-filling groundwater, and in shallow pore waters (McCollom, 2013). This means that the inputs of carbon to Earth crust from above (earth surface) and below (upper mantle) are in highly oxidized forms (i.e. CO₂, HCO₃⁻). Therefore, any hydrocarbon found in fluids circulating in Earth's crust that do not derive from deep within the mantle or from a biologic source must be formed by abiotic reduction of inorganic carbon within the crust itself (McCollom, 2013).

Two sets of conditions which favor the formation of methane via Sabetier reaction [equation 1-14] have been identified (McCollom, 2013; Mccollom and Seewald, 2007). The first, is decrease in temperature which stabilizes methane over CO₂ at the P/T and fO_2

prevailing at the crustal level, as shown by Figure 1-20. The second is an increase in f_{H_2} , for instance, by water-rock interactions in the sea floor. In that case, this means that the predominant equilibrium carbon species can shift from CO_2 to CH_4 as fluids interact with rocks, even without a change in temperature (McCollom, 2013).

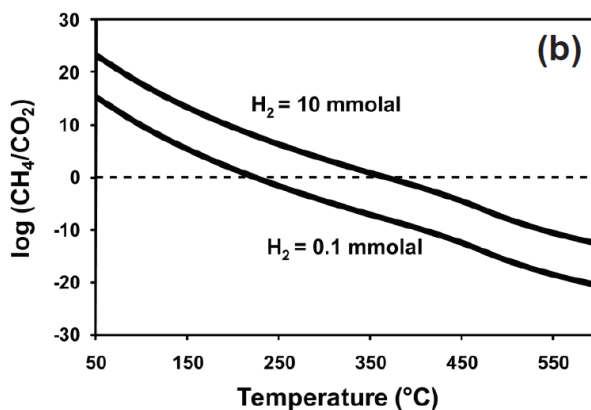


Figure 1-20. Variation of Log (CH_4/CO_2) as a function of temperature obtained from (McCollom, 2013). The calculated equilibrium (CH_4/CO_2) ratios as a function of temperature at two values of H_2 concentration that bracket those found in reducing environments within the crust are shown. Data shown are for a pressure of 50 MPa. Values for log K calculated using thermodynamic data from SUPCRT92 (Johnson et al. 1992) and Shock et al. (1989).

Although the thermodynamic conditions such as those explained above, could favor the formation of methane, kinetic inhibitions could still prevent the reaction from occurring. Seemingly, even at high P/T conditions (-close to serpentinization) and high concentration of H_2 , only traces of inorganic carbon has been converted into hydrocarbons (eg. <2.%) in hydrothermal experiments after months of reaction, indicating that formation of methane even at temperatures of 300 °C is kinetically extremely slow (Berndt et al., 1996; Berndt et al., 1996; Fu et al., 2007; Horita and Berndt, 1999; McCollom and Seewald, 2001; Fu et al., 2008).

Seewald et al., (2006) conducted experiments to study the speciation of carbon at sub-seafloor hydrothermal conditions (150 -300 °C and 300 bar), by reacting aqueous fluids containing H_2 and various sources of carbon, such as CO_2 , CO, $HCOOH$, $NaHCO_3$, $NaHCOO$. In that experiment, the reduction of CO_2 into methane was found to occur via a step-wise process involving $HCOOH$, CO, CH_2O , and CH_3OH without any solid minerals. This process is schematically shown in Figure 1-21. The compounds such as $HCOOH$ and CO were found to equilibrate rapidly whereas the reduction of CH_3OH to methane was kinetically hindered resulting accumulation of high concentrations of methanol regulated by metastable thermodynamic equilibrium. The experiments of Seewald et al. (2006) were conducted without any potential mineral catalyst for abiotic hydrocarbon production. Even though the mechanism is still not very clear, in natural systems, the abiotic hydrocarbons are thought to occur through FTT reactions i.e. surface catalyzed reduction of inorganic carbon into organic compounds.

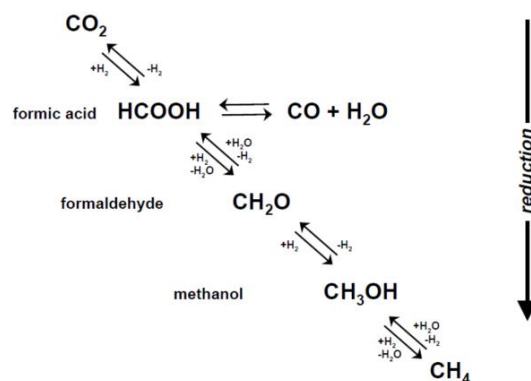


Figure 1-21. Schematic representation of (a) redox reactions that may regulate the speciation of single carbon compounds under hydrothermal conditions (Seewald et al., 2006) (b) organic compounds and their relative concentrations (numbers given in blue boxes) observed by (McCollom et al., 1999) via FTT synthesis at 175 °C using formic acid (-source of H and C) and montmorillonite (-as a potential catalyst).

1.3.3.2 Fischer-Tropsch type (FTT) synthesis

Based on the theoretical and experimental evidences, two major processes of abiotic hydrocarbons formation on Earth have been identified (i) magmatic processes, and (ii) gas-water-rock interactions (Etiope and Sherwood Lollar, 2013). The Fischer-Tropsch type (FTT) synthesis comes under the second category and is one of the most invoked pathways of production of abiotic hydrocarbons in nature. In a geological context, this reaction refers to the reduction of any inorganic carbon source into organic compounds on the surface of a heterogeneous catalyst. The first step involves the binding of carbon source, most commonly CO, or CO₂ on to a catalyst surface by chemisorption, to form carbonyl unit (-C=O) which then undergoes a cascade of reduction to surface bound carbide (-C), methylene (-CH₂) and methyl (-CH₃) groups (McCollom, 2013). The formation of alkanes with >C1 occurs by the addition of methylene groups by polymerization and the chain growth terminates by addition of a methyl group or a hydrogen rather than another methylene group (Figure 1-22a). The hydrocarbons formed according to this type of polymerization are known to exhibit a linear decrease in their abundance as a function of number of carbons in the carbon chain, according to Schulz-Flory distribution (Flory, 1936; Schulz, 1999), as shown by Figure 1-22b.

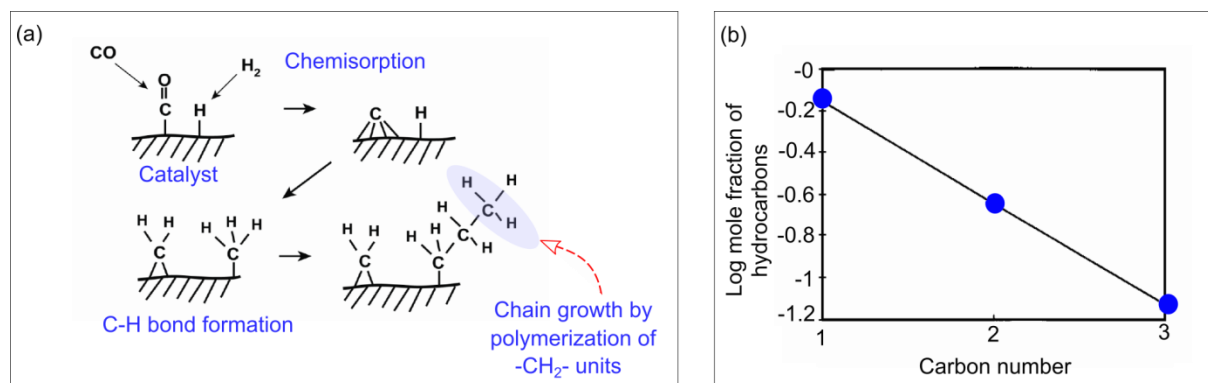


Figure 1-22. (a) Generalized reaction mechanism for Fischer-Tropsch synthesis of hydrocarbons, modified from (McCollom, 2013). The reaction is initiated with binding of CO to the catalyst surface to form a carbonyl unit ($-\text{CO}$), which then undergoes sequential reduction to surface-bound carbide ($-\text{C}$), methylene ($-\text{CH}_2$), and methyl ($-\text{CH}_3$) groups. Chain growth occurs as methylene groups polymerize to one another, and terminates when the growing chain combines with a methyl group or surface-bound H rather than another methylene, and (b) A typical Schultz-Flory distribution of hydrocarbons resulted from FTT synthesis, showing the linear decrease in abundance with increasing the number of carbon in carbon chain (modified from (Berndt et al., 1996)).

1.3.3.3 Rates of conversion of inorganic carbon into organic carbon

Production of alkanes with a Schulz-Flory distribution has been reported by (Berndt et al., 1996), during the experiments conducted at 300 °C and 35 MPa, reacting olivine, and NaHCO_3 in a Au-Ti flexible cell reactor. The authors were able to demonstrate for the first time, the ability of natural minerals to catalyze abiotic production of alkanes. In their experiment, magnetite, which is produced during the serpentinization of olivine was thought to be the heterogeneous catalyst. However, in order to trace the carbon source of these produced hydrocarbons, (McCollom and Seewald, 2001) reproduced the same experiment with ^{13}C labelled NaHCO_3 source. McCollom and Seewalds' experiment yielded similar amounts of H_2 and C1-C3 hydrocarbons to those reported by Berndt et al. (1996), but, the isotopic analysis of the hydrocarbon products indicated that only a small fraction of the CH_4 contained the ^{13}C label (2-15%), while none of the C_2H_6 or C_3H_8 was labeled. This result thus indicated that, except for a small fraction of the CH_4 , the C1-C3 hydrocarbons generated in the experiments were not the product of reduction of dissolved CO_2 , but were instead generated from thermal decomposition of other sources of reduced carbon already present among the reactants at the start of the experiment. In addition, both experiments were conducted at high temperature (300 °C), and high hydrogen fugacities (eg. 158 mmol/kg), typical conditions strongly favored the reduction of inorganic carbon into methane. Even at these conditions, only a small fraction of carbon was reduced into methane ($\ll 1\%$) even after three months of reaction, thus clearly demonstrating that the production of methane is kinetically extremely sluggish.

1.3.3.4 Dissolved organic compounds/ reduced carbon compounds formed during laboratory simulations of abiotic hydrocarbon synthesis at hydrothermal conditions

The concentration of dissolved H_2 , CO_2 , alkanes C1-C4, formate, formic acid and other organic compounds reported by the previous studies has been compiled in Table 5-1 to Table 5-5. As shown by these tables, most experimental studies on abiotic hydrocarbon synthesis using minerals as potential catalysts, report the formation of methane. But only few studies have reported the formation of other simple alkanes such as ethane, propane, butane. In addition, among the possible organic compounds that might occur in the dissolved form, only formate has been reported. However, the recent study by Milesi et al., 2016 reported the formation of formic-acid ($HCOOH$), acetic-acid (CH_3COOH), methanol (CH_3OH), ethanol (C_2H_5OH), propanol (C_3H_7OH) and acetone (C_3H_6O), graphite ($C_{(s)}$) during the formation of methane by reduction of bicarbonate. The quantity of dissolved H_2 and CO_2 in these experiments varies between few tens of mmols/L to few hundreds of mmol/L. In addition, the concentration of dissolved CH_4 varies between few tens of $\mu\text{mol/L}$ to few hundreds of $\mu\text{mol/L}$. In general, the quantity of dissolved CO_2 decreases in these studies as a function of time, as it is consumed to produce hydrocarbons. These results indicate that the reduction of inorganic carbon into alkanes occur through intermediate reduced carbon species in dissolved form.

The experiments of (Berndt et al., 1996), report the formation of methane, ethane and propane during the serpentinization of olivine. In addition, a metastable solid carbonaceous-phase was also reported, which was later identified as a contaminant. Similar products were observed by (McCollom and Seewald, 2001), who re-produced the same experiment with ^{13}C labeled NaHCO_3 . In addition to the alkanes, they also reported the production of C2- and C3-alkenes, and formate (>90% ^{13}C), followed by the injection of $\text{NaH}^{13}\text{CO}_3$. The authors claimed that the reduction of CO_2 to formate occurred rapidly during the serpentinization of olivine, but further reduction of carbon was kinetically inhibited, resulting only in small concentrations of methane. Catalytic potential of magnetite was also studied by (Fu et al., 2007), who documented the C1-C3 alkane formation. The experimental study on catalytic effect of pentlandite by (Fu et al., 2008), observed only methane. Recent experimental investigation of production of abiotic hydrocarbon catalyzed by magnetite (-produced during siderite dissolution) by (Milesi et al., 2015), observed the formation of methane in the gas phase, and also able to detect formic-acid ($HCOOH$), acetic-acid (CH_3COOH), methanol (CH_3OH), ethanol (C_2H_5OH), propanol (C_3H_7OH) and acetone (C_3H_6O). The authors also detected a solid carbon phase which coated around siderite and magnetite grains Figure 1-23. The study by (Milesi et al., 2015), therefore provides important insights on the reaction path during the surface catalyzed carbon reduction by magnetite.

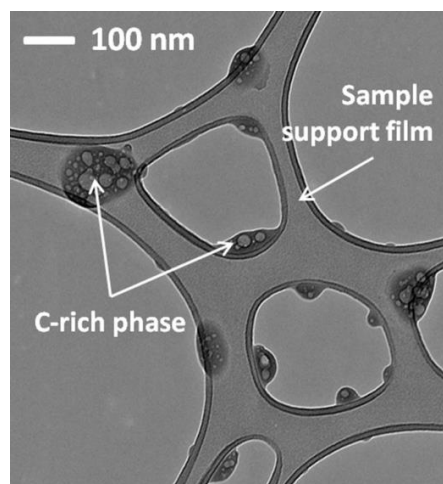


Figure 1-23. Carbon phase coating the siderite and magnetite grains observed in (Milesi et al., 2015).

1.4 Problematic

As discussed in the previous sections, mineral sequestration is considered one of the most efficient process for permanent storage of CO_2 , since $\text{CO}_{2(\text{aq})}$ is converted into stable carbonates (eg. FeCO_3 , MgCO_3 or CaCO_3) by reacting with Mg, Ca, or Fe rich-minerals. If this reaction occurs in Fe-rich systems, under specific P-T conditions, (i.e. Fe silicate- H_2O - CO_2), the redox reaction between H_2O and Fe^{2+} is also prone to generate H_2 in large quantities, which could become a major green energy source, the significantly cost-effective compared to the main industrial hydrogen production methods. However, most of the previous studies have been focused either on carbonate yield or H_2 yield as separate processes. The main objective of this thesis work is to combine these two scenarios to find out a set of P-T conditions that would maximize the yield of carbonation and H_2 production simultaneously. We conducted experiments using olivine ($\text{Mg}_{1.8}\text{Fe}_{0.2}\text{SiO}_4$)-bearing New Caledonian mine tailings, to incorporate hydrogen production and carbonation as two potential pathways to valorize the mine tailings. The experiments and analysis were conducted using the facilities at IFPEN, Rueil Malmaison and IPGP, while also using the analytical facilities at UPMC, IEMN-Lille and CRPG-Nancy. The quantitative results of these experiments will be presented in chapter III, and published in *Applied Geochemistry*. The detailed mineralogical results addressing the gas-water-rock interactions during hydrogen production and carbonation of mine tailings will be presented in chapter IV, and is in preparation to submit to *Chemical Geology*.

The second part of this thesis will be focused on studying the catalytic potential of natural minerals for Fischer-Tropsch Type (FTT) synthesis of hydrocarbons. As has been mentioned before, FTT synthesis is a highly catalytic process, largely used in the industry for the production of methane and other light hydrocarbons, by reacting a gas phase (CO /or CO_2) with H_2 in the presence of various synthetic catalysts. However, though this reaction has been widely studied, little is still known about the catalytic activity of natural mineral phases other than oxides for FTT synthesis of hydrocarbons in geological environments largely dominated

by water. The present work aims to study the potential of natural sulfides; sphalerite (ZnS) and marcasite (FeS_2), to catalyze the FTT synthesis of hydrocarbons. Laboratory experiments were performed by reacting various mineral assemblages such as iron-rich olivine ($\text{Mg}_{1.8}\text{Fe}_{0.2}\text{SiO}_4$), fayalite (Fe_2SiO_4) and Fe-rich chlorite (Chamosite – $(\text{Fe}_5\text{Al})(\text{AlSi}_3)\text{O}_{10}(\text{OH})_8$) together with a solution of NaHCO_3 in the presence of each potential catalyst (as mentioned above) in sealed gold capsules. All the experiments were performed at $T = 300^\circ\text{C}$, $P = 30 \text{ MPa}$. The first reaction produces H_2 by oxidizing iron from the Fe-rich minerals; H_2 then reacts with the dissolved CO_2 in the presence of a catalyst to form methane and other light hydrocarbons. The preliminary results of this study will be presented in chapter V. All the experiments and analysis of these experiments were performed using facilities at IFPEN, Rueil Malmaison and at IPGP, and LRCS-Amiens.

The details of all the experiments performed, and the instrumentation will be presented in the Materials and methods, in chapter II. The main conclusions and the perspectives will be given in the chapter VI.

Chapter 2

Materials and methods

2. Materials and methods

Ex-situ carbon dioxide (CO₂) sequestration is the fixation of CO₂ in mafic and ultramafic minerals in the form of carbonates such as calcite (CaCO₃), magnesite (MgCO₃), dolomite (Ca_{0.5}Mg_{0.5}CO₃), siderite (FeCO₃) and possible solid solutions among these minerals. The success and wide applicability of this technique relies upon the high abundance of mafic and ultramafic minerals in nature and their fast solubility kinetics. Olivine (MgFeSiO₄), which is the major and only constituent in dunite, a major constituent in basalt and peridotites, and one of the fastest dissolving Mg-silicate, has been widely studied for both in-situ and ex-situ sequestration of CO₂. Both Fe and Mg in olivine contribute to the sequestration of CO₂ by precipitating Fe-bearing magnesite. In particular, at temperatures between 200-300 °C, Fe²⁺ within olivine oxidizes into Fe³⁺ in magnetite, producing hydrogen during the serpentinization reaction take place in hydrothermal vents along the mid oceanic ridges, producing enormous fluxes of hydrogen into deep sea floor. Although olivine has been extensively subjected to experimentations of CO₂ sequestration and hydrogen production, the studies focusing on both these strategies are scarce. We combined these two phenomena to valorize New Caledonian mine tailings, which is an olivine bearing byproduct of nickel (Ni) extraction from the New Caledonian ophiolite. In the first section of this chapter, we present the detail characterization of mine tailings, the experimental protocol of HP/HT experiments used for simultaneous ex-situ CO₂ sequestration and hydrogen production, as well as the analytical procedures. Our experimental set-up was developed to facilitate the simultaneous monitoring of the compositional variations of the liquid and gas phases in the batch reactor. The aim of this experimental study is to determine the P/T conditions favorable for both these two reactions to occur and also quantify the amounts of sequestered CO₂ and produced hydrogen that could be achieved per unit mass of mine tailings. Furthermore, the mineralogical analysis of the reaction products along with the thermodynamic modelling will allow us to understand the nature of water-rock interaction during the hydrothermal alteration of mine tailings, and processes which could potentially slow down carbonation and hydrogen production.

Interactions of water- CO₂-mafic and ultramafic systems at hydrothermal conditions may result carbonation and/or hydrogen production, as discussed above. Although the mechanism is not clearly understood, the formation for abiotic methane and light hydrocarbons in such systems, rich in dissolved H₂ and CO₂ has been widely documented. The production of abiotic hydrocarbons has been attributed to occur via Fischer-Tropsch Type (FTT) reactions, catalyzed by various mineral surfaces which can be considered as the natural analogues of industrial Fischer-Tropsch Type catalysts. We simulated the conditions of abiotic hydrocarbon synthesis in nature by reacting Fe-bearing minerals to produce hydrogen in-situ; providing a close approximation to serpentinization-type reaction. We introduced into the system sphalerite (ZnS) and marcasite (FeS₂); two sulfide minerals common in hydrothermal and sedimentary environments, to test their surface catalytic ability to synthesis abiotic hydrocarbons. In the second section of this chapter, we present the natural minerals we used for this simulation, the experimental and analytical protocols used to synthesis abiotic hydrocarbons from inorganic carbons sources and in-situ formed hydrogen

and to study if sphalerite and marcasite have the ability to catalyze this reaction. We also aim to study whether the reaction paths followed during the reduction of inorganic carbon source into abiotic hydrocarbon by analyzing the liquid medium and also via thermodynamic models.

2.1 Section I- Experimental investigation of simultaneous ex-situ carbon dioxide sequestration and hydrogen production from New Caledonian mine tailings

2.1.1 General introduction

New Caledonia is one of the world's largest producers of nickel (Ni), who contributes to ~8% of the world's Ni supply (Wacaster, 2008). The New Caledonian ophiolite is the source of Ni, which has been extensively mined to produce ~107 kilo tons of Ni per year (1ton = 1000 kg). The residue after nickel (Ni) extraction from the ophiolite, or the mine tailings, therefore contain various amounts of olivine and pyroxene depending on the P/T conditions of ore processing. Approximately 12 million tons (Wacaster, 2013) of mine tailings are produced annually, most of which has been used as a filling material. Figure 2 -1 a, shows the nickel mining sites in New Caledonia, a common open-pit mine (Figure 2-1 b) and piles of mine tailings (Figure 2-1 c). Due to its high content of Mg and Fe, it is an interesting material to study for CO₂ storage and hydrogen production, and applying these techniques to such a large scale industrial byproduct could definitely be a cost effective method of CO₂ storage and hydrogen production. However, mine tailings inherit some textural features due to the process of Ni extraction and therefore the conditions of ore processing will be summarized here.

A sketch of Ni extraction process is shown in Figure 2-2 a. During this process, first the ore is been pre-heated in order to maintain the moisture content below 20%, and then heated up to >1173 K, in the presence of a limited air supply during the process of "calcination". During this step, moisture is completely removed and metal oxides are reduced. In the final step, the ore has been heated to temperatures >1873 K using an electrode for fusion reduction of metals, extracting ferronickel for industry purposes. The hot molten slag is then quenched by spraying sea water on the pouring slag at the electric oven outlet which is the residual "mine tailings"(Bodénan et al., 2014). In petrological point of view, these processing conditions resemble the "dry" melting of peridotite under atmospheric pressure (Takahashi, 1986). A schematic of dry melting of pyrolite; a model mineral assembly (Earth's mantle composition) resulting a pyroxene melt and partially molten olivine is shown in Figure 2-2 b. Mine tailings therefore could be simply considered as a mineral assemblage of orthopyroxenes, clinopyroxenes and olivine. According to Jaques and Green (1980) and Bonin and Moyen (2011), this mineral assemblage melts eutectically, starting at temperature slightly above 1323 K at 1atm. The first melt contains clino-pyroxenes. Then, when the assemblage is further heated, all clinopyroxenes melt as the temperature reaches 1473 K at 1 atm. All the ortho-pyroxenes then melt when temperature reaches 1523 K at 1atm. Only a fraction of olivine will also be molten, but crystalline olivine will coexist with the melt until the temperature reaches 2023 K at 1 atm. As a result, the melt composition (-or glass, after cooling of the melt) essentially represents pyroxene composition (no miscibility

gap between ortho- and clinopyroxenes and alkali pyroxenes at temperatures above 1473 K). The resulting mine tailings is therefore an inter-locking mixture of glass and olivine.

Although mine tailings have been recently studied for its ability to sequester CO₂ , (Bodéan et al., 2014), literature on its mineralogy, and detailed characterization are rare. In this section, we report the full characterization of this material using the state-of-art facilities available for mineralogical studies. The experimental work flow of our experiments is summarized in Figure 2-3, and the following sections contain details of each experimental set-up, and analytical method included in this work-flow.

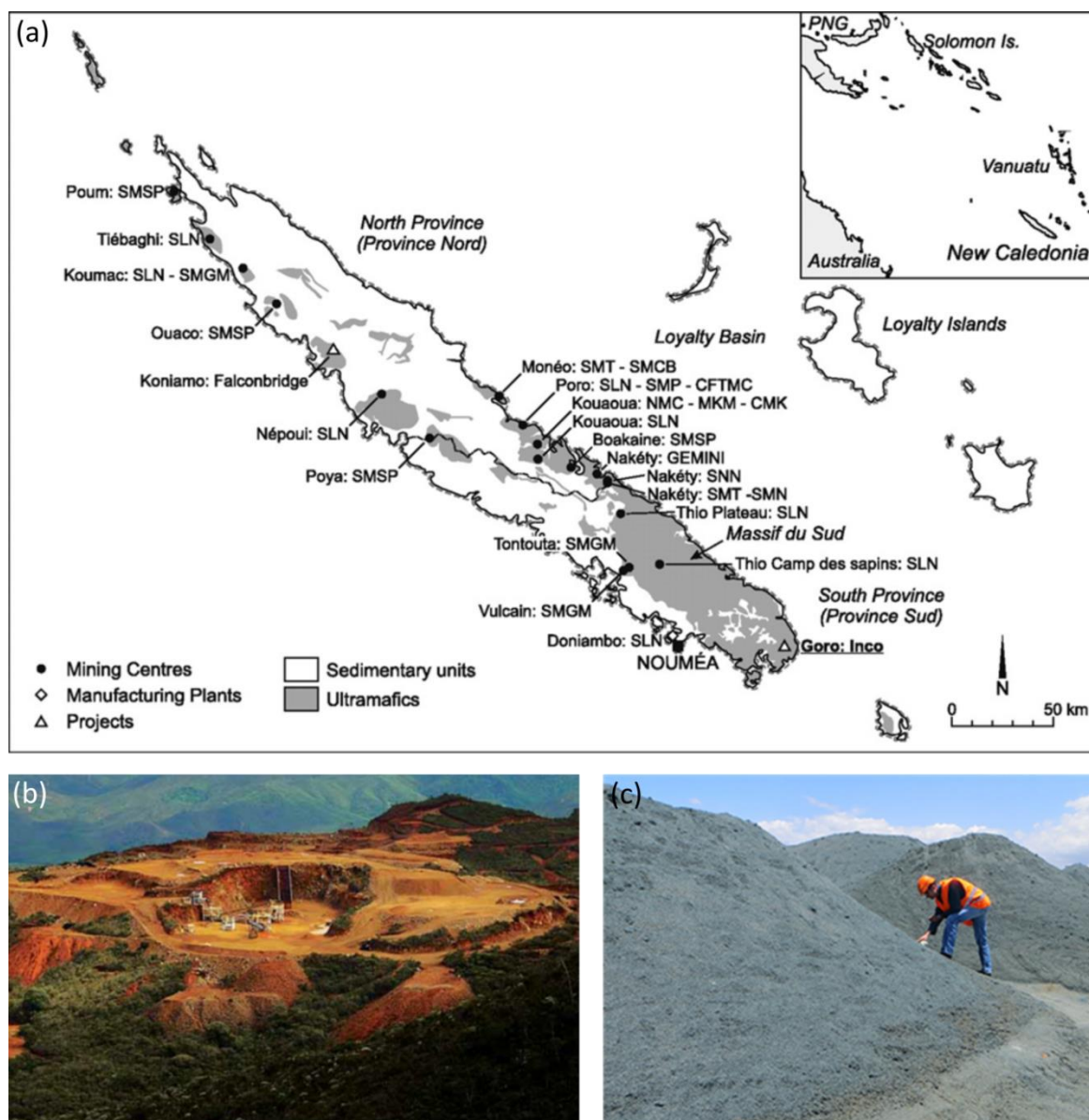


Figure 2-1. Nickel mining in New Caledonia (a) map of Nickel Mining Sites, Courtesy of the European Journal of Mineralogy (b) an open pit mine (c) Mine tailings accumulated near mining sites.

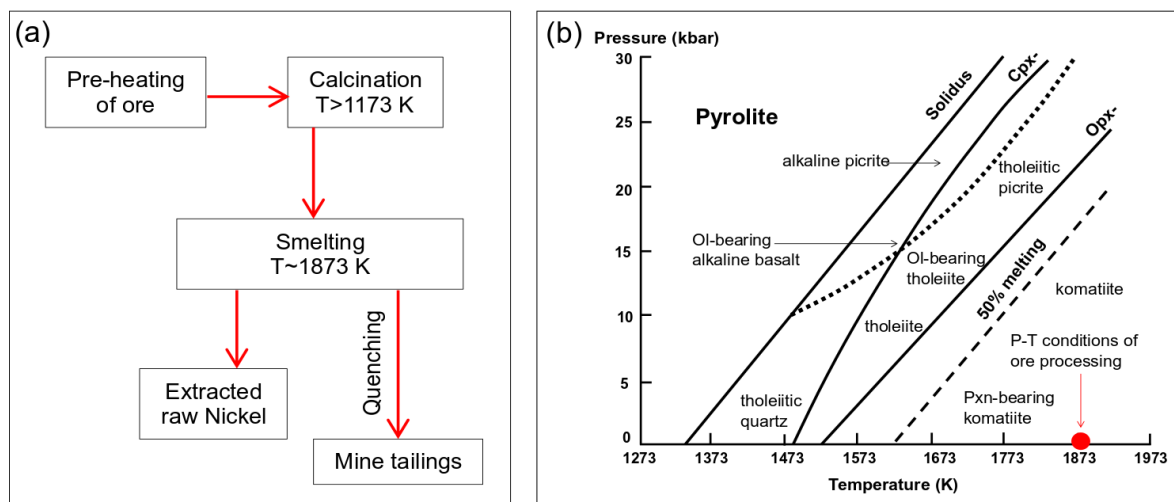


Figure 2-2. Ore processing for extraction of Ni (a) Schematic of ore processing conditions showing the major steps of Ni extraction and formation of mine tailings (b) schematic of the P-T diagram for partial melting of pyrolite (model mantle composition), and the nature of the liquids formed under dry melting conditions (Modified from Jaques and Green, 1980; Bonin and Moyen, 2011). The P/T condition reached during Ni ore processing is also shown. The solid lines represent the solidus and the limit of disappearance of clinopyroxene (cpx-) and orthopyroxene (opx-); the dashed line represents the curve of 50% melting; the dotted line represents the boundary of tholeiitic and calc alkaline compositions.

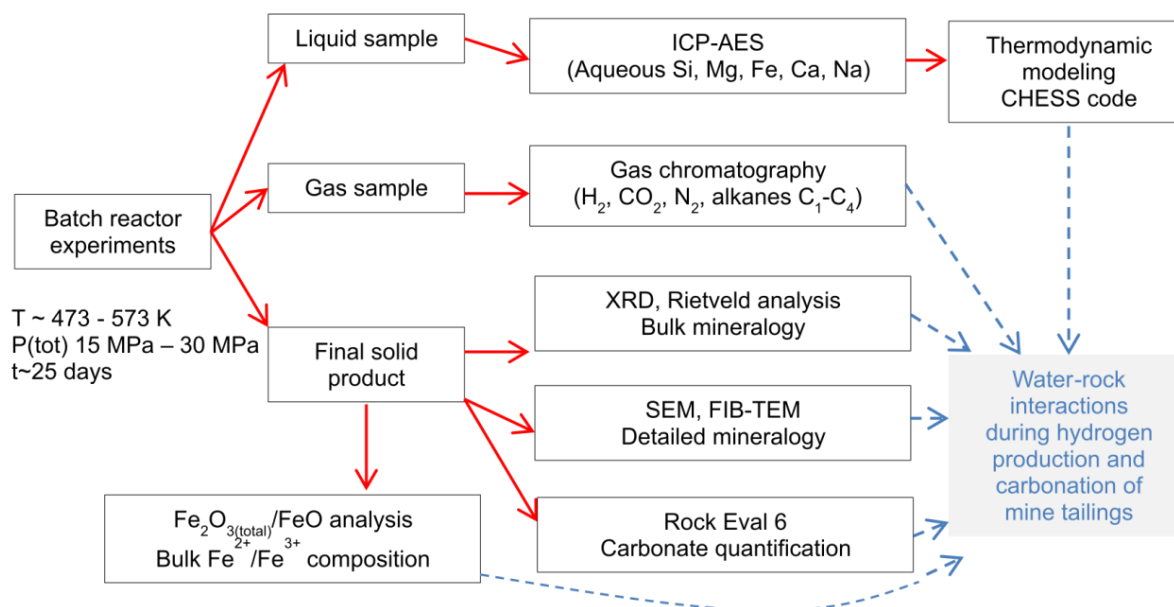


Figure 2-3. Experimental workflow to investigate simultaneous ex-situ carbon dioxide sequestration and hydrogen production from New Caledonian mine tailings.

2.1.2 Characterization of mine tailings

Mine tailings resulted from ore processing, consisted of dark green to pale brown, angular particles. They are grains are opaque to translucent grains and contained no visible inclusions and impurities. The size of these particles vary from few millimeter to <1 cm, and poorly sorted (Figure 2-4). Figure 2-4.



A hand specimen of mine tailings

2.1.2.1 Polarizing petrographic microscopy

Thin slices of few grains of mine tailings were glued onto a glass slide, and polished down to approximately 30 μm thickness, using a silicone (Si) abrasive. The sample was observed using a polarizing petrographic microscope under plane polarized light (PPL) and crossed polarized light (CPL). A mesh-like texture of olivine embedded in glass has been resulted from quenching the molten slag (Figure 2-5 a and b). In addition, reaction rims (“aureoles”) possibly resulted from the reaction between olivine with the melt could be observed around olivine skeletons (Figure 2-5 c and d).

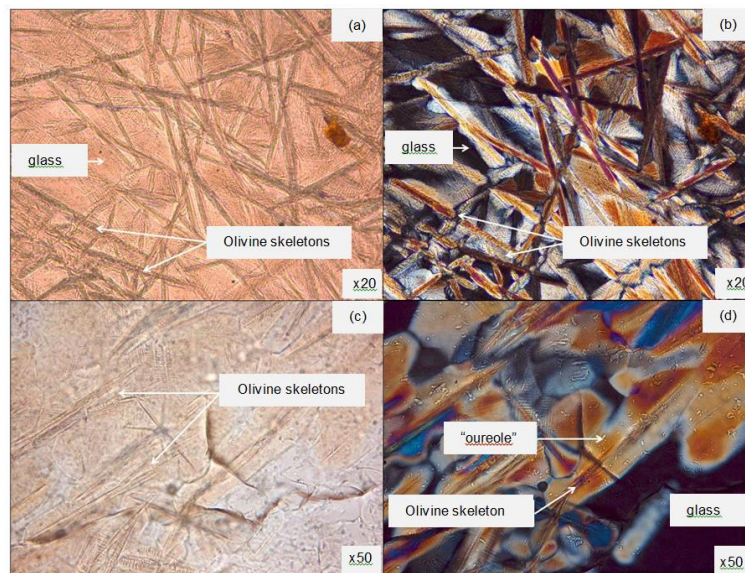


Figure 2-5. Mine tailings observed under polarizing petrographic microscopy with magnification of x20 under (a) PPL showing skeletons of olivine making a mesh-like texture and, (b) CPL, showing high birefringent olivine embedded in glass (black). At magnification x50, (c) under PPL, the olivine skeletons are more visible (d), under CPL, reaction rims between olivine and glass are visible (aureoles).

2.1.2.2 XRD analysis

X-ray diffraction analysis was performed on powdered mine tailings sample in order to obtain the bulk mineralogical composition and also to determine the amount of glass in mine tailings. The acquisition was performed on an X'Pert PRO (PANalytical) x-ray diffractometer with a Cu anode ($\text{Cu K}\alpha = 1.5418 \text{ \AA}$), operated under 45 kV and 40 mA. Then, the full powder patterns analysis were performed using XPert High ScorePlus software and the peak identification was done by peak-search-matching, using the available PDF database (Powder Diffraction File) a widely used database of ICDD (International Center for Diffraction Data). For the determination of the amount of glass, the internal standard method was used. For this purpose, the powdered mine tailings sample was spiked with 20 wt.% of corundum (Al_2O_3), used as the internal standard. The weight of a phase in a mixture is proportional to the product of the scale factor, as derived in a multi-component Rietveld analysis of the powder diffraction pattern, with the mass and volume of the unit cell. If all phases are identified and crystalline, the weight fraction W of crystalline phase p is given by;

$$W_p = \frac{S_p(ZMV)}{\sum_i S_i(ZMV)_i} \quad [2-1]$$

where, S , Z , M and V are, respectively, the Rietveld scale factor, the number of formula units per unit cell, the mass of the formula unit and the unit-cell volume. This is the basis of a method providing accurate phase analyses without the need for standards or for laborious experimental calibration procedures.

However, when the phase mixture contains an amorphous phase, a known weight of internal standard is added to the mixture. For this purpose, the powdered mine tailings sample was spiked with 20 wt.% of corundum (Al_2O_3), the internal standard. When the internal standard is added;

$$W_{p(\text{meas})} = W_{\text{std}(\text{meas})} \frac{S_p(ZMV)_{p(\text{meas})}}{S_{\text{std}}(ZMV)_{\text{std}(\text{meas})}} \quad [2-2]$$

The absolute weight of the crystalline phase is given by;

$$W_{p(\text{abs})} = W_{p(\text{meas})} * \frac{W_{\text{std}(\text{known})}}{W_{\text{std}(\text{meas})}} \quad [2-3]$$

The weight fraction of amorphous phase is given by;

$$W_{\text{Am}(\text{abs})} = 1 - \sum_{k=1}^k W_{k(\text{abs})} \quad [2-4]$$

More theoretical details have been reported by (Bish and Howard, 1988; Bish and Post, 1993; McCusker et al., 1999). The XRD pattern collected on the mine tailings sample mixed with corundum is given in (Figure 2-6 a). The amorphous quantification using the above described internal standard method indicated the presence of 55 wt.% of glass and 45 wt.% of crystalline olivine (+traces of enstatite), as shown in (Figure 2-6 b).

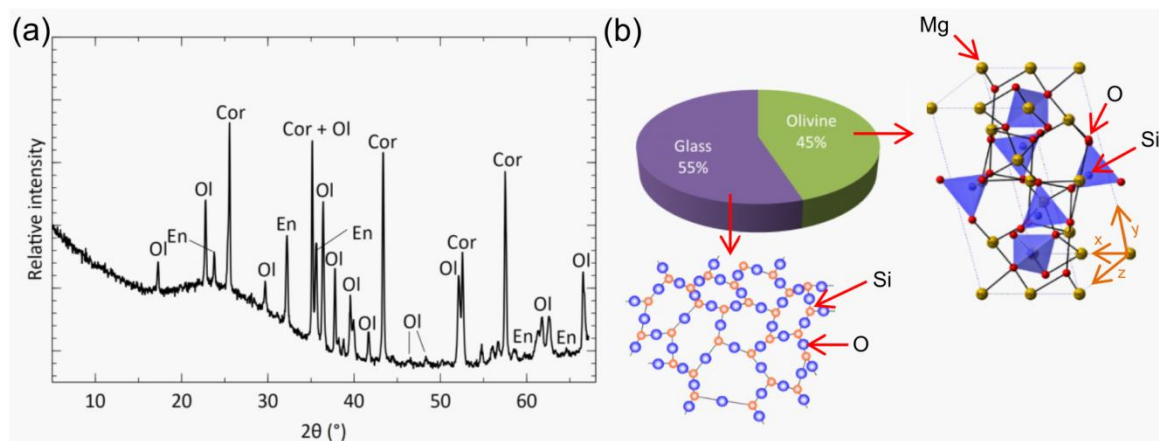


Figure 2-6. Mineralogy of mine tailings (a) XRD pattern showing characteristic peaks for olivine (Ol). The presence of glass is identified by the bumps at low angle diffraction. Corundum, added as an internal standard for quantifying glass also appear in the pattern (cor), (b) the percentage of glass and olivine obtained by Reitveld quantification. Also shown are (i) the simple atomic structure of forsterite (Michel et al., 2013), (ii) the silicate tetrahedra are held by Mg^{2+} ions, and (iii) the structure of glass which has no crystallinity and the silicate tetrahedra are polymerized to form a 3D array (www.materials.unsw.edu.au).

2.1.2.3 Electron probe micro analysis (EPMA)

Electron probe micro analysis was performed on few randomly selected grains mounted on epoxy and polished with silicon based abrasive. The polished surface was carbon coated and the composition of both glass and olivine was analyzed. The weight percentages of NaO, MgO, SiO₂, Al₂O₃, CaO, TiO₂, Cr₂O₃, FeO, MnO, CoO and NiO in olivine and glass are reported in Table 2-1. The average composition of mine tailings and magnesium number (Mg #) of glass and olivine are also reported. The magnesium number ($Mg\# = Mg/(Mg+Fe)$) was calculated on molar basis (i.e. by dividing the wt.% oxide value of MgO and FeO by their gram-formula weights) using the average oxide wt.% obtained by EPMA.

In addition to point analysis; element mapping was performed on two regions, in order to determine the variation of the elements among olivine and glass. In the first region, we observed olivine in contact with glass free of olivine inclusions (Figure 2-7). The element mapping showed that, glass is rich in Si and depleted in Mg compared to olivine. In addition, a considerable contrast of concentration of Al, Mn, Ca and K elements exist between glass and olivine. However, Ni and Cr have been distributed equally among the two phases. Ti seemingly disseminated equally between the two phases, whereas Ca and P exist as a line of spots, which could presumably be inclusions. In the second region, we observed a quench-texture, in which flakes of olivine creating a mesh-like structure in glass (Figure 2-8). A clear contrast of Mg, Fe, Si, Al, Mn, Ca, Cr elements exist between glass and olivine, however Ni, Ti, K, and P were equally distributed among the two phases.

As indicated by EPMA, mine tailings is a silicate, rich in Mg and Fe, therefore, compositionally favourable for both carbonation and hydrogen production. Mg is expected to be the main cation involved in sequestering carbon dioxide, during the hydrothermal

experiments, while Fe is expected to contribute in hydrogen production via its oxidation under hydrothermal conditions (as well as accelerate carbonate nucleation). However, the textural and chemical inhomogeneities within the material could have impacts on its dissolution in comparison to more homogeneous materials (eg. olivine) commonly used for experimental carbonation or hydrogen production.

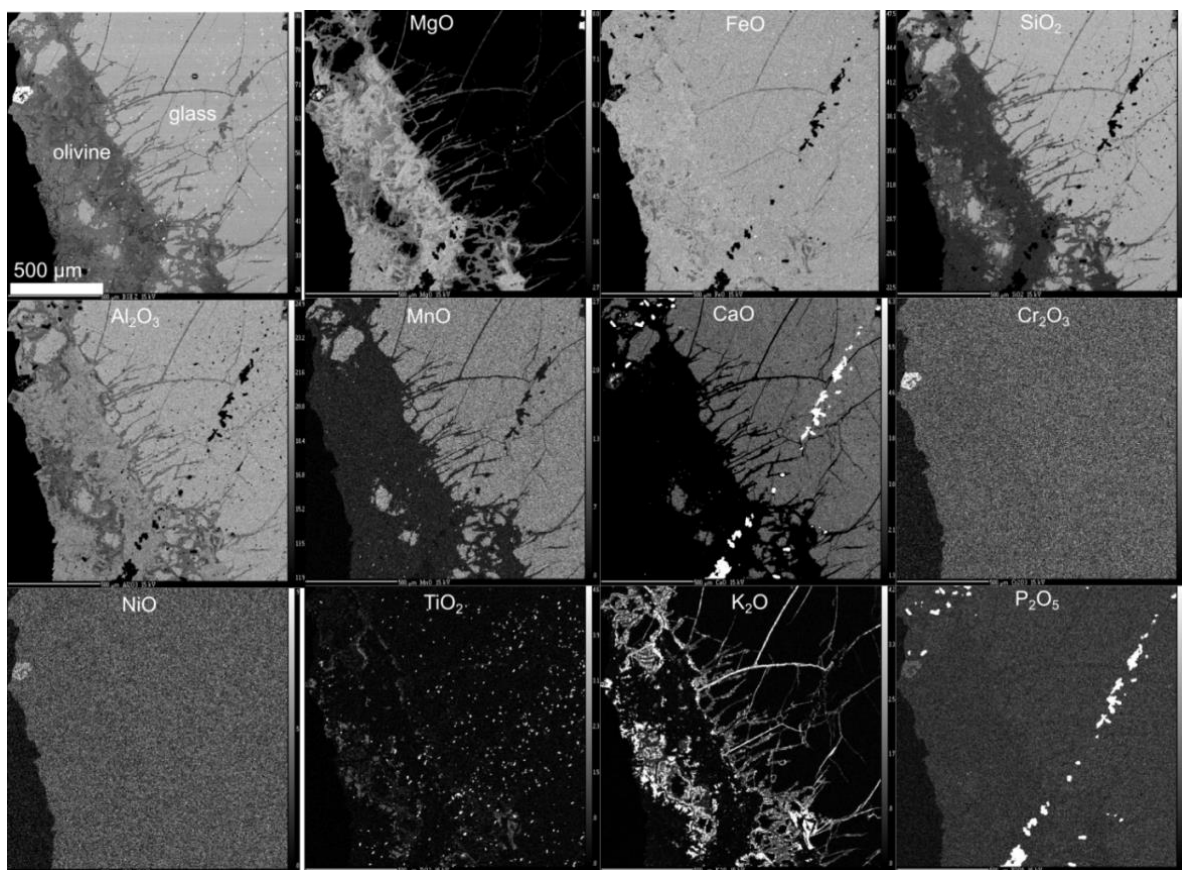


Figure 2-7. Element mapping performed using EPMA, showing Si-rich and Mg-poor glass, and Si-poor, Mg-rich olivine. Considerable contrast of Al, Mn, Ca, K elements exist between glass and olivine whereas Ni and Cr have been distributed equally among the two phases. Ti disseminates equally whereas Ca and P exist as a line of spots (inclusions?).

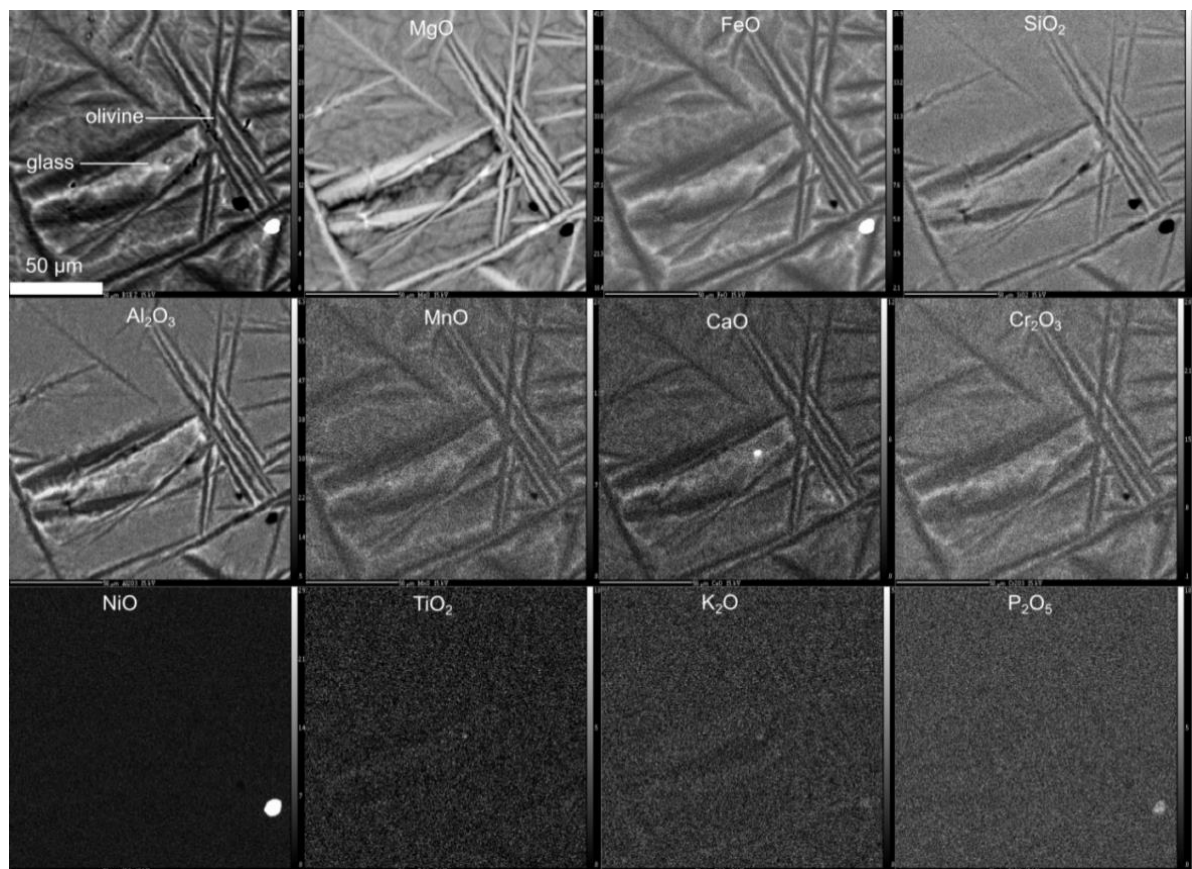


Figure 2-8. Element mapping performed using EPMA, showing the quench-textures in mine tailings where olivine creating a mesh-like structure in glass. A clear contrast of Mg, Fe, Si, Al, Mn, Ca, Cr elements exist between glass and olivine, however Ni, Ti, K, and P are equally distributed among the two phases.

2.1.2.4 $\text{Fe}_2\text{O}_3(\text{total})/\text{FeO}$ analysis

The amounts of Fe^{2+} and total iron in the non-reacted mine tailings were analyzed at the Centre de Recherches Pétrographiques et Géochimiques (CRPG), Nancy, France. The aim was to determine the iron available for hydrogen production (i.e. Fe^{2+}). The sample was boiled in $\text{HF}/\text{H}_2\text{SO}_4$ to release Fe^{2+} which is then quantified by volumetric titration with $\text{K}_2\text{Cr}_2\text{O}_3$. Then, another fraction of the sample was heated with LiBO_2 at 1223 K and acid digested (4 vol.% HNO_3) to convert all species of iron (eg. Fe^0 and Fe^{2+}) contained in the sample into Fe_2O_3 (Fe^{3+}). The resulting ferric iron was measured by atomic absorption spectrophotometer (AAS). According to this analysis, mine tailings contain 9.39 wt.% of FeO and 10.37 wt.% Fe_2O_3 . A sample of 2.0 g of mine tailings would contain 0.19 g of FeO and 0.21 g of Fe_2O_3 , which would yield 2.6 mmol and 1.3 mmol of FeO (71.8 g/mol) and Fe_2O_3 (159.7 g/mol) respectively. Since, Fe_2O_3 contains twice the iron content of FeO, this calculation clearly indicates that all the Fe^{2+} in mine tailings has been oxidized into Fe^{3+} upon heating with LiBO_2 at 1223 K. This suggests that the mine tailings are free of initial metallic iron (Fe^0) or Fe^{3+} .

2.1.3 Preparation of starting materials

The main objective of this study was to investigate the P/T conditions that would maximize the yield of carbonate and simultaneously produce H₂ through reacting olivine bearing mine tailings and CO₂ saturated water under hydrothermal conditions. Therefore, cautious choice of experimental conditions and parameters were crucial. The particle size of the starting mine tailings were selected to fall in the range of 40 - 63 µm in order to maintain rapid dissolution kinetics, as well as to facilitate microscopic observations. In addition, the grain sizes were in the same range than those used in the few previous studies on hydrogen generation (Malvoisin et al., 2013, 2012a, 2012b), thus making the comparison easier. Furthermore, even though the choice of nano-scale particles could have provided a considerably faster reaction, the mineral surfaces available for microscopic studies of the run products would have been limited. Finally, for industrial purposes, grinding large quantities of solid down to the nanometer scale would largely increase the cost of the process. According to these requirements, the sample was crushed using a ball mill and sieved to obtain the 40- 63 µm grain size fraction. The selected sieve fraction was subsequently ultrasonically cleaned in ethanol for 8-10 min to remove the fine particles adhering to the surface. This process was repeated until the supernatant became clear. The powder was oven dried at 70 °C overnight after cleaning with ultra-pure de-ionized water (electrical conductivity = 18.2 MΩ cm). Very few fine particles remained adhering to the grain surfaces of the above dried powder, when observed under Scanning Electron Microscopy (SEM). SEM images of powdered mine tailings sample before and after cleaning are shown in Figure 2-9. The specific surface area (SSA) of the cleaned starting powder was determined by Kr adsorption analysis, according to the Brunauer–Emmett–Teller (BET) method (Brunauer et al., 1938), yielding a value of 0.23 m²/g.

Table 2-1. The chemical composition of New Caledonian mine tailings, determined by electron probe micro analysis (EPMA) performed on crystalline olivine and glass, expressed in weight percent (wt.%) of corresponding oxide.

	Si	Mg	Fe	Al	Cr	Mn	Ca	Ni	Na	Ti	Co	K	Total	Mg# ^a
Olivine	40.88	47.27	11.67	0.07	0.02	0.12	0.11	0.38	0.05	0.04	0.05	0.01	100.68	0.88
Glass	55.22	23.94	14.23	3.81	1.68	0.9	0.48	0.01	0.04	0.06	0.01	0.01	100.39	0.75
Avg ^b	48.05	35.61	12.95	1.94	0.85	0.51	0.30	0.20	0.05	0.05	0.03	0.01	100.54	0.815

^aThe magnesium number; Mg# = Mg/(Mg+Fe)

^bAverage composition of mine tailings

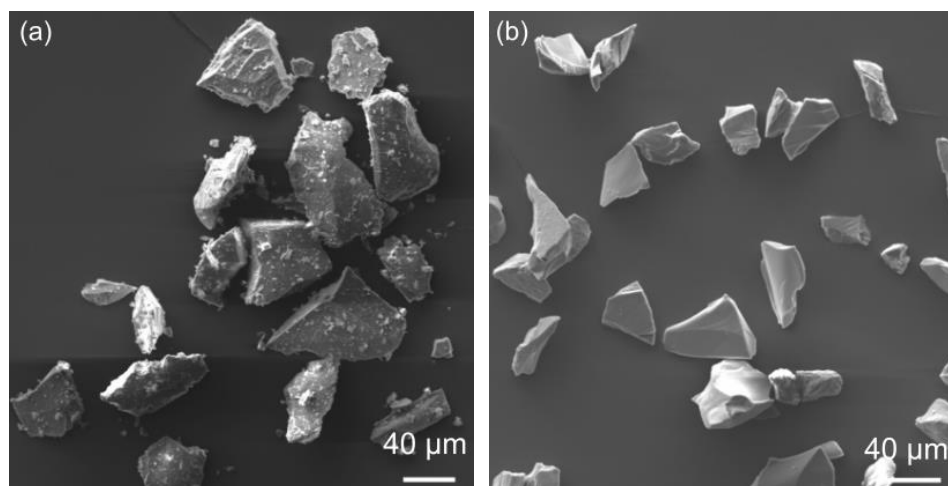


Figure 2-9. Secondary electron image of mine tailings powdered sample prepared for experiment (a) before and, (b) after cleaning with ethanol to remove adhered particles.

2.1.4 High pressure and high temperature experiments

2.1.4.1 Experimental set-up

The ex-situ CO₂ sequestration experiments were conducted in Parr[®] hastelloy stirring-type batch reactors. Hastelloy is a nickel (Ni) based alloy (Alloy C-276), which can sustain high P/T and resistant to corrosion. The exact composition of hastelloy is shown in the table 2-2. The maximum pressure and temperature limit of these pressure vessels are 40 MPa and 623 K, respectively. The batch reactor consists of a reactor vessel made out of hastelloy, lined with a TiO₂ recipient, into which the sample/ solutions are loaded; a cylindrical heater; and a head equipped with a pressure transducer, a stirrer and a thermocouple. The reactors are pressurized by pumping gases (eg: CO₂, Ar). In addition, they can be used as closed systems, or open systems. For instance, this set-up allows sampling-out, or pumping-in fluids during the course HP/HT experiment. The images of experimental set-up are shown in Figure 2-10 and the schematic of full set up is given in Figure 2-11. The samples are loaded into the reactor vessel which is then properly closed by the head using the screws. The reactor is heated by turning-on the power supply. The vessel is pressurized by pumping gas (Eg. CO₂) at the desired pressure. The pressure, temperature, duration of the experiment and stirring speed must be programmed at the beginning of the experiment. In general, the pressure and temperature stabilizes within 1.5-2 hrs since the beginning of heating. An example in which the P/T stability has been reached after 1.5 hrs since heating is shown in (Figure 2-12). The intended P and T of this experiment were 200 °C and 150 bar.

Table 2-2. Nominal chemical composition of pressure vessel material (hastelloy, Alloy – 276)

	Fe	Ni	Cr	Mo	Ni	W	Co
Major element (%)	6.5	53	15.5	16	1	4.0	2.5

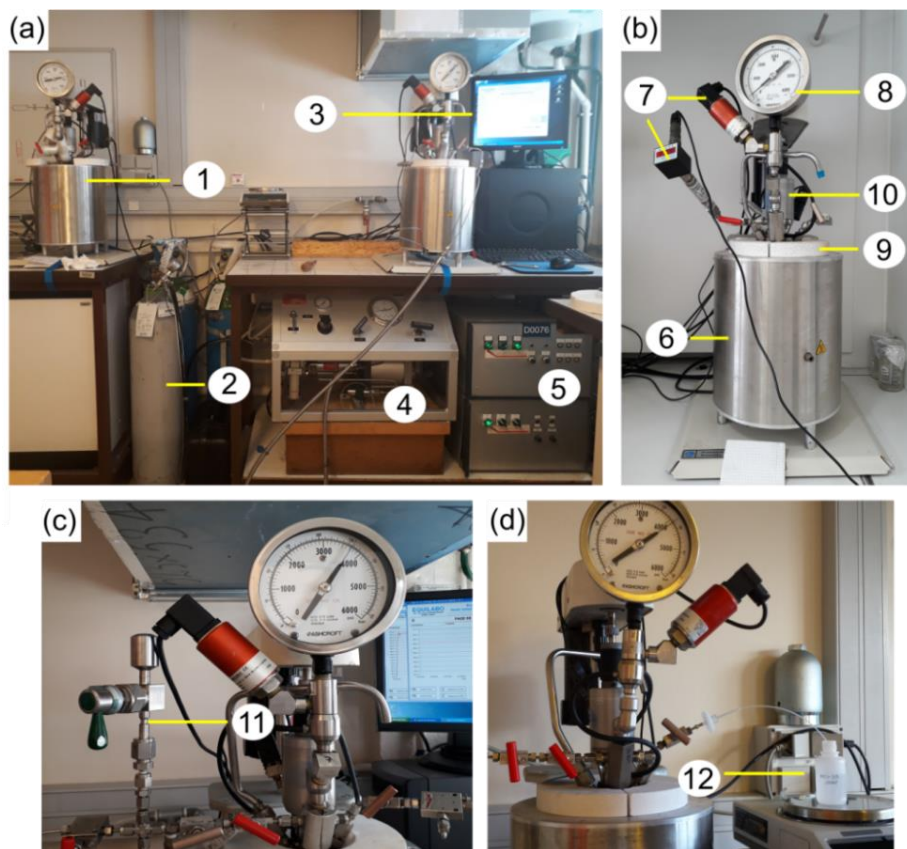


Figure 2-10. Images showing (a) experimental set-up used for ex-situ CO₂ storage in mine tailings (b) a Parr® hasteloy batch reactor (c) sampling the gas out of batch reactor (d) sampling the liquid out of the batch reactor. The labeled components are, 1. Batch reactor 2. CO₂ supply 3. Computer program used to monitor P/T inside batch reactor 4. Compressor 5. Power supply and P/T controller 6. Heater 7. Pressure cap 8. Pressure gauges 9. Heat insulator (Al₂O₃) 10. Stirrer, (* a thermocouple goes parallel to the stirrer, which is not visible in the figure). 11. Swaglock tube to collect gas sample 12. Plastic bottle connected through a plastic tube to collect liquid sample.

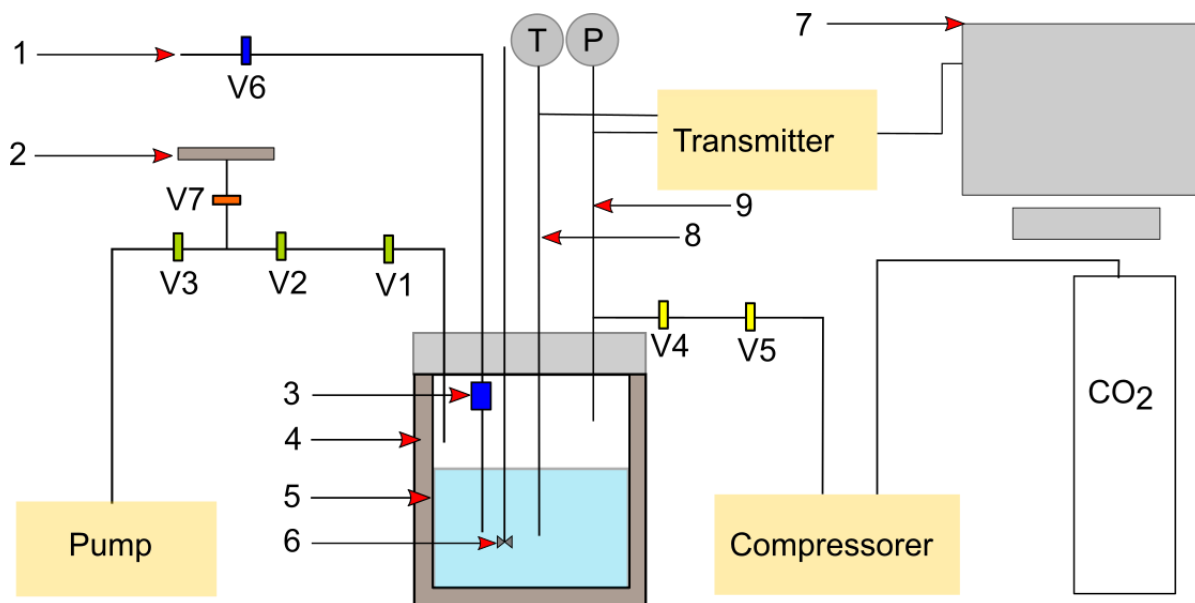


Figure 2-11. Schematic of the experimental set-up used for ex-situ CO₂ storage in mine tailings. The labelled components are; 1. Liquid outlet 2. Gas outlet 3. Titanium (Ti) micro filter (10 μm) 4. Heater 5. Reactor vessel 6. Stirrer 7. Computer 8. Thermocouple 9. Pressure sensor connected to pressure gauge.

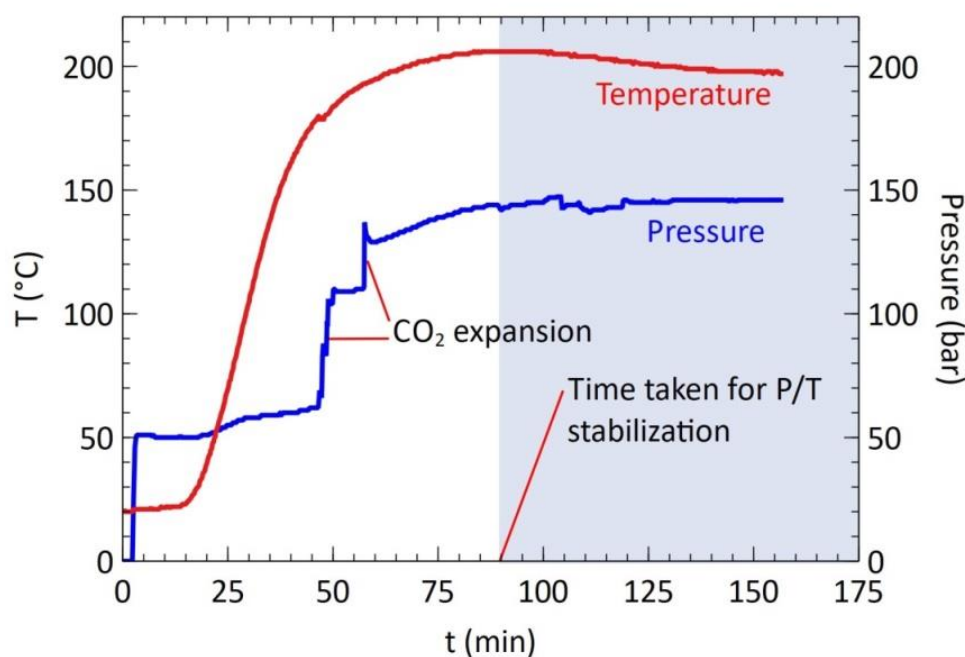


Figure 2-12. The time taken to reach pressure and temperature stability in a batch reactor experiment conducted at 200 °C and 150 bar.

2.1.4.2 Experimental protocol

Powdered mine tailings and ultra-pure de ionized water was loaded into the reactor vessel in 1:100 mass ratio. The reactor vessel is properly closed by using the Teflon gasket and then tightening the screws. Then, CO₂ is pumped at low pressure, for nearly ~30 min to degas all the oxygen in the gas headspace and dissolved in water. In order to reach 30 MPa for instance, in the first step, CO₂ is pumped into the reactor up to about 20 MPa. Then, the pressure, temperature, duration and stirring speed are programmed. Once heating has begun, the pressure of the reactor increases due to the expansion of CO₂. Release of CO₂ from the reactor is necessary in order to maintain the pressure below the desired level. The pressure and temperature of the reactor vessel stabilizes within approximately 1-1.5 hr. Each 2-3 days, the liquid and gas phase were sampled. After 25 days of reaction, the experiments were quenched to ambient conditions by cooling the reactor cell in a water bath for ~20-30 min. The autoclaves were opened after releasing the pressurized CO₂ inside the reactor. The solid run products were recovered and oven dried at 333 K overnight, then used for further analysis.

2.1.5 Gas sampling and gas chromatography analysis

At the HP/HT hydrothermal conditions of our experiments, mine tailings were expected to dissolve, releasing Mg, Fe and Si, and other minor elements, into the solution, which will then be involved in carbonate precipitation and hydrogen production. The variation of gas phase composition, especially the quantity of hydrogen is of our interest. For this purpose, the gas head space, which is in equilibrium with the solution, was sampled at 2-3 days intervals throughout the experiment, according to the sampling protocol given below.

2.1.5.1 Protocol of gas sampling

The gas outlet of the batch reactor, the valves (V1, V2 and V3) along this line are shown in Figure 2-11. A VCR swagelock gas-sampling tube was connected to the batch reactor gas outlet as shown in Figure 2-10 and 2-11. The valve V1 remained closed, and was only opened during the gas sampling. After connecting the Swagelock tube, its valve was opened (V7), in order to allow the sampling of gas (through the gas line). Then, a strong vacuum of 10⁻⁵ bar was created throughout the gas line up to valve V1, including the sampling tube, using a Turbo pump. The vacuum was held until it reached 10⁻⁵ bar, and longer. This ensured that the gas line was clean, and free of any contamination. Occasional inabilities to reach 10⁻⁵ bar indicated that there was a leak along the gas line; thus all the valves and joints were carefully checked before sampling. For sampling, first, the valve V3 was closed in order to isolate the gas line from pump. Then, valve V2 was closed as well. The gas in the batch reactor, which is at HP/HT, was then allowed to pass into the gas line by opening valve V1, for about 1-2 min. Then, the valve V1 was closed again, leaving an isolated gas sample between V1 and V2. The gas sample was finally allowed to pass into the sampling tube by opening valve V2. After 1-2 min equilibration time, the valve of the Swagelock tube (V7) was closed. The collected gas samples collected were then analyzed using gas chromatography within 1-2 weeks.

2.1.5.2 Protocol of gas analysis

The gas samples were analyzed in a Varian CP-3800 gas chromatograph, equipped with two TCD detectors and one FID detector (TCD=thermal conductivity detector; FID=field ionization detector), at IFPEN. The schematic of the GC is shown in Figure 2-13. The GC technique involves injection of the gas sample (which is a mixture of gases) into the instrument inlet, where it is carried by an inert carrier gas (eg. He, N₂), through a series of columns whose inner walls are coated with a stationary phase (eg. a liquid with high boiling point adsorbed onto a surface of an inert solid). As the gas mixture travels through the heated column the components are continuously exchanged between the mobile phase and the stationary phase. The difference of the rate of exchange of the analyzed components leads to their separation and is associated with different retention times in the column. In the case of hydrocarbons, the stationary phase is usually non-polar and the retention time is controlled by the molecular weight of the hydrocarbons (lighter hydrocarbons have shorter retention times) and by the shape of the molecule (eg. branched hydrocarbons have smaller retention times compared to straight chain hydrocarbons of the same number of carbon atoms). As a result, the components exit the column in a sequence.

The gases are detected by two types of detectors, TCD and FID. The first TCD (carrier N₂) is used exclusively for quantifying He and H₂. The FID is used for quantifying C-H compounds such as hydrocarbons. Finally, the second TCD (carrier He) is used for all other gases. The TCD detector senses changes in the thermal conductivity of the column effluent and compares it to a reference flow of carrier gas. Since most compounds have a thermal conductivity much less than that of the common carrier gases (eg. He, Ar, H₂), when an analyte elutes from the column the effluent thermal conductivity is reduced, and a detectable signal is produced. This detector is sensitive to both inorganic and organic gases such as. H₂, He, N₂, CO₂, O₂, Ar, methane, but the sensitivity for organic gases is low. The FID detector is 1000 to 3000 times more sensitive to hydrocarbon detection than the TCD. It detects the ions formed during the combustion of hydrocarbons in a hydrogen flame. The production of ions is proportional to the concentration of organic species in the gas sample. The FID detects organic gases of very low and very high concentrations with a linear response of 10⁷. The sensitivity of TCD and FID to inorganic and organic gases is further illustrated in Figure 2-14. Figure 2-14a shows the gas chromatogram of standard 2 (std 2, composition of air as given in table 2-3) injected at 1100 mbar pressure showing He, H₂, O₂, N₂ and CH₄ peaks detected on TCD. Figure 2-14b shows the gas chromatogram of standard 1 (std 1, containing hydrocarbons, as given in table 2-3) injected at 1100 mbar showing the C1-C4 hydrocarbons peaks, CO₂ and N₂ detected on TCD. Figure 2-14c shows the C1-C4 hydrocarbons detected on FID. The quantification limit of gases are given in Table 2-4. The gas chromatograph that we used is unable to detect carbon monoxide (CO) and hydrogen sulfide (H₂S). The data acquisition is done by the Galaxy chromatography data system version 1.10.1.2006, and the injection of sample is done through T496Pegaz apparatus developed by IFPEN, which can adjust injection pressures.

To begin an analysis of a gas sample, firstly, a vacuum was created along the complete loop through which the gases circulate, in order to clean the gas line. Then, two

blanks were injected. First, standard nitrogen (N₂) was injected at 1100 mbar, as a blank, to verify that the instrument doesn't contain traces of relict hydrocarbons from previous analysis. The second is the blank under vacuum, which is maintained for 1 min after closing down the pumping. This is necessary to verify any leaks in the system, before injecting the sample. These blanks were confirmed valid if they did not contain peaks for other inorganic or organic gases. Then, several standards were analyzed in order to check the performance of the detectors, and to obtain response factors for each gas. Those response factors are essential to determine the concentration of gases in actual samples. The different types of standards used are given in table 2-3. These standards were injected at 1100 mbar. The standards 2 and 4 have the composition close to air, while standards 1 and 5 were rich in hydrocarbons. Standard 3 contains 1% of inert noble gases (He, Ar, Ne, Kr and Xn). The composition of standard 4 is calculated from the response factors measured with standard 2, and both analysis were performed on the same day. Similarly, the composition of standard 5 is calculated from the response factors measured with standard 1, and similarly, both analysis were performed on the same day. After performing the confirmation of blanks and standard, the samples were injected.

The concentration of gases was calculated by:

$$\text{Concentration in \%} = \frac{\text{Surface (x)} \times \text{response factor}}{P_{\text{inj}}} \quad [2-5]$$

where, surface (x) is the surface area of the signal on GC (in μVS^{-1}), and P_{inj} is the injection pressure of the sample. Calculation of gas composition based on the GC measurements are given in Appendix I.

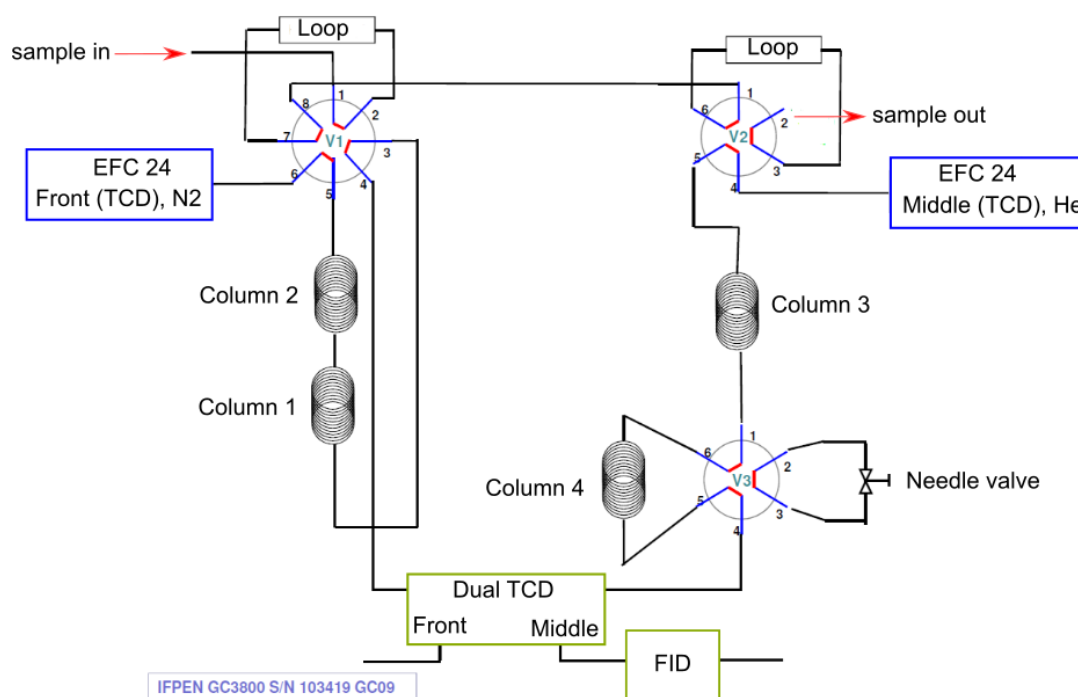


Figure 2-13. Schematic of gas chromatograph (IFPEN)

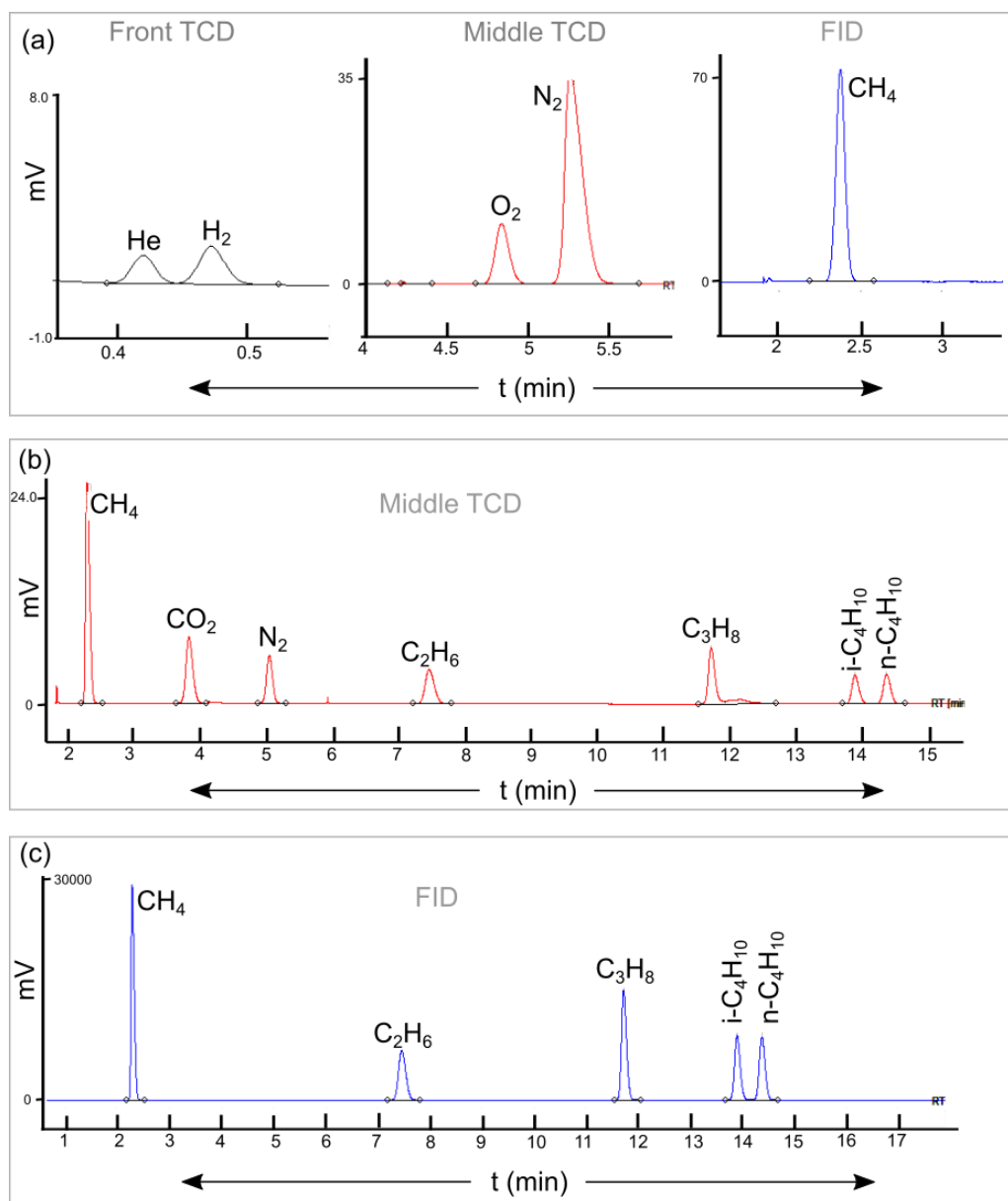


Figure 2-14. Peak positions of inorganic and organic gases on TCD, and FID detectors of gas chromatogram

Table 2-3. Composition of standards used in gas chromatography analysis.

Elements	STANDARDS				
	1 (HC)	2 (Air)	3 (rare gases)	4 (~Air)	5 (HC)
He	2%	0,10%	1%	0,20%	1%
H ₂	3%	0,10%	-	0,20%	2%
CH ₄	~40% (QS)	0,10%	-	0,20%	~55% (QS)
CO ₂	15%	0,10%	~95% (QS)	0,20%	10%
O ₂	-	20%	-	15%	-
N ₂	10%	~80% (QS)	-	~85% (QS)	20%
C ₂ H ₆	10%	-	-	-	5%
C ₃ H ₈	10%	-	-	-	5%
iC ₄ H ₁₀	5%	-	-	-	1%
nC ₄ H ₁₀	5%	-	-	-	1%
Ne	-	-	1%	-	-
Ar	-	-	1%	-	-
Kr	-	-	1%	-	-
Xe	-	-	1%	-	-

Table 2-4. Uncertainty and limit of quantification of gases analyzed by gas chromatography

	He	H ₂	CH ₄	CO ₂	O ₂	N ₂	C ₂ H ₆	C ₃ H ₈	iC ₄ H ₁₀	nC ₄ H ₁₀
Pressure range (mbar)	300-2000	300-2000	500-2000 (TCD)	300-2000	500-2000	300-2000	300-2000 (TCD) 800-2000 (FID)	300-2000 (TCD) 500-1100 (FID)	300-2000 (TCD) 500-1500 (FID)	300-2000 (TCD) 500-1500 (FID)
Concentration range (%)	0.01 à 100	0.005 à 2	0.001 à 40	0.01 à 100	5 à 20	-	0.01 à 10	0.01 à 10	0.05 à 5	0.05 à 5
Uncertainty in analysis (%)	6	5.4	0.6	1.3	5.2	3.3	1.2	1.2	1.3	1.1
Quantification limit (ppm)	100	100	10	100	-	-	100	100	500	500

2.1.6 Liquid sampling and ICP-AES analysis

At the hydrothermal conditions of our experiments, mine tailings dissolve precipitating carbonates as the main secondary phase. This dissolution releases various quantities of Mg, Fe, Si, and other minor elements into the solution, which will then precipitate depending on the saturation state of the fluid. The determination of mineral solubilities and saturation indices of minerals is the key to understand the reaction paths, which are calculated through thermodynamic modeling. In order to model the closed system in which the dissolution of mine tailings and precipitation of secondary phases take place, the accurate concentrations of released cations, and $\text{SiO}_{2(\text{aq})}$ are necessary. We sampled liquid phase in the batch reactor throughout the experiment in order to study its evolution. The liquid was sampled through the liquid outlet of the batch reactor (Figure 2-10 and 2-11). Approximately 2.0 g aliquot of the liquid was sampled directly into a clean and dry plastic bottle containing 40 ml of de-ionized water (electrical conductivity = 18 M Ω cm) acidified with nitric acid (HNO_3) 2% by volume, so that the sample was 20 fold diluted. Acidification is necessary to avoid precipitation of silica and to avoid oxidation of Fe^{2+} in the solution.

An inductively coupled plasma – atomic emission spectroscopy (ICP-AES; Thermo scientific iCAP 6000 series) with an Ar plasma was used to analyze the aqueous concentrations of Mg, SiO_2 , Fe, Al, Na, K, Ca, Mn, Ni, Cr, and S in the collected liquid sample. The ICP-AES is composed of two parts: the ICP and the optical (emission) spectrometer. The principle of this technique is based on the fact that excited electrons emit energy at a given wavelength as they return to ground state after excitation by high temperature (flame temperature; 6000 -10000 K) Argon Plasma (Figure 2-15). The fundamental characteristic of this process is that each element emits energy at certain wavelengths specific to its atomic character. The energy transfer for electrons when they fall back to ground state is unique to each element as it depends upon the electronic configuration of the orbital. The energy transfer is inversely proportional to the wavelength of electromagnetic radiation, as given by;

$$E = \frac{hc}{\lambda}$$

where h is Planck's constant, c the velocity of light and λ is wavelength, and hence the wavelength of light emitted is also unique. Although each element emits energy at multiple wavelengths, in the ICP-AES technique it is most common to select a single wavelength (or a very few) for a given element. The intensity of the energy emitted at the chosen wavelength is proportional to the amount (concentration) of that element in the sample being analyzed. Thus, by determining which wavelengths are emitted by a sample and by determining their intensities, this analysis enables qualitative and quantitative determination of elements from the given sample relative to a reference standard. The wavelengths used in AES ranges from the upper part of the vacuum ultraviolet (160 nm) to the limit of visible light (800 nm). As borosilicate glass absorbs light below 310 nm and oxygen in air absorbs light below 200 nm, optical lenses and prisms are generally fabricated from quartz glass and optical paths are evacuated or filled by a non-absorbing gas such as Argon.

For the ICP-AES analysis, the original liquid samples were transferred into 20 ml standard tubes and loaded into the automatic sampler of the instrument. A sample blank with same acidity (HNO_3 2% by volume) was also prepared. A series of standard solutions of Mg, SiO_2 , Fe, Al, Na, K, Ca, Mn, Ni, Cr, and S, with concentrations of 3, 9, 40, 1000, 4000 ppm were prepared for the calibration of the instrument. The external standard solutions (“quality controls”) of each element were analyzed under two or three different wavelengths (Table 2-5). An element, Mg for instance, was measured under two wavelengths 279.6 nm and 285.2 nm), and the best wavelength under which the concentration measurement was closest to that of the theoretical concentration of the standard was selected for the measurement of the sample. The analytical uncertainty of the fluid analysis by ICP- AES is around 5%.

Table 2-5. The wave lengths under which Mg, Fe, Si and Al standards were analyzed in ICP-AES

	λ_1 (nm)	λ_2 (nm)
Mg	279.6	285.2
Fe	238.2	259.9
Si	394.4	396.2
Al	394.4	396.2

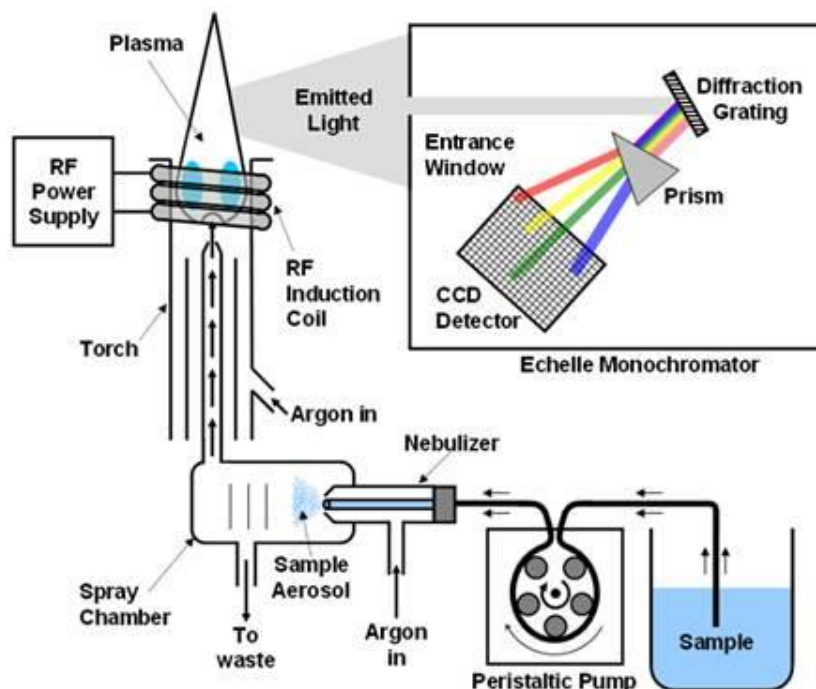


Figure 2-15. Schematic of the ICP-AES instrument (<http://sites.cord.edu>)

2.1.6.1 Test analysis to determine dissolved organic compounds

Another fluid sample was collected with the aim of determining the dissolved organic species that may have formed due to possible reactions between H_2 and CO_2 at the considered pressure and temperature conditions. To this end, approximately 1.0 g of the fluid was sampled through the a 2,4 DNPH silica cartridge (2,4 Dinitrophenylhydrozene). This method is based on the reaction of 2,4 DNPH with the carbonyl-carbon in aldehydes and ketones, converting them into relevant hydrozone derivatives which will then be analyzed by liquid chromatograph with a UV detector (LC-UV). Due to the very low detection limits for aldehydes and ketones (eg; the detection limits of formaldehyde and acetaldehyde are 6 ppb and 4.5 ppb respectively) it could be a promising method for quantifying aldehydes and ketones. However, the other organic molecules which could also be present in the solution such as alcohols and carboxylic acids were not be quantified through this method.

2.1.7 Solid product analysis

2.1.7.1 XRD and SEM analysis

The X-ray powder diffraction analysis was performed on the recovered powder products for preliminary identification of new phases formed during the reactions. The peaks on the XRD patterns were identified by peak-search-matching and the semi quantitative analysis was performed to obtain the relative amount (in wt.%) of phases. The analytical conditions are described in section 2.1.2.3. Separate fractions of the run products from each experiment were mounted on gold (Au) coated adhesive carbon-taped sample holders. They were then observed under scanning electron microscope (SEM) to study the dissolution features on the surfaces of the starting powder, and the morphological characteristics of secondary products formed after reacting at hydrothermal conditions. For further analysis, the cut and polished sections of these reacted powders were prepared by fixing the powder in epoxy resin and cut and polished with diamond grit ($<0.25\ \mu m$) or lapping film ($<1\ \mu m$). The samples were then carbon coated and analyzed under SEM via EDX

2.1.7.2 FIB-TEM analysis

Focused ion beam (FIB) thin sections were prepared at IGP and at Institute of Electronics, Microelectronics and Nanotechnology (IEMN), Lille using a Zeiss neon EesB40 FIB/FEG-SEM system. The instrumentation is similar to the scanning electron microscope, but, instead of a beam of electrons, the FIB apparatus is equipped with a beam of ions (here we used gallium (Ga) beam). This technique allows to prepare ultra-thin sections, which are transparent to electrons ($<200\ nm$), by milling with a beam such as gallium (Ga^+), which can be observed under TEM.

A schematic showing the cross section of the sample during FIB milling is given in Figure 2-16. The images showing the procedure of preparation of FIB ultra-thin sections of our experiments are shown in a Figure 2-17. For cutting the FIB section, first, the reaction products of the HP/HT experiments were fixed on epoxy resin and polished using an ion beam. These ionically polished sections were observed under the FIB/SEM to identify the

reaction boundaries between glass-phyllsilicate contact and glass-magnesite contacts. The line along which the thin section has to be cut is marked by depositing platinum ($\sim 1\ \mu\text{m}$ thickness). First, the milling with Ga ion beam was performed on one side of the Pt deposition which cuts a trench in the sample. Then the milling was performed on the other side. We used a 30 kv Ga⁺ beam operating at 20 nA to cut the thin section to a depth of $\sim 5\ \mu\text{m}$. The last step consisted of ion milling at much lower beam currents ($\sim 100\ \text{pA}$), to achieve a final thickness of approximately $\sim 80\ \text{nm}$. The $\sim 15\ \mu\text{m} \times 5\ \mu\text{m} \times 80\ \text{nm}$ thinsection was removed from the sample with a micromanipulator and placed onto a carbon-coated copper TEM grid for subsequent TEM analyses. TEM analyses were carried out with a JEOL 2100F (FEG) operated at 200 kV (IMPMC,UPMC, Paris). TEM-EDX analysis, and electron diffraction patterns of mineral phases were collected.

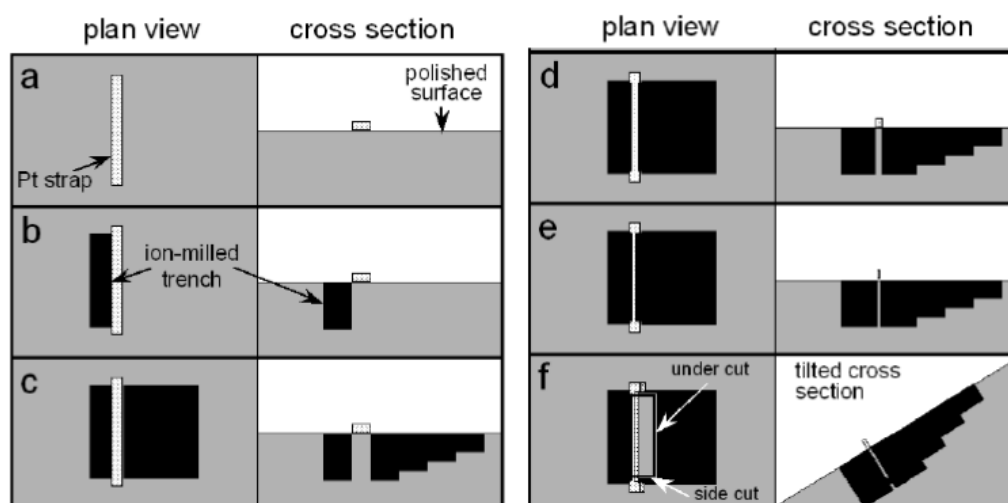


Figure 2-16. A schematic representation of the focused ion beam extraction sequence (Heaney et al., 2001) (a) the deposition of a Pt; (b and c) the ion milling of trenches on both sides of the Pt deposition; (d and e) thinning of the specimen foil; and (f) tilting of the specimen for side and under cuts.

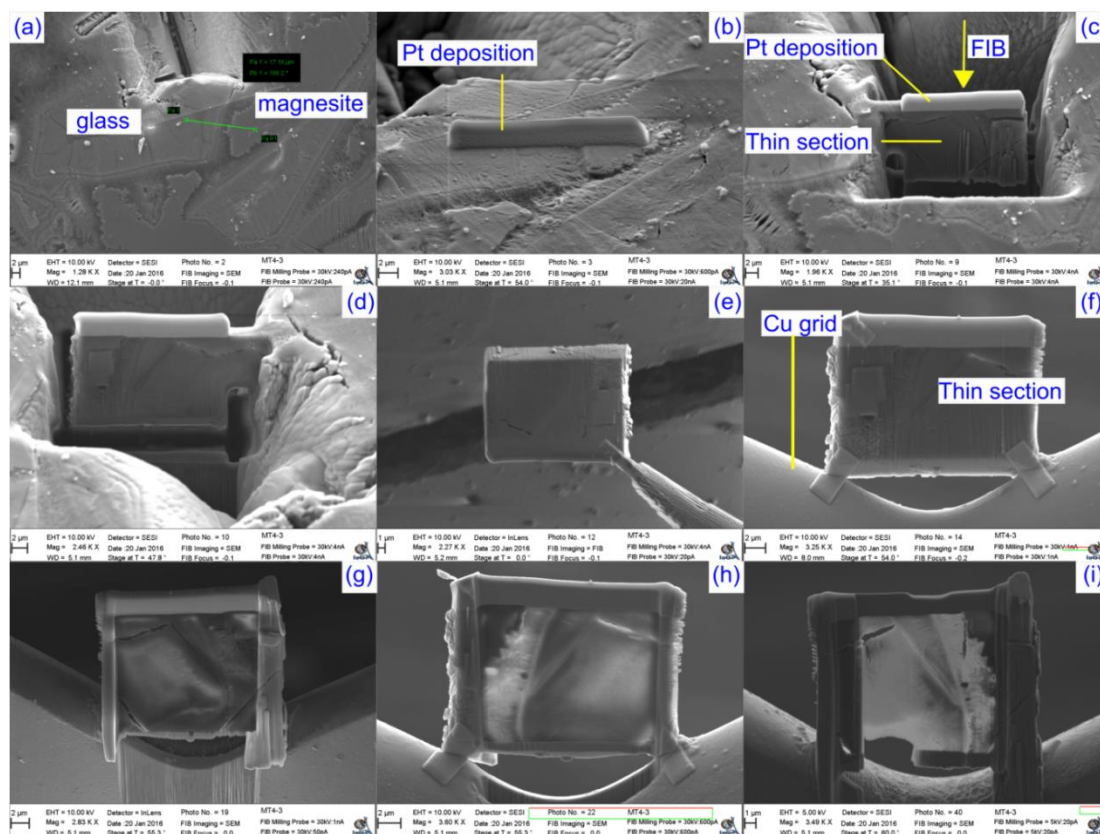


Figure 2-17. Images showing focused ion beam extraction sequence (a) selecting the area to cut section (b) Pt deposition (c) thinsection lying in the ion-milled trench (d) thin section detached from LHS (e) lifting the thin section from the sample (f) thin section glued into the Cu grid (g, h) further milling the thinsection (i) final thin section with thickness <200 nm.

2.1.7.3 Rock-Eval 6 analysis

Carbonates in the reaction products were first identified using XRD analysis. However, Rock-Eval 6 analysis was performed for better detection and quantification of carbonate. The quantification limit of Rock-Eval 6 is ~0.02 wt.% C, which corresponds to ~0.15 wt.% MgCO_3 , and this method more than one order of magnitude more sensitive than the phase quantification by XRD. More details on sample preparation, instrumentation and analysis of the Rock-Eval 6 technique can be found in (Behar et al., 2001; Lafargue et al., 1998). The instrument consists of two furnaces, one of which conducts pyrolysis of the sample (~40 mg) by progressive heating in an inert atmosphere (eg. N_2), while the other furnace oxidized the sample by burning it under an air flow (Figure 2-18a). CO_2 and CO liberated upon pyrolysis and/or oxidation are sent to an infra-red detector in real time. Since the sample is combusted, the method relies on a destructive analysis.

It involves pyrolysis and oxidation of ~40 mg of sample in an inert gas flow above 400 °C and oxidation at temperatures between 650°C–900°C (magnesite reacts at 650°C, dolomite at 850°C, calcite at 900°C) (Figure 2-18b). The gaseous CO_2 produced during the pyrolysis and oxidation cycles is analyzed by an infra-red analyzer (eg; S3' peak and S5 peak respectively) in real time and the peak areas of S3' and S5 peaks (Figure 2-18c) are

deconvoluted by the software to calculate the relative amount of carbonates (wt.%) according to the equations,

$$\text{PyroMinc (wt. \%)} = \frac{\left[S3' \times \frac{12}{44} \right] + \left[\left(\frac{S3' \text{CO}}{2} \right) \times \left[\left(\frac{S3' \text{CO}}{2} \right) \times \frac{12}{28} \right] \right]}{10} \quad [2-6]$$

$$\text{OxyMinc (wt. \%)} = \frac{S5 \times \frac{12}{44}}{10} \quad [2-7]$$

The amount of total mineral carbon (MinC) in the sample is obtained by the addition of weight percent (wt.%) of mineral carbon produced from pyrolysis cycle (PyroMinC) and oxidation cycle (OxyMinC) as below,

$$\text{MinC (wt. \%)} = \text{PyoMinC} + \text{OxyMinC} \quad [2-8]$$

Calculations for the amount of CO₂ trapped can be performed as follows:

$$m_{\text{CO}_2 \text{ trapped}} = \frac{M_{\text{CO}_2}}{M_{\text{carbonate}}} \times m_{\text{carbonate}} \quad [2-9]$$

$$m_{\text{CO}_2 \text{ trapped}} = \frac{M_{\text{CO}_2}}{M_{\text{carbonate}}} \times (\text{wt}\%_{\text{carbonate}} \times m_{\text{run products}}) \quad [2-10]$$

$$m_{\text{CO}_2 \text{ trapped}} = \frac{M_{\text{CO}_2}}{M_{\text{carbonate}}} \times \text{wt}\%_{\text{carbonate}} \times (m_0 \text{ mine tailings} + m_{\text{CO}_2 \text{ trapped}}) \quad [2-11]$$

Since the Rock-eval apparatus was initially developed for petroleum applications, it is also equipped with an FID detector to quantify and characterize the various fractions of hydrocarbons under pyrolysis.

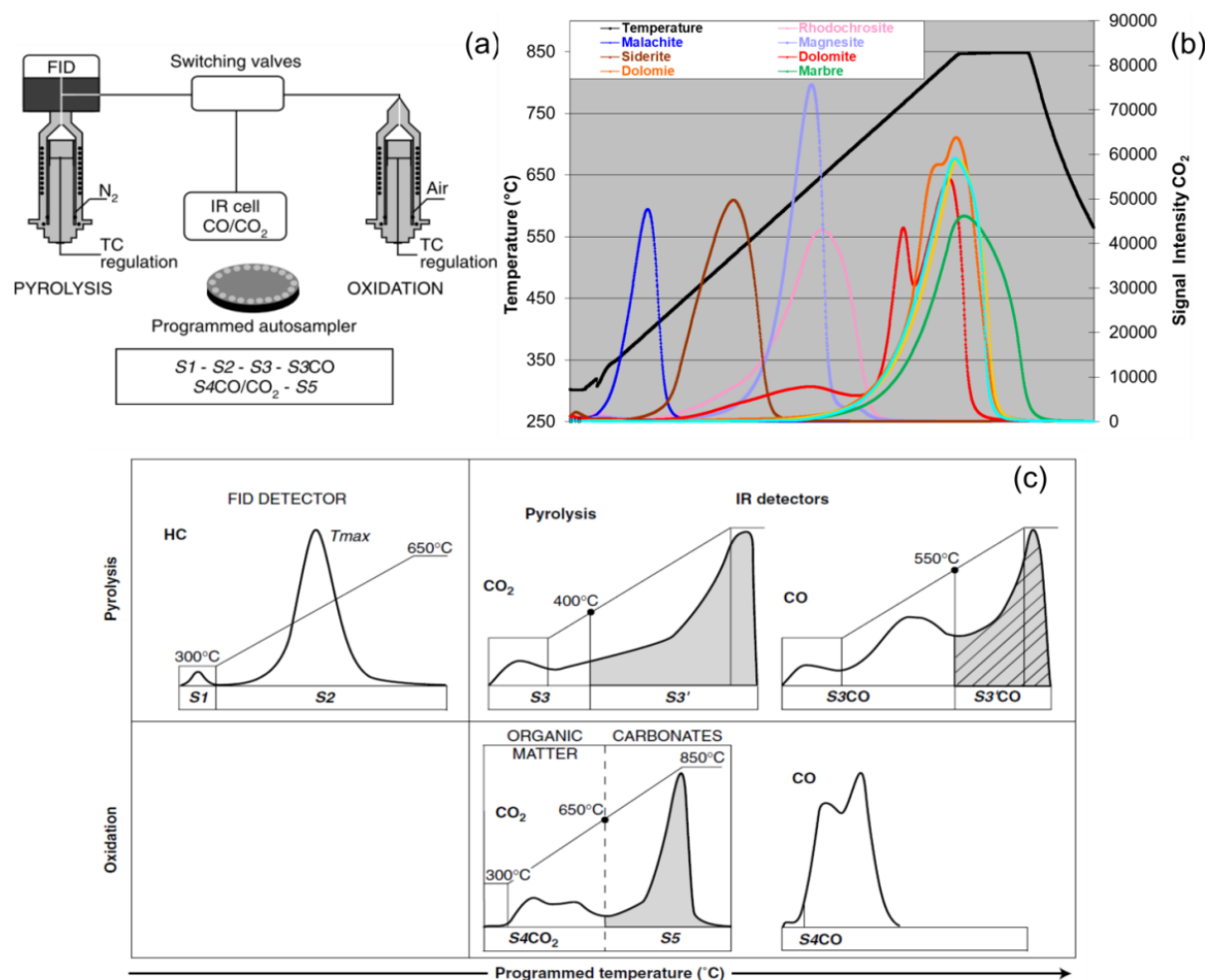
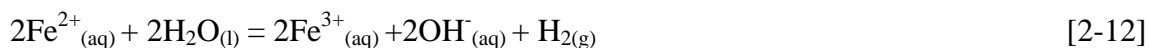


Figure 2-18. Sketch of a standard Rock-Eval 6 instrument, showing its major components (pyrolysis and oxidation furnaces, IR detector and sampler) (Behar et al., 2001). The different peaks due to pyrolysis and oxidation are shown by S1 to S5. (b) Peak temperatures at which different carbonates decomposed, and the intensity of CO₂ signal corresponds to each peak (for decomposition of ~40 mg of sample) (Source: IFPEN) (c) Analytical procedure for mineral carbon analysis by Rock-Eval 6 (Behar et al., 2001).

2.1.7.4 Fe₂O₃(total)/FeO analysis

The amounts of Fe²⁺ and total iron in the non-reacted mine tailings, and the three experimental run products were analyzed at the Centre de Recherches Pétrographiques et Géochimiques (CRPG), Nancy, France. The samples were boiled in HF / H₂SO₄ to release Fe²⁺ which was then quantified by volumetric titration with K₂Cr₂O₇. Another fraction of the sample was then heated with LiBO₂ at 1223 K and acid digested (4 vol.% HNO₃) to convert all species of iron (e.g. Fe⁰ and Fe²⁺) contained in the sample into Fe₂O₃ (Fe³⁺). The resulting ferric iron was measured by atomic absorption spectrophotometer (AAS). The amount of Fe³⁺ in the non-reacted mine tailings sample was calculated by subtracting the Fe²⁺ molar amount measured in the FeO analysis to the (Fe²⁺ + Fe³⁺) amount measured in the Fe₂O₃ analysis. The value being close to 0 suggests there is little to no oxidized iron in the initial material. The quantities of H₂ measured by GC at the end of the experiments were compared to the amounts

calculated from the loss of Fe^{2+} (through oxidation and simultaneous H_2 production) in the run products. In order to estimate the amount of Fe^{3+} formed during the experiments, the amount of Fe^{2+} measured in the run products were subtracted to the one measured in the initial non-reacted mine tailings; the quantity of H_2 produced was then extrapolated from the oxidized iron (Fe^{3+}) according to:



where, the stoichiometric proportion of $\text{Fe}^{2+} : \text{H}_2$ is 2:1.

2.1.8 Thermodynamic modeling

Mineral solubilities (or saturation indices, SI), solution pH and activities of aqueous species were calculated using the geochemical code CHESS - CHemical Equilibrium with Species and Surfaces (van der Lee and De Windt, 2002) using the LLNL EQ3/6 thermodynamic database. For the calculation of solution equilibrium, we used the aqueous concentrations of SiO_2 , Mg, Fe, Ca, Al, N and K obtained from ICP AES analysis, the temperature of the experiment and the fugacity of CO_2 as input parameters.

The fugacity of CO_2 ($f\text{CO}_2$) at $T=473$ K and total pressure of 15 MPa, is calculated according to the equation;

$$f\text{CO}_2 = \varphi * P \quad [2-13]$$

where φ is the fugacity coefficient of CO_2 calculated according to Peng-Robinson equation using the ThermoSolver 1.0 software (Barnes, C.S and Koretsky, 2004; Barnes, 2007). At 473 K, 15 MPa, $\varphi = 0.8713$, and therefore $f\text{CO}_2 = 13$ MPa (13.1 MPa) (Table 2-6).

Table 2-6. Fugacity coefficients and CO_2 fugacity in our experiments

Experiment	P (total) (bar)	T (°C)	fugacity coefficient of CO_2 (φ)	$f\text{CO}_2$
MT1	150	200	0.8713	130.69
MT2	300	250	0.8812	264.36
MT3	300	300	0.9391	281.73

We calculated the concentration of aqueous Si, and Mg at which the solution reaches saturation with respect to amorphous silica ($\text{SiO}_{2(\text{am})}$) and magnesite (MgCO_3) respectively. Precipitation of $\text{SiO}_{2(\text{am})}$ or magnesite requires the solution to be at equilibrium or oversaturated with respect to ($\text{SiO}_{2(\text{am})}$) and magnesite(MgCO_3). Saturation ratio (Ω) or SI are used to describe the degree of saturation. The saturation ratio (Ω) of a mineral given by the equation,

$$\Omega = Q/K_s \quad [2-14]$$

For instance, for the reaction of magnesite precipitation at high pH;



the K_s (solubility product), is the activity product of the ions at equilibrium,

$$K_s = \frac{a[Mg^{2+}].a[CO_3^{2-}]}{a[MgCO_3]} \quad [2-16]$$

Where the activity of a solid, such as $MgCO_3$, is equal to 1.

The IAP (ion activity product) will be the activity product of these species at any instant, also known as Q

$$Q = a[Mg^{2+}].a[CO_3^{2-}] \quad [2-17]$$

The saturation index is the logarithm of saturation ratio.

$$SI = \log \Omega \quad [2-18]$$

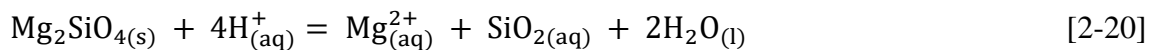
The thermodynamic states with respect to a minerals phase such as, equilibrium, undersaturation and supersaturation is indicated by zero, negative or positive value of SI respectively. These saturation indices were used to calculate the reaction Gibbs free energy ($\Delta G(r)$) for the dissolution reactions according to the equation,

$$\Delta G(r) = RT \ln_{10}(SI) \quad [2-19]$$

where, R is the universal gas constant ($Jmol^{-1}K^{-1}$) and T is the temperature measured in kelvin (K).

We considered the dissolution reactions of forsterite, amorphous silica and magnesite, written according to the CHESSE database requirements (i.e. in terms of metal cations, $H^+_{(aq)}$, $SiO_{2(aq)}$ and $HCO^-_{3(aq)}$)

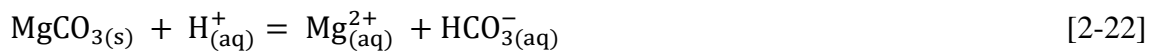
forsterite dissolution;



amorphous silica dissolution;



magnesite dissolution;



The saturation indices of each mineral was obtained from CHESSE equilibrium calculation, and then the $\Delta G(r)$ with respect to forsterite, amorphous silica and magnesite were calculated considering the above dissolution equations.

2.2 Section II – Experimental investigation of catalytic potential of sphalerite and marcasite for abiotic hydrocarbon generation

2.2.1 General introduction

We performed laboratory experiments to simulate the abiotic hydrocarbons production, a natural phenomena known to occur in many geological settings including sea floor hydrothermal systems, land-based serpentinizing systems and sedimentary environments. It has been proposed that abiotic hydrocarbons are generated via Fischer-Trosch type reactions catalyzed by mineral surfaces; however the mechanism is still not fully understood. The aim of our experiments were to re-produce the conditions similar to sea floor hydrothermal environment, in which hydrogen necessary for the reaction is produced by iron oxidation (eg. via serpentinization), and the inorganic carbon is dissolved in water. Two sulfide minerals were introduced as prospective catalyst for the FTT reaction. We used natural minerals for the reaction. The analysis workflow is described Figure 2-19. Our first aim was to recover the gas phase after the reaction, and analyze it for simple hydrocarbons that could have been potentially produced. The second aim was to analyze the liquid phase to determine potential dissolved organic compounds, which could be an indication of the reaction path. Finally, thermodynamic modeling of the liquid phase will be performed to estimate the quantities of dissolved organic compounds in order to model the reaction path.

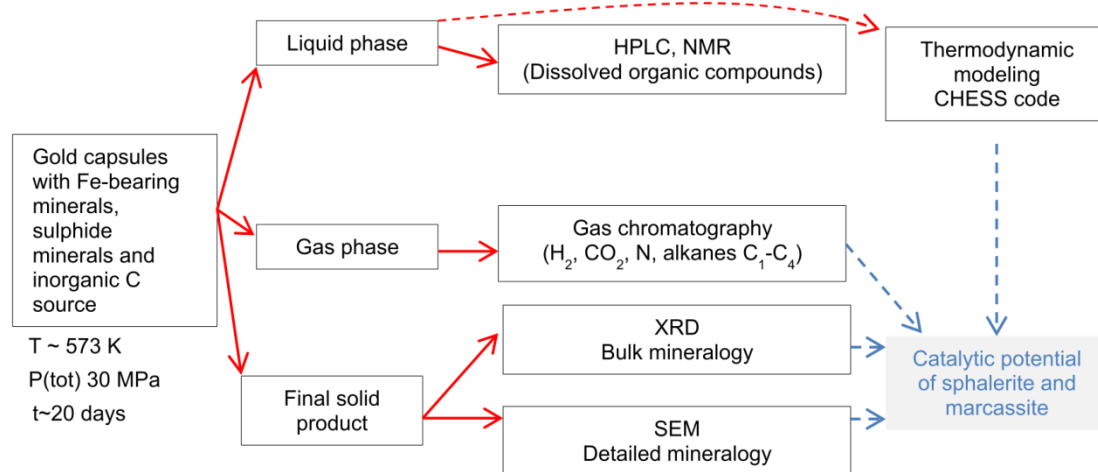


Figure 2-19. Experimental workflow to investigate abiotic hydrocarbon production in the presence of sulfide minerals.

2.2.2 Starting materials

The catalytic activity of two natural minerals (sphalerite, ZnS and marcasite, FeS₂) on Fischer-Tropsch Type (FTT) synthesis was experimentally studied. The experiments were performed on natural Fe-rich minerals such as forsterite (Fo90), fayalite and chlorite. These minerals were known to be involved in production of H₂ by the redox reaction coupled with oxidation of Fe²⁺ and reduction of water in mafic lithologies.

Natural olivine from San Carlos, (Arizona, USA) with Fo90 composition obtained from Wards mineral company. The crystals were green color, transparent to translucent which contained traces of enstatite (MgSiO_3) and iron oxides which were not removed during the sample preparation.

Natural fayalite samples (Bellerberg, Germany) were obtained from Mikon mineral company, and these were gray color polycrystalline samples which contained abundant magnetite as an impurity. Magnetite was removed using a hand magnet during the preparation.

Natural chamosite (iron end-member of the chlorite group with a general formula, $(\text{Fe}^{2+})_5\text{Al}(\text{AlSi}_3\text{O}_{10})(\text{OH})_8$) was obtained from Ward's mineral company.

Unaltered natural sphalerite from Vladivostok, Russia, was used as a catalyst in these experiments. The sphalerite samples were crushed and powdered using an agate mortar and pestle and sieved to obtain the $<40\ \mu\text{m}$ grain size fraction.

Natural samples of marcasite from Rheims, France were obtained from wards' mineral company and were used as a catalyst in these experiments. They are black color translucent to opaque crystals with fresh surfaces.

The samples were crushed and powdered using a ball mill (FRITSCH Planetary Micro Mill PULVERISETTE 7 premium line) to obtain $<20\ \mu\text{m}$ grain size fraction, and those samples present in small quantity were crushed and powdered using agate mortar and pestle (eg; fayalite).

2.2.3 Preparation of gold capsules

The starting materials were loaded into cylindrical gold capsules with a length of 30 or 35 mm and outer diameter of 5 or 6 mm (wall thickness of 0.2 mm). The gold tubes were first cleaned by dipping them in 6 M hydrochloric (HCl) acid overnight followed by heating at $700\ ^\circ\text{C}$ in a high temperature furnace for about 10 min. After cleaning the gold tubes, one side of the tube was pressed tight using a pair of flat pointed pliers, and welded using a Lampert PUK1.0 welding machine (electric arc welding), equipped with 0.5 mm Pt electrodes (Figure 2-21). First, the mode of welding in the instrument is set to "gold" and needle oriented perpendicular to the surface. In general, for the welding of gold tube of 0.2 mm wall thickness, power of 40 % and pulse time of 5 ms were selected. Then the flat edge of the gold tube was welded, while observing under microscope in the welding machine, to avoid holes along the edge. Afterwards, the starting material were weighed, and filled into the gold capsule. Three types of material were included; an Fe-bearing mineral for generation of hydrogen by oxidation of Fe^{2+} (olivine, fayalite or chlorite), a sulfide mineral as a catalyst (sphalerite or marcasite), and 0.64 M NaHCO_3 solution as the inorganic carbon source. Experimental blanks were prepared by loading only the Fe-bearing mineral and NaHCO_3 solution to test the effect of catalyst mineral. A set of capsules were prepared using de-ionized water instead of NaHCO_3 as blanks. Approximately 100 mg of powdered of Fe bearing mineral; 10 mg of sulfide mineral and 200 μL of 0.64 M NaHCO_3 solution were

loaded into the gold capsules. The NaHCO_3 solution was prepared using de-ionized water (18.2 M Ω cm) bubbled with nitrogen gas ($\text{N}_2(\text{g})$) for about 2 hours to eliminate dissolved oxygen. The weighting and loading the minerals were done in normal atmosphere, and the NaHCO_3 solution was then filled into the capsule under inert atmosphere (N_2 glove box). Then the un-welded end of the capsule was tightened to flat. The flat end of the gold capsule was cut using a pair of sharp cutting pliers in order to seal the capsule temporarily, and then the capsule was taken out of the glove box for welding. The tightened end of the capsule was welded shut using the arc welding machine. The weight of the empty gold tube, the starting material and the final weight of the capsule were recorded for further use. Once the capsule was welded, it was kept in an oven at 60°C overnight to test for leaks by taking into account the mass difference before and after heating. The capsules without leaks were used for HP/HT experiments.

2.2.4 High pressure high temperature experiments

The high pressure and high temperature experiments were conducted in a Parr® Hastelloy autoclave with volume of 75 ml pressurized by water and argon (Ar). The gold capsules prepared for experiment were loaded into the autoclave and the reactor vessel was partially filled with water to induce better temperature conduction and homogenization in the batch reactor. The reactor was properly sealed. Pressurized argon (Ar) gas was pumped into the reactor vessel, and the system was then heated up to the desired temperature. In general, maximum of 10 capsules were loaded in an autoclave. All the experiments were conducted at 573 K and 30 MPa, for 20 days. After 20 days of reaction period, the experiment was quenched to ambient conditions by cutting off the power supply and immersing the reactor in a cold water bath. At the end of the experiment, the recovered capsules were air dried and weighed to confirm that the capsules had not leaked during the experiment. The successful capsules were pierced for gas analysis, liquid analysis and to recover the solid reaction products, as discussed in following sections.

2.2.5 Analysis of gas phase

The gases produced in the capsules were analyzed using gas chromatography (GC). The capsules were pierced and the gases were collected by the method employed by Malvoisin et al. (2013). However, for convenience, a glass tube with a piercer needle was adapted for the analysis (Figure 2-20). We performed the first trial analysis, by creating a vacuum inside the piercer, closing isolating the piercer from the vacuum (by closing the blue valve, see Figure 2-20), and piercing a gold capsule. Two important observations were made; firstly, release of a considerable amount of water vapor in the vacuum upon piercing the capsule induced a non-negligible gas pressure. Secondly, the total pressure after piercing was approximately 40-60 mbar. The low injection pressure and water vapor lowered the quality of analysis. Therefore, in the second trial we followed the procedure of Malvoisin et al (2013), by injecting the sample with an inert gas at 1 bar and then at 1.5 and 2.5 bar (we used Ar instead of He). We also used the cold trap in order to avoid water vapor injection into the GC. However, the results were inconsistent, especially for hydrocarbons. The study of vapor-pressure curves showed that except for methane, the other alkanes, ethane, propane and

butane become liquid upon cooling down at high pressure (eg. 1.5 - 2 bar in our trials). The Figure 2-21 show the saturation curves of C1-C4 alkanes, constructed using standard NIST data (NIST, 2017). The vapor pressure was calculated using the Antoine equation;

$$P = 10^{\left\{A - \frac{B}{(T+C)}\right\}} \quad [2-23]$$

Or,

$$\text{Log } P = A - \frac{B}{(T+C)} \quad [2-24]$$

Where, P is the vapor pressure (bar), A,B,C are constants, and T is the temperature in kelvin.

The constants A,B, C for saturation curve of methane has been obtained by the experimental and theoretical calculations performed by (Cutler, A.J.B. and Morrison, 1965; Hestermans and White, 1960; Prydz and Goodwin, 1972; Regnier, 1972). The values of A,B,C parameters for all the four gases are given in Table 2-7.

Table 2-7. Antoine equation parameters for methane, ethane, propane and butane

	Temperature (K)	A	B	C	Reference
methane	90.99 - 189.99	3.9895	443.028	-0.49	(Cutler, A.J.B. and Morrison, 1965; Hestermans and White, 1960; Prydz and Goodwin, 1972; Regnier, 1972)
	96.89 - 110.19	2.00253	125.819	-48.823	
	93.04 - 107.84	3.80235	403.106	-5.479	
	110.00 - 190.5	4.22061	516.689	11.223	
ethane	91.33 - 144.13	4.50706	791.3	-6.422	(Carruth and Kobayashi, 1973; Loomis and Walters, 1926)
	135.74 - 199.91	3.93835	659.739	-16.719	
propane	277.6 - 360.8	4.53678	1149.36	24.906	(Hegleson and Sage, 1967; Kemp and Egan, 1938; Rips, 1963)
	230.6 - 320.7	3.98292	819.296	-24.417	
	166.02 - 231.41	4.01158	834.26	-22.763	
butane	135.42 - 212.89	4.70812	1200.475	-13.013	(Aston, J.G.; Messerly, 1940; Carruth and Kobayashi, 1973; Das et al., 1973)
	272.66 - 425.	4.35576	1175.581	-2.071	
	195.11 - 272.81	3.85002	909.65	-36.146	

The curves show that the C1-C4 alkanes won't condense if they are injected at low pressure (eg. few mbars), while still using the cold trap to condense water. Therefore, the samples were injected at low pressure, without Ar and with a cold trap. The detailed protocol of gas analysis is explained below:

- the reacted gold capsule was inserted into the piercer and positioned below the piercer needle (Figure 2-22 b).
- Then, the glass piercer was connected to the GC as shown in Figure 2-22 c.
- A cold trap was prepared by mixing finely crushed dry ice and ethanol into a thick slurry, with a temperature of approximately -70 °C (which remained stable for about 30 min).
- The elongated vertical tube at the end of the piercer (label no 4 on Figure 2-22 a), was dipped into the dry ice-ethanol mixture to trap water (in the capsule) by condensation.
- The blue valve of the piercer was opened, so that the piercer was connected to the GC.
- A vacuum was created in the piercer and the rest of the gas line (10^{-5} mbar). This step ensured the absence of leaks.
- A blank was injected ($p_{inj} = 1$ mbar), to confirm that the gas line was free of contamination.
- After the analysis of blank, a vacuum was created again, along the line including the piercer (-with capsule).
- The piercer was isolated by closing the blue valve.
- The gold capsule was pierced by lowering the needle by tightening the screw.
- Once the capsule was properly pierced, a waiting time of 2 min was applied to let the gas and water vapor escape from the capsule, and condense.
- Then the blue valve was opened and an equilibration time of 1 min was applied.
- Finally, the gas sample was injected for analysis.

Around 4-5 capsules were analyzed per day. A conventional procedure of passing standards and blanks was conducted prior to each capsule analysis (see section 2.1.5). Furthermore, in-between each injection (standards or samples), the line was cleaned by creating a vacuum; in-between each successive sample, a blank was analyzed to ensure the line remained free of contaminants.

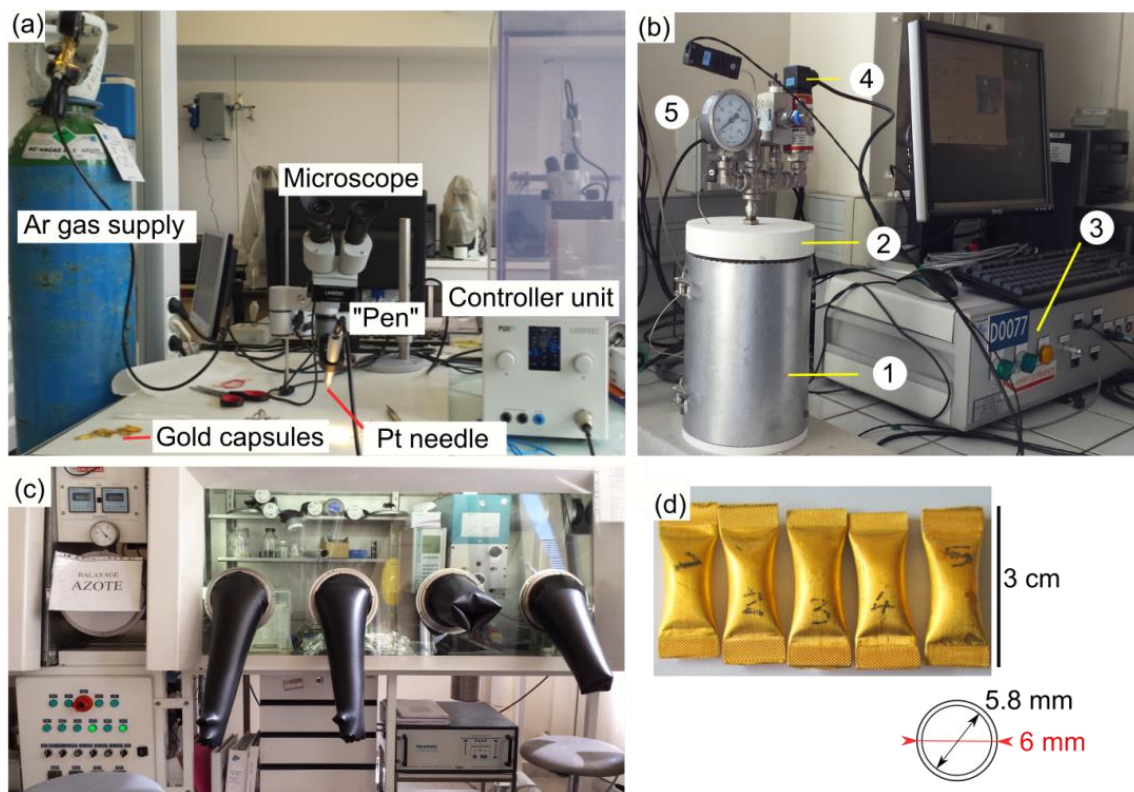


Figure 2-20. Preparation of gold capsules for the experimental simulation of abiotic hydrocarbon generation (a) PUK Lampert 4.1 welding machine with its accessories (b) non-stirred autoclaves used for HP/HT experiments (c) N₂ glove box used for the closing the loaded capsules in an inert atmosphere (d) welded capsules showing its dimensions. The labeled components in (b) are; 1. Autoclave in the oven 2. Alumina insulator 3. P/T controller and power supply 4. Pressure sensor 5. Manometer

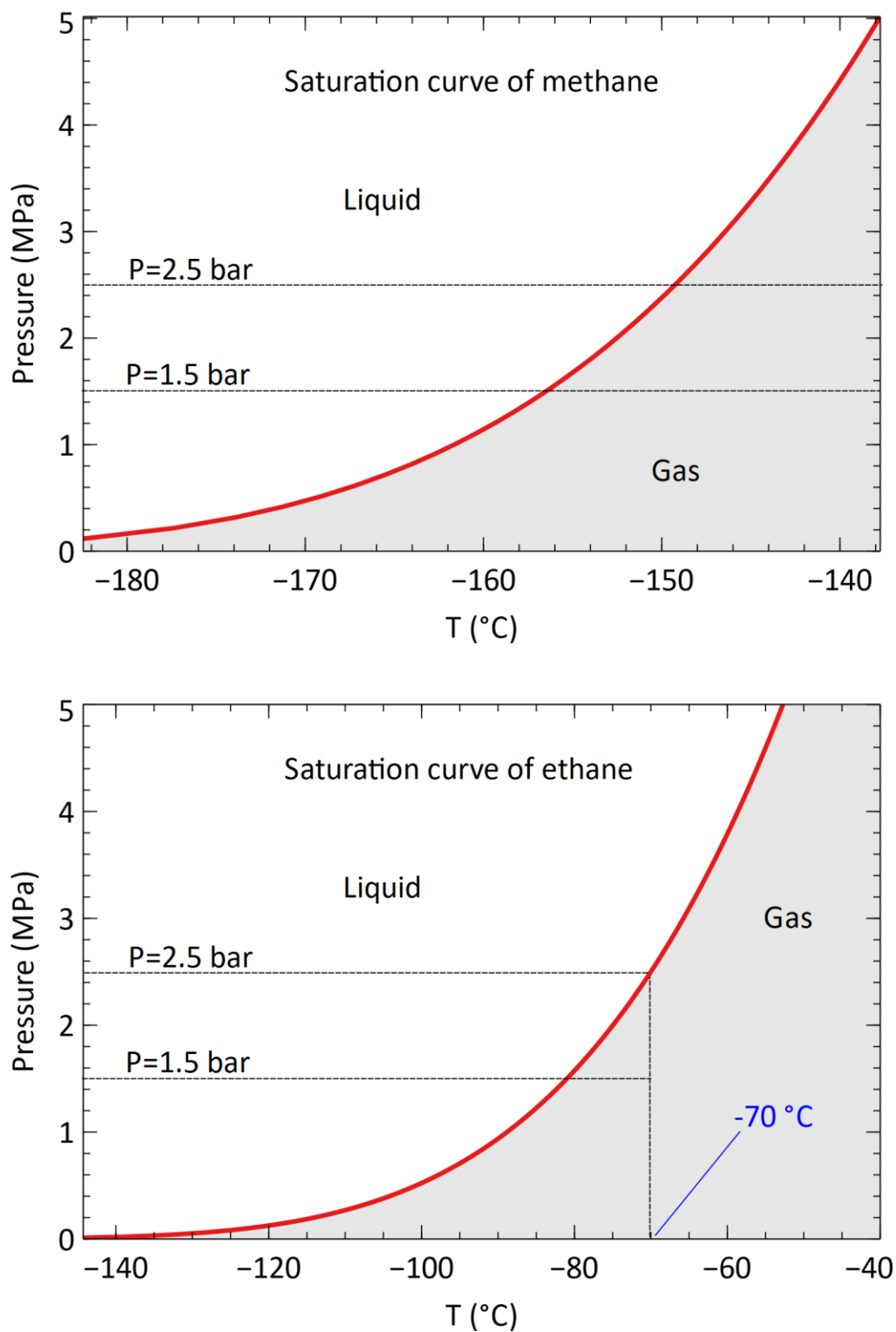
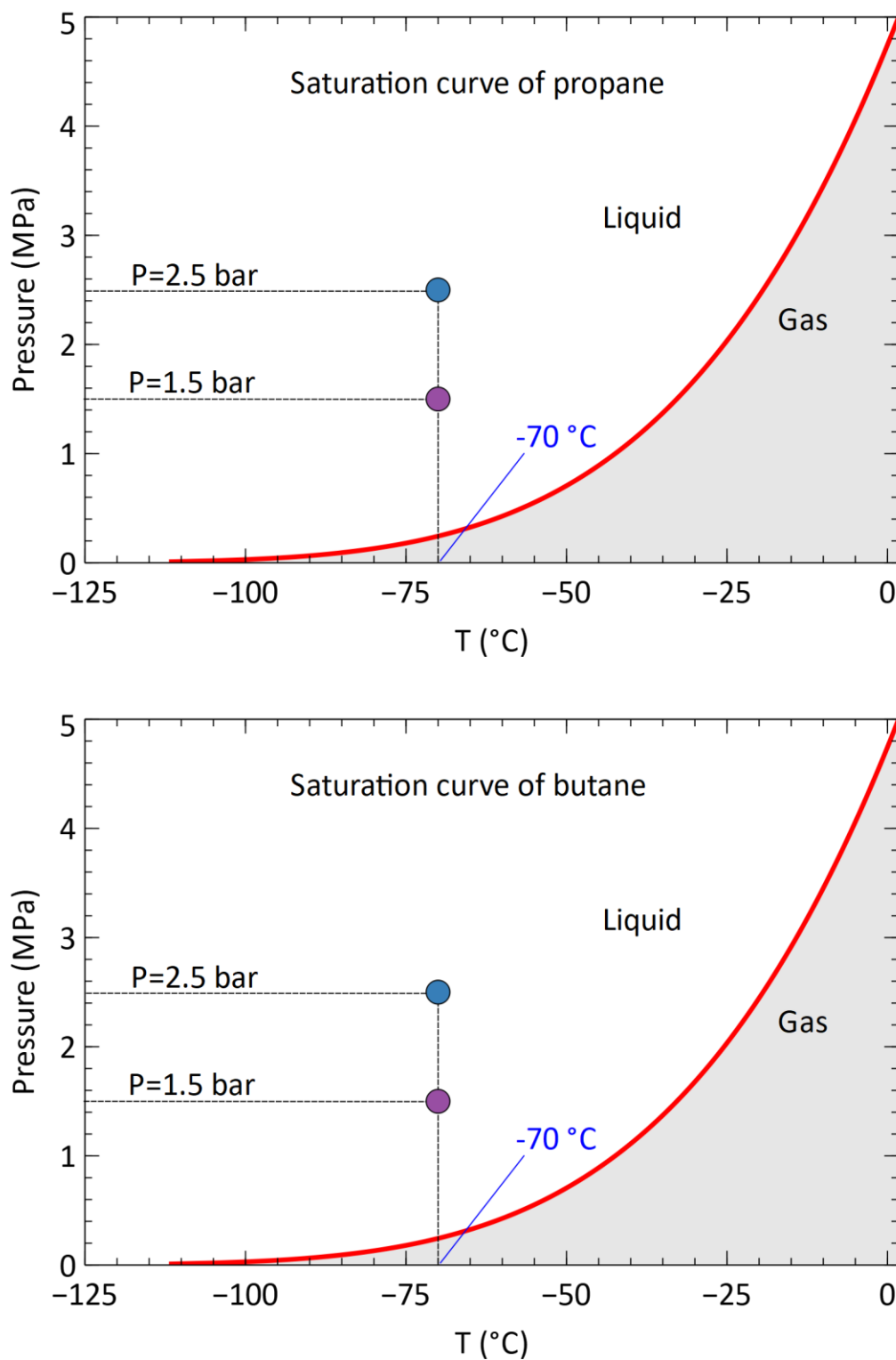


Figure 2-21. Saturation curves of C1-C4 alkanes constructed based on NIST standard data. The data points show the P/T conditions of trials. The curves demonstrate that except methane, the other alkanes, ethane, propane and butane are condensed at -70°C at high pressure (cont).



Cont..

Figure 2-21. Saturation curves of C1-C4 alkanes constructed based on NIST standard data. The data points show the P/T conditions of trials. The curves demonstrate that except methane, the other alkanes, ethane, propane and butane are condensed at -70°C at high pressure.

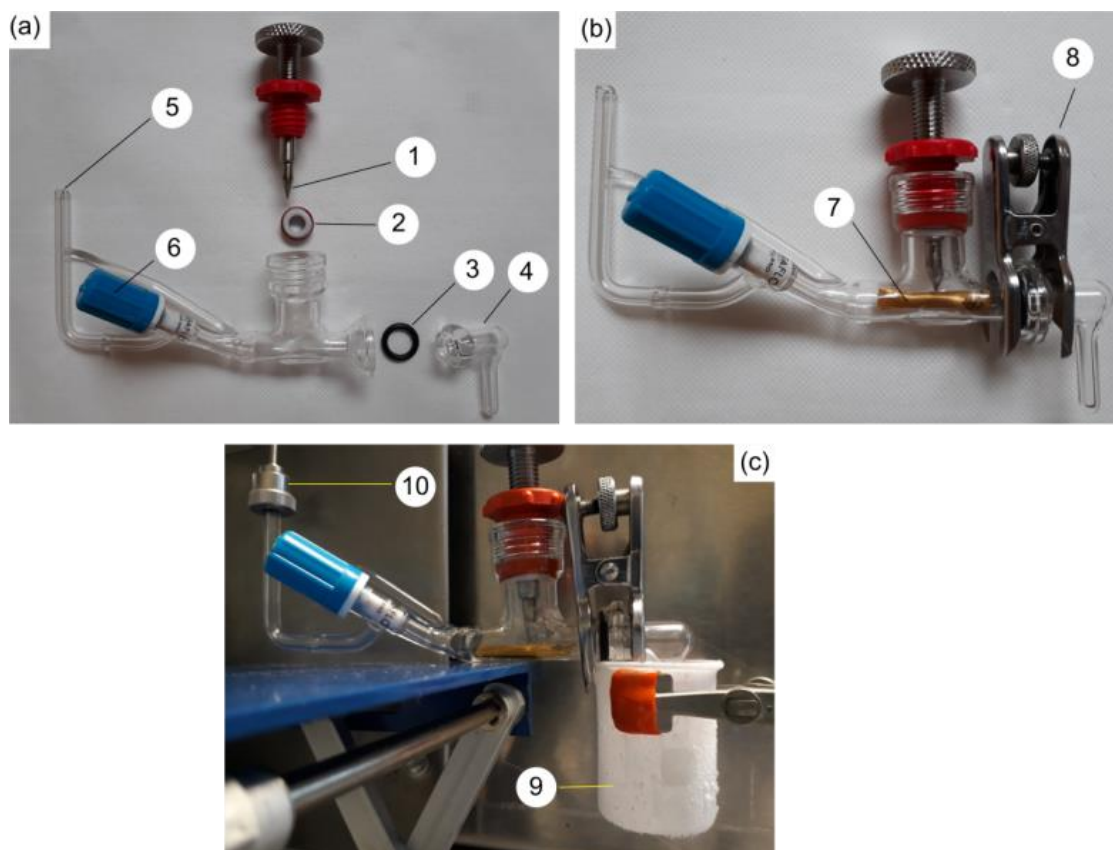


Figure 2-22. Gas extraction from the reacted gold capsules and injection of gas into GC (1) glass piercer showing its accessories (b) assembled piercer with a gold capsule ready to pierce (c) Piercer connected to the GC and ready for gas analysis. The labeled components are; 1. Metal needle 2. Rubber gasket 3. Rubber gasket 4. Glass piece with water trap 5. Glass connection to GC 6. The valve used to isolate the gold capsule from the vacuum 7. Gold capsule 8. Clamp 9. Cold trap with ethanol and dry ice 10. Metal connection to GC

2.2.6 Analysis of Liquid phase

2.2.6.1 High-performance liquid chromatography (HPLC-UV) analysis

The liquid contained in capsules were analyzed using HPLC technique at unite de Biologie Fonctionnelle et Adaptative (BFA) at University of Paris Diderot, using a Shimadzu HPLC system (Shimadzu, Kyoto, Japan), with a Supelco RP- C8 column (250 × 4.6 mm and 5 μm) (Sigma-Aldrich Corporation, Bellefonte, PA, USA), and equipped with a UV detector. Initially, each capsule contained 200 μL of NaHCO₃. However, a fraction of water became trapped either as structural water, or molecular water in the secondary minerals such as serpentine, brucite and phyllosilicates. As a result, the expected quantity of solution at the end of the experiment was <200 μL. In addition, since the starting materials and the final products were micrometric in size, the final solutions became grayish/translucent suspensions. To obtain a clear solution, a fraction of 20 μL was centrifuged and micro-filtered before and injecting into HPLC. The samples, together with the solvent, were injected at a pressure of 1-5 bar, which then passed through a column filled with a solid adsorbent material. Each component in the sample interacted slightly differently with the adsorbent

material, causing different flow rates for the different components and leading to the separation of the components as they flow out the column. The schematic of this technique is shown in Figure 2-23.

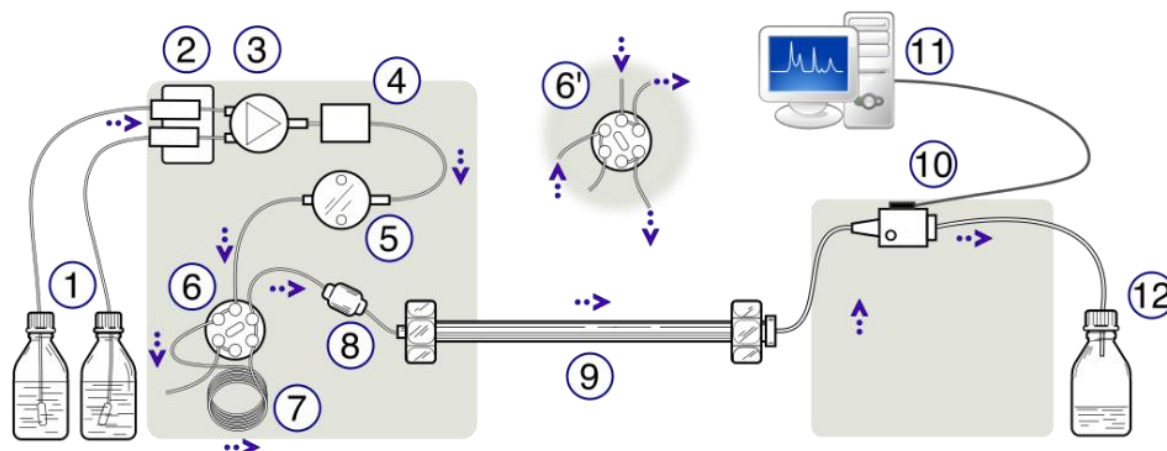


Figure 2-23. Schematic representation of an HPLC unit. (1) Solvent reservoirs. (2) Solvent degasser. (3) Gradient valve. (4) Mixing vessel for delivery of the mobile phase. (5) High-pressure pump. (6) Switching valve in "inject position". (6') Switching valve in "load position". (7) Sample injection loop. (8) Pre-column (guard column). (9) Analytical column. (10) Detector (i.e. IR. UV). (11) Data acquisition. (12) Waste or fraction collector. (Source: Wikipedia. based on Mayer. 2004).

2.2.6.2 Nuclear Magnetic resonance spectroscopy (NMR) analysis

The liquid contained in large capsules, were analyzed using NMR spectroscopy facility at the department of "Caractérisation des matériaux", at IFP Energies Nouvelles (IFPEN), Solaize. During this type of analysis, either water (D_2O) or chloroform ($CHCl_3$) is used as the solvent, in order to locate the magnetic field homogeneously. The principle of NMR spectroscopy relies upon the resonance of the 1H nuclei (1H NMR), or ^{13}C nuclei (^{13}C NMR) within the organic molecule, when the molecules are subjected to an external magnetic field (Figure 2-24). Tetramethylsilane or $(CH_3)_4Si$ (TMS), is the internal standard used for calibrating chemical shifts for both 1H and ^{13}C NMR spectroscopy in organic solvents (where TMS is soluble). Since all twelve hydrogen atoms in a TMS molecule are equivalent with respect to their chemical environment, its 1H NMR spectrum consists of a singlet. The chemical shift δ of this singlet is assigned an initial value of $\delta = 0$, and all other chemical shifts are determined relative to it. Similarly, all four carbon atoms in a TMS molecule are equivalent. In a fully decoupled ^{13}C NMR spectrum, the carbon in the TMS appears as a singlet. The chemical shift of this singlet is also set to be $\delta=0$ in the ^{13}C spectrum, and all other chemical shifts are determined relative to it. For the same compound, 1H NMR could be obtained faster, but with broad and coupled signals, whereas, a ^{13}C spectrum consists of sharp and discrete peaks (Figure 2-24) representing each non-equivalent carbons in the structure, but requires longer data acquisition time. The approximate chemical shifts (δ), of the functional groups that are possibly formed during the reaction are listed in Table 2-8.

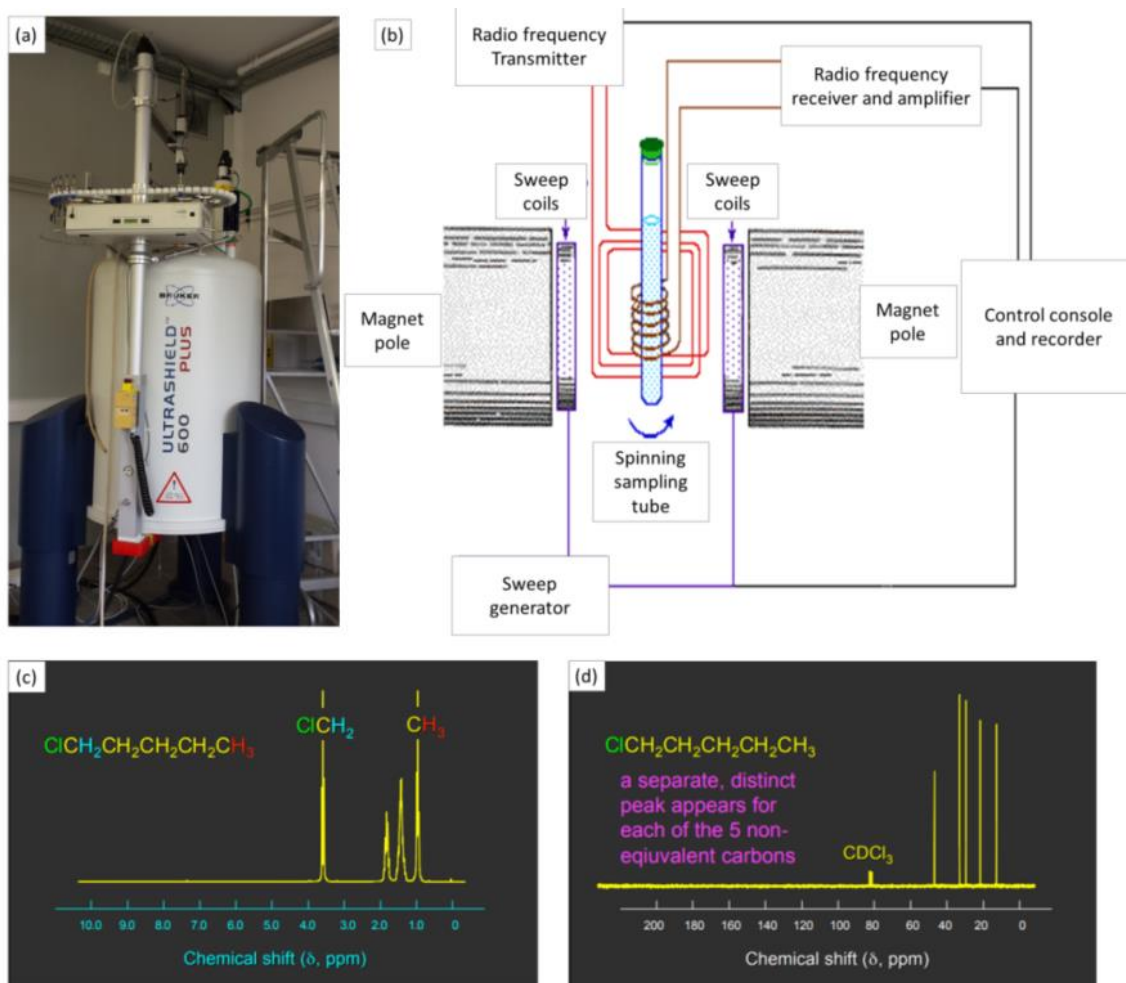


Figure 2-24: Instrumentation and principle of NMR spectroscopy (a) NMR instrument at IFPEN, Solaize (b) Schematic representation of continuous wave NMR spectrometer showing the sample tube, magnets, sweep coils and electronics (source: <https://chem.libretexts.org>). Comparison of NMR spectra of $\text{C}_5\text{H}_{11}\text{Cl}$ showing (c) broad and coupled peaks obtained by ^1H NMR and (d) sharp and discrete peaks of its ^{13}C NMR.

Table 2-8. Approximate chemical shifts of ^1H NMR (www.cpp.edu) and ^{13}C NMR (www.xula.edu) of most commonly identified intermediate compounds of Fischer Tropsch Type (FTT) synthesis.

Functional group	Chemical environment of proton/carbon	Chemical shift (ppm)
<u>^1H NMR</u>		
R-CH ₃	Alkyl (methyl)	0.9
R-CH ₂ -R	Alkyl (methylene)	1.3
R ₃ C-H	Alkyl (methine)	1.5-2
RCO-CH ₃	H is on a C attached to a carbonyl carbon	2-2.3
RCO-H	H is directly attached to carbonyl carbon	9.7
R-OH	alcohol	0.5-5
R-COOH	Carboxylic acid	10-13
<u>^{13}C NMR</u>		
R-CH ₃	Alkyl (methyl)	8-35
R ₂ -CH ₂ -R	Alkyl (methylene)	15-50
R ₃ C-H	Alkyl (methine)	20-60
R-CO-R	ketone	190-200
R-CO-H	aldehyde	205-220
R-CH ₂ -OH	alcohol	50-80
R-COOH	Carboxylic acid	175-185

2.2.7 Thermodynamic modeling of dissolved organic compounds

Thermodynamic equilibrium between the reactant minerals and the NaHCO_3 solutions at 573 K was calculated using CHESSE geochemical code (Van der lee), version 3.0, release 4 (2003). The CHESSE software simulates the reactions between minerals and a given solution by minimizing the Gibbs free energy of the overall system, finally converging into mineral phases and the fluid composition coexisting at the given temperature through several iterations. By taking into account mass balance, CHESSE calculations results the masses of each mineral phase in the final equilibrium assemblage. The composition of the coexisting fluid is given in terms of concentration of each dissolved ions/ species. In addition, the calculation results saturation indices of all the minerals which have the possibility to precipitate in the system depending on their chemical composition. The results of equilibrium calculations could be slightly different depending on the database used for the calculations. By default, CHESSE provides several databases which were developed based on the LLNL (EQ3/6) database. For instance, chess.tdb, eq36.tdb, minteq.tdb, freeqc.tdb, nea.tdb, wateq4f.tdb are CHESSE-formatted versions of EQ3/6 (V.8-R.6) database (Wolery 1992), full version of the same database, MINTEQA, PHREEQC, NEA thermochemical database and WATEQ4F code respectively (Van der lee, 2002 cookbook). The original chess database does not contain thermodynamic data of organic compounds. Therefore, all the calculations were performed using a modified chess.tdb in which thermodynamic data for simple organic compounds were added from the eq36.tdb.

The activity coefficients of aqueous species were calculated with the truncated-Davies model. The calculations were performed without including any pressure term. The pH of the system was allowed to vary freely as the reaction proceeds.

Chapter 3

Simultaneous ex-situ CO₂ mineral sequestration and hydrogen production from olivine-bearing mine tailings

[This chapter has been published in Applied geochemistry]

Abstract

Hydrothermal alteration batch experiments were conducted on olivine bearing mine tailings in order to investigate two potential valorization methods: the ex-situ CO₂ sequestration and hydrogen production. The originality of this work lies in the simultaneous investigation of these two processes. We reacted powdered mine tailings with CO₂-saturated water at three different sets of P/T conditions, 473K/ 15 MPa, 523 K/30 MPa and 573K/30 MPa. After 25 days of reaction, CO₂ was sequestered in the form of Fe-bearing magnesite, (Mg,Fe)CO₃ in all the experiments. Maximum carbonation yield was achieved at 523 K and 30 MPa, which was 53.8 wt.% of run product, equivalent to the trapping of 320.5 g of CO₂ per kg of mine tailings. Hydrogen gas was produced via the redox reaction between Fe²⁺ in olivine and water. The highest quantity of hydrogen (H₂) was produced at 573 K/ 30 MPa which was 0.57 g of H₂ per kg of mine tailings. It suggests that the temperatures between 523 K and 540 K at pCO₂=30 MPa are favorable for simultaneous ex-situ CO₂ mineral sequestration and hydrogen production from New Caledonian mine tailings.

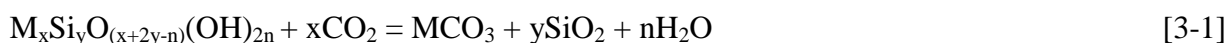
The combined method of ex-situ CO₂ storage and hydrogen production proposed by this study offsets 90% of New Caledonia's annual CO₂ emissions while compensating ~10 % of New Caledonia's annual energy demand. More globally, it has implications for cost effective disposal of industrial CO₂ emissions and production of hydrogen gas (clean energy) at a large scale; those two processes could be combined using the residual heat provided by a third one such as the high temperature smelting of ore.

Key words: New Caledonia, Nickel, Carbonation, Hydrogen, Hydrothermal, Olivine, Glass

3.1 Introduction

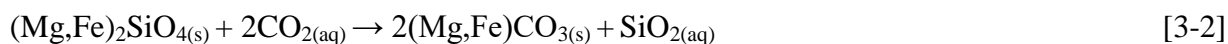
Since the industrial revolution, the atmospheric carbon dioxide (CO₂) level has been substantially increased up to its present day value of ~407 ppm (NOAA, 2016), eventually causing enormous climatic changes such as global warming, ocean acidification, and glacial melting (Manabe and Stouffer, 1993; Oelkers, 2005). Up to 65% of the global CO₂ emissions were attributed to fossil fuel combustion (Edenhofer et al., 2014), directing the CO₂ mitigation measures essentially towards CO₂ sequestration mechanisms and introduction of alternate energy sources to fossil fuels.

Scientists have considered the CO₂ sequestration in minerals as the so-called permanent method to capture and store industrial emissions of CO₂. This method was first suggested by Seifritz (1990), based on the natural phenomena of silicate weathering into carbonates (Abu-Jaber and Kimberley, 1992; Ece et al., 2005; Lugli et al., 2000; Oskierski et al., 2013; Palinkaš et al., 2012; Zedef et al., 2000), during which CO₂ reacts with silicates precipitating thermodynamically stable solid carbonates as given by the generalized equation below:



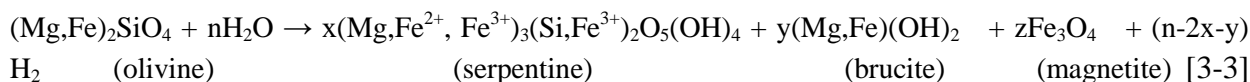
where (M²⁺) represents a divalent cation such as, Fe²⁺, Mg²⁺ and Ca²⁺ in a silicate mineral, and MCO₃ thus represents the carbonate incorporating the element M. Once CO₂ is converted into a carbonate following reaction (1), it won't be released into the atmosphere over geological time scales.

For the last three decades various aspects of CO₂ mineral sequestration have been experimentally investigated, on several silicates such as olivine, serpentine, pyroxenes, and mafic or ultramafic rocks containing those minerals (Daval et al., 2009a; Lackner et al., 1995; Matter et al., 2014; Matter and Kelemen, 2009; O'Connor et al., 2000; Sissmann et al., 2014, 2013). Among the minerals which consist of divalent Ca, Mg or Fe in their structure, olivine ((Mg,Fe)₂SiO₄) is considered the most favorable for carbonation due to several reasons. Firstly, olivine is abundant in nature in mafic and ultramafic environments (e.g. basalt, peridotites, and dunites). Secondly, it's one of the fastest dissolving silicates (Guyot et al., 2011). Olivine, which contains both Fe and Mg, may form Fe-bearing magnesite ((Mg,Fe)CO₃) during the carbonation process, according to equation (3-2):



A recent study by Gerdemann et al. (2007), who conducted carbonation experiments on olivine under a wide range of temperature (25 °C < T < 250 °C) and CO₂ partial pressure (10 atm < pCO₂ < 250 atm), has shown that olivine (< 75 μm) could be carbonated efficiently, with ca. 85% completion of reaction within an extremely short period of time (around 6 hours), by reacting with a solution of 0.64M NaHCO₃ + 1M NaCl, at T = 458 K and pCO₂ = 15 MPa. This study also demonstrated that the extent of olivine carbonation is directly proportional to the CO₂ partial pressure in the system (pCO₂). In addition, the authors showed that, at a given pCO₂, the extent of carbonation was negligible at lower temperatures (< 363 K), while a decrease in the extent of reaction was observed at high temperatures (>458 K). It indicated that at low

temperatures, the carbonation reaction is kinetically not favorable due to slow mineral dissolution, whereas if the temperature is too high, although mineral dissolution is kinetically favorable, the extent of carbonation nevertheless decreases. This is due to the formation of Mg-rich phyllosilicates during the competing reaction of serpentinization, in which extensive oxidation of Fe²⁺ also occurs, producing hydrogen, as shown by:



The stoichiometric parameters n , x , y and z in this equation strongly depend of how iron is partitioned among the reaction products (McCollom et al., 2016). Large quantities of hydrogen are added to the deep sea floor by this reaction which takes place at the mid oceanic ridge hydrothermal systems. A number of studies reported the temperature, thermodynamic, and compositional controls on serpentinization (Janecky and Seyfried, 1986; Klein et al., 2013, 2009; Klein and Garrido, 2010; McCollom et al., 2016; McCollom and Bach, 2009a; Seyfried et al., 2007). Two important information from these studies indicate that high temperatures (~300 °C) favor large quantities of hydrogen due to (i) an increase of overall reaction rate of serpentinization, and (ii) an increased partitioning of Fe into brucite (Mg(OH)₂), rather than into magnetite (Fe₃O₄). In addition to the hydrothermal alteration of olivine, pure iron or iron-rich materials have also been experimentally studied for hydrogen production (Crouzet et al., 2017; Malvoisin et al., 2013).

Olivine, which contains both Mg and Fe, could therefore be favorable for simultaneous CO₂ mineral sequestration and hydrogen production, when reacting within a specific range of pressure, temperature and pH conditions, under which carbonation and serpentinization reactions won't inhibit one another. Therefore, this method is a clear improvement on current CO₂ mitigation methods, as it proposes reduction of CO₂ emissions by mineral storage, and also hydrogen production which is a green energy source. Compared to Fe, Mg-bearing pure minerals or rocks, mine tailings serve as an alternative source of mineral alkalinity that are readily and cheaply available (Bobicki et al., 2012), and can be valorized by the above method (Bobicki et al., 2012; Harrison et al., 2016, 2013; Power et al., 2013; Wilson et al., 2014; Malvoisin et al., 2013). However, these previous studies on mine tailings have only focused on either CO₂ storage or H₂ production separately. The present study aims to investigate the potential of combining the strategy of CO₂ mineral storage with hydrogen production by reacting olivine-bearing mine waste material obtained from nickel (Ni) extraction mines in New Caledonia. In order to maintain both of these reactions, the mine tailings were reacted with CO₂-saturated water at P/T range slightly inferior to the conditions previously identified as optimum for ex-situ carbonation (Gerdemann et al., 2007), and close to optimum hydrogen production in hydrothermal systems (McCollom et al., 2016; McCollom and Bach, 2009a; McCollom and Bach, 2008; Tutolo et al., 2018; Meyhew et al., 2018). We present the quantities of CO₂ that can be stored in mine tailings, and the quantities of H₂ that can be produced by this method. Based on these experimental values, we estimated the CO₂ offset and compensation of energy demand of New Caledonia. Although the application of this process is centered on New Caledonian mine tailings, it could be translated to other industrial sites where Mg and Fe remain major components of the wastes after ore processing.

3.2 Materials and methods

3.2.1 Starting materials

All the experiments were performed on olivine bearing mine tailings from industrial nickel (Ni) extraction sites in New Caledonia, where Ni is extracted from laterite and saprolite ores (Wacaster, 2013). The hand specimens of mine tailings consisted of light- to dark-green irregular shaped grains with sizes ranging from few millimeters to < 1 cm. The X-ray diffraction (XRD) analysis performed on a finely powdered sample indicated the presence of olivine, traces of enstatite and an amorphous phase (glass). The amount of glass was quantified by XRD Rietveld analysis performed on the diffraction pattern of a mixture of powdered mine tailings and alumina (20 wt.%) where alumina serves as the internal standard (Bish and Howard, 1988; Bish and Post, 1993; McCusker et al., 1999). According to this analysis the sample was composed of 55 wt.% of glass and 45 wt.% of crystalline olivine. The chemical composition of mine tailings was obtained by electron probe micro analysis (EPMA) operated at 15 keV and 40 nA, on few randomly selected macroscopic grains mounted on epoxy resin. The analysis was performed on multiple points on glass and olivine, which appeared texturally different under SEM, and the average compositions were reported in Table 3-1. This is in good agreement with the composition reported by Bodéan et al. (2014), who used the same material for CO₂ sequestration experiments. The magnesium numbers ($Mg\# = Mg/(Mg+Fe)$) of the glass and crystalline olivine were 0.75 and 0.88 respectively, and were calculated on molar basis (i.e. by dividing the wt.% oxide value of MgO and FeO by their gram-formula weights) using the average oxide wt.%.

Mine tailings were crushed in a ball mill to obtain 40 - 63 μm size fraction. This size fraction was chosen in order to maintain rapid dissolution kinetics, as well as to facilitate microscopic observations. Furthermore, those grain sizes are in the same range than those used in the few previous studies on hydrogen generation (Malvoisin et al., 2013, 2012a, 2012b), thus making the comparison easier. Even though the choice of nano-scale particles could have provided a considerably faster reaction, the mineral surfaces available for microscopic studies of the run products would have been limited. Finally, for industrial purposes, grinding large quantities of solid down to the nanometer scale would largely increase the cost of the process.

The selected sieve fraction was subsequently ultrasonically cleaned in ethanol for 8-10 min to remove the fine particles adhered to the surface. This process was repeated until the supernatant became clear. The powder was dried in oven at 70 °C overnight after cleaning with ultra-pure de-ionized water (electrical conductivity = 18.2 M Ω cm). Very few fine particles remained adhering to the grain surfaces of the above dried powder, when observed under SEM (Figure 3-1a). The specific surface area (SSA) of the cleaned starting powder was determined by Kr adsorption analysis, according to the Brunauer–Emmett–Teller (BET) method (Brunauer et al., 1938), yielding a value of 0.23 m²/g.

Scanning electron microscopic (SEM) analysis performed on a polished section of mine tailings indicate that it consists of inclusion of free and textured glass with embedded olivine crystals, resulting in a “dendritic texture” or a “quench texture” (Figure 3-1b). The glass and dendritic texture were assumed to be the result of two steps in the ore processing. The first is the “calcination” performed by pre heating the ore at >1173 K for moisture removal and first

phase of metal oxide reduction. The second is the “fusion reduction” by which the ore is melted using an electrode operated at <1973 K, separating Ni from the residue or mine tailings. We assume that these conditions reached the “dry” melting-point of peridotite (-approximate composition for the ophiolite) under atmospheric pressure (Takahashi, 1986), where olivine can coexist with pyroxene melt up to about 2023 K at 1 atm during the eutectic melting of peridotite, which could probably explain the quench texture in mine tailings.

Table 3-1. The chemical composition of New Caledonian mine tailings, determined by electron probe micro analysis (EPMA) performed on crystalline olivine and glass, expressed in weight percent (wt.%) of corresponding oxide.

	Na ₂ O	MgO	SiO ₂	Al ₂ O ₃	K ₂ O	CaO	TiO ₂	Cr ₂ O ₃	FeO	MnO	CoO	NiO	Total	Mg# ^a
Olivine	0.05	47.27	40.88	0.07	0.01	0.11	0.04	0.02	11.67	0.12	0.05	0.38	100.68	0.88
Glass	0.04	23.94	55.22	3.81	0.01	0.48	0.06	1.68	14.23	0.9	0.01	0.01	100.39	0.75
Avg ^b	0.05	35.61	48.05	1.94	0.01	0.30	0.05	0.85	12.95	0.51	0.03	0.20	100.54	0.82

^aThe magnesium number; $Mg\# = Mg/(Mg+Fe)$

^bAverage composition of mine tailings

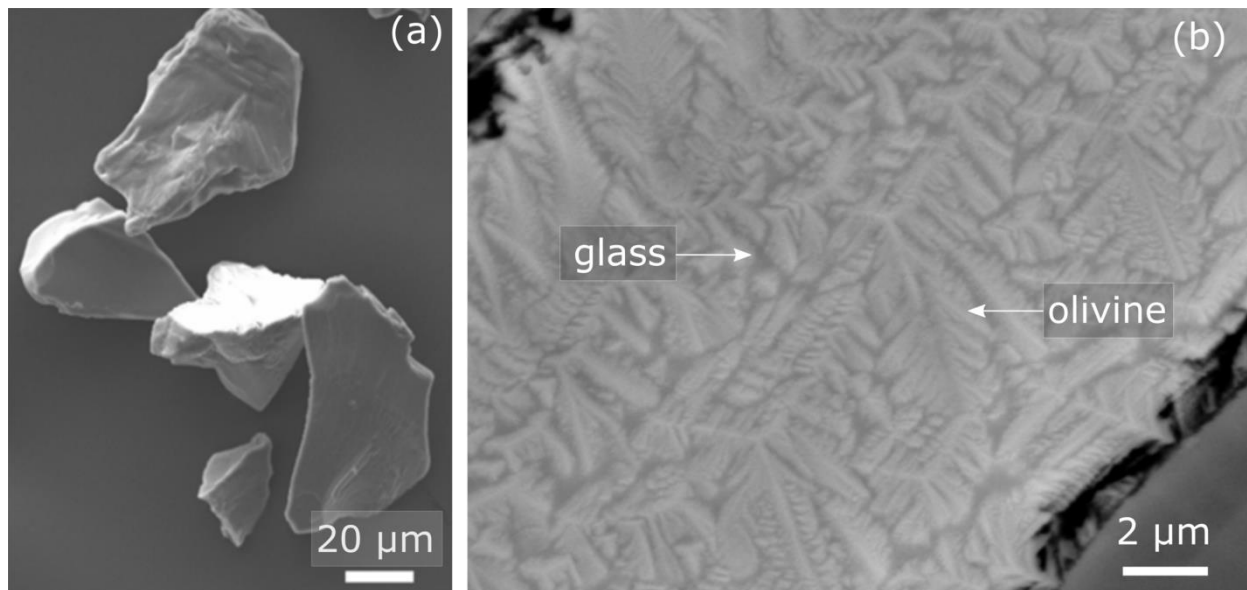


Figure 3-1. Powdered mine tailings observed under SEM (a) secondary electron image of powdered and cleaned sample used for the experiments. The grain surfaces are free of any adhered particles (b) angle selective back scattered image of a polished section of mine tailings showing the olivine crystals (white), embedded in glass (gray matrix) resulting a dendritic texture.

3.2.2 High pressure and high temperature experiments

Three batch experiments were conducted at different P/T conditions, in order to investigate the most favorable conditions for simultaneous CO₂ sequestration and H₂ production. All the experiments were performed in 250 ml volume Parr[®] hastelloy stirring- type batch reactors (impeller speed, 100 r.p.m), with a TiO₂ inner lining. Powdered mine tailings and water (1:100 mass ratio) were added to the batch reactor and pressurized with CO₂ (99.9% purity).

The first experiment (MT1) was conducted at 473K/ 15 MPa, which was slightly above the known optimum temperature reported for the CO₂ mineral sequestration, i.e. 453 K/15 MPa, using a solution of 0.64M NaHCO₃/1M NaCl. In contrast, pure water saturated with CO₂ was used in this study (Daval et al., 2009b; Sissmann et al., 2014, 2013). The second and third experiments were conducted at P/T conditions more favorable for H₂ production by serpentinization, such as 473 K and 673 K and 30-50 MPa (Allen and Seyfried, 2003; Andreani et al., 2012; Berndt et al., 1996; Janecky and Seyfried, 1986; Malvoisin et al., 2012a; McCollom and Bach, 2009b; McCollom and Seewald, 2001). These conditions are known to accelerate the serpentinization rate while producing large amounts of H₂. The second experiment (MT2) was thus conducted at 523 K/30 MPa, both temperature and pressure being slightly above MT1. The third experiment (MT4) was performed at 573 K/30 MPa. Two more experiments were conducted as blank runs (MT2b, and MT4b) to determine possible contaminations in gas phase. They were conducted under similar conditions (-in terms of amount of water, pCO₂, T) to those of MT2 and MT4, but without any solid phases added in the reactor. Details of these experiments are reported in Table 3-2. The run duration of all the experiments was approximately 25 days. The pCO₂ of the experiments punctually decreased during the run due to; (i) CO₂ consumption by carbonation reaction, and (ii) sampling out aliquots of gas from the batch reactor (0.1 to 0.5 MPa). The pressure was re-adjusted to the initial pressure by pumping CO₂ gas back to the batch reactor. At the end of the 25-days run, the experiments were quenched rapidly to ambient conditions by cooling the reactor cell in a water bath for ~20-30 min. The autoclaves were then opened right after releasing the pressurized CO₂ inside the reactor, minimizing the potential formation of secondary products at this stage. The solid run products were recovered and oven-dried at 333 K overnight, then used for further analysis, as described below.

At these P/T conditions, most of the CO₂ pumped into the reactor exists as CO_{2(aq)} with a smaller amount of HCO₃⁻_(aq) and traces of CO₃⁻²_(aq), which can therefore be summed up to a binary mixture of CO₂-H₂O that has not reached critical condition. The initial pH at P/T relevant to experimental conditions was calculated by the CHES geochemical code (van der Lee and De Windt, 2002) for each reaction temperature, creating a closed system with water and CO₂ (fCO₂ at each P/T conditions was calculated using the Thermosolver program (Barnes and Koretsky, 2004). The experimental conditions and the calculated initial pH of the solutions are reported in Table 3-2.

3.2.3 Sampling and analytical methods

3.2.3.1 Gas sampling and analysis

The gas phase in the head space of the batch reactor was sampled every 2-3 days during the reaction, by connecting a gas-sampling tube to the batch reactor. Before sampling, a vacuum of 10^{-5} bars was created along the tubings of the batch reactor and also in the sampling tube. The vacuum was held for about 10-15 min. This procedure ensures the absence of any leak and contaminations in the tubings. Collected gas samples were then analyzed with a Varian CP-3800 gas chromatograph (GC) to identify and quantify the gaseous products of the reaction. For this purpose, two standards were first analyzed: one with an atmospheric composition, and the other being a mixture of H₂, He, N₂, CO₂ and alkanes up to four carbons (C₁-C₄). The samples and the standards were injected to the GC at ~1200 mbar at room temperature. Before analyzing a standard or a sample, a blank measurement was carried out by injecting N₂. Finally, the percentages (%) of each gas in the analyzed samples were calculated using the response factors (k) obtained. The uncertainty on H₂, CO₂, CH₄ and other simple alkanes abundances (C₂-C₄) measured by GC were 5.4%, 1.3%, 0.6% and ~1.2% respectively.

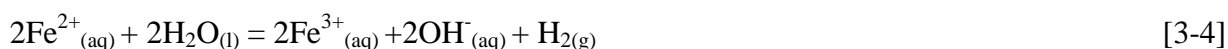
3.2.3.2 Solid product analysis

The mineralogical composition of bulk solid products was obtained through XRD analysis performed on finely powdered reaction products, using a X'Pert PRO (PANalytical) x-ray diffractometer with a Cu anode (Cu K α = 1.5418 Å), operated under 45 kV and 40 mA. The detection limit of XRD is ~1%. Rock-Eval 6 analysis was performed for better detection and quantification of carbonate. The quantification limit of Rock-Eval 6 is ~0.02 wt.% C, which corresponds to ~0.15 wt.% MgCO₃; this method is one order of magnitude more sensitive than the phase quantification by XRD. More details on sample preparation, instrumentation and analysis of the Rock-Eval 6 technique can be found in Behar et al. (2001) and Lafargue et al. (1998). The analytical details and the calculation of carbonates are reported in Appendix II, S6. Energy dispersive X-ray analysis in transmission electron microscope (TEM-EDX) was performed on ultra-thin sections prepared by focused ion beam milling (FIB), in order to obtain the composition of magnesite: more details are given in Appendix II, S10.

A separate fraction of the reaction products was mounted on adhesive carbon-taped sample holders, gold (Au) coated and observed under “high vacuum” conventional SEM, EVO MA 10, Carl Zeiss SMT with a tungsten filament operated under 15 kV and 100 mA. A 150 pA beam was applied for secondary electron (SE) imaging to observe the surface topography with a high spatial resolution, while the back scattered electron detector (BSE) was used to obtain images with atomic number contrast. Qualitative chemical analyses were performed by energy dispersive X-ray analysis (EDX), with a probe current at 700 to 750 pA (Oxford). The silicon drift detector is calibrated on cobalt (Co) for quantitative analyzes during 10 s at 10 to 15 keV with a dead time of about 15 s. In addition, SEM element mapping was performed on the reaction products mounted on epoxy resin, finely polished by ion beam milling.

3.2.3.3 Fe(III) / Fe(II) analysis

The amounts of Fe²⁺ and total iron in the non-reacted mine tailings, and the three experimental run products were analyzed at the Centre de Recherches Pétrographiques et Géochimiques (CRPG), Nancy, France. The samples were boiled in HF / H₂SO₄ to release Fe²⁺ which was then quantified by volumetric titration with K₂Cr₂O₃. Another fraction of the sample was then heated with LiBO₂ at 1223 K and acid digested (4 vol.% HNO₃) to convert all species of iron (e.g. Fe⁰ and Fe²⁺) contained in the sample into Fe₂O₃ (Fe³⁺). The resulting ferric iron was measured by atomic absorption spectrophotometer (AAS). The amount of Fe³⁺ in the non-reacted mine tailings sample was calculated by subtracting the Fe²⁺ molar amount measured in the FeO analysis to the (Fe²⁺ + Fe³⁺) amount measured in the Fe₂O₃ analysis. The value being close to 0 suggests there is little to no oxidized iron in the initial material. The quantities of H₂ measured by GC at the end of the experiments were compared to the amounts calculated from the loss of Fe²⁺ (through oxidation and simultaneous H₂ production) in the run products. In order to estimate the amount of Fe³⁺ formed during the experiments, the amount of Fe²⁺ measured in the run products were subtracted to the one measured in the initial non-reacted mine tailings; the quantity of H₂ produced was then extrapolated from the oxidized iron (Fe³⁺) according to:



where, the stoichiometric proportion of Fe²⁺ : H₂ is 2:1.

Table 3-2. Summary of experimental conditions, pH of the solutions, carbonate yields, measured hydrogen and methane in each batch experiment.

	P(total) (MPa)	P(CO ₂) ^a (MPa)	T (K)	t (days)	Mine tailings (g)	Pure water (g)	m/V ratio ^b (g/L)	Initial pH ^c	CO ₂ storage ^d (g/kg)	Hydrogen(max) measured by GC (g/kg) ^e	Methane(max) (g/kg) ^e
MT1	15	13.1	473	25	2.0	201	10.2	3.55	114.4	0.04	nd
MT2	30	26.4	523	25	1.7	170	10.0	3.65	320.5	0.24	0.02
MT4	30	28.2	573	24	1.7	170	10.0	3.94	118.5	0.57	0.05
MT2b (blank)	30	26.4	523	24	-	170	-	-	nd	nd	0.01
MT4b (blank)	30	28.2	573	24	-	170	-	-	nd	nd	0.06

^aCalculated for the given temperature and P(total) using the thermosolver software (Barnes and Koretsky, 2004)^bSolid mass to solution volume ratio^cpH at experimental conditions calculated using the CHESS geochemical code (van der Lee and De Windt, 2002)^dgrams of molecular CO₂ trapped in 1 kg of mine tailings^egrams of hydrogen (H₂), or methane (CH₄) produced per 1kg of mine tailings

nd = not detected in the gas chromatography analysis

3.3 Results

3.3.1 Secondary products

XRD pattern of non-reacted mine tailings and the reaction products of three experiments are shown in Figure 3-2c. The non-reacted mine tailings sample primarily consisted of olivine. The peaks of corundum (Figure 3-2c), in this diffraction pattern are due to pure corundum which was added to mine tailings as the internal standard for quantification of glass. The run products consisted of Fe-rich magnesite as the major phase, small quantities of phyllosilicates and traces of non-reacted olivine (Figure 3-2c). Fe-bearing magnesite was identified by the characteristic reflections at $2\theta = 35.9^\circ$ and 50° (Giammar et al., 2005; Garcia et al., 2010). SEM element mapping performed on a polished section of MT2 sample showed the presence of abundant magnesite compared to other phases such as olivine, glass, and phyllosilicate, and therefore is well in agreement with the XRD results (Figure 3-2a). The SEM analysis performed on a carbon-coated reaction product of the same sample indicates the growth of rhombohedral magnesite containing both Fe and Mg, as confirmed by the EDX spectra collected on SEM (Figure 3-2b). Figure 3-3 shows the SEM analysis performed on polished sections of solid run products of the three experiments, each mounted on epoxy resin. At 473 K /15 MPa, mine tailings have been altered, precipitating anhedral magnesite, and thin layers of phyllosilicate (Figure 3-3a). Magnesites precipitated along a grain of textured mine tailings are shown on Figure 3-3b. At 523 K /30 MPa, the run product contained thick phyllosilicate layers around mine tailings and subhedral magnesite with Fe and Mg compositional zoning (Figure 3-3c). At 573 K /30 MPa, the run products contained anhedral magnesites and mine tailings heavily covered by a thick fibrous phyllosilicate layer (Figure 3-3c). More SEM images with EDX analysis on these samples are given in Appendix II (S7, S8 and S9). The chemical composition of magnesites analyzed by TEM-EDX yielded $\text{Mg}_{0.92}\text{Fe}_{0.08}\text{CO}_3$, $\text{Mg}_{0.58}\text{Fe}_{0.42}\text{CO}_3$ and $\text{Mg}_{0.83}\text{Fe}_{0.17}\text{CO}_3$ at 473 K /15 MPa, 523 K /30 MPa and 573 K /30 MPa respectively, showing different concentrations of iron further discussed in section 3.4.2. The details of TEM analysis is given in Appendix II (S10).

Compared to the diffraction pattern of the non-reacted sample, the peak intensity of olivine gradually decreases with the increasing temperature of the experiments, indicating olivine dissolution has mostly increased along with temperature. The semi-quantitative phase analysis on the collected diffraction patterns indicated that approximately 23.3 wt.%, 9.4 wt.% and 12.2 wt.% of olivine were still remaining in the reaction products of 473 K /15 MPa, 523 K /30 MPa and 573 K /30 MPa experiments respectively. The peaks for phyllosilicates are broad and less intense in all experiments, and the number of phyllosilicate peaks visible on the diffractogram increased with temperature, indicating more phyllosilicates formed with higher temperature. A preliminary identification of these phyllosilicates was obtained by applying a treatment with ethylene glycol to verify their expansion properties, which suggested that they were smectite clay minerals. However, due to the inherent limitations of the equipment, the amount of phyllosilicate and remaining glass could not be quantified separately.

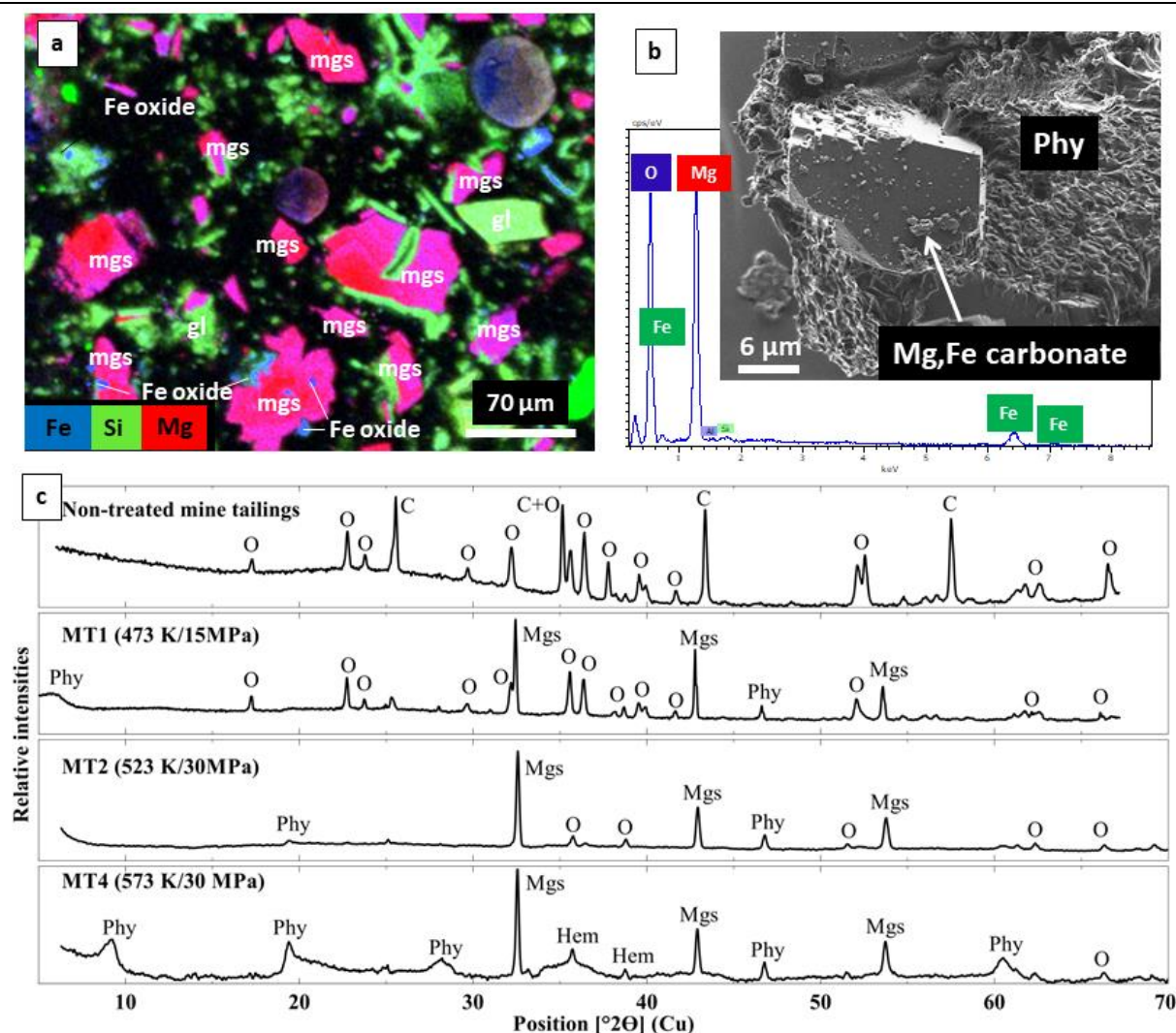


Figure 3-2. Mineralogical analysis of experimental run products (a) Element mapping (SEM) performed on a polished section the run product of experiment MT2 ($T = 523$ K and $P = 30$ MPa), showing formation of magnesite in large quantities (color coded by blue (Fe), green (Si) and red (Mg)). Magnesite crystals are shown in pink and initial silicate glass and traces of phyllosilicate is shown in green. A very small amount of iron oxide phases (not detectable through XRD) was observed only in this region of the sample and is marked in blue. (b) SEM secondary electron (In-lens detector) image of the same experimental run product taken on carbon coated powder showing euhedral grain of Fe-bearing magnesite (-as shown in SEM-EDX spectra) embedded in phyllosilicate. (c) X ray powder diffraction pattern of non-treated mine tailings sample and the run products of the three batch experiments, showing the progressive disappearance of olivine (O) peaks and the formation of magnesite (Mgs) during the reaction at high pressure and high temperature. The other secondary phases were phyllosilicates (Phy), and hematite (Hem). The peaks labeled (C) in the non-treated sample are the reflections of corundum which was added to the sample as the internal standard to quantify the fraction of glass (amorphous) in the initial non-reacted main tailings.

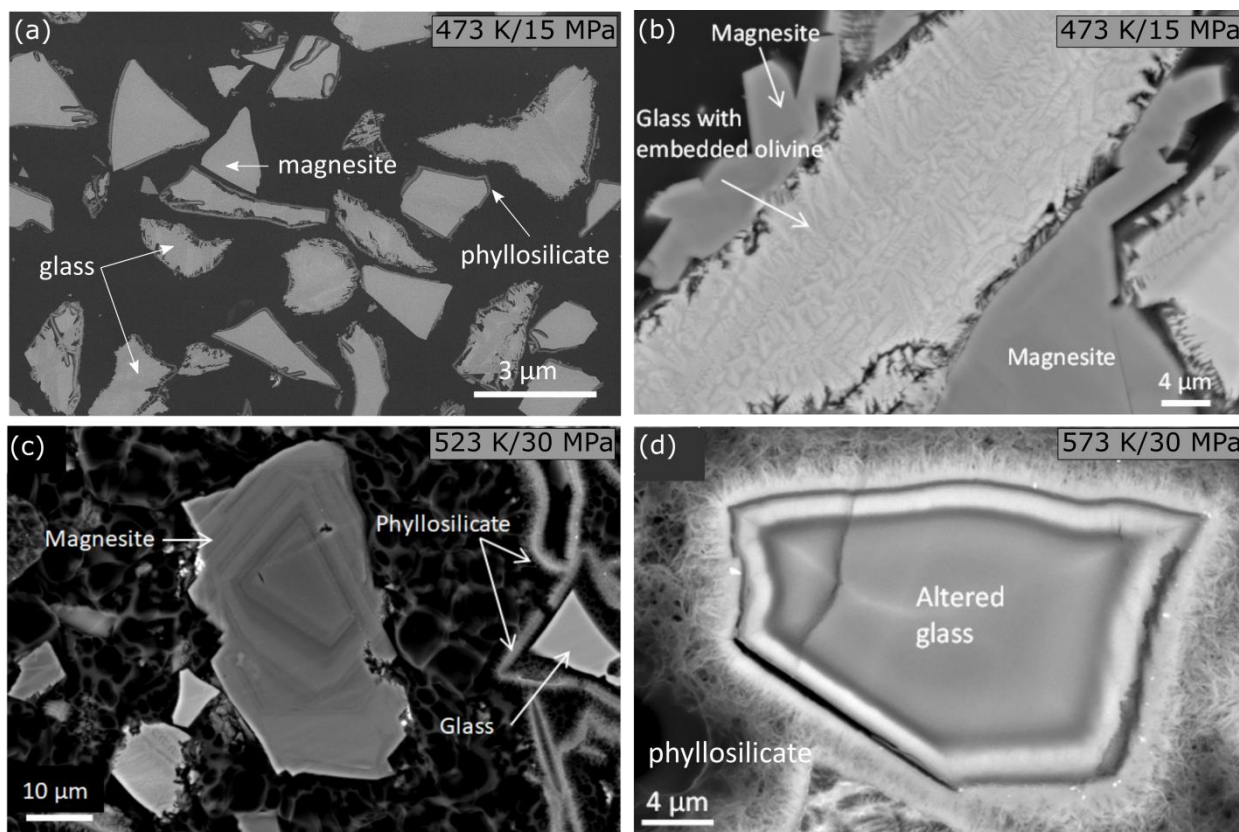


Figure 3-3. (a) SE image of the experimental run product at 473 K/15 MPa, showing some remaining glass, thin phyllosilicate layer formed around mine tailings and newly formed magnesite crystals; (b) a grain of mine tailing with olivine embedded in glass, which reacted to form anhydrous magnesite crystals; (c) large magnesite crystals formed at 523 K/ 30 MPa showing Fe, Mg compositional zoning, and phyllosilicates which apparently detached from the original grains; (d) glass altered at 573 K/ 30 MPa forming a thick phyllosilicate layer.

3.3.2 Carbonate yield

The presence of carbonates and their precise quantification were further confirmed using the Rock-Eval 6 technique. The only carbonate phase produced in all the experiments were Fe-bearing magnesites, (Mg,Fe)CO₃, in accordance with the results of XRD analysis. Carbonate quantification by Rock-Eval 6 resulted as 20.3%, 44.9% and 21.6% at 473 K/ 15 MPa, 523 K/ 30 MPa and 573 K/ 30 MPa respectively (the calculation is given in Appendix II, S6); those carbonation yields are averages of duplicate experiments. These yields suggest that 1.00 kg of mine tailings could capture 115g, 321g and 119 g of molecular CO₂ by a reaction with pure water at 473 K/ 15 MPa, 523 K/ 30 MPa and 573 K/ 30 MPa, respectively (Table 3-2 and Appendix II, S6).

3.3.3 Hydrogen production

As the starting mine tailings material is iron-rich (average of 10.9 wt.%), its reaction with water at high pressure and high temperature leads to the production of H₂, as a result of iron oxidation through water reduction (also written for the serpentinization reaction given by eq.3-3). However, the produced hydrogen in all the experiments is approximately three orders of magnitude lower than the CO₂ in the gas phase, since CO₂ was injected to reach a total pressure of either 15 or 30 MPa. The variations in gas phase composition in each experiment are given below.

At 473 K and 15 MPa: Figure 3-4a, illustrates the cumulative production of hydrogen as a function of time for MT1. Hydrogen was produced gradually reaching a maximum of 20.0 $\mu\text{mol/g}$ of mine tailings after 25 days of reaction, which indicates that the reaction is still in progress. The maximum hydrogen production of 20.0 $\mu\text{mol/g}$ is equivalent to producing around 0.04 g of H₂ for 1.0 kg of mine tailings. Hydrogen was produced at a rate of approximately 0.7 $\mu\text{mol/g/day}$, obtained by the gradient fitted through the data. Traces of methane (<0.30 $\mu\text{mol/g}$) were detected in the gas phase after 9.8 days of reaction, but other light hydrocarbons (C₂-C₄) were not detected (Appendix II, S1).

At 523 K and 30 MPa: The cumulative hydrogen production as a function of reaction time of MT2 experiment is shown in Figure 3-4a. Hydrogen continues to be produced at a rate of 1 $\mu\text{mol/g/day}$ until ~9 days, as the reaction proceeds. After 9 days, hydrogen production increases abruptly and then continues to increase at a rate of 3.2 $\mu\text{mol/g/day}$. The maximum amount of gaseous hydrogen measured in this experiment was 117.6 $\mu\text{mol/g}$ or 0.24 g/kg of mine tailings, which is approximately 5 times more than in MT1. No hydrogen was detected in the gas phase of an experimental blank (MT2b) conducted at the same P/T conditions, on pure water (without adding mine tailings) confirming that hydrogen was produced only by reaction between pure water and mine tailings (Figure 3-4b). Light hydrocarbons such as CH₄, C₂H₆, C₃H₈ and C₄H₁₀ were also observed in the gas phases of both the experiment and experimental blank, but in trace quantities (Appendix II, S2 and S4).

At 573 K and 30 MPa: Cumulative hydrogen production of MT4 experiment is shown in Figure 3-3c. At the initial stage, hydrogen was produced at a rate of 21 $\mu\text{mol/g/day}$ (0<t<8.8 days), reaching a maximum of 283.5 $\mu\text{mol/g}$ or 0.57 g/kg. This is the highest quantity of hydrogen produced among all three experiments, and is confirmed by the H₂ production inferred from Iron(III) measured at the end of the experiments (265 $\mu\text{mol/g}$, see Table 3-2). Then, the amount of hydrogen decreased drastically, reaching a plateau with an average of 41 $\mu\text{mol/g}$ (Figure 3-4c). Similarly to MT2, hydrogen was not detected in the gas phase of an experimental blank (MT4b) conducted at the same P/T conditions, which confirmed there was no contamination of hydrogen in the experiment (Figure 3-4c and Appendix II, S3). This decrease in cumulative hydrogen could be explained by the formation of short-chained organic molecules through its interaction with CO₂, as discussed by Seewald (2006). In addition, CH₄, C₂H₆, C₃H₈ and C₄H₁₀ were detected in the gas phase, in which the detected methane was above the 10% uncertainty of the concentration detected in the experimental blank (Appendix II, S5).

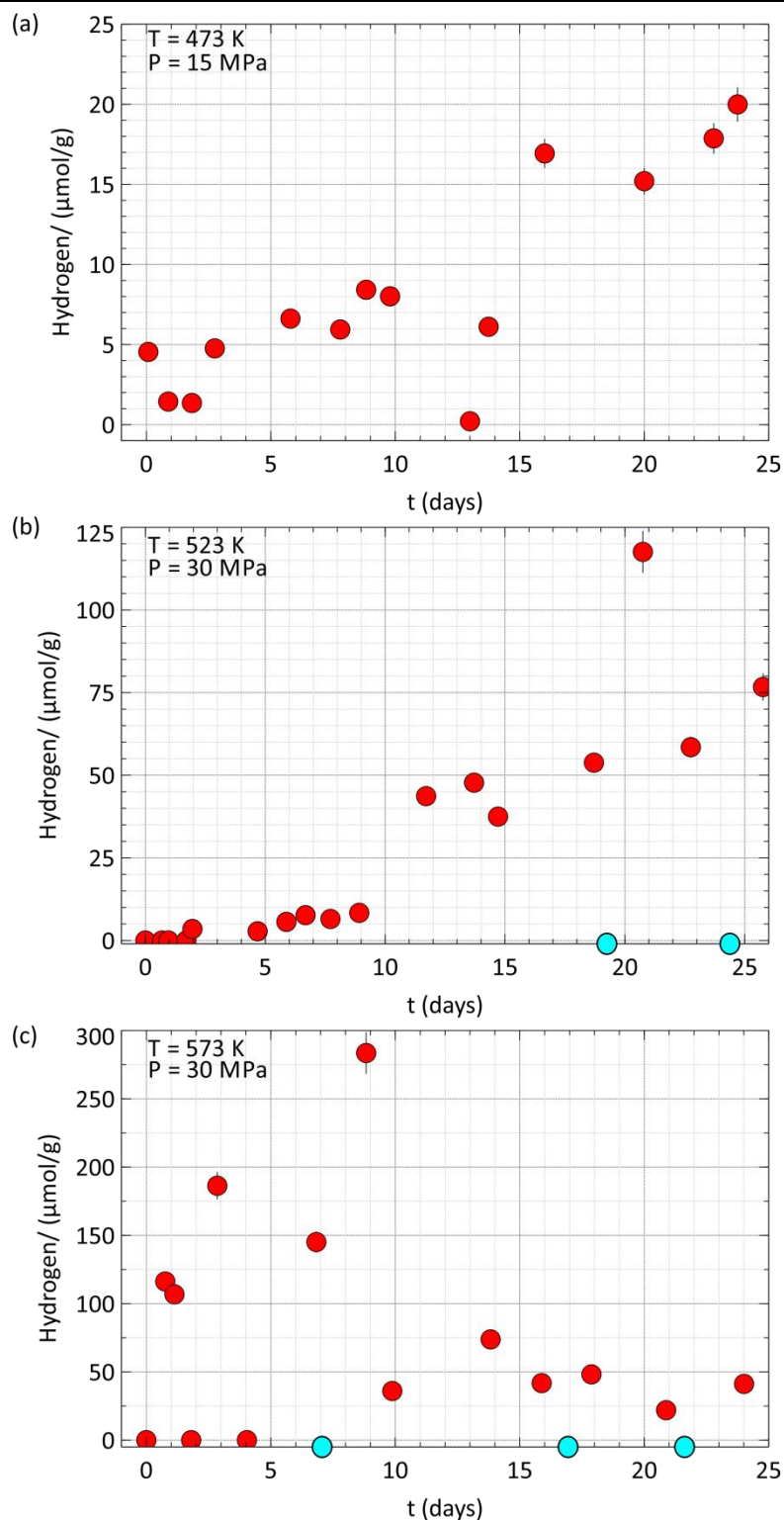


Figure 3-4. Variations in the production of H₂, measured in the gas phase as a function of time (red points). The blue points represent blank experiments, which didn't yield any measurable concentrations of hydrogen. The error bars around the data points (smaller than the marker for most of them) represent a 5% uncertainty associated with the concentration measurements of hydrogen (H₂) by gas chromatography.

3.3.4 H₂ production estimated by Fe(III)/Fe(II) analysis

As previously stated, hydrogen is produced via the oxidation of Fe²⁺ in the starting material according to equation 3-4 (section 3.2.3.4). Therefore, the difference between the amounts of FeO measured in the starting material and the reaction products quantifies the Fe²⁺ that has been oxidized at high pressure and high temperature.

The analysis shows that the starting mine tailings sample contained, 1.3 mmol/g of FeO, whereas the reaction products of MT1, MT2 and MT4 experiments contained 1.3, 1.1 and 0.8 mmol/g of FeO, respectively. According to this result, the initial mine tailings and the MT1 experiment contained the same amount of FeO, meaning that no Fe²⁺ oxidation took place. However, 20 µmol/g of hydrogen was detected in the gas chromatography analysis of this experiment. This could possibly suggest an analytical error in detecting such a low level of FeO quantity due to the detection limit of the method used. The H₂ production estimated from the stoichiometric ratio with Fe³⁺ (given in eq. 3-4) are reported in Table 3-3 for the three experimental runs. Except for MT1, the estimated values of hydrogen are in good agreement with those observed in gas chromatography analysis.

Moreover, if all the Fe²⁺ in initial mine tailings (i.e. 1.3 mmol/g) was to completely oxidize into Fe³⁺, then following the equation 3-4 (1 mole of H₂ produced for 2 moles of Fe²⁺ oxidized), it could produce 655 µmol of H₂ per one gram of mine tailings. This value can be used to calculate the reaction progress with respect to Fe oxidation in the system. Although the value for MT1, as mentioned earlier, is too low and thus unreliable to be properly exploited, the estimation shows that MT2 and MT4 reach 17.6 % and 40.5% completion of reaction respectively (see Table 3-3).

Table 3-3. Production of hydrogen in each experiment estimated from FeO analysis. Reaction progress calculated based on the hydrogen production is also reported (Rx%).

Exp.	Wt (g)	T (K)	FeO wt%	FeO (mmol/g)	ΔFeO (mmol/g)*	Eq. H ₂ ^a (µmol/g)	Eq. H ₂ (g/kg)	Rx %
MT ^b	2	-	9.39	1.31	0	no		
MT1	2	473	9.65 ^c	1.34	-0.03	-15	-0.03	-2.3
MT2	2	523	7.74	1.08	0.23	115	0.23	17.6
MT4	2	573	5.61	0.78	0.53	265	0.53	40.5

^aEquivalent hydrogen

^bMT refers to non-treated mine tailings

^cThis is an analytical error (see text), causing the successive negative values.

3.4 Discussion

3.4.1 Preferential dissolution of olivine within mine tailings at 473-573 K and 15-30 MPa

The suitability of geological material as carbon sequestration and hydrogen production feedstocks depends primarily on their reactivity and chemical composition (Power et al., 2013). Mafic and ultramafic rocks are rich in Ca²⁺, Mg²⁺ and Fe²⁺, and therefore, are the ideal sources for this purpose. New Caledonian mine tailings contained abundant Mg²⁺ and Fe²⁺, and thus their chemical composition and reactivity favored CO₂ sequestration and hydrogen production. Mineral dissolution, is essentially the first step that makes Mg²⁺ and Fe²⁺ available for both carbonation and hydrogen production reactions, and is a function of crystal chemistry, particle size of reacting mineral, pH, and temperature. As shown in Figure 3-2, olivine dissolved gradually with increasing temperature of our experiments, indicating that for our grain sizes and pH, increasing temperatures were favoring the dissolution of olivine. Inevitably, XRD pattern does not indicate the dissolution of glass due to its lack of crystallinity. In acidic to neutral pH, the dissolution of olivine has been reported to be faster than dissolution rate of basaltic glass, which is an approximation that can be made for mine tailings (Gudbrandsson et al., 2011; Snæbjörnsdóttir et al., 2017). These two previous studies suggest that the constituent minerals of crystalline basalt dissolve faster than basaltic glass by more than one order of magnitude (olivine, a nesosilicate with a Q₀ structure, has all silicate tetrahedrons disconnected from each other, as opposed to glass, and thus faster dissolution kinetics), indicating that olivine is the major contributor to the Mg²⁺ and Fe²⁺ cations in the solution.

3.4.2 Reaction path and formation of secondary Mg-silicates

The XRD patterns of the run products indicated that the reaction of mine tailings with CO₂-saturated water, resulted in Fe-rich magnesite, and small quantity of phyllosilicates. Hydrogen is the gaseous product of this reaction. Hematite (Fe₂O₃) was observed only in MT4 (573 K/30 MPa) experiment. Although, we anticipated the production of hydrogen through serpentinization reaction, our result showed that the reaction which occurred precipitated smectites. However, formation of proto-serpentine-like phase using New Caledonian mine tailings was reported by Bodenan et al. (2014), in an experimental work where the reactions took place either in water or in a 0.43 M NaCl/0.27 M NaHCO₃ solution at 453 K at a pCO₂ of 10 and 90 bar. This result points to the likelihood that acidic pH favored the formation of smectite compared to neutral to basic pH conditions. Although the experiments of Bodenan et al (2014) were complementary to our study, the comparison with our results is not reasonable due to the differences in reaction duration, pCO₂, grain size, and temperatures of the two studies. Despite the low pCO₂ (10 bar), they reported 5.97 wt.% of MgCO₃ precipitated within one day of reaction, using a 0.43 M NaCl/0.27 M NaHCO₃ solution; which is significant.

3.4.3 Fe-rich magnesite precipitation and hydrogen production

Fe-rich magnesite was the only carbonate precipitated in our experiments as confirmed by XRD and Rock-Eval 6 analysis. Theoretically, mine tailings could precipitate a maximum of 77 wt.% of magnesite, assuming 100% dissolution of mine tailings (S11). The quantities of Fe-rich magnesite precipitated at 473 K/15 MPa, 523 K/30 MPa and 573 K/30 MPa were 20.3, 44.9 and 21.6 wt.%, respectively. If the reaction completion (Rx) with respect to carbonate precipitation is given by the ratio between the observed carbonate wt.% versus the calculated maximum carbonate wt.%, multiplied by 100, then 26.4%, 58.3% and 28.1% of reaction completion were achieved respectively during the experiments. Interestingly, the iron content in magnesite followed the same trend as reaction completion, with 0.08, 0.58 and 0.17 moles of iron in one mole of magnesite at 473 K/15 MPa, 523 K/30 MPa and 573 K/30 MPa respectively. This would indicate that the lower temperature and low pCO₂ in MT1 (473 K/15 MPa) slowed down kinetics of the dissolution and precipitation reactions resulting in low quantities of magnesite with small quantity of iron, compared to the other two experiments. The MT2 and MT4 experiments, which were conducted at same pCO₂ (30 MPa), revealed that almost all the olivine dissolved at increasing temperature up to 573 K. But, the precipitated magnesite at 523 K was twice higher than at 573 K. As Mg is the major element in magnesite, this result clearly indicates the competition of Mg incorporation into magnesite vs. secondary Mg-silicates in the 523-573 K temperature range. In addition, the quantity of iron incorporated in magnesite at 523 K is twice higher than at 573 K, indicating that temperatures >523 K favored the incorporation of iron into other phases than magnesite. The correlation between iron incorporation into secondary phases and hydrogen production is worth mentioning because it demonstrates the competition between another two reactions in the system: the iron incorporation into magnesite versus secondary Mg-silicates (\pm iron oxides). As the temperature increased from 523 K to 573 K, hydrogen production was approximately doubled, producing more Fe³⁺. At 523 K, the most likely secondary phase to host Fe³⁺ was the secondary phyllosilicate, whereas at 573 K, it could possibly be incorporated into phyllosilicate and into iron (III) oxides as well. Although, ferric-hydrate complexes could host Fe³⁺ ions, we assumed their quantities to be negligible. Magnesite structure accommodates only Fe²⁺. Therefore, the results clearly indicate that temperatures >523 K favors the iron oxidation, whereas temperatures between 473 K and 523 K favors the iron incorporation into magnesite. The competition between Mg and Fe incorporation among the secondary phases seems to control the quantities of magnesite precipitation and hydrogen production. Moreover, Figure 3-5, which shows the magnesite production (in wt.%) versus hydrogen production clearly demonstrates that temperatures between 523 K and 540 K at pCO₂=30 MPa (shown by shaded area) would be the most favorable conditions for reacting mine tailings in order to maintain both carbonation and hydrogen production in significant quantities. Although the P/T conditions of maximum carbonation in our experiments differ slightly from those of Gerdermann et al. (2007), it can be argued that this discrepancy arises from the different solutions used in two studies; a CO₂-saturated water here compared with a 0.64M NaHCO₃, 1M NaCl solution in Gerdermann et al. (2007).

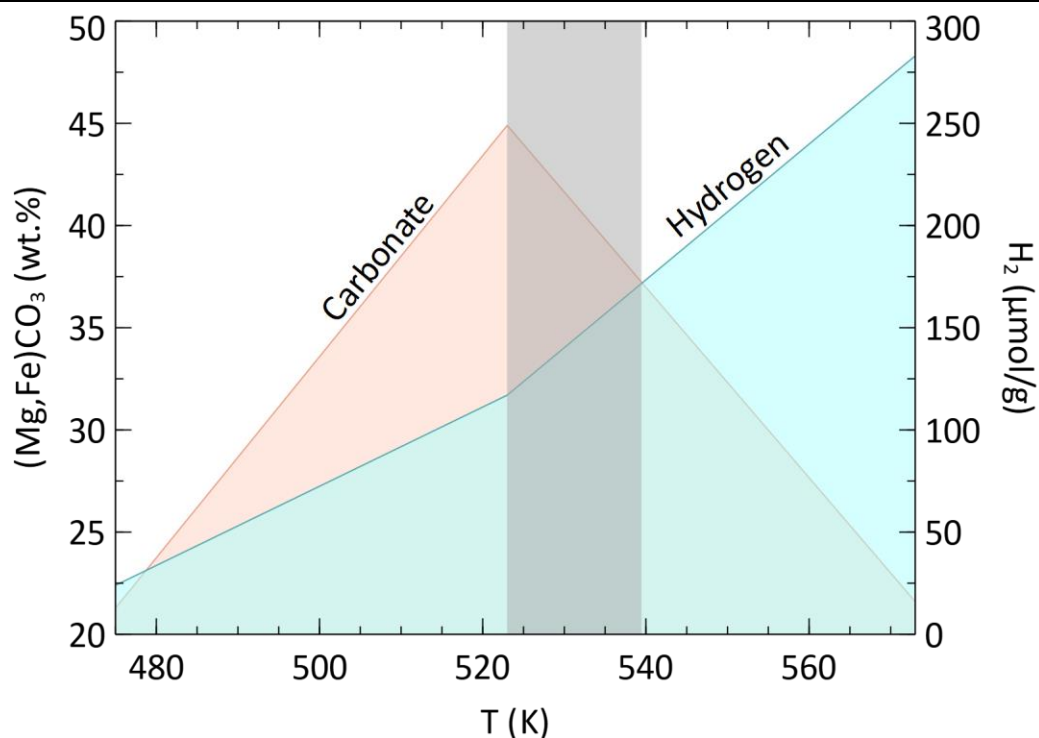


Figure 3-5: Quantities of magnesite precipitation and hydrogen production, obtained during the reaction of New Caledonian mine tailings, with CO₂-saturated water and as a function of temperature. The diagram emphasizes the competition between the two reactions. The shaded area indicates the temperature range at 30 MPa, recognized as the best conditions for the simultaneous carbonation and hydrogen production from mine tailings.

The analysis of FeO in the starting material and the run products were used to evaluate the amount of iron oxidation, and to further confirm the hydrogen amounts measured by gas chromatography. As mentioned in section 3.3.4, the Fe(III) / Fe(II) analysis of non-reacted mine tailings confirmed that the starting material does not contain any Fe³⁺ that could have resulted from ore processing. Assuming the mine tailings have been well homogenized after crushing and sieving, the Fe²⁺ measured in the experimental run products was expected to be lower than in the initial sample, due to the oxidation of Fe²⁺ during the experiment. However, the amount of Fe²⁺ measured for MT1 is slightly above the value measured for the initial non-reacted sample. Such an inconsistency could be explained by potential inhomogeneities caused by a sampling bias of the starting material or the run products, or due to detection limit for low Fe concentrations in this sample. Nevertheless, the estimated hydrogen production from MT2 and MT4 experiments are in good agreement with the measured hydrogen quantities using gas chromatography (Table 3-3).

The variation of hydrogen production as a function of reaction time (Figure 3-4) indicates that the hydrogen production at 473 K/15 MPa and 523 K/ 30 MPa continued until the end of the experiment, whereas at 573 K/30 MPa, it suddenly decreased after 9 days of reaction, reaching a plateau. Although it is not the focus of this study, this decrease could be

due to the consumption of hydrogen to form various light organic compounds. The former observation clearly indicated that the formation of secondary phyllosilicates does not passivate the dissolution of mine tailings providing Fe²⁺ to the solution at 473 K/15 MPa and 523 K/ 30 MPa. However, in the latter conditions, it appears that the hydrogen production has been ceased by the limitation of Fe²⁺ supply, possibly slowed down by the secondary phyllosilicates acting as passivating layers.

3.4.4 Carbonation and hydrogen production from mine tailings vs. other slags

First our results on CO₂ sequestration were compared with two experimental studies by Bobicki et al. (2014) and Garcia et al. (2010), who conducted experiments at T~423 K and PCO₂ ~15 MPa. Bobicki et al. (2014) used chrysotile from two nickel (Ni) mines (Okanogan nickel deposit in Washington State, USA (OK ore) and Thompson Nickel Belt in Manitoba, Canada, (Pipe ore), respectively) (table 3-4). The ores contained 6.0 and 7.8 wt.% of MgO, with approximately <7 wt.% of CaO+FeO. In contrast, Garcia et al. (2010) used pure olivine (Fo91), with 55.5 wt.% of MgO (theoretical), which is also close to the average MgO content of this study (53.6 wt.%), but containing nearly half of the iron compared to mine tailings in this study (12.95 wt.%). Our results on carbonation yields lie within the same order of magnitude compared to the two studies considered here. However, despite the large granulometry of the starting materials, Bobicki et al. (2014) was able to store CO₂ at a higher rate (~200 g/kg CO₂ within one hour) compared to the other two studies, by reacting the heat treated chrysotile at the conditions previously suggested by Gerdemann et al. (2007). This suggests that the rate of CO₂ storage in our experiments could have been enhanced if a NaHCO₃/NaCl solution was used. However, even though the rate is slower, MT2 experiment stored more CO₂ compared to Bobicki et al. (2014) and Garcia et al. (2010).

It is highly probable that the higher temperature range presumably limits carbonation by mobilizing Mg into phyllosilicates, while the lower range may limit H₂ generation by promoting Fe-carbonation. Nevertheless, this study proves that intermediate conditions can be set to make both processes work simultaneously.

The amounts of hydrogen produced in our experiments were compared with two similar studies (Crouzet et al., 2017; Malvoisin et al., 2013), who attempted to produce hydrogen by using pure wüstite (FeO) and Fe-rich steel slag (Table 3-5). For the sake of comparison, hydrogen produced at 473 K or 573 K, and 30 MPa after ca. 69 or 160 hours of each study were used. The study by Malvoisin et al. (2013) used a carbonated basic oxygen furnace (CARBOF) containing 2.7 wt.% Fe(0), 20.58 wt.% FeO and 3.16 wt.% Fe₂O₃. The grain size of original steel slag used for carbonation was 1 -50 µm. The second study (Crouzet et al., 2017) is a follow-up study of Malvoisin et al. (2013) that investigates the hydrogen production under acidic pH conditions using 50-100 µm size pure wüstite (FeO). Because the chemical composition of steel slag, wüstite and New Caledonian mine tailings largely differ from each other, we calculated the hydrogen production per mass unit of FeO of each material. In our study, the hydrogen measured by gas chromatography, and average FeO in mine tailings (12.95 wt.%) were used for this calculation.

As shown in Table 3-5, at 473 K, the steel slag of Malvoisin's study produced the smallest quantity of hydrogen compared to FeO and mine tailings. This is due to the presence of CaO in steel slag which buffered pH by producing Ca(OH)₂ which increased pH, lowering the solubility of steel slag. At pH~3, the reaction of FeO with acetic acid reported by Crouzet et al. (2017) produced the two orders of magnitude higher H₂ than the H₂ production of this study, due to the thermal stability and the potential of ligand-promoted Fe(II) dissolution of acetic acid which yields significant quantities of H₂ compared to water. At 573 K, the similar pH effect caused the steel slag to produce lower quantity of H₂ compared to Crouzet et al. (2017) and this study. However, mine tailings seemingly produced more H₂ compared to FeO at 573 K, and pH~3.

3.4.5 Implications for CO₂ sequestration and hydrogen production in New Caledonian mining sites and other Ni mining sites

New Caledonia is the 11th largest Ni producer in the world, preceded by the United states, Australia, Brazil, Canada, China, Columbia, Cuba, Guatemala, Indonesia and Madagascar (U.S. Geological Survey, 2017). When scaled to land area, however, its production of Nickel is in the top 3, implying a high environmental fingerprint. In 2013, New Caledonia produced 127,027 metric tons (t) of nickel from 7.8 million metric tons (Mt) of saprolite ore and 36,839 t of nickel from 4.2 Mt of laterite ore, resulting approximately 12 million metric tons (Mt) of mine tailings per year (Wacaster 2013). The management of mine tailings such as collection, storage and re-usage are costly to process. Currently these mine tailings were used for geo-technical aspects such as building roads, dams, and land filling. Compared to the traditional valorization methods, those proposed by this study are novel and meet today's energy demands. In addition, implementing a simultaneous ex-situ CO₂ storage and hydrogen production plant in the vicinity of mining sites provides a safe and permanent disposal of CO₂ emitted by the nickel industry. We believe that the energy needed for heating the material could be obtained passively by locating this plant near high temperature furnaces used for ore-processing.

The annual CO₂ emission of New Caledonia is about 4.29 Mton/year (Boden et al., 2017). Our experiments having shown that at 523 K and 30 MPa, mine tailings can trap at least 320 g of CO₂ per kg of mine tailings (Appendix II, S6), it follows that the annual mine tailings production could potentially trap 3.84 Mton/year of CO₂, which represents about 90% of New Caledonia's annual emissions.

The annual electrical consumption of New Caledonia is approximately 2398 GWh; (New Caledonia Department of Energy, 2013). The maximum hydrogen production in our experiments was 0.57 g hydrogen per kg of mine tailings at 573 K and 30 MPa. According to this value, the annual mine tailings produced in New Caledonia is able to produce 6840 tons of hydrogen per year, which is equivalent of generating 229 GWh/yr (with H₂ combustion generating around 120.5 MJ/kg or 33.5 kWh/kg). It represents around 10 % of New Caledonia's annual electrical consumption. Furthermore, assuming an average family consumes 3400 kWh/yr (New Caledonia Department of Energy, 2013), the energy produced would be sufficient to sustain around 67350 families.

One limiting factor regarding this method is the separation of small quantities of hydrogen from CO₂ in the reactor. Separating CO₂ and H₂ from industrially important gas mixtures (synthesis gas or natural gas) are widely performed using membrane methods (Korelskiy et al., 2015). These membranes could be either made from polymers (Ghadimi et al., 2014; Rabiee et al., 2014), or ceramic (Korelskiy et al., 2015), and they provide cost, effective means of separating gases in large scale. In our opinion, a membrane method would be suitable to separate hydrogen from CO₂ in this process.

We believe that the simultaneous application of ex-situ CO₂ sequestration and hydrogen production using New Caledonian mine tailings could be easily applied to various mining industries of mafic rocks, which presumably produce mine wastes of similar compositional and mineralogical characteristics. By using the residual heat provided by a third process such as the high temperature smelting of ore, those two processes could be translated into a high-value, cost-effective industrial way of storing wastes and generating clean energy.

Table 3-4. Comparison of ex-situ CO₂ sequestration at 573K <T>423 K and P<30 MPa

Composition	d (μm)	P (MPa)	T (K)	t (h)	Solution	CO ₂ (g/kg) ^a	Reference
chrysotile (OK)	425-1000	12.4	428	1	1M NaCl, 0.64M NaHCO ₃	183.0	Bobicki et al., 2015
chrysotile (Pipe)	425-1000	12.4	428	1	1M NaCl, 0.64M NaHCO ₃	157.0	Bobicki et al., 2015
				33			Garcia et al., 2010
Olivine	20-80	15	423	6	supercritical CO ₂	261.0	This study_MT1
				60			This study_MT2
Olivine	40-63	15	473	0	CO ₂ -saturated water	114.4	This study_MT2
				60			This study_MT4
Olivine	40-63	30	523	0	CO ₂ -saturated water	320.5	This study_MT4
				57			
Olivine	40-63	30	573	6	CO ₂ -saturated water	118.5	

^aGrams of molecular CO₂ captured by one kg of starting material

Table 3-5. Comparison of hydrogen production by experiments conducted at 473 and 573 K.

Reference	Material	Solution	pH	T	t (h)	^b (H ₂ g/kg)
Malvoisin et al., 2013	^a CARBOF	water	6.9	473	69.2	0.01
Crouzet et al., 2017	FeO	0.05M acetic	3	473	72	5.34
This study	mine tailings	CO ₂ +water	3.6	473	66	0.07
Malvoisin et al., 2013	CARBOF	water	6.9	573	141	1.38
Crouzet et al., 2017	FeO	water	6	573	144	2.18
This study	mine tailings	CO ₂ +water	3.9	573	164	2.26

^aCARBOF=carbonated basic oxygen furnace steel slag

^bgrams of H₂ produced by 1 kg of FeO

3.5 Conclusions

Our work has led us to conclude that the batch experiments conducted between 473 K - 573 K under high pCO₂ of 15-30 MPa have demonstrated the viability of using New Caledonian mine tailings in ex-situ carbonation process, while producing H₂ as a byproduct. The results suggest that, mine tailings were altered into Fe-rich magnesite and phyllosilicates when reacted with CO₂-saturated water at the above mentioned conditions. We have outlined that the competition between Mg and Fe incorporation among the secondary phases seems to control the quantities of magnesite precipitation and hydrogen production. Taken together, these results suggest that the temperatures between 523 K and 540 K at pCO₂=30 MPa would be the most favorable conditions for reacting mine tailings in order to maintain both carbonation and hydrogen production in significant quantities.

This work has demonstrated the applicability of this method to treat New Caledonia's annual CO₂ emissions and energy demands cost-efficiently by recycling the heat used in metal extraction (>1273 K), providing a novel valorization method for New Caledonian mine tailings. This approach can be globally applied to nickel (Ni) mine tailings as well as other industrial waste materials containing Ca, Ma, and Fe; however we believe that the optimum P/T conditions might vary depending on the mineral composition and textural features of individual material.

[This chapter has been published in Applied geochemistry, appendix IV]

Chapter 4

Water-rock interactions during simultaneous ex-situ CO₂ mineral sequestration and hydrogen production from New Caledonian mine tailings

[This chapter has been submitted to Applied Geochemistry]

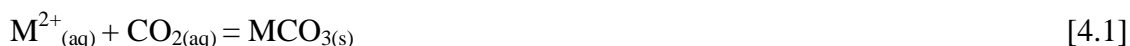
Abstract

New Caledonian mine tailings were reacted with carbon dioxide (CO₂)-saturated water at 473 K-573 K and at high CO₂ partial pressures (pCO₂ of 15 -30 MPa), in order to investigate its potential for simultaneous ex-situ CO₂ sequestration and hydrogen production. While CO₂ sequestration in minerals allows safe and long-term disposal of CO₂, hydrogen provides an alternative energy source which does not produce CO₂ upon combustion. In addition, ultramafic mine wastes provide potential low cost feedstocks for CO₂ sequestration and hydrogen production at industrial scale. Previous works have largely focused either on carbonation or hydrogen production individually and on the yields of carbonates and hydrogen. The aim of this study is to perform carbonation on mine tailings and generate hydrogen simultaneously to obtain significant yields from both processes, and understand the nature of water-rock interactions and mineral replacement reactions through this method. The experiments were conducted in stirred batch reactors for short durations (2-6 days) and long durations (24 days), while performing detailed analysis on liquid, gas and the solid products. The results suggest that mine tailings could be carbonated simultaneously producing substantial quantities of hydrogen (0.57 g H₂/kg of mine tailings), by reacting with CO₂-saturated water at acidic pH ~4. During the reaction, mine tailings mainly alter into Fe-rich magnesite and Mg-rich phyllosilicates such as, nontronite and vermiculite. At 473 K/ 15 MPa, Mg-rich magnesite precipitation occurred due to carbonation of Mg-rich phyllosilicates, whereas at 523 K/30 MPa and 573 K/30 MPa, Mg-rich magnesite seemed to precipitate directly from the solution. Finally, we put forward qualitative overall reactions for mine tailings alteration at 473 K/ 15 MPa, 523 K/30 MPa and 573 K/30 MPa, based on the phases present in the final products. Although significant quantities of CO₂ could be sequestered while producing important quantities of hydrogen, the reactivity of mine tailings is significantly lowered by the low soluble pyroxene glass, which is a major constituent of mine tailings.

Key words: New Caledonia, Mine tailings, Carbonation, Hydrogen, Alteration, Water-rock interactions, Olivine, Glass

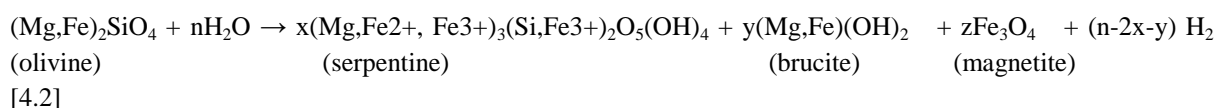
4.1 Introduction

Carbon dioxide (CO₂) capture and storage in minerals and hydrogen production via mineral reactions are two popular fields of applied geochemical research which have been growing independently over years. CO₂ storage in minerals is the fixation of CO₂ in the form of solid carbonates such as calcite (CaCO₃), dolomite (Ca_{0.5}Mg_{0.5}CO₃), magnesite (MgCO₃) and siderite (FeCO₃) or their solid solutions, as given by the generalized equation;



where M²⁺ refers to the divalent cations such as Fe²⁺, Mg²⁺ and Ca²⁺. Such minerals are stable over geologic time scales. Therefore, it is considered to be the safest method of CO₂ capture and storage as a permanent remedy for reducing harmful levels of atmospheric CO₂ (greenhouse effect). Since the emergence of the concept of CO₂ mineral storage (Seifritz, 1990) there has been number of studies on carbonation of silicates minerals (eg. olivine, pyroxenes, serpentines), mafic/ ultramafic rocks (eg. basalt, peridotite, dunite, harzburgite), and hydroxides (eg. brucite) (Daval et al., 2009b; Gerdemann et al., 2007; Giammar et al., 2005; Guyot et al., 2011; Sissmann et al., 2014, 2013). Considering the high abundance in nature, fast dissolution compared to other Mg-silicates, olivine, (Mg,Fe)₂SiO₄ has been used in many studies for the carbon dioxide storage. Although mineral carbonation has been widely studied in the industrial approach for CO₂ storage, the phenomena is based on the natural mineral carbonation in the context of alteration of silicates. Numerous field-based studies report the formation of carbonate deposits during the weathering of ultramafic host rocks and subsequent interactions with CO₂ rich fluids. Those deposits are either ultramafic-hosted massive magnesite deposits (Hansen et al., 2005; Pohl, 1990), or magnesite veins in serpentinized fields (Abu-Jaber, 1991; Abu-Jaber and Kimberley, 1992; Barnes et al., 1978; Dabitzias, 1980; Ghoneim et al., 2003).

Hydrogen production strategies are being investigated as alternate sources of energy for fossil fuel combustion, which is the major anthropogenic source of atmospheric CO₂. The idea is also based on the natural phenomena, "serpentinization", mainly associated with the deep sea midoceanic-ridge systems, where the hydrothermal alteration of mafic/ultramafic oceanic crust occurs at low (<100°C) or high temperatures (250°C - 350°C) producing large quantities of hydrogen in the deep sea floor (Charlou et al., 2002), according to the redox reaction given below;



Hydrogen produced by this process provides energy to sustain the deep sea life where sun light does not penetrate and photo-autotrophs cannot survive. In addition, this reaction creates highly reducing conditions in the sea floor which mediates the Fischer-Tropsch type reactions, potentially producing abiotic hydrocarbons (Allen and Seyfried, 2003; Charlou et al., 2002; Etiope and Sherwood Lollar, 2013; Fu et al., 2007; Klein et al., 2009; McCollom and Seewald, 2003; McDermott et al., 2015; Proskurowski et al., 2008). Hydrogen production

via serpentinization has been studied experimentally by reacting mafic/ultramafic minerals/rocks such as lherzolite (Marcaillou et al. (2011)), olivine (Malvoisin et al. (2012)), (Mayhew et al. (2013)); with water, under hydrothermal conditions. Mayhew et al. (2013) further documented the reactions on petedunnite $\text{Ca}(\text{Zn}, \text{Mn}^{2+}, \text{Mg}, \text{Fe}^{2+})\text{Si}_2\text{O}_6$, magnetite (Fe_3O_4), fayalite (Fe_2SiO_4) and hedenburgite ($\text{CaFe}^{2+}\text{Si}_2\text{O}_6$). A theoretical study on thermodynamic constrains of serpentinization of olivine could be found in McCollom and Bach (2009). It has been shown that the most favourable conditions for hydrogen production by serpentinization of olivine is at high temperatures $<400^\circ\text{C}$, most specifically around 300°C (Malvoisin et al. (2012)). An extrapolation of these theoretical and laboratory simulations towards more applied research was the basis for the recent studies on hydrogen production using FeO (Crouzet et al. (2016)), or industrial waste materials rich in iron (Malvoisin et al. (2013)).

Minerals such as olivine contains Fe^{2+} and Mg^{2+} in their structure. Both these ions have the potential to store CO₂ as carbonates (Eq.1), while Fe^{2+} has the potential for H₂ production (Eq.2). Therefore, the materials containing both Mg and Fe provide a possibility for CO₂ storage and hydrogen production. Malvoisin et al. (2013), showed that basic oxygen furnace (BOF) steel slag (which contains ca. 20% of FeO, ca. 5% of MgO and 45% of CaO) could be carbonated and then could be used for the hydrogen production. The authors also claimed that the carbonated BOF steel slag is more efficient for hydrogen production in comparison to the non-carbonated BOF steel slag. Kularatne et al., 2017 (submitted) experimentally demonstrated the possibility of using an olivine bearing mine tailing for CO₂ storage and hydrogen production simultaneously under chosen experimental conditions. Both studies show that the industrial waste materials containing suitable M^{2+} cations could be successfully valorized by using them for carbonation and hydrogen generation.

Both those processes are the final results of a series of reactions, where the dissolution of starting mineral is generally the rate-controlling reaction. Then, the compromises between the dissolution and the effect of any passivation determine the reaction progress. Dissolution-precipitation reactions taking place at the reaction front determine the extent of carbonation and hydrogen production, as well as the formation of secondary phases. Consequently, the reactions taking place at the water-rock interface important. This study focuses on the water-rock interactions taking place during simultaneous carbonation and hydrogen production by reacting New Caledonian mine tailings in CO₂ saturated water at hydrothermal conditions, using detailed mineralogical analysis performed in XRD, SEM and FIB-TEM techniques and thermodynamic models, in order to understand the reactions at micro-scale and nano-scale.

4.2 Materials and methods

4.2.1 Starting materials

Mine tailings from nickel (Ni) mines of New Caledonia and natural olivine ($\text{Mg}_{1.8}\text{Fe}_{0.2}\text{SiO}_4$) was also used for this study. The chemical composition of mine tailings and olivine were determined by electron probe micro analysis (EPMA), and listed in table 4-1.

Table 4-1. Chemical composition of starting materials obtained from electron probe micro analysis (EPMA)

	MgO	FeO	SiO ₂	CaO	Al ₂ O ₃
Mine tailings	35.61	12.95	48.05	0.30	1.94
olivine	47.99	9.34	41.95	0.11	0.16

Samples were crushed using a ball mill (FRITSCH Planetary Micro Mill pulverisette 7 premium line) and sieved to recover 0-45 µm size fraction of olivine and mine tailings for the short duration experiments (2-6 days), and 40-63 µm size fraction of mine tailings for long duration experiments (24 days). For the latter, the mine tailings powder was cleaned ultrasonically in absolute ethanol in order to remove fine particles adhered to the grain surface. The process was repeated until the cloudy appearance of alcohol supernatant disappears. Then, it was cleaned with ultra-pure deionized water and oven-dried at 333 K overnight, and observed under scanning electron microscope (SEM) (Figure 4-1a). The specific surface area (SSA) of this powder determined by Kr adsorption analysis according to the Brunauer-Emmett-Teller (BET) method was 0.23 m²/g (Brunauer et al., 1938).

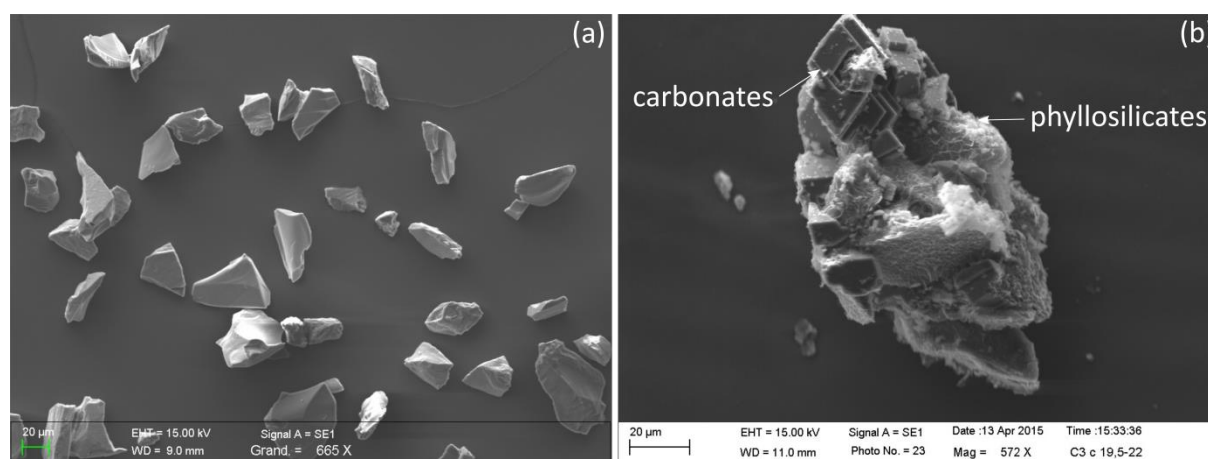


Figure 4-1. SEM secondary electron images of mine tailings (a) before, (b) after reaction with CO₂ saturated water at 523 K and 30 MPa.

4.2.2 Experiments and analytical methods

All the experiments were conducted in PARR® hastelloy stirring-type batch reactors (volume 250 ml). Approximately 2.0 g of starting material (olivine or mine tailings), and 200 ml of ultra-pure deionized water were added to the batch reactor. The reactor was then sealed using PTFE (Teflon®) gaskets. Carbon dioxide (CO₂) gas was pumped into the batch reactor at approximately 10 MPa lower than the desired pressure (~15-30 MPa). During the first 10 minutes, the gas was purged in order to evacuate dissolved oxygen. Then the reactor was heated up to desired temperature. At the end of the heating process, the pressure was adjusted to the value needed for the experiment either by pumping more CO₂ into the reactor or removing excess CO₂. A summary of all the experiments is provided in table 4-2.

4.2.2.1. Short duration experiments to compare the reactivity of mine tailings Vs. olivine

Two short term experiments were performed. The first was conducted using mine tailings (0-45 μm) at three temperatures; 363 K, 523 K and 573 K and at CO₂ pressure of 30 MPa for 2 days, in order to examine the carbonation of mine tailings as a function of temperature. The second consisted of two parallel experiments conducted using 0-45 μm fractions of olivine and mine tailings at 523 K/30 MPa for 2,4 and 6 days in order to compare the rate of carbonation of mine tailings with olivine. The experiments were quenched down to ambient conditions at the end of the reaction period by cutting off the heating and immersing the reactor in a water bath (room P/T). The solid reaction products were recovered and oven dried at 333 K overnight. They were crushed in an agate mortar for homogeneization and subsequently analyzed under Rock-Eval 6, to quantify the amount of carbonate precipitated.

4.2.2.2. Long duration experiments on carbon mineralization and hydrogen production from mine tailings

The long duration experiments were conducted using mine tailings (40-63 μm) for 25 days, while constantly sampling the gas and liquid from the on-going experiment. The experiments were quenched down to ambient conditions and the solid reaction products were recovered and oven dried at 333 K overnight. The details of gas and liquid sampling, as well as of the analysis conducted on both those fluid phases and the solid run products are given below

The gas samples were collected into Swagelock VCR® Metal Gasket Face Seal Fittings sampling tubes connected to the batch reactor. A vacuum of 10^{-5} bar was created along the sampling apparatus, to avoid atmospheric contaminations in these tubes. Collected gas samples were then analyzed with a Varian CP-3800 gas chromatograph (GC), to quantify the hydrogen produced during the reaction. Two standards were analyzed; one standard with a composition approximately similar to the atmospheric air, and the other one was a mixture of H₂, He, N₂, CO₂ and alkanes up to four carbons. The samples and the standards were injected to the GC at ~1200 mbar at room temperature. Between each analysis, a blank measurement was carried out by injecting N₂ as a quality control of the analysis. The uncertainty on H₂ measured by this method was 5.4%.

The liquid samples (~2.0 g) were collected into clean and dry plastic bottles containing de-ionized water (electrical conductivity = 18 M Ω .cm) acidified with nitric acid (HNO₃) (2% by volume). They were subsequently analyzed by an inductively coupled plasma atomic emission spectroscopy (ICP-AES; Thermo scientific iCAP 6000 series) with an Ar plasma, to obtain the aqueous concentrations of Mg, Si, Fe, Al, Na, K, Ca, Mn, Ni, Cr, and S. The analytical uncertainty of the fluid analysis by ICP- AES is below 5%. The concentrations of aqueous species obtained from the AES analysis were further used for the thermodynamic modeling of the liquid phase equilibria, and will be described in subsection 4.2.3.

The solid products were finely ground and analyzed using an X'Pert PRO (PANalytical) x-ray diffractometer with a Cu anode (Cu K α = 1.5418 Å), operated under 45 kV and 40 mA to determine the mineral phases present. However, one major limitation of this study was the inability to quantify glass and phyllosilicate in the final products using this method, which consequently hampered the quantitative determination of Fe, and Mg partitioning among the phases. Further work needs to be done to quantify amorphous phase (eg. glass) and phyllosilicates individually.

Rock-Eval 6 analysis was performed on the run products for better detection and quantification of carbonates (Figure 4-1b). The quantification limit of Rock-Eval 6 is ~0.02 wt.% C, which corresponds to ~0.15 wt.% MgCO₃, and this method is one order of magnitude more sensitive than the phase quantification by XRD (Behar et al., 2001; Lafargue et al., 1998).

SEM analysis was performed on solid products mounted on adhesive carbon-taped sample holders, gold (Au) coated and observed under “high vacuum” conventional SEM, EVO MA 10, Carl Zeiss SMT with a tungsten (W) filament operated under 15 kV and 100 mA. The secondary electron (SE) images were used for observing the surface topography, while back-scattered electron detector (BSE) was used to obtain images with atomic number contrast. A 150 pA beam was used for SE imaging at high spatial resolution. Qualitative chemical analyses were performed by energy dispersive X-ray analysis (EDX), with a probe current at 700 to 750 pA for EDS (Oxford) analysis. The silicon drift detector was calibrated on cobalt (Co) for quantitative analyzes during 10 s at 10 to 15 kcps with a dead time of about 15 s. In addition, SEM element mapping was performed on the reaction products mounted on epoxy resin, finely polished by ion beam milling.

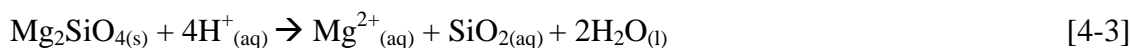
Transmission electron microscopy (TEM) analysis was performed on ultra-thin sections (<200 nm) of our run products using a JEOL 2100F (FEG) instrument operated at 200 kV (IMPMC, UPMC, Paris). These thin sections were prepared using focused ion beam milling (FIB), using a metal-liquid Gallium (LMIS Ga⁺) beam operated at 5 kV and 1pA-20nA beam current (at IPGP and IEMN, Lille).

4.2.3 Thermodynamic modeling

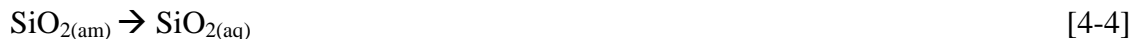
Mineral solubilities, solution pH and activities of aqueous species were calculated using the geochemical code CHESS - CHemical Equilibrium with Species and Surfaces (van der Lee and De Windt, 2002) using the LLNL EQ3/6 thermodynamic database. For this calculation we used the aqueous concentrations of SiO₂, Mg, Fe, Ca, Al, N and K obtained from ICP AES analysis, the temperature of the experiment and the fugacity of CO₂ as input parameters. The CO₂ fugacities were 130.7 bar, 264.4 bar and 281.7 bar at 473K/15 MPa, 523K/30 MPa and 573K/30 MPa respectively, as calculated using the Thermosolver software (Barnes and Koretsky, 2004).

Saturation indexes (SI) of amorphous silica (SiO_{2(am)}), forsterite, and magnesite were computed with the CHESS code considering their dissolution reactions, as given below;

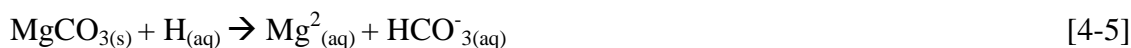
forsterite dissolution;



amorphous silica dissolution;



magnesite dissolution;



The Gibbs free energy of ($\Delta G_{(r)}$) of above dissolution reactions were calculated from the saturation indexes obtained from CHESS equilibrium calculation, according to the relationship given below;

$$\Delta G_{(r)} = RT \ln_{10}(\text{SI}) \quad [4-6]$$

where R is the universal gas constant ($\text{J} \cdot \text{mol}^{-1} \cdot \text{K}^{-1}$) and T the temperature (K).

Table 4-2. Experimental details

Experiment	Starting material	d (μm)	PCO ₂ (MPa)	T (K)	T (days)	Carbonate wt%	CO ₂ storage (g/kg)	R _x *
MT6	Mine tailings	45-63	30	363	2	0	0	0
MT7	Mine tailings	45-63	30	473	2	9.51	5.9	1.6
MT8	Mine tailings	45-63	30	523	2	15.32	8.7	2.6
MT-d2	Mine tailings	0-45	30	523	2	8	28.9	10.1
MT-d4	Mine tailings	0-45	30	523	4	19	82.2	25.0
MT-d6	Mine tailings	0-45	30	523	6	28	121.6	36.7
Ol-d2	Olivine	0-45	30	523	2	55	271.8	74.5
Ol-d4	Olivine	0-45	30	523	4	66	347.2	88.6
Ol-d6	Olivine	0-45	30	523	6	74	412.8	99.9
MT1	Mine tailings	40-63	15	473	25	20.3	114.4	26.3
MT2	Mine tailings	40-63	30	523	25	44.9	320.5	69.8
MT4	Mine tailings	40-63	30	573	24	21.6	118.5	28.0

*R_x = extent of reaction, calculated according to:

$$R_x = \frac{X_{(\text{carb})}}{X_{(\text{max})}} * 100$$

where, X(carb) is the weight % of precipitated carbonate, X_(max) is the wt% of carbonate assuming 100 % stoichiometric conversion of Mg into magnesite.

4.3 Results

The quantities of carbonate (Fe-rich magnesite) measured using Rock-Eval 6, calculated weight of CO₂ stored by 1 kg of olivine or mine tailings were reported in table 2. The maximum carbonation yield of mine tailings and olivine were calculated assuming all the Mg will precipitate with a mean composition of Mg_{0.8}Fe_{0.2}CO₃ for all short-duration experiments (for the long-duration ones (MT1, MT2 and MT4) the exact compositions of carbonates analyzed under SEM were used). The maximum carbonation of olivine and mine tailings were calculated to be 74 wt.% and 77 wt.% (Supplementary 4-1). Using these values we calculated the extent of reaction (R_x) of each experiment with respect to carbonate precipitation, according to the formula:

$$R_x = \frac{X_{(carb)}}{X_{(max)}} * 100 \quad [4-7]$$

where, X(carb) is the weight % of precipitated carbonate , X_(max) is the wt% of carbonate assuming 100 % stoichiometric conversion of Mg into magnesite. The R_x values were also reported in table 2.

4.3.1. Short duration experiments

In the first short duration experiment conducted using mine tailings and CO₂-saturated water, magnesite ((Mg,Fe)CO₃) was the only carbonate precipitated as confirmed by the Rock-Eval 6 analysis.

Magnesite precipitated at 363, 473 and 523 K were 0, 9.51 and 15.32 wt.% (table 2 and figure 4-2a). The results clearly showed that there was no carbonate precipitation at 363 K, but the quantity of carbonate clearly increased as a function of temperature.

In the second short duration experiment which was conducted to compare the carbonation between mine tailings and olivine as a function of reaction time at 523 K/30 MPa, magnesite ((Mg,Fe)CO₃) was the only carbonate observed in all the run products. In the olivine experiments 55, 66 and 74 wt.% of magnesite were formed after 2,4 and 6 days of reaction respectively (table 4-2 and figure 4-2b). In the mine tailings experiments, only 8, 19 and 28 wt.% of magnesite were precipitated after 2,4 and 6 days of reaction respectively (table 4-2 and figure 4-2b).

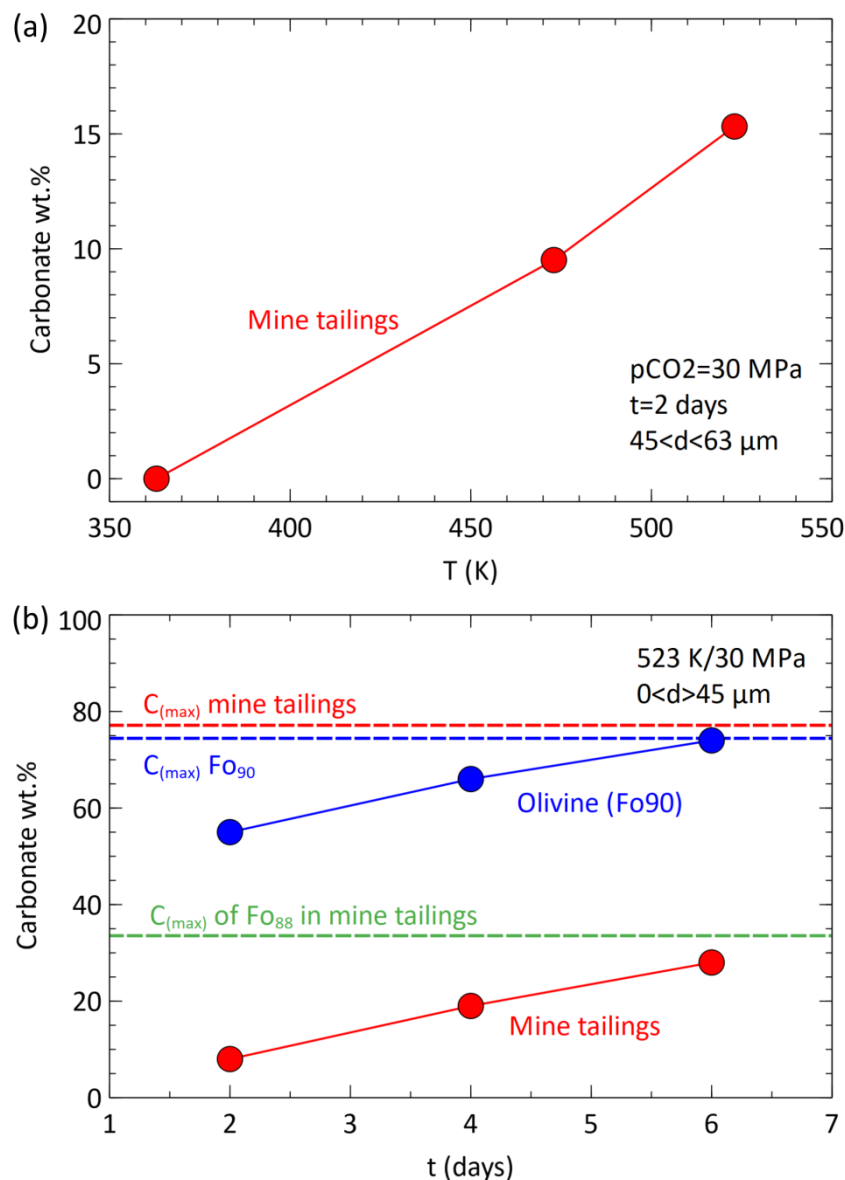


Figure 4-2. Carbonation of mine tailings (a) as a function of reaction temperature at $p\text{CO}_2 = 30 \text{ MPa}$, showing that the carbonate percentage increases with time; (b) in comparison to olivine, showing that mine tailings is less carbonated than olivine under similar P/T and pH conditions.

4.3.2 Long duration experiments

4.3.2.1 Chemistry of aqueous solutions

The concentrations of aqueous Si, Mg, Fe, Ca, Al, Na and K measured during the 25 days long batch experiments conducted at 473 K/ 15 MPa, 523 K/ 30 MPa, and 573 K/ 30 MPa were summarized in tables 4-3, 4-4 and 4-5. The tables also consist the calculated [Mg]/[Si] ratio and reaction Gibbs free energies ($\Delta G_{(r)}$) with respect to forsterite, amorphous silica and magnesite.

The reactions took place in acidic solutions due to the dissolution of CO₂ in water. However, our experimental set up doesn't allow in-situ pH measurement at high temperature, and therefore the initial pH of the solutions was calculated using the CHES geochemical code, using the solution volume, pCO₂, and temperature as input parameters, which resulted pH=3.55, 3.64 and 3.94 at 473 K/ 15 MPa, 523 K/ 30 MPa, and 573 K/ 30 MPa respectively. Upon the consumption of H⁺ during the dissolution of mine tailings, the solutions became slightly "basic" (4.48, 4.13 and 4.44 at 473 K/15 MPa, 523 K/30 MPa and 573 K/30 MPa respectively), compared to the initial pH, as calculated by considering the equilibrium of the solution with respect to measured aqueous Si, Mg, Fe, Ca, Al, Na and K of each experiment (tables 3 -5 and Appendix III, Figure A1).

The variation of dissolved Si and Mg in the three experiments as a function of reaction time is illustrated in figure 3. According to these plots and the reported [Mg]/[Si] values, Si and Mg have been released incongruently into the solution during the dissolution of mine tailings, where calculated [Mg]/[Si] ratios for the solutions were one to three orders of magnitude lower than the corresponding [Mg]/[Si] values of olivine and glass (1.72 and 0.65) in mine tailings, suggesting a non-stoichiometric dissolution. In addition, the [Mg]/[Si] ratios systematically decreased with the increasing temperature of our experiments (Appendix III, Figure A2).

The concentration of aqueous Mg at which the solutions will saturate with respect to pure magnesite, were 1.49, 0.69 and 0.18 mmol/L at 473 K/ 15 MPa, 523 K/30 MPa and 573 K/30 MPa experiments respectively, and corresponds to blue dashed lines on figure 3a,b and c. This calculation indicated that at 473 K/15 MPa, the solution was oversaturated with respect to pure magnesite (MgCO_{3(s)}) at the first seven days of experiment and then the concentration of Mg in the solution remained close to the Mg concentration-with respect to magnesite saturation, for the rest of the reaction period. But, at 523 K/30 MPa and 573 K/30 MPa, the solutions remain slightly under saturated with respect to pure magnesite saturation.

The concentrations of aqueous Si at which the solutions will saturate with respect to possible secondary silicate phases were also calculated and shown in Figure 4-3. At 473 K/15 MPa, 523 K/30 MPa and at 573 K/30 MPa, the solutions were saturated with respect to numerous secondary phyllosilicate phases, such as beidelite, montmorillonite, saponite (smectites) and kaolinite, at silica concentrations 12.1, 13.5 and 14.3 mmol/L, respectively. The smectite saturation is indicated in Figure 4-3. In addition, at 473 K/15 MPa, the

concentration of Si at which the solution saturates with respect to amorphous silica was 14.89 mmol/L. According to the measured Si concentration, the solution reached near saturation with respect to amorphous silica, but it stayed undersaturated throughout the reaction period, indicating amorphous silica would not precipitate at these conditions ($\Delta G_{(r)SiO_{2am}} > -0.55$) (see Table 4-3). At 523 K/30 MPa, the solution was over-saturated with respect to pyrophyllite ($Al_2(Si_4O_{10})(OH)_2$), since the beginning of the experiment until 20 days and became slightly soluble (see Table 4-4). The concentration of Si at which the solution becomes saturated with respect to pyrophyllite was 13.48 mmol/L. At 573 K/30 MPa, 0-4 days of reaction, the solution was over-saturated with respect to quartz (see table 4-5), and then became undersaturated until 21 days finally reaching equilibrium. Quartz saturation at this P/T conditions occur as the concentration of Si reaches 9.7 mmol/L.

As reported in tables 4-3 to 4-5, the $\Delta G(r)$ with respect to forsterite remained close to -40 kJ/mol throughout the reaction period of all the experiments, indicating that the dissolution of forsterite is thermodynamically favored at the conditions of our experiments. Although mine tailings contained olivine (Fo88), we used the thermodynamic data for forsterite as an approximation for Fo88 in mine tailings since the CHESSE database does not incorporate the thermodynamic data for the olivine solid solution. In addition, the thermodynamics of dissolution of glass could not be predicted with the CHESSE thermodynamic calculations due to insufficient data. In addition, as reported in the tables 4-3 to 4-5, the $\Delta G(r)$ with respect to chrysotile and antigorite showed that the precipitation of serpentines was thermodynamically not favored at the conditions of our experiments. The precipitation of lizardite has not been modeled since the thermodynamic data for lizardite was not included in CHESSE database. However, when the solution composition is simplified to three components MgO-SiO₂-H₂O, the solutions were in equilibrium with antigorite and sepiolite, which are the least soluble and thermodynamically favorable phases, showing the effect of Al and Fe on the formation of secondary phases (Appendix III, Figure A3).

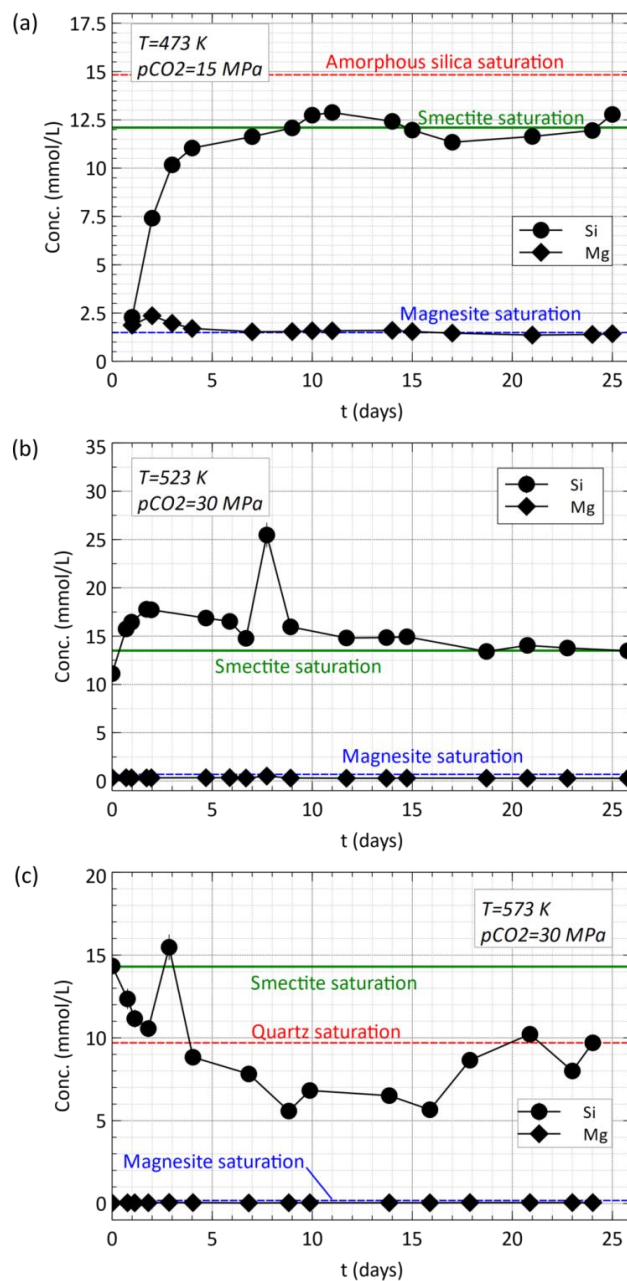


Figure 4-3. Chemical evolution of Mg and Si in the aqueous fluid during batch experiment conducted on mine tailings at (a) T=473 K and 15 MPa (b) T=523 K and 30 MPa (c) T=573 K and 30 MPa. The dashed lines in blue indicate the saturation condition with respect to magnesite in each experiment. The dashed lines in red indicate the saturation with respect to amorphous silica and quartz. The solid green line indicates the Si concentration at which the solution saturate with respect to smectite.

Table 4-3. Summary of results of MT1 experiment, performed at 473 K and 15 MPa ($f\text{CO}_2 = 130.69$ bars)

Sample#	t (days)	SiO ₂ (mmol/L)	Mg (mmol/L)	Fe (mmol/L)	Ca (mmol/L)	Al (mmol/L)	Na (mmol/L)	K (mmol/L)	Ratio Mg/Si	pH	$\Delta G(r)$ Fo (kJ/mol)	$\Delta G(r)$ SiO ₂ am (kJ/mol)	$\Delta G(r)$ Mag (kJ/mol)
MT1-1	1	2.28	1.87	1.66E-03	0.15	1.25E-03	0.10	0.02	0.82	4.59	-41.12	-7.37	2.27
MT1-2	2	7.41	2.36	3.79E-03	0.10	9.37E-04	0.09	0.03	0.32	4.67	-32.65	-2.73	4.19
MT1-3	3	10.17	1.97	4.56E-03	0.07	3.94E-04	0.08	0.03	0.19	4.60	-34.66	-1.48	1.22
MT1-4	4	11.04	1.70	2.85E-03	0.07	2.50E-04	0.10	0.03	0.15	4.54	-37.02	-1.16	1.19
MT1-5	7	11.63	1.53	6.86E-03	0.06	5.21E-05	0.09	0.03	0.13	4.51	-38.68	-0.96	0.29
MT1-6	9	12.08	1.54	3.94E-03	0.06	2.87E-04	0.11	0.03	0.13	4.51	-38.46	-0.81	0.32
MT1-7	10	12.74	1.58	4.60E-03	0.05	2.41E-04	0.10	0.03	0.12	4.52	-37.82	-0.60	0.54
MT1-8	11	12.88	1.58	2.87E-03	0.05	2.09E-04	0.12	0.04	0.12	4.52	-37.73	-0.55	0.56
MT1-9	14	12.42	1.60	2.32E-02	0.05	6.25E-04	0.11	0.04	0.13	4.52	-37.66	-0.70	0.67
MT1-10	15	11.97	1.54	3.53E-03	0.05	2.07E-03	0.12	0.05	0.13	4.51	-38.52	-0.84	0.31
MT1-11	17	11.34	1.46	1.64E-03	0.05	6.01E-04	0.13	0.05	0.13	4.49	-39.71	-1.06	-0.18
MT1-12	21	11.64	1.36	1.21E-02	0.06	4.38E-04	0.13	0.04	0.12	4.46	-40.77	-0.95	-0.76
MT1-13	24	11.95	1.39	5.90E-03	0.05	5.40E-04	0.14	0.04	0.12	4.47	-40.33	-0.85	-0.59
MT1-14	25	12.78	1.43	5.37E-03	0.05	1.55E-03	0.12	0.05	0.11	4.48	-39.54	-0.59	-0.33

The $\Delta G(r)$ with respect to each mineral phase and pH of the solution was obtained by thermodynamic modeling using CHES geochemical program (Van der Lee and De Windt, 2002) by using the concentrations of SiO₂(aq), Fe₂+(aq), Mg₂+(aq), Ca₂+(aq), Al₃+(aq), Na+(aq) K+(aq) obtained from the ICP-AES analysis. The abbreviations associated with $\Delta G(r)$ term are: Fo=forsterite, SiO₂am=amorphous silica, Mag=magnesite. The fugacity coefficient of CO₂ (Peng-Robinson) at 200 °C/ 15 MPa is 0.8713 and was calculated using the Thermosolver software. $f\text{CO}_2$ was obtained by multiplying the experimental pressure by the fugacity coefficient ($f\text{CO}_2 = 15 \text{ MPa} \cdot 0.8713$).

Table 4-4. Summary of results of MT2 experiment, performed at 523 K and 30 MPa ($f\text{CO}_2 = 264.36$ bars)

Sample#	t (days)	SiO ₂ (mmol/L)	Mg (mmol/L)	Fe (mmol/L)	Ca (mmol/L)	Al (mmol/L)	Na (mmol/L)	K (mmol/L)	Ratio Mg/Si	pH	$\Delta G(r)$ Fo (kJ/mol)	$\Delta G(r)$ SiO ₂ am (kJ/mol)	$\Delta G(r)$ Mag (kJ/mol)	$\Delta G(r)$ Pyro (kJ/mol)
MT2_1	0.00	11.12	0.34	1.41E-03	0.03	8.24E-04	0.08	0.05	0.03	4.19	-41.25	-2.28	-5.17	-1.63
MT2_2	0.70	15.74	0.34	3.22E-03	0.02	6.49E-04	0.06	0.04	0.02	4.17	-40.50	-0.91	-5.48	1.96
MT2_3	0.97	16.45	0.32	2.58E-03	0.02	3.03E-04	0.07	0.04	0.02	4.15	-41.29	-0.74	-5.95	-3.28
MT2_4	1.72	17.78	0.32	4.02E-03	0.02	1.75E-03	0.08	0.04	0.02	4.16	-40.99	-0.43	-5.96	13.66
MT2_5	1.96	17.72	0.33	2.74E-03	0.02	6.84E-04	0.08	0.04	0.02	4.16	-40.57	-0.44	-5.74	5.37
MT2_6	4.69	16.87	0.34	6.59E-03	0.02	1.09E-03	0.09	0.05	0.02	4.19	-39.84	-0.64	-5.28	8.41
MT2_7	5.88	16.52	0.35	6.25E-03	0.04	2.50E-03	0.09	0.05	0.02	4.20	-39.31	-0.72	-4.98	15.15
MT2_8	6.69	14.77	0.31	1.36E-03	0.03	2.55E-03	0.09	0.05	0.02	4.17	-41.47	-1.16	-5.83	13.60
MT2_9	7.73	25.47	0.51	5.22E-03	0.05	2.41E-03	0.14	0.09	0.02	4.34	-31.02	0.99	-1.68	22.00
MT2_10	8.92	15.96	0.31	1.56E-03	0.03	1.11E-03	0.09	0.05	0.02	4.17	-40.86	-0.86	-5.80	7.46
MT2_11	11.71	14.81	0.29	6.88E-03	0.03	1.37E-03	0.10	0.06	0.02	4.17	-42.00	-1.15	-6.11	8.27
MT2_12	13.71	14.85	0.29	7.92E-03	0.06	7.63E-03	0.09	0.06	0.02	4.18	-41.74	-1.14	-5.98	23.01
MT2_13	14.73	14.93	0.30	4.57E-03	0.02	4.43E-04	0.09	0.06	0.02	4.16	-42.06	-1.12	-6.15	-2.47
MT2_14	18.71	13.41	0.29	5.82E-03	0.02	5.87E-04	0.09	0.06	0.02	4.15	-42.83	-1.54	-6.32	-0.80
MT2_15	20.75	14.04	0.29	4.14E-03	0.02	2.80E-04	0.09	0.06	0.02	4.15	-42.66	-1.36	-6.33	-6.04
MT2_16	22.75	13.77	0.28	6.16E-03	0.02	1.03E-03	0.09	0.06	0.02	4.14	-43.44	-1.43	-6.68	4.13
MT2_17	25.77	13.48	0.28	6.13E-03	0.02	6.90E-04	0.08	0.06	0.02	4.13	-43.84	-1.52	-6.84	0.67

The $\Delta G(r)$ with respect to each mineral phase and pH of the solution was obtained by thermodynamic modeling using CHESS geochemical program (Van der Lee and De Windt, 2002) by using the concentrations of SiO₂(aq), Fe²⁺(aq), Mg²⁺(aq), Ca²⁺(aq), Al³⁺(aq), Na⁺(aq) K⁺(aq) obtained from the ICP-AES analysis. The abbreviations associated with $\Delta G(r)$ term are: Fo=forsterite, SiO₂am=amorphous silica, Mag=magnesite, Pyro=pyrophyllite. The fugacity coefficient of CO₂ (Peng-Robinson) at 250 °C/ 30 MPa is 0.8812 and was calculated using the Thermosolver software. $f\text{CO}_2$ was obtained by multiplying the experimental pressure by the fugacity coefficient ($f\text{CO}_2 = 30 \text{ MPa} \times 0.8812$).

Table 4-5. Summary of results of MT4 experiment, performed at 573 K and 30 MPa ($f\text{CO}_2 = 281.73$ bars)

Sample#	t (days)	SiO ₂ (mmol/L)	Mg (mmol/L)	Fe (mmol/L)	Ca (mmol/L)	Al (mmol/L)	Na (mmol/L)	K (mmol/L)	Ratio Mg/Si	pH	$\Delta G(r)$ Fo (kJ/mol)	$\Delta G(r)$ SiO ₂ am (kJ/mol)	$\Delta G(r)$ Mag (kJ/mol)	$\Delta G(r)$ Qtz (kJ/mol)
MT4_1	0.00	14.34	0.03	1.36E-03	0.03	4.71E-04	0.09	0.05	0.00	4.34	-37.85	-2.08	-9.52	2.01
MT4_2	0.77	12.35	0.04	1.76E-03	0.02	<dl	0.12	0.07	0.00	4.38	-35.33	-2.67	-7.96	1.30
MT4_3	1.13	11.16	0.04	1.86E-03	0.02	1.19E-03	0.12	0.07	0.00	4.39	-35.71	-3.06	-7.95	0.82
MT4_4	1.81	10.56	0.04	1.81E-03	0.02	4.57E-04	0.12	0.07	0.00	4.39	-36.54	-3.28	-8.26	0.55
MT4_5	2.85	15.47	0.06	3.49E-03	0.02	2.45E-04	0.18	0.12	0.00	4.42	-30.68	-1.78	-6.08	2.37
MT4_6	4.04	8.83	0.05	2.10E-03	0.01	2.60E-04	0.15	0.09	0.01	4.45	-34.61	-3.98	-6.95	-0.30
MT4_7	6.83	7.82	0.03	2.05E-03	0.01	1.95E-04	0.10	0.06	0.00	4.32	-40.86	-4.46	-9.83	-0.88
MT4_8	8.83	5.58	0.04	2.65E-03	0.01	8.42E-04	0.12	0.07	0.01	4.36	-39.68	-5.79	-8.58	-2.49
MT4_9	9.88	6.82	0.04	2.02E-03	0.01	3.91E-04	0.13	0.08	0.01	4.38	-38.98	-5.00	-8.62	-1.53
MT4_10	13.85	6.51	0.04	1.74E-03	0.01	5.93E-04	0.10	0.06	0.01	4.33	-40.18	-5.18	-9.13	-1.75
MT4_11	15.88	5.66	0.04	1.92E-03	0.01	6.57E-04	0.12	0.06	0.01	4.35	-39.65	-5.73	-8.59	-2.42
MT4_12	17.88	8.65	0.05	1.07E-03	0.00	3.09E-04	0.12	0.07	0.01	4.38	-36.21	-4.07	-7.70	-0.40
MT4_13	20.88	10.22	0.05	6.83E-04	0.02	5.43E-03	0.15	0.08	0.00	4.44	-33.41	-3.41	-6.63	0.40
MT4_14	23.00	8.00	0.05	9.86E-04	0.01	1.17E-03	0.15	0.09	0.01	4.43	-34.38	-4.37	-6.63	-0.77
MT4_15	24.02	9.70	0.05	5.12E-04	0.01	6.99E-04	0.16	0.09	0.01	4.44	-33.74	-3.62	-6.69	0.15

The $\Delta G(r)$ with respect to each mineral phase and pH of the solution was obtained by thermodynamic modeling using CHESS geochemical program (Van der Lee and De Windt, 2002) by using the concentrations of SiO₂(aq), Fe²⁺(aq), Mg²⁺(aq), Ca²⁺(aq), Al³⁺(aq), Na⁺(aq) K⁺(aq) obtained from the ICP-AES analysis. The abbreviations associated with $\Delta G(r)$ term are: Fo=forsterite, SiO₂am=amorphous silica, Mag=magnesite, Qtz=quartz. The fugacity coefficient of CO₂ (Peng-Robinson) at 300 °C/ 30 MPa is 0.9391 and was calculated using the Thermosolver software. $f\text{CO}_2$ was obtained by multiplying the experimental pressure by the fugacity coefficient ($f\text{CO}_2 = 30 \text{ MPa} \times 0.9391$).

4.3.2.2 Hydrothermal production of hydrogen

The variation of measured hydrogen as a function of reaction time is given in Figure 4. Cumulative hydrogen production increased gradually as a function of time at 473 K/ 15 MPa and 523 K/30 MPa reaching a maximum of 20.0 and 117.6 μmol of hydrogen per g of mine tailings, respectively, whereas, at 573 K/30 MPa the hydrogen concentration increased up to 283.5 μmol of hydrogen per g and then stabilized. No hydrogen was measured in the blank experiments conducted at 523 K/30 MPa and 573 K/30 MPa as indicated by the blue circles on the sample plot (Figure 4b and c).

4.3.2.3 Hydrocarbons production

The variation of measured methane in the experiment at 473 K/15 MPa as a function of reaction time is shown in figure 5. Methane was observed only on four samples, and the concentration varied between ~ 1.5 -0.3 $\mu\text{mol/g}$.

The variation of measured methane in the experiment at 523 K/30 MPa as a function of reaction time is shown in figure 6a. The quantity of methane increased until 14 days reaching a maximum of 12.3 $\mu\text{mol/g}$, and then gradually decreased. A similar variation was observed for C₂-C₄ alkanes (Figure 6b). The Schulz-Flory distribution of the alkanes measured at 11.7 days and 13.7 days are given in Figure 6c and d, with their Schulz-Flory correlation coefficients (R^2) values 0.66 and 0.85 respectively. The values used to plot the Schulz-Flory distribution are reported in table 6.

The variation of measured methane in the blank experiment at 523 K/30 MPa as a function of reaction time is shown in figure 7a. The concentration of methane increased gradually with time until the end of the experiment. The C₂-C₄ alkanes detected in the experiment and blank were shown in figure 7b. These alkanes were detected only after ~ 12 days of reaction. The Schulz-Flory distribution of the alkanes measured at 19.2 days and 24.2 days are given in Figure 7c and d, with their Schulz-Flory correlation coefficients (R^2) values 0.0012 and 0.004 respectively.

The variation of measured methane in the experiment at 573 K/30 MPa as a function of reaction time is shown in figure 8a. The quantity of methane increased until 3 days reaching a maximum of 26 $\mu\text{mol/g}$, and then gradually decreased. The C₂-C₄ alkanes showed a zig-zag variation with time (Figure 8b). The Schulz-Flory distribution of the alkanes measured at 2.9 days, 9.9 days and 24 days are given in Figure 8c,d and e, with their Schulz-Flory correlation coefficients (R^2) values 0.62, 0.64 and 0.60 respectively.

The variation of measured methane in the blank experiment at 573 K/30 MPa as a function of reaction time is shown in figure 9a. The concentration of methane remained nearly constant throughout the experiment at ~ 7.5 $\mu\text{mol/g}$. The C₂-C₄ alkanes detected in the experiment and blank were shown in figure 9b. The concentration of these alkanes increased gradually until 19 days and then decreased. The Schulz-Flory distribution of the alkanes measured at 7.2 days and 19.2 days are given in Figure 9c,d and e, with their Schulz-Flory correlation coefficients (R^2) values 0.50, 0.008 and 0.04 respectively.

Formaldehyde and acetaldehyde were detected in preliminary liquid chromatography analysis at IFPEN, on the samples obtained from the two experiments at 523 K/30 MPa and at 573 K/30 MPa. The quantities of formaldehyde and acetaldehyde were ~1-2 ppm (Appendix III, Figure A4).

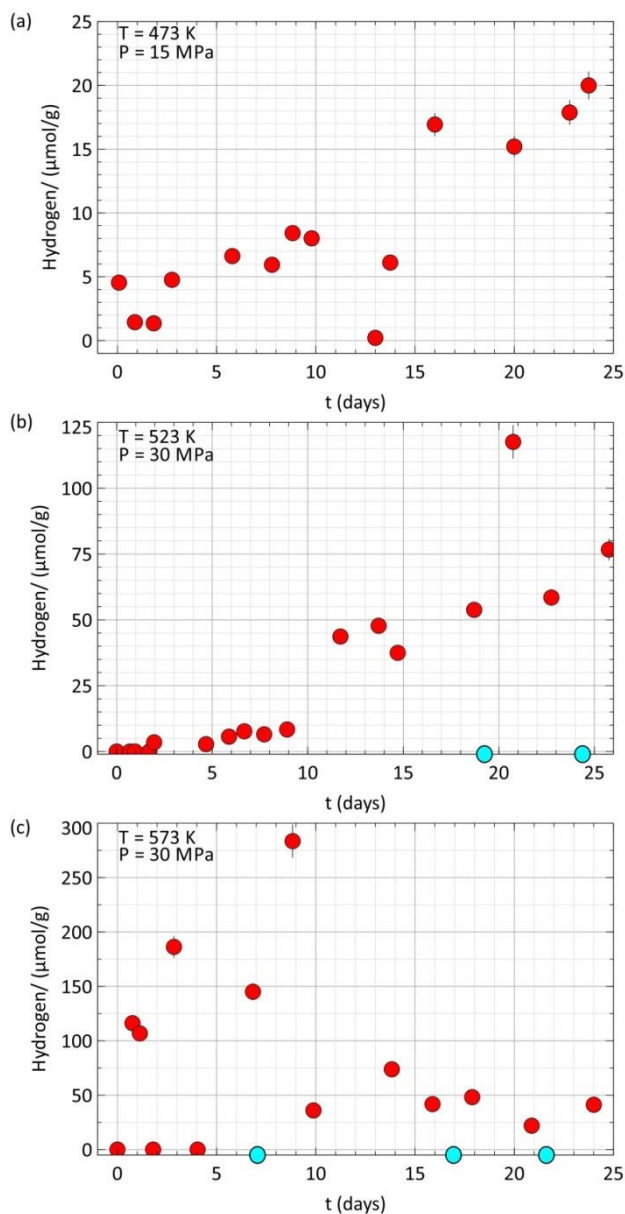


Figure 4-4. Variation of measured hydrogen as a function of time. The error bars around the data points (smaller than the marker for most of them), represent a 5% uncertainty associated with the concentration measurements of hydrogen (H₂) by gas chromatography.

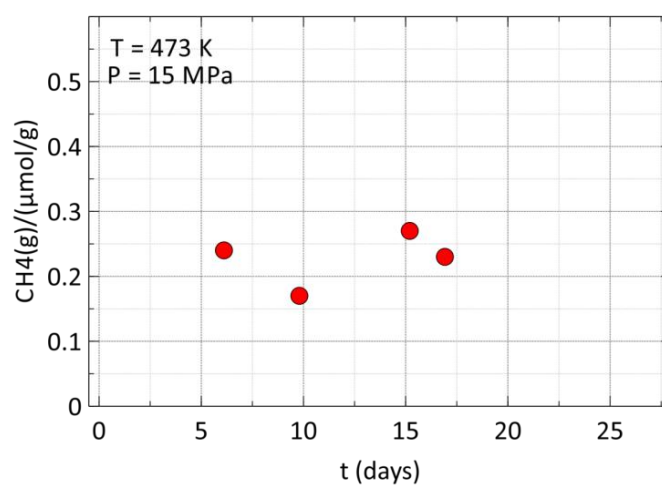


Figure 4-5. Variation of measured methane as a function of time at 473 K and 15 MPa. The error bars around the data points (smaller than the marker for most of them) represent a 5% uncertainty associated with the concentration measurements of methane (CH_4) by gas chromatography.

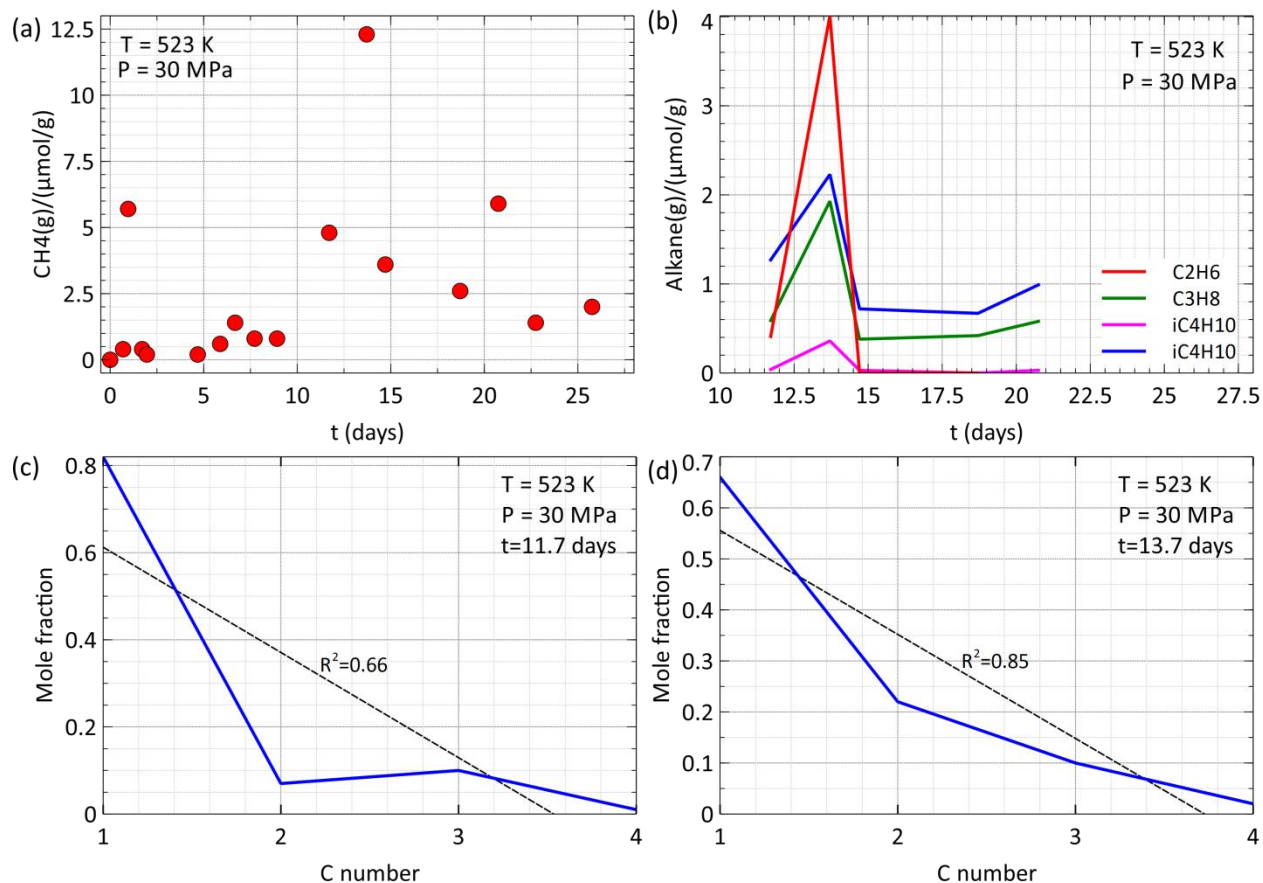


Figure 4-6. Measured hydrocarbons in the experiment conducted at 523 K and 30 MPa (a) variation of measured methane as a function of time; (b) variation of C₂-C₄ alkanes as a function of time; Schulz-Flory distribution of the alkanes measured at (c) t=11.7 days; (d) t=13.7 days. The $R^2 < 0.90$ in the above plots indicate a thermogenic origin of methane (Etiope and Sherwood Lollar, 2013).

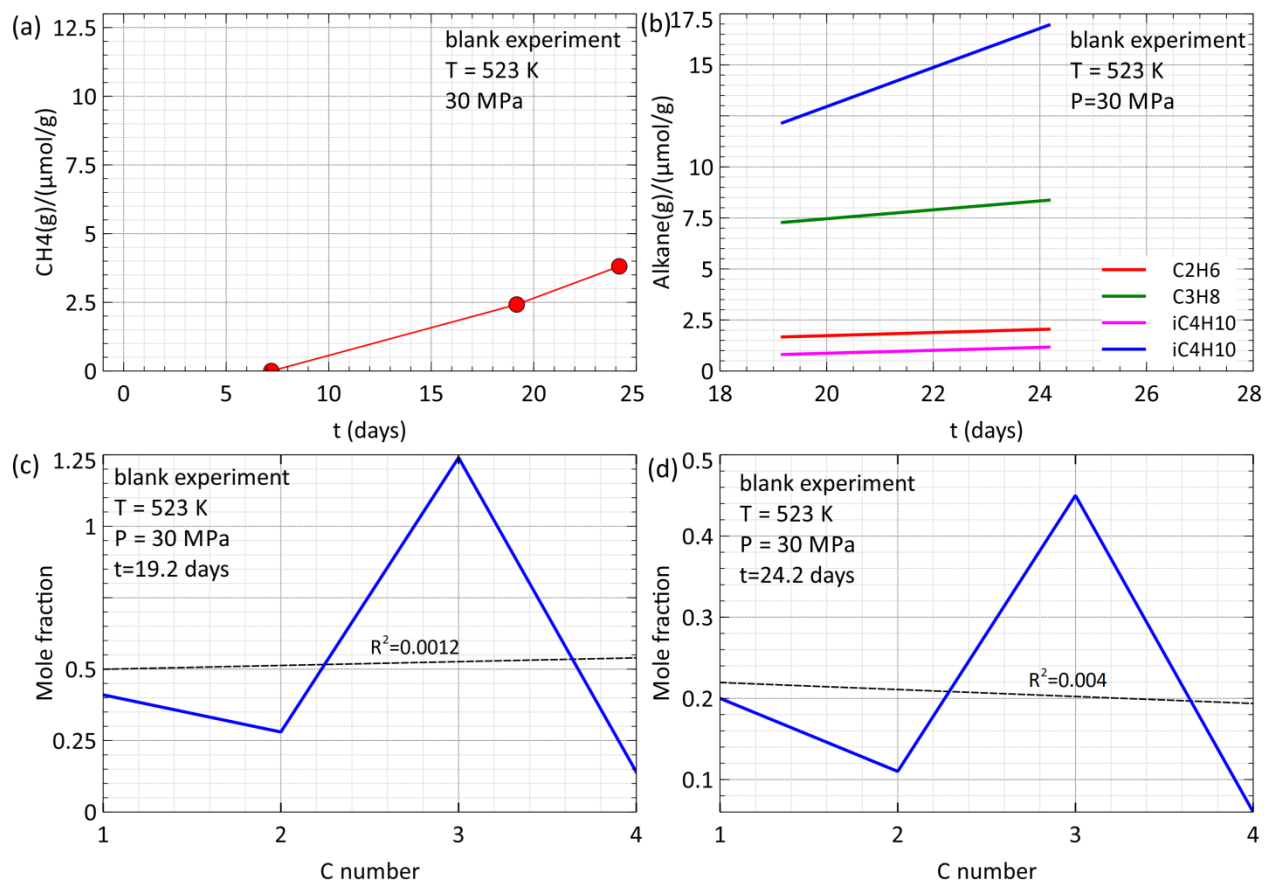


Figure 4-7. Measured hydrocarbons in the blank experiment conducted at 523 K and 30 MPa (a) variation of measured methane as a function of time; (b) variation of C₂-C₄ alkanes as a function of time; Schulz-Flory distribution of the alkanes measured at (c) t=19.2 days; (d) t=24.2 days. The $R^2 \ll 0.90$ in the above plots indicate a thermogenic origin of methane (Etiope and Sherwood Lollar, 2013).

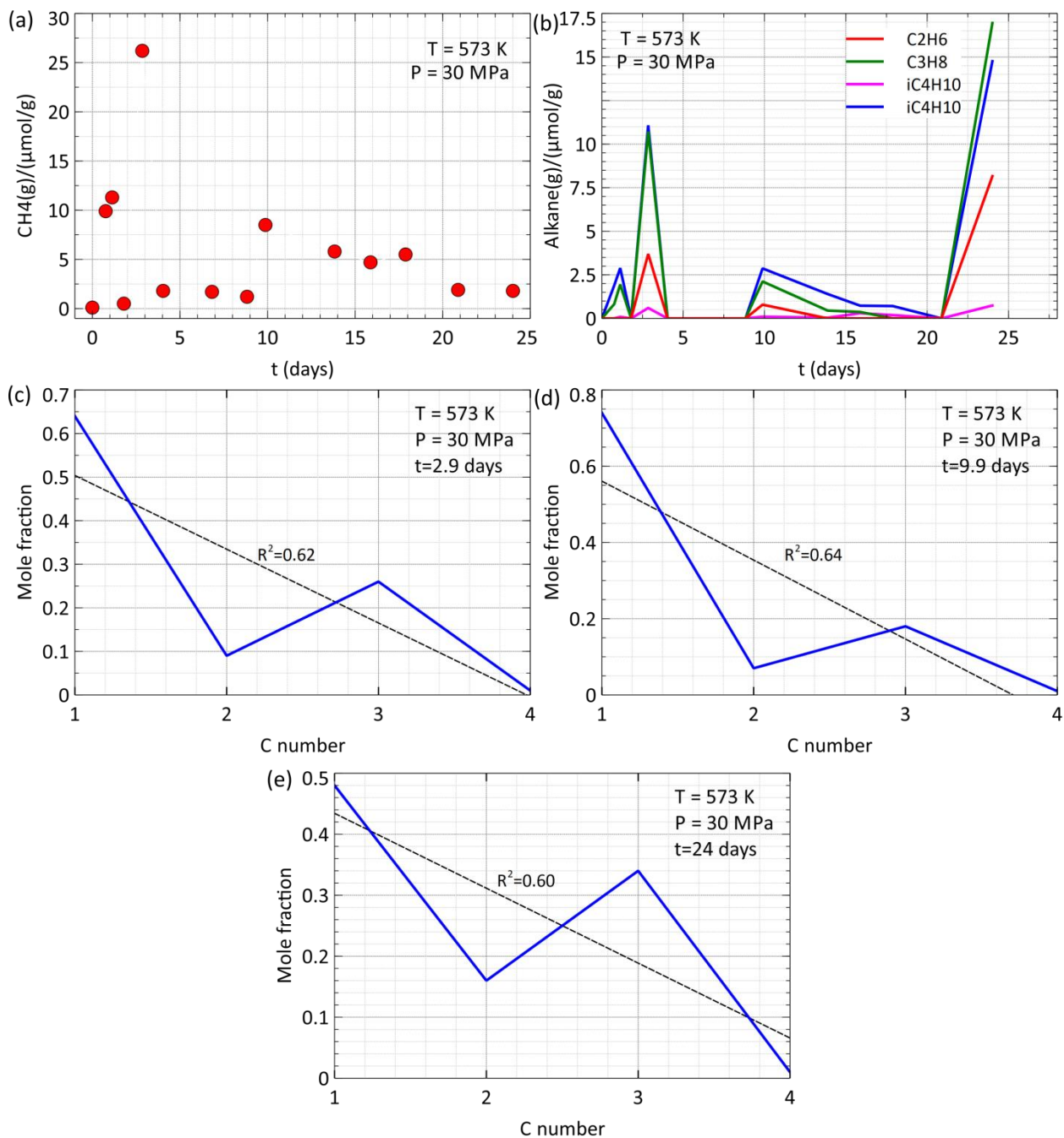


Figure 4-8. Measured hydrocarbons in the experiment conducted at 573 K and 30 MPa (a) variation of measured methane as a function of time; (b) variation of C2-C4 alkanes as a function of time; Schulz-Flory distribution of the alkanes measured at (c) $t = 2.9$ days; (d) $t = 9.9$ days; (e) $t = 24$ days.

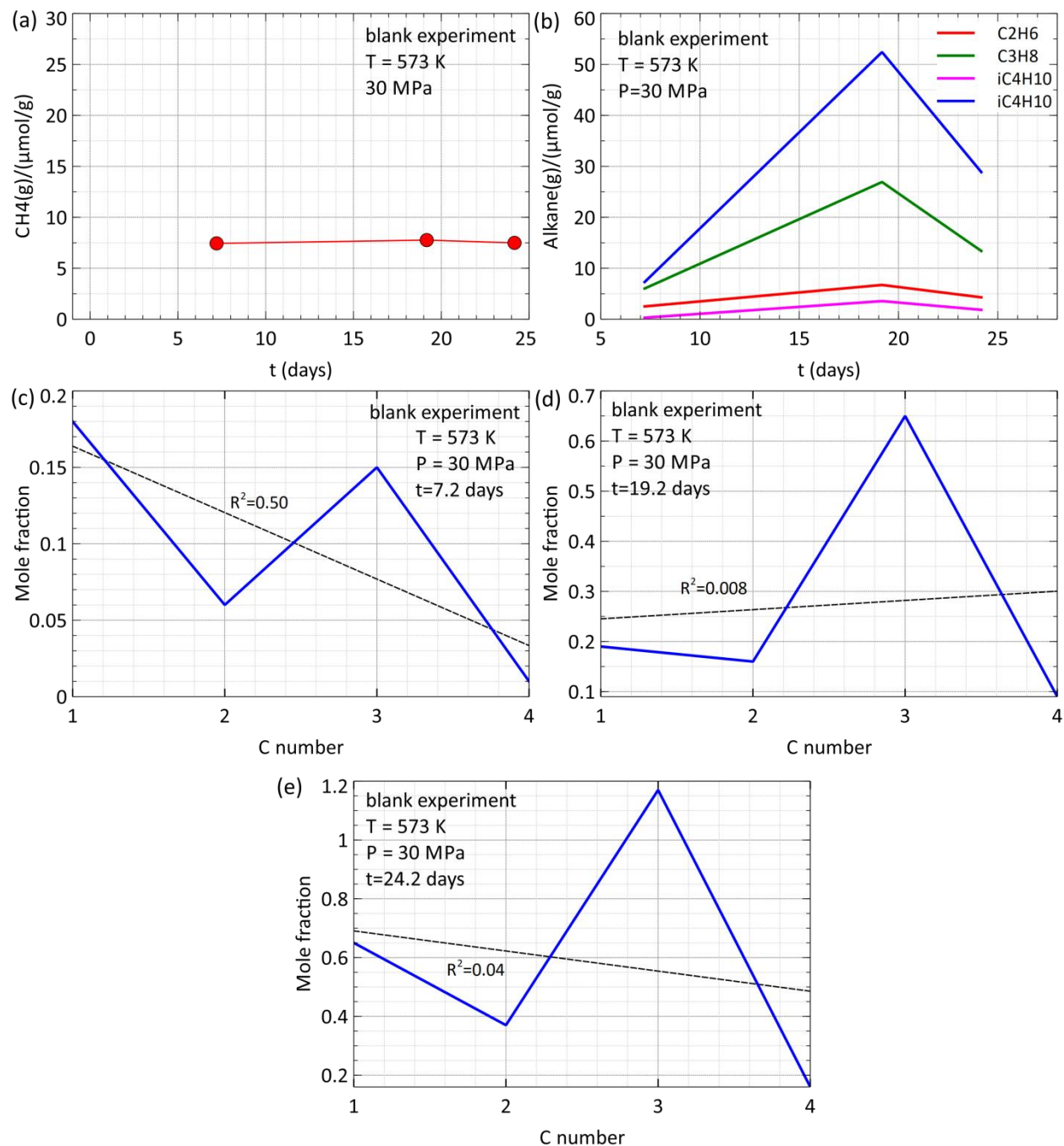


Figure 4-9. Measured hydrocarbons in the blank experiment conducted at 573 K and 30 MPa (a) variation of measured methane as a function of time; (b) variation of C₂-C₄ alkanes as a function of time; Schulz-Flory distribution of the alkanes measured at (c) t=7.2 days; (d) t=19.2 days; (e) t=24.2 days. The $R^2 < 0.90$ in the above plots indicate a thermogenic origin of methane (Etiope and Sherwood Lollar, 2013).

Table 4-6. Calculation of mole fractions for Schulz-Flory plots. The expected abundance of C1>C2>C3>C4 was not observed due to higher production of C1 and C3, causing C3>C2.

Experiment MT2 (523 K/ 30 MPa)						1	2	3	4
$\mu\text{mol/g}$						mole fraction			
t (days)	C1	C2	C3	C4	total	C1	C2	C3	C4
11.7	4.82	0.41	0.59	0.04	5.86	0.82	0.07	0.10	0.01
13.7	12.33	4.01	1.93	0.36	18.63	0.66	0.22	0.10	0.02
Experiment MT4 (573 K/ 30 MPa)									
$\mu\text{mol/g}$						mole fraction			
t (days)	C1	C2	C3	C4	total	C1	C2	C3	C4
2.85	26.19	3.7	10.72	0.6	41.21	0.64	0.09	0.26	0.01
9.88	8.47	0.79	2.12	0.1	11.48	0.74	0.07	0.18	0.01
24.01	24.14	8.16	16.95	0.74	49.99	0.48	0.16	0.34	0.01
Blank MT2b (523 K/ 30 MPa)						1	2	3	4
$\mu\text{mol/g}$						mole fraction			
t (days)	C1	C2	C3	C4	total	C1	C2	C3	C4
19.17	2.42	1.67	7.28	0.81	12.18	0.41	0.28	1.24	0.14
24.17	3.81	2.05	8.37	1.17	15.4	0.20	0.11	0.45	0.06
Blank MT4b (573 K/ 30 MPa)									
$\mu\text{mol/g}$						mole fraction			
t (days)	C1	C2	C3	C4	total	C1	C2	C3	C4
7.21	7.44	2.51	6.02	0.3	16.27	0.18	0.06	0.15	0.01
19.17	7.76	6.72	26.92	3.55	44.95	0.19	0.16	0.65	0.09
24.17	7.49	4.29	13.39	1.84	27.01	0.65	0.37	1.17	0.16

4.3.2.4 Precipitation of magnesite and other secondary phyllosilicates

The XRD pattern of mine tailings before and after reaction with CO₂ saturated water at hydrothermal conditions, showed the precipitation of magnesite and secondary phyllosilicates upon disappearance of olivine (Figure 10). Fe-rich magnesite was the main alteration product in all the experiments.

Secondary phases formed at 473 K/ 15 MPa: At 473 K/ 15 MPa, the magnesite was precipitated as anhedral aggregates of crystals of 10-20 μm as shown by figure 11a and b. Two FIB sections were cut on this sample as shown in the two yellow lines on (figure 11a), labeled FIB section 1 and 2. The FIB section 1 was cut along the glass-phyllsilicate contact, whereas FIB section 2 is cut along the glass-magnesite contact.

Glass-phyllsilicate contact: Figure 11c and d, shows the TEM analysis performed on the FIB section cut through glass-phyllsilicate contact. Although the CHES thermodynamic calculation showed that the solution remained undersaturated (-but near equilibrium) with respect to amorphous silica; an amorphous silica layer was observed between the glass and the phyllsilicate layer (figure 11c). A magnified image of the same view area showed that the phyllsilicate consists of four layers; two dense and two "porous". The chemical composition of glass and the phyllsilicate layers were analyzed by TEM-EDX (annex 4-1). The phyllsilicate III has a different chemical composition compared to the other phyllsilicates. It is Fe rich (48.46 wt%) but poor in Mg, Si, Al compared to the other three phyllsilicates. Compositionally, the phy III represents a typical Fe-rich nontronite ($\text{Na}_{0.3}\text{Fe}_2\text{Si}_4\text{O}_{10}(\text{OH})_2 \cdot 4\text{H}_2\text{O}$), and this result agrees with the XRD analysis. Sodium (Na) was not detected by TEM EDX, because it is a light element. The other phyllsilicates (phy I, II, IV) has a chemical composition close to vermiculite ($\text{Mg}_{0.7}(\text{Mg}, \text{Fe}^{3+}, \text{Al})_8(\text{Si}, \text{Al})_8\text{O}_{20}(\text{OH})_4 \cdot 8\text{H}_2\text{O}$), however, presence of vermiculite was not detected by the XRD analysis of the solid product.

Glass-magnesite contact: Figure 11e and f, shows the TEM analysis performed on the FIB section cut through glass-magnesite contact. Glass in contact with magnesite contained elongated olivine crystals embedded in it. The glass and magnesite boundary was marked by a thin (ca. 0.2 μm) phyllsilicate layer and the magnesite grain near this boundary seemingly stressed as shown by the arrows (figure 11e,f). The composition of this phyllsilicate layer is similar to the composition of phy I, II, and IV that we observed in above mentioned glass-phyllsilicate contact (figure 11c), and therefore the composition is close to a vermiculite ($\text{Mg}_{0.7}(\text{Mg}, \text{Fe}^{3+}, \text{Al})_8(\text{Si}, \text{Al})_8\text{O}_{20}(\text{OH})_4 \cdot 8\text{H}_2\text{O}$). The TEM-EDX analysis of magnesite, phyllsilicate, olivine and glass are given in supplementary annex 4-2. Based on the TEM-EDX analysis, the composition of magnesite was estimated to be $\text{Mg}_{0.92}\text{Fe}_{0.08}\text{CO}_3$.

Secondary phases formed at 523 K/ 30 MPa:

At 523 K/ 30 MPa, almost all the iron rich magnesite crystals observed under microscopy were, 20-40 μm rhombohedral crystals containing compositional zoning (figure 12). SEM element mapping shows the alternation of Mg and Fe concentrations in these zones.

However, in the solution, Mg concentration was approximately constant with one peak concentration after 8 days of reaction. In contrast, the Fe concentration in the solution highly fluctuated during the experiment and also could explain the zoning in precipitated magnesite. FIB-TEM analysis of the solid product showed the presence of a thin phyllosilicate layer between the glass and magnesite, similar to the glass-magnesite contact of the solid product of 473 K/15MPa experiment (Figure 4-13b). Chromite (Cr₂O₃) crystals of ~100 nm were embedded in the phyllosilicate layer (Figure 4-13(c)). These crystals should be present in traces since they were not detected in the XRD analysis of bulk sample. In addition, needle-like crystals of Fe-oxide were precipitated in the phyllosilicate layer very close to the contact with magnesite (Figure 4-13(d)). These crystals were 100 -200 nm in length and occurred as an aggregate. Similar to chromite, iron oxides were not detected by the XRD analysis of the bulk solid sample, but observed under SEM analysis.

Secondary phases formed at 573 K/ 30 MPa:

At 523 K/ 30 MPa, the precipitated Fe rich magnesite was 30-40 µm anhedral crystals with serrated edges resembling rhombohedral cleavages (figure 14a and b). These crystals were mostly surrounded by phyllosilicate with a highly disordered-proto serpentine (figure 14c). Most of the glass in this sample was heavily altered into fibrous proto-serpentine. Fe oxide crystals were found disseminated along the boundary of glass and proto-serpentine. Some other altered glass grains contained bulk precipitations of iron oxide along the boundary between glass and proto-serpentine (figure 14d).

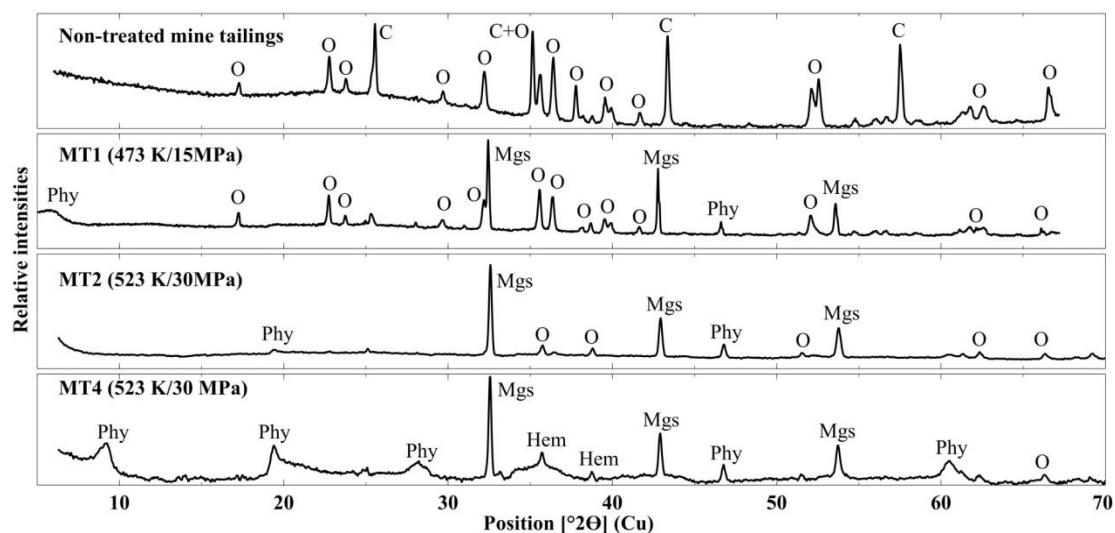


Figure 4-10. XRD pattern of mine tailings before and after reaction with CO₂ saturated water at hydrothermal conditions, showing precipitation of magnesite and secondary phyllosilicates upon disappearance of olivine. The abbreviations are (O=olivine, Mgs=magnesite, Phy=phyllosilicate, Hem=hematite).

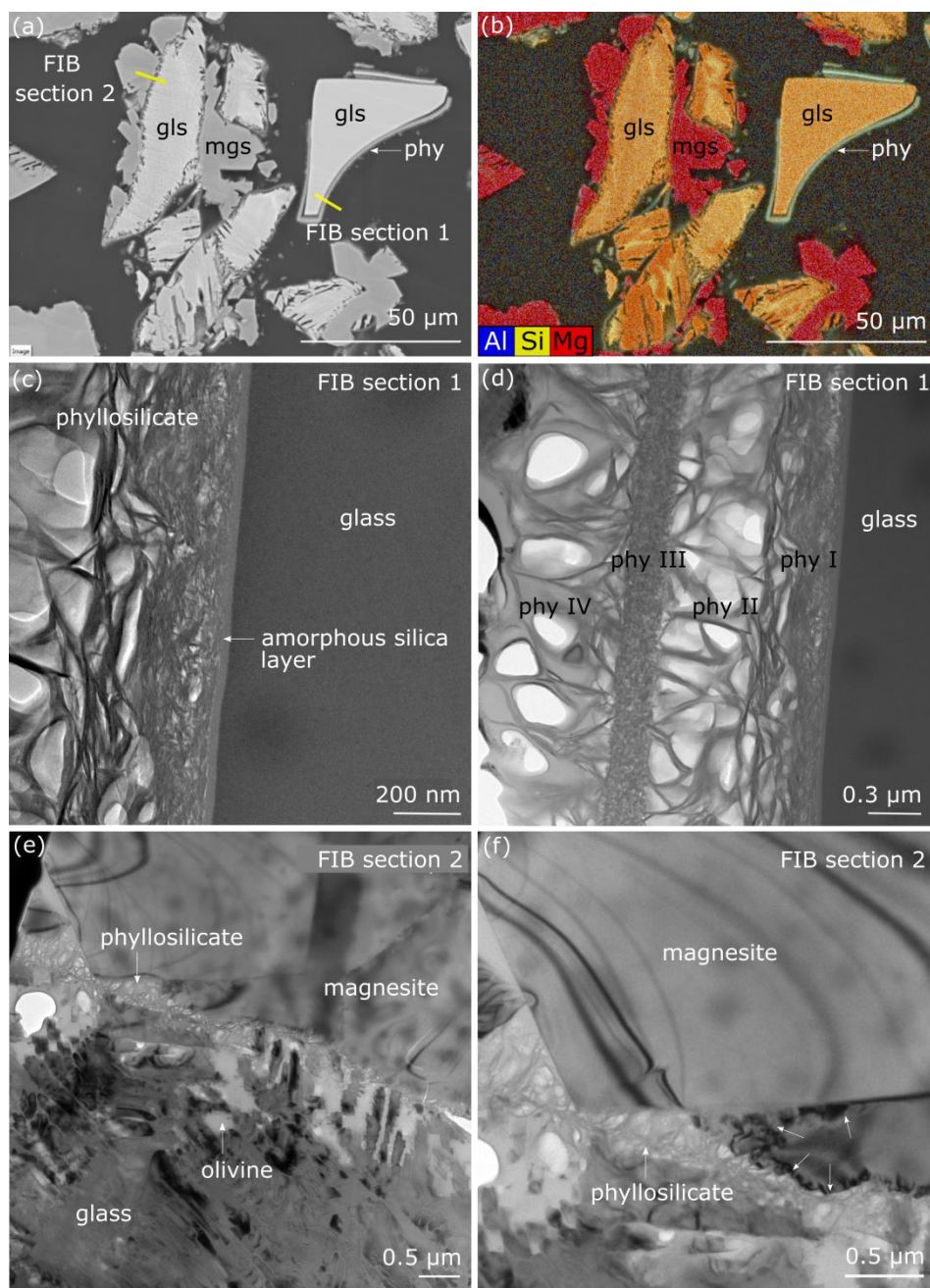


Figure 4-11. The solid product of MT1 experiment (a) SEM image of the polished section. Two FIB sections were cut along the two yellow lines shown on the image; (b) SEM element mapping on the same image (a), color coded blue, yellow and red representing Al, Si, and Mg respectively; (c) TEM image showing the analysis performed on the FIB section 1 cut along the glass-phyllosilicate contact which consist an amorphous silica layer; (d) A magnified image of the same area as figure (c) showing discrete phyllosilicate layers which are dense or porous. Compositionally they are either vermiculite (ver) or nontronite (non); (e) TEM image showing the analysis performed on the glass-magnesite contact. The glass consists of unreacted olivine which is embedded in it. A thin phyllosilicate layer marks the boundary between glass and magnesite; (f) enlarged view of the same image (e) showing a perfectly crystalline magnesite grain and a deformed magnesite grain in the right hand side of the image.

Table 4-7. TEM-EDX analysis of secondary phases shown in 11d (from MT1 experiment). The element concentrations are reported in mass%. The chemical composition of Phy I, II and IV, is close to vermiculite ((Mg_{0.7}(Mg, Fe³⁺, Al)₈(Si, Al)₈O₂₀(OH)₄·8H₂O)). The Phy III, which contains small amount of Mg (~2 mass%) , and higher Fe (~48 mass%), is compositionally close to nontronite (Na_{0.3}Fe₂Si₄O₁₀(OH)₂·4H₂O).

Element	Glass	Phy I	Phy II	Phy III	Phy IV
Mg	35.18	12.29	12.27	2.11	11.96
Al	2.87	12.79	12.35	11.13	13.29
Si	45.57	43.64	50.28	27.99	52.95
Cr	1.22	4.54	4.62	8.85	5.22
Mn	0.86	0.42	na	0.09	0.27
Fe	14.29	12.70	12.25	48.46	10.89
Ni	na	13.62	8.22	1.37	5.42
Total	100.00	100.00	100.00	100.00	100.00

Annex 4-8. TEM-EDX analysis of secondary phases shown in 11e (from MT1 experiment). The element concentrations are reported in mass%.

Element	Magnesite	Phyllosilicate	Olivine	Glass near Ol
Mg	82.83	15.93	47.18	31.63
Al	na	15.44	na	9.63
Si	na	50.74	35.76	39.28
Cr	na	5.42	1.44	3.5
Mn	na	na	na	na
Fe	17.17	12.46	15.62	15.96
Ni	na	na	na	na
Total	100.00	100.00	100.00	100.00

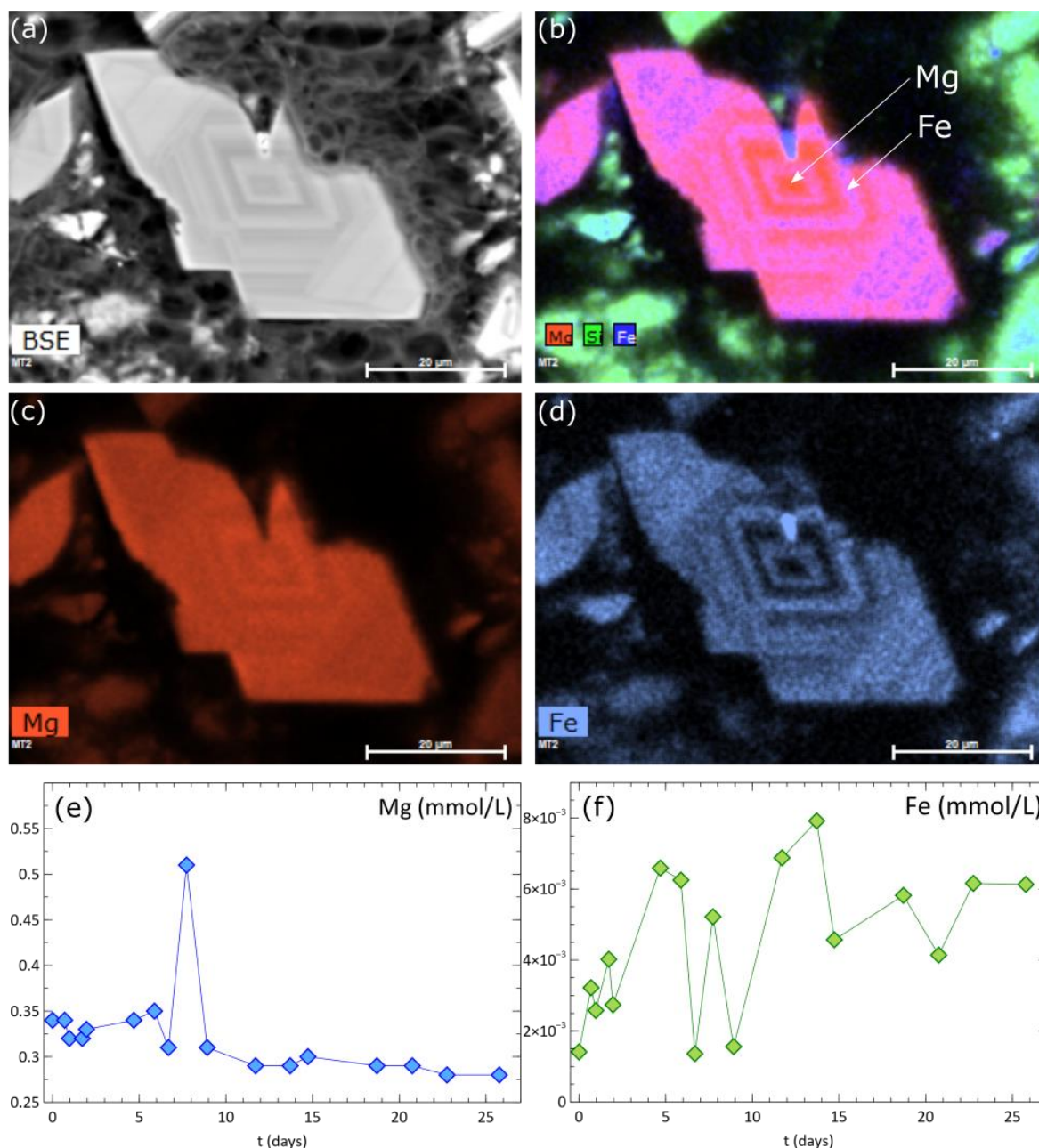


Figure 4-12. Magnesite precipitated at T=523 K/ 30 MPa experiment (a) SEM back scattered electron image showing a rhombohedral magnesite crystal with strong zoning; (b) Fe, Mg superposed element mapping of the magnesite crystal shown in image (a). Note that the core of the magnesite crystal consists Mg, instead of Fe reported in most of the studies; (c) element mapping of Mg; (d) element mapping of Fe; (e) Variation of aqueous Mg concentration in the solution; (f) Variation of aqueous Fe concentration in the solution.

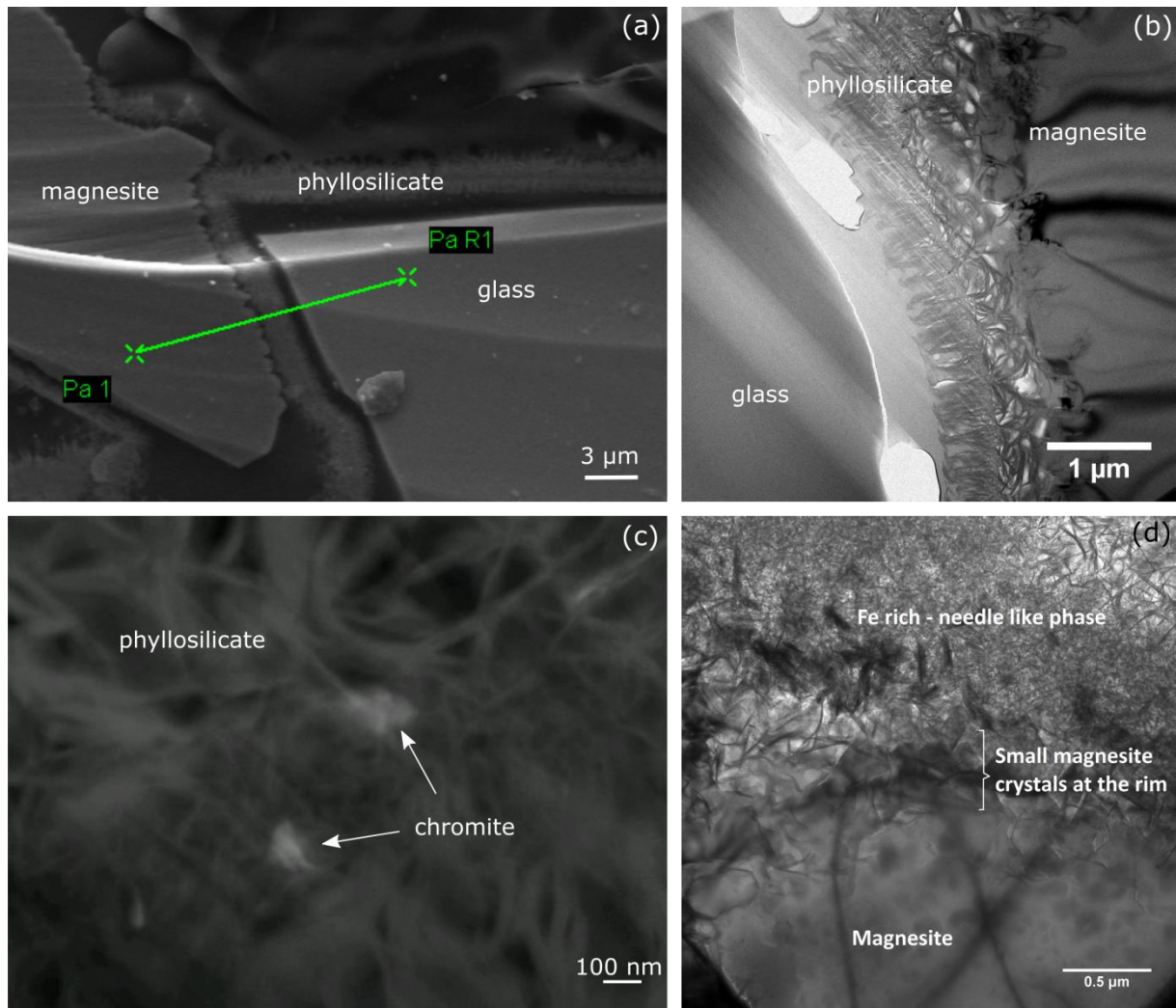


Figure 4-13. The solid product of T=523 K/ 30 MPa experiment (a) SEM image of the polished section in which a FIB section was cut along the green line shown on the image; (b) TEM image of the FIB section showing the contact between glass and phyllosilicate. The phyllosilicate layer has been mechanically detached from the glass and held by the epoxy resin as seen also in (a); (c) chromite crystals precipitated within the phyllosilicate later; (d) Fe rich needle-like phase precipitated at the boundary between magnesite and phyllosilicate contact.

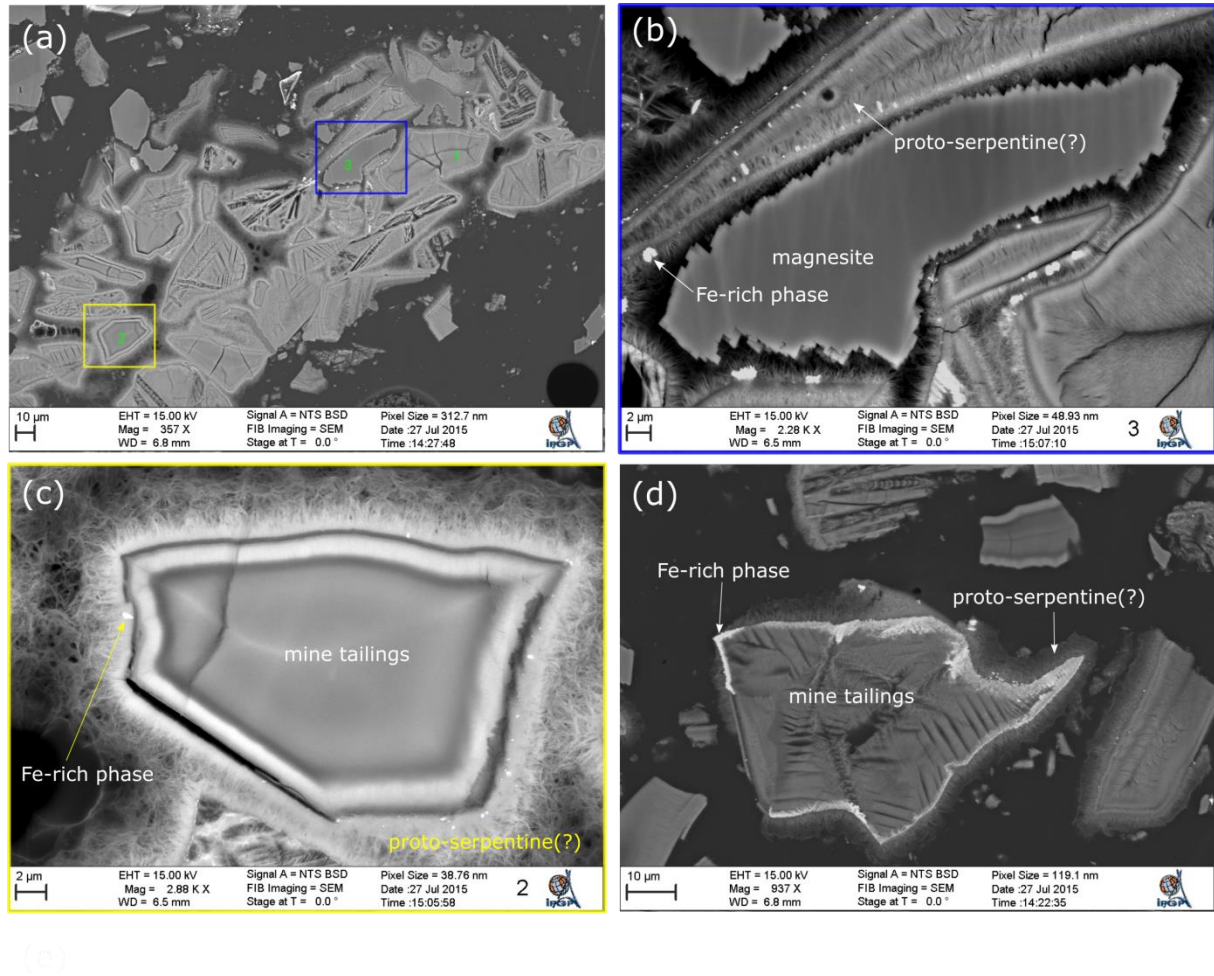


Figure 4-14. SEM images of run product of T=573 K/ 30 MPa experiment showing (a) a low magnified image of the run product showing precipitated anhydrous magnesite grains (eg. Blue square) and highly altered mine tailings (eg. yellow square); (b) the magnesite grain shown by blue square in (a), which is an anhydrous grain with rhombohedral edges; (c) highly altered mine tailings with proto-serpentine; (d) iron oxide precipitation along mine tailings.

4.4 Discussion

The main goal of this work was to find the reactivity of mine tailings compared to its natural analogue, olivine, and to investigate its reaction pathways which is crucial to understand the capacity of mine tailings as a feedstock for CO₂ storage and hydrogen production. Numerous processes and routes involving these two processes at ambient to hydrothermal conditions have been previously proposed in the literature providing important insights on implementing these reactions in sufficiently large scale industrial processes to mitigate rising CO₂ levels and alternate method of producing hydrogen. However, the core of these reactions is defined by the fundamental geochemical processes: (1) silicate dissolution, (2) precipitation of secondary silicates and carbonates (3) redox reactions producing hydrogen. In the following subsections we discuss these three processes in the context of the study's various experimental conditions, and finally their global implications.

4.4.1. Reactivity of mine tailings vs. olivine

Our first short term experiment showed the temperature dependence of mine tailings carbonation at constant pCO₂=30 MPa, for 2 days (figure 2a). The results demonstrated that no carbonates precipitation occurred at 363 K, but up to 2.0 wt.% magnesite precipitation was observed when the temperature was increased up to 523 K. In contrast to this observation, the CHES thermodynamic modeling indicated that the dissolution of olivine is thermodynamically favorable at 363 K, saturating the solution with respect to magnesite consequently precipitating it. The calculation was performed for 0.9 g of olivine to represent actual content of olivine in 2.0 g of mine tailings used for experiment, assuming a closed system of 250 ml of water, pCO₂=283 bar, equivalent to the conditions of batch reactor we used. As a result, our findings indicate that, even though the precipitation of magnesite is thermodynamically favorable at 363 K, this temperature is not sufficient to overcome the strong kinetic barrier for magnesite precipitation in this system. This result is in complete agreement with the previous study by Sissmann et al (2013), who observed ~1 wt.% of carbonation by reacting olivine (Fo88) with CO₂-saturated water at 363 K/ 28 MPa, even after 3 weeks of reaction period. In contrast, carbonate precipitation upon dissolution of olivine at 368 K/ ~9 MPa and 363 K/ 15 MPa, has been previously observed by Giammar et al (2005) and Gerdemann et al (2007) respectively, where the former used solutions of 0.01-0.5 M NaHCO₃ and 0.01-0.25 M MgCl₂ solutions of pH 5-6, whereas the latter used a solution of 0.63 M NaHCO₃ and 0.1 M NaCl solution of pH ~8. The magnesite precipitation at observed at 363 K in these two previous studies therefore indicate the strong dependence of pH on magnesite precipitation over the kinetic barrier, due to the stability of carbonates at alkaline pH compared to acidic pH conditions. In addition, based on this experiment, the temperature of long term experiments were chosen to be 473 K, 523 K and 573 K, in order to observe carbonate precipitation and hydrogen production which is favored at T~573 K.

Our second short term experiment conducted on 0-45 µm fraction of mine tailings and olivine, at 523 K/30 MPa reacted for 2,4 and 6 days showed that olivine precipitates more magnesite compared to mine tailings when reacted under similar conditions (figure 2b). In addition, the figure 2b also showed that olivine reaches its maximum theoretical carbonation

of 74 wt.% within 6 days of reaction whereas mine tailings reach 28 wt.% of carbonation, which is less than half of its theoretically calculated carbonation capacity of mine tailings (77 wt.%), and slightly lower than the calculated carbonation capacity of olivine in mine tailings (33.6 wt.%). Olivine is the natural analogue to mine tailings and here we used it as a model mineral. Thus, any difference in reactivity of mine tailings should arise from the additional mineralogical, chemical or structural features in mine tailings. Compared to pure olivine, mine tailings contained 55 wt.% of glass, which mainly provided a matrix in which hosted olivine, creating a dendritic texture. We believe strongly that the attenuated reactivity of mine tailings is a result their slow dissolution compared to pure olivine. Our results imply that glass dissolved slowly compared to olivine, decreasing the mean dissolution rate of mine tailings, which subsequently limited carbonate precipitation. Previous studies have shown that the crystallinity could largely govern the rate of dissolution at far from equilibrium conditions (Power et al. (2013) and references therein). Gislason and Oelkers (2003) and Wolff-Boenisch et al. (2006) reported that dissolution of glass was approximately two orders of magnitude faster than compositionally similar crystalline equivalents. Although we are lacking experimental results for dissolution of glass (contained in mine tailings of this study), which seemed to have a composition close to pyroxene, it clearly dissolved slower than olivine (contained in mine tailings). Furthermore, our results are in line with previous findings of Bodénan et al (2014), who conducted direct carbonation of New Caledonian mine tailings (similar to present study). They showed that at 90 MPa, mine tailings react with demineralized water to precipitate 2.18 wt.% of magnesite within 24 hrs, which is approximately similar to what our experiments would yield if the line going through the data (figure 2b) is extrapolated to 24 hrs reaction duration. The study of Bodénan also showed that mine tailings would precipitate slightly more magnesite (5.97 wt.%) when it was reacted with a NaCl/NaHCO₃ solution at 10 MPa for 24 hrs. However, their findings significantly differ from previous results reported for Mount Keith nickel mine tailings of western Australia, which could store only ~1.95 wt.% of hydromagnesite within 70 days by reacting with atmospheric CO₂ and moisture, according to simulations (Wilson et al., 2014).

These contradictions in carbonate yields between olivine and mine tailings could arise due to the differences in their dissolution rate. Both olivine and mine tailings are rich in Fe, Mg, and their dissolution is the first step during which these divalent cations Mg²⁺ and Fe²⁺ are released to the solution. The rate of dissolution of silicates depends on two main factors. The first is the differences in mineralogical composition of mine tailings and olivine. The second is the effect of secondary layers which act as passivating layers slowing down the dissolution of mine tailings (section 4.1.1). In addition, the reactivity of mine tailings could also be lowered by secondary phases which act as passivating layers (section 4.1.2).

4.4.1.1 Effect of crystal structure on dissolution rate

Mineral dissolution may be rate-limiting for certain carbon mineralization strategies such as ex-situ mineral carbonation and its applications in industrial reactors as well as the hydrogen producing reactions (Crouzet et al., 2017; Power et al., 2013). There are two major types of bonds in common rock-forming silicates; the metal-oxygen (M-O) bonds and the

silicon-oxygen bonds (Si-O). As summarized in the review by Power et al. (2013), the dissolution rate of a mineral is related to the strength of M-O bonds (controlled by cation size and co-ordination number) and, in the case of silicate minerals, the degree of silica polymerization. The destruction of the slowest-breaking M-O bond that is essential to the crystal structure (typically, the shortest and strongest bond) is the rate-limiting step for dissolution (Schott et al. 2009). Under acidic conditions, the rate of metal-oxygen bond breakage in common silicate minerals generally decreases with increasing metal ion valence from monovalent to trivalent (Oelkers 2001). The Si-O bond is typically the strongest bond in the structure of a silicate mineral and is consequently the slowest to break. The relative difference in Si-O and M-O bond strength may lead to non-stoichiometric dissolution and the development of Si-rich layers that may passivate the reactive surface, potentially slowing dissolution (Luce et al. 1972; Pokrovsky and Schott 2000a; Béarat et al. 2006; Jarvis et al. 2009; Schott et al. 2009, 2012). Dissolution rates tend to decrease with increasing silica polymerization which is defined by the average number of Si-O-Si bonds in a crystal structure (given by Q_i ; Brantley 2008a). Orthosilicates (also known as nesosilicates), such as forsterite, are completely unpolymerized (Q^0) and will therefore tend to dissolve more rapidly than pyroxenes (Q^2), such as diopside and enstatite, and phyllosilicates (Q^3), such as serpentine group minerals like chrysotile (Schott et al. 2009). Similarly, the rate of brucite dissolution is orders of magnitude greater than that of Mg-silicate minerals, as it lacks the strong Si-O bonding (e.g., Bales and Morgan 1985; Pokrovsky and Schott 2004). Due to the comparatively weak Ca-O bond, Ca-silicates tend to dissolve at faster rates than Mgsilicates for a given connectedness (Brantley 2003; Schott et al. 2009). The crystallinity (i.e., extent of long-range structural order) of the solid also influences its rate of dissolution. For instance, Gislason and Oelkers (2003) and Wolff-Boenisch et al. (2006) documented that dissolution of glassy rocks was approximately two orders of magnitude faster than compositionally similar crystalline phases. The crystal chemistry of feedstock for carbon mineralization may therefore determine the method of artificial acceleration that should be employed. In this study, as described above, the reactivity of mine tailings has been largely impeded by the presence of glass, which might consequently have affected the dissolution rate of mine tailings. The glass has pyroxene composition and therefore, it appears that the dissolution of this glass is slower than crystalline olivine in mine tailings.

4.4.1.2 Effect of secondary phases on dissolution rate

Depending on their chemistry, the secondary phases could passivate the reaction surfaces of the primary minerals slowing down their dissolution rates. For example, the secondary phases such as amorphous silica with Si-Fe³⁺ or those with porosity clogged by Fe³⁺ phases are known to act as passivating layers around olivine (Sissmann et al., 2013), whereas those without Fe³⁺ has only a minor passivation effect (Daval et al., 2009b). The amorphous silica layer observed in our experiments at 473 K/ 15 MPa, however seemed to have a negligible effect on dissolution of mine tailings, as hydrogen continued to produce throughout the experiment (figure 4a). Similarly, the secondary phyllosilicates formed at 523 K/ 30 MPa, do not have a significant passivating effect on dissolution of mine tailings, due to the same reason (figure 4b). However, at 573 K/ 30 MPa, the phyllosilicates and the Fe-oxide

phases seemed to passivate the reactive surface slowing down the dissolution of mine tailings after ~9 days of reaction (figure 4c, figure 13 c and d).

4.4.2 Mine tailings carbonation and hydrogen production

The goal of our long-term experiments was to determine whether mine tailings could be carbonated while producing hydrogen simultaneously. In contrast to our short term experiments, we analyzed gas and liquid samples from the on-going long-term experiments and finally we conducted a detailed mineralogical analysis on run products to study the gas-water-rock interactions at the nanometric scale.

The results of liquid analysis and the thermodynamic modeling of the three experiments showed many noteworthy features regarding the dissolution of mine tailings (tables 3, 4 and 5). Firstly, the solutions of all three experiments contained more silica ($\text{SiO}_{2(\text{aq})}$) compared to $\text{Mg}_{(\text{aq})}$, and traces of aqueous Fe, Ca, Al, Na, and K. This result indicates non-stoichiometric release of cations with respect to the primary silicates, and thus suggests preferential incorporation of Mg into secondary minerals compared that of Si. In these experiments Mg is hosted mainly by the newly precipitated Fe-rich magnesite which is the major phase in all run products, and by Mg-bearing phyllosilicates. In contrast, Si is hosted only by the phyllosilicate which is a minor phase in all the experiments, and traces of amorphous silica precipitated only at 473 K/ 15 MPa. Secondly, the Mg/Si ratio calculated for these experiments were far from those estimated for congruent dissolution of olivine, indicating mine tailings dissolved incongruently. However, for olivine carbonated at 363 K/ 28 MPa, previous studies, using CO₂-saturated water with and without organic ligands (Daval et al., 2011a; Sissmann et al., 2013) and NaHCO₃/MgCl₂ solutions of pH~5 (Giammar et al., 2005), have reported more Mg in the solution compared to SiO₂, as well as near congruent dissolution of olivine. The high Mg content in solution of these three results were therefore due to lower incorporation of Mg in the secondary phases as they reported extremely smaller (0-1.0 wt.%) amounts of magnesite, while Si is reported to be largely precipitated as amorphous silica, thus resulting in low silica concentrations in the solutions, at T~363 K. In these previous studies, no crystalline secondary phases have been observed under XRD analysis of run product. In contrast, the higher temperatures and presence of Al, Na, K in our experiments have limited the formation of amorphous silica and promoted the precipitation of hydrous aluminosilicates. This supports previous findings by Bodéan (Bodéan et al., 2014) on carbonation of mine tailings (from New Caledonia similar to present study), who reported the formation of crystalline secondary silicate phases such as proto-serpentine, using an alkaline NaHCO₃/NaCl solution over CO₂-saturated water, at 453 K/ 1 MPa.

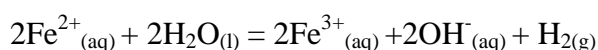
The CHESS thermodynamic modeling of our experiments showed that the dissolution of olivine (Fo) and precipitation of magnesite (MgCO₃) are thermodynamically favored at the conditions of our experiments. In the following subsections, we discuss the effect of solution chemistry, thermodynamic modeling and secondary phases on the carbonation and hydrogen production particularly at each P/T condition studied; we finally put forward a possible chemical reaction.

4.4.2.1. At 473 K/ 15 MPa

The reaction of mine tailings with CO₂-saturated water at 473 K/ 15 MPa, resulted in Fe-rich magnesite (major phase) and phyllosilicate (minor), producing hydrogen (figure 4). No iron oxide phases were observed within the run product. We discuss below the precipitation of magnesite, production of hydrogen, precipitation of secondary silicates and finally the overall reaction.

Precipitation of iron rich magnesite: Fe-rich magnesite was precipitated when the solution reached saturation with respect to magnesite (MgCO₃), as showed by the thermodynamic model (figure 3a). Being the major phase in the run product, Fe-rich magnesite (Mg_{0.92}Fe_{0.08}CO₃) hosted almost all the Fe²⁺ released by the dissolution of mine tailings. According to figure 5a, the large anhedral grains of magnesite formed along the grains of mine tailings could potentially act as a passivation layer and diminishing the reactive surface area slowing down the dissolution of mine tailings.

Hydrogen production: Our results showed that hydrogen was produced continuously throughout the experiment, during which a maximum of 20 µmol per gram of mine tailings was produced. Hydrogen was likely produced through the redox reaction involving Fe²⁺ and water :



It showed that a maximum of 20 µmols of Fe³⁺ contained in the run product; however, we were unable to quantify the Fe³⁺ in our run products. If Fe³⁺ occurred as an iron oxide phase (such as magnetite), it would be approximately <0.05 wt.% and thus not detectable by XRD. On the other hand Fe³⁺ could also have been accommodated by the phyllosilicates (discussed below).

Precipitation of amorphous silica: Amorphous silica in the run product was observed only under FIB-TEM analysis as a thin layer between mine tailings (glass), and secondary phyllosilicate layer (discussed below). According to our solubility calculations, the aqueous solution never reached the saturation with respect to amorphous silica throughout the reaction duration (figure 3a). This result is consistent with one of the experiments (Fo-150) of Saldi et al. (2013), in which amorphous silica was found to precipitate between olivine and magnesite, whereas in other cases, surface coatings of amorphous silica have been documented (Daval et al., 2011b; Sissmann et al., 2013). Moreover, according to the figure 3d, it seems that the amorphous silica layer has been precipitated as a result of dissolution of mine tailings, followed by rapid incorporation of Mg into magnesite and phyllosilicate leaving behind a Si-rich layer.

Precipitation of nontronite and vermiculite: The major phyllosilicate formed in this experiment was Na-nontronite, which is an iron rich-smectite group clay mineral, a common alteration product of mafic and ultramafic rocks (eg. basalt in deep sea hydrothermal vents). In addition, a phyllosilicate close to vermiculite were observed in FIB-TEM analysis of the run product (figure 5d). Though it was not possible to definitely identify the cause of

alternating layers of dense nontronite and more porous Al-rich vermiculite observed in Figure 11d, these observations suggest distinct precipitation events, during which dissolution-precipitation reactions or Mg-leaching from the vermiculite could occur to release Mg into solution available for carbonation, leaving a thin Mg-poor Fe-nontronite behind. Such a contribution of the glass phase to carbonation yield would still remain negligible compared to olivine dissolution.

Overall reaction mechanism: There are several possible reaction paths that would result in magnesite and the phyllosilicates discussed above, via the reaction between CO₂-saturated water and mine tailings. First, we could summarize the overall reaction according to the mineral phases observed (and not taking into account the stoichiometric relations);

Mine tailings + water + CO₂ = (Fe, Mg)CO₃ (ferroan-magnesite) + Na_{0.3}Fe₂Si₄O₁₀(OH)₂·4H₂O (nontronite) + Mg_{0.7}(Mg, Fe³⁺, Al)₆(Si, Al)₈O₂₀(OH)₄·8H₂O (vermiculite) + SiO₂ (amorphous silica) + H₂ (hydrogen)

where, amorphous silica and vermiculite are present in traces. As mafic rocks such as basalt alters into nontronite at deep sea hydrothermal vents, there is a high probability that this reaction also occurs in our experimental conditions.

Secondly, by carefully observing the magnesite-phyllosilicate contact showed in figure 11e and d, one can also see that the Mg-bearing phyllosilicate layer has undergone the carbonation. The magnesite grains in figure 5d contained serrated grain boundaries indicating strain during its growth. The results point to the likelihood that the reaction given above could also be an overall reaction consisting two steps; first, the serpentinization and then the carbonation of serpentinization products.

Mine tailings + water = (Mg,Fe,Al)₃Si₂O₅(OH) (serpentine) + (Mg,Fe)(OH)₂ (brucite) + Fe₃O₄ (magnetite) + H₂ (hydrogen)

(Mg,Fe,Al)₃Si₂O₅(OH) (serpentine) + Fe₃O₄ (magnetite) + O₂ + HCO₃⁻ = Na_{0.3}Fe₂Si₄O₁₀(OH)₂·4H₂O (nontronite) + Mg_{0.7}(Mg,Fe³⁺,Al)₆(Si,Al)₈O₂₀(OH)₄·8H₂O (vermiculite) + (Fe, Mg)CO₃ (ferroan-magnesite) + OH⁻ + H₂O

At high HCO₃⁻ activity and more oxidizing conditions, the latter reaction could completely mask the existence of serpentinization products (depending on the reaction kinetics and thermodynamic stability of the phases). A similar reaction has been previously reported by Abu-Jaber and Kimberly (1992), investigating the genesis of ultramafic hosted magnesite vein deposits.

However, they reported that this reaction occurred at the shallow depths (near surface), at low P/T, in contrast to the hydrothermal P/T conditions of our study.

4.4.2.2. At 523 K/ 30 MPa

At 523 K/ 30 MPa, the CO₂-water-mine tailings interaction resulted in iron rich magnesite, vermiculite and hydrogen. In addition, chromite and a needle-like iron-rich phase were

identified on FIB-TEM analysis, though quantitatively they remain below the detection limit of XRD analysis. Production of each phase is discussed below; a possible reaction mechanism is finally suggested.

Precipitation of iron rich magnesite: Fe-rich magnesite precipitated even though the solution remained slightly undersaturated with respect to pure magnesite (MgCO₃), as showed by the thermodynamic model (figure 3b). Similar to the above experiment (MT1), being the major phase in the run product, Fe-rich magnesite (Mg_{0.58}Fe_{0.42}CO₃) hosted almost all the Fe²⁺ released by the dissolution of mine tailings. Figure 4-13a and b, clearly showed the presence of a phyllosilicate between glass and magnesite at 523K. This strongly suggests that the phyllosilicate could be an intermediary phase formed through the alteration of glass, and subsequently carbonating into magnesite. The contribution of glass to the overall carbonation mechanism would nevertheless remain negligible compared to olivine, as is suggested by the composition of the run products. According to figure 12 and 1b, the large rhombohedral magnesite crystals containing compositional zoning of Fe and Mg were characteristic to this experiment. Interestingly, this observation was correlated with the fluctuation of iron content in the solution, while Mg_(aq) was apparently stable throughout the course of the experiment (figure 12e and f). Apart from the two well-known theories for compositional zoning, which are: (1) end-members of the solid solution having solubilities differ by orders of magnitudes (Saldi et al, 2013 and references therein), and (2) end-members having significantly different growth rates (Saldi et al, 2013 and references therein), supply of Fe via an anomalous dissolution of mine tailings, could also explain the compositional zoning. However, the reasons behind the formation of perfect rhombohedral magnesites with compositional zoning at 523 K/ 30 MPa, remain unclear. This type of magnesite formation has been documented previously based on experiments (Saldi et al, 2013; olivine carbonation at 423 K/10 MPa) and based on field studies (Lindahl and Nilsson, 2008).

Hydrogen production: Hydrogen was produced continuously throughout the experiment, reaching a maximum of 117 µmol per gram of mine tailings. Similar to the experiment at 473 K/15 MPa, it is very likely that the redox reaction of Fe²⁺ and water produced hydrogen. The maximum hydrogen production of 117 µmols/g accounts to approximately <1.0 wt.% of Fe³⁺ and thus not detectable by XRD. However, the presence of iron-rich needle like phase was detected under FIB-TEM analysis, which could be a possible host of Fe³⁺. In addition, vermiculite could also accommodate Fe³⁺ in the structure.

Precipitation of vermiculite: Vermiculite precipitation is likely during the alteration of mafic rocks under hydrothermal conditions. We did not observed interstratified structure of vermiculite in this sample. We were also unable to model the vermiculite saturation using the chess thermodynamic database, since the vermiculite data is not present.

Overall reaction mechanism: According to all the secondary phases observed during the reaction between CO₂-saturated water and mine tailings, we could qualitatively write the following overall reaction;

Mine tailings + water + CO₂ = (Fe, Mg)CO₃ (ferroan-magnesite) + Mg_{0.7}(Mg, Fe³⁺, Al)₆(Si, Al)₈O₂₀(OH)_{4.8}H₂O (vermiculite) + Fe oxide (Fe_xO_y) + chromite (Cr₂O₃) + H₂ (hydrogen)

where iron oxide and chromite were present in traces.

4.4.2.3. At 573 K/ 30 MPa

At 573 K/ 30 MPa, the CO₂-water-mine tailings interaction resulted in iron-rich magnesite, nontronite, hematite, proto-serpentine and hydrogen. Production of each phase will be discussed below and finally we propose a possible reaction mechanism.

Precipitation of iron-rich magnesite: Fe-rich magnesite was precipitated even though the solution remained slightly undersaturated with respect to magnesite (MgCO₃), as showed by the thermodynamic model (figure 3c). Similar to all previous experiments, Fe-rich magnesite was the major phase in the run product (Mg_{0.83}Fe_{0.17}CO₃) and hosted almost all the Fe²⁺ released by the dissolution of mine tailings. According to figure 14a and b, where magnesite seems to grow independently surrounded by phyllosilicates, the carbonates seem to have mostly precipitated directly from the solution, while only a minority may be due to the carbonation of phyllosilicates.

Hydrogen production: Hydrogen was produced continuously until 9 days of reaction, reaching a maximum of 283 μmol per gram of mine tailings followed by a plateau of ~50 μmol/g. Similarly to all previous experiments, the redox reaction involving water and Fe²⁺ released upon dissolution of mine tailings is responsible for the production of hydrogen. The above mentioned maximum hydrogen production accounts to approximately 2.6 wt.% of Fe³⁺. In the run product, the main Fe³⁺-bearing phase was detected as hematite (Fe₂O₃) by XRD. Therefore the iron-rich phase observed in figure 14d could be hematite. It is interesting to note that the iron oxide (figure 14d) precipitated along the grain of mine tailings could potentially act as a passivating layer, limiting the carbonation and production of hydrogen.

Precipitation of nontronite and proto-serpentine: In this experiment, the XRD analysis of bulk run product indicated the presence of nontronite whereas FIB-TEM analysis showed the presence of proto-serpentine in this sample. As both serpentine and nontronite are typical alteration products of hydrothermal alteration of mafic minerals, mostly basalt, it is very likely that both of these minerals are formed, but only nontronite is present in quantities large enough to detect under XRD.

Overall reaction mechanism: According to all the secondary phases observed during the reaction between CO₂-saturated water and mine tailings, we could qualitatively write the following overall reaction;

Mine tailings + water + CO₂ = (Fe, Mg)CO₃ (ferroan-magnesite) + Na_{0.3}Fe₂Si₄O₁₀(OH)_{2.4}H₂O (nontronite) + proto-serpentine + Fe oxide (Fe_xO_y) + H₂ (hydrogen)

where proto-serpentine was present in traces.

4.4.3 Methane production

Our results showed that methane was produced at 473 K and 15 MPa, while C1-C4 alkanes were produced at 523 K and 573 K at 30 MPa. The two blank experiments conducted under 523 K and 573 K at 30 MPa also contained C1-C4 alkanes confirming that light hydrocarbons are most likely a contamination but at 573 K at 30 MPa. It is widely accepted that the abiotic production of methane in this type of hydrothermal systems via Fischer-Tropsch type (FTT) reactions needs catalysts for the activation of C-H bond formation (McCollom, 2013). In natural environments, certain minerals could act as such catalysts. In our experiments even though a catalytic mineral has not been introduced on purpose, the traces of chromium (Cr), or nickel (Ni) bearing phases contained in mine tailings have the ability of catalyzing such reactions (Foustoukos and Seyfried, 2004; Horita and Berndt, 1999). The Schulz-Flory distribution of hydrocarbons in Figures 6 to 9, which compare the actual experiments with blanks, suggest a noteworthy difference in the C1-C4 concentration trends. This could reflect the formation of abiotic hydrocarbons (mixed with hydrocarbons contamination, as the trends are not perfect; however, the R^2 factor still goes up to 0.85). It could be observed from (Figure 4c), that the hydrogen production increased gradually as a function of time and then decreased instantly. The composition of gas phase showed that this sudden decrease is not correlated to possible dilution of the gas phase due to the re-injection of CO₂ into batch reactor followed by sampling out gas phase. Although it is not clear exactly the why hydrogen content decreased drastically, such a decrease followed by stabilization could explain the consumption of hydrogen for abiotic methane or dissolved short-chain Carbon compounds formation, and then hydrogen reaching the equilibrium with methane production. Even though, the calculations show that the hydrogen in C1-C4 alkanes does not account for the large drop of hydrogen concentration, other reduced carbon compounds such as volatile fatty acids could indeed have formed in water, that were not quantified in this study.

4.5 Conclusions

In this chapter we have presented the water-rock interactions occurring during simultaneous carbonation and hydrogen production, by reacting New Caledonian mine tailings in CO₂ saturated water at hydrothermal conditions. The results of our short-duration studies suggest that mine tailings could be carbonated efficiently at high temperatures >473 K, although its reactivity is lower compared its natural analogue, olivine. It is very likely that the pyroxene glass in mine tailings have a lower solubility compared olivine, which negatively affected the overall reactivity kinetics of mine tailings. The results of our long term experiments suggest that mine tailings could be carbonated simultaneously producing substantial quantities of hydrogen, by reacting with CO₂-saturated water at acidic pH ~4. Mine tailings were mainly altered into Fe-rich magnesite and Mg-rich phyllosilicates such as, nontronite and vermiculite. Although there is CO₂ and hydrogen and potential minerals which could act as catalysts for FTT synthesis (eg. Chromite and iron oxide), hydrocarbons were not formed during the reaction, or in negligible amounts. At 473 K/ 15 MPa, Mg-rich magnesite precipitation occurred due to carbonation of Mg-rich phyllosilicates, whereas at 523 K/30

MPa and 573 K/30 MPa, Mg-rich magnesite seemed to precipitate directly from the solution. Finally, we have proposed a qualitative overall reaction for mine tailings alteration at 473 K/15 MPa, 523 K/30 MPa and 573 K/30 MPa based on the phases present in the final products.

Nevertheless, this study enhances our understanding of reactions take place at the mineral-water interfaces down to nanometric scale during the interaction of CO₂-saturated water with mine tailings. It also emphasizes the necessity of mineralogical analysis of primary materials which are being used as feedstocks for ex-situ CO₂ storage and hydrogen production at the industrial scale, in order to understand their reactivity.

This chapter has been published in Applied Geochemistry (appendix IV)

Chapter 5

Laboratory simulation of abiotic hydrocarbon
production: investigating the role of iron and
zinc sulfides

Abstract

Hydrogen and abiotic hydrocarbons-rich fluids have been reported in deep sea mid-oceanic-ridge (MOR) hydrothermal systems and some continental settings, where serpentinization is prominent. These hydrocarbons are thought to form via Fischer-Tropsch type synthesis (FTT), which is a highly catalytic process, by which inorganic carbon species are converted into organic compounds. In natural geological settings, this reaction was thought to be catalyzed by the transition-metal bearing minerals associated with serpentinization and hydrothermal vents. Several minerals such as magnetite (Fe_3O_4), awaruite (Fe_3Ni) and chromite (Cr_2O_3) have been suspected. A recent study by (Shipp et al., 2014), reported that sphalerite (ZnS) catalyzes the C-H bond formation, using synthetic sphalerite and organic compounds that are far from those present in geological environments. In this work, we attempted to study the ability of sphalerite and marcasite (FeS_2) to catalyze abiotic hydrocarbon formation, especially at the conditions relevant to natural geological environments.

We conducted hydrothermal experiments at 573 K and 30 MPa using gold (Au) capsules pressurized in autoclaves. Fe(II)-rich silicates (forsterite ($\text{Mg}_{1.8}\text{Fe}_{0.2}\text{SiO}_4$), fayalite (Fe_2SiO_4) and chamosite ($(\text{Fe}^{2+})_5\text{Al}(\text{AlSi}_3\text{O}_{10})(\text{OH})_8$)), were reacted with a 0.64 M NaHCO_3 solution, to produce hydrogen (H_2) within the capsules by Fe^{2+} oxidation. To test their catalytic effect, we introduced either sphalerite or marcasite in the capsules. Nine mineral assemblages (Fe-rich silicate±catalyst) were tested. All the minerals were finely powdered in order to increase the kinetics of the reaction, by increasing the effective surface area. After ~20 days of reaction, the gases extracted from these capsules were analyzed to study if any hydrocarbons were formed by the reaction between H_2 with CO_2 , or HCO_3^- within the capsules. In addition, the liquid extracted from the capsules was also studied to detect any soluble organic compounds formed as intermediary products of the FTT reaction.

After reaction, C1-C4 alkanes were formed in all the capsules. Methane (CH_4) was present in all the samples with concentrations <0.5 mmol/L (background carbon contamination ~0.1-0.3 mmol/L). We also observed that conversion rates (in %) of inorganic carbon (CO_2 , or HCO_3^-) into alkanes ($\text{C}_1\text{-C}_4$) in our experiments were extremely low (<0.25%). The Schulz-Flory distributions of produced alkanes in all these experiments were far from those expected for abiotic hydrocarbons. Although carbon and hydrogen mass balance indicated possible formation of other organic compounds than gaseous phases, dissolved organic compounds were not formed in detectable quantities. The results suggest that the synthesis of abiotic hydrocarbons by the Fe,Zn-sulfide-catalyzed FTT synthesis maybe limited in the hydrothermal systems at 573 K and 30 MPa. Despite its inability to catalyze FTT synthesis of hydrocarbons, our results do suggest that sphalerite may potentially catalyze the hydrogen production at the studied P/T and pH conditions.

Key words: Abiotic hydrocarbons, Fischer-Tropsch type synthesis (FTT), hydrogen, hydrothermal, mid oceanic ridge, serpentinization, dissolved organics, methane

5.1 Introduction

Understanding the pathways leading to the formation of abiotic hydrocarbons is important in a wide range of scientific fields, such as petroleum exploration to explain the formation of abiotic hydrocarbons in reservoir (Guo et al., 1997; Jenden et al., 1993; Kutcherov and Krayushkin, 2010; Szatmari, 1989), global carbon cycle (Manning et al., 2013), but also in planetary sciences to explain origin of methane (CH₄) in Mars, Titan and Enceladus (Krasnopolsky, 2006; Krasnopolsky et al., 2004; Levin and Straat, 2009; Mousis et al., 2009; Tobie et al., 2006). More interestingly, the formation of abiotic hydrocarbons on Earth is a crucial question for understanding the origin of life on Earth, since answering it could explain the key mechanisms leading to the appearance of precursor carbon molecules (Etiope et al., 2011). In the past decades, hydrocarbons with an abiotic origin have been widely reported in fluids venting from hydrothermal systems along mid oceanic ridges (Charlou et al., 2013, 2002; Konn et al., 2009; Petrova et al., 2009; Proskurowski et al., 2008; Schmidt et al., 2007; Von Damm, 2001). These fluids are hot (90 - 350 °C), mineral-rich, and essentially rich in hydrogen (2-16 mmol/L), formed through interactions between aqueous fluids and mafic/-ultramafic systems during hydrothermal circulation and serpentinization of olivine ((Mg,Fe)₂SiO₄), creating highly reducing conditions favorable for reduction of inorganic carbon, present as magmatic CO₂, or dissolved HCO₃²⁻ in sea water.

The Fischer-Tropsch synthesis (FTT) is the most widely invoked pathway for the formation of hydrocarbons and other organic compounds in natural environments (McCollom, 2013). This process refers to the surface-catalyzed reduction of CO by H₂ in gas mixtures, typically at temperatures of 150-300°C and pressures of ~1 MPa. It has been widely applied in the industrial synthesis of hydrocarbons where gaseous CO and H₂ were reacted in the presence of synthetic catalysts (transition metals including Ru, Co, Fe), obtaining ~90-100% conversion rates. However, more generally in Earth Sciences, the term “Fischer-Tropsch-type” synthesis (FTT) is used to describe the conversion of an inorganic carbon source into organic compounds in nature, where the process is suspected to be catalyzed by transition metal-containing minerals (McCollom, 2013). Large number of potential catalyst minerals exists in the nature and the most efficient mineral phases have yet to be defined. Another important concern is the medium in which the FTT synthesis takes place. In contrast to the industrial process, natural processes occur in water dominated environments where the carbon sources mostly exist in the dissolved form CO_{2(aq)} or HCO₃⁻_(aq).

Recent laboratory experiments have shown that the FTT production of hydrocarbons occur under hydrothermal conditions by reacting CO or HCOOH and water at 175°C-250°C and at 25 MPa, without any solid phases (McCollom et al., 1999; McCollom et al., 2010; McCollom and Seewald, 2006). Methane, and even long chain alkanes, alkanols, and alkanoic acids formed in this study showed a decrease in the abundance with increasing carbon number, which is characteristic for FTT synthesis (McCollom and Seewald, 2006). These experiments thus showed that FTT synthesis is not inhibited under hydrothermal conditions. In his review, McCollom (2013) pointed out that the synthesis in these experiments were probably catalyzed either by native-Fe included in the reaction vessel, or

by the walls of the steel tube used for some of the experiments; therefore these experiments do not necessarily represent catalysts present in natural environment. In addition, these experiments do not demonstrate adequately whether the reaction took place in the liquid phase, vapor headspace or whether H₂-rich vapor bubbles formed within the reactor. The first experimental investigation of FTT catalysis at conditions similar to natural serpentinization systems was that of Berndt et al. (1996), who reported on the production of C₁-C₃ alkanes with a Schulz-Flory distribution, during the serpentinization of olivine at 300°C and 50 MPa, in an Au-Ti flexible reactor with no gas headspace. Magnetite (Fe₃O₄), formed during serpentinization, was proposed to be the catalyst for the FTT synthesis. Their experimental results demonstrated that the FTT synthesis can occur in the presence of water and natural minerals (eg. magnetite), which can catalyze the synthesis. Later, McCollom and Seewald (2001) used a ¹³C labeled NaHCO₃ solution to show that, except for a small fraction of methane, hydrocarbons were not produced by the reduction of introduced carbon source via FTT synthesis at the conditions of Berndt's experiment but by the maturation of organic C from contamination, initially present in the starting material. McCollom (2013) also highlighted that, even though these experiments were conducted at thermodynamic conditions strongly favorable for the reduction of dissolved CO₂ into CH₄ (high temperature of 300 °C, high hydrogen availability of 158 mmol/kg), only a small fraction of carbon was reduced into methane (<<1%) even after three months of reaction, which clearly demonstrates that the production of methane could be kinetically extremely sluggish even at 300°C. In addition, the lack of significant hydrocarbon production suggests magnetite is not an efficient catalyst for FTT synthesis of hydrocarbons in geological systems. In contrast, a study by Horita and Berndt (1999) showed the ability of Ni-Fe alloy to synthesize high concentrations of CH₄ alone, with conversion rates of >40% at 200°C and almost 100% at 300°C. These rates are higher than what Berndt et al (1996) observed. The concentration of H₂ in Horita and Berndt (1999) experiments was high: 170-300 mmol/kg. Their results provided the first documentation that kinetic inhibitions to the reduction of dissolved CO₂ to CH₄ could be effectively overcome by naturally occurring minerals, and that Ni-Fe alloy was a very effective catalyst in promoting the reaction (McCollom, 2013). However, Fe-Ni sulfides appear to produce lower quantities of CH₄ with lower conversion rate of inorganic carbon into organic carbon. The experimental study by Fu et al. (2008) evaluated the catalytic potential of pentlandite (Fe, Ni sulfide: (Fe,Ni)₉S₈), using ¹³C-labeled HCOOH (providing both H₂ and carbon source) at 400°C and at 50 MPa. Only micromolar concentrations of C₁-C₃ alkanes with a <0.01% conversion of dissolved CO₂ was achieved after several weeks of reaction. On the other hand, recent study by Shipp et al. (2014) showed that sphalerite (ZnS) could significantly catalyze the formation of C-H single bonds. The experiments were conducted at 300°C and at 100 MPa in gold capsules, using *trans*- or *cis*-dimethylcyclohexane and water as the reactants. In the presence of sphalerite, the reaction led to one major product: the corresponding stereoisomer (Shipp et al., 2014). In the absence of mineral, the reaction was extremely slow and generated multiple products. In contrast to sphalerite, their experiments with Fe-sulfide resulted in extremely complex products, at sluggish rates.

First, we examined the catalytic potential of several oxides (magnetite and chromite) and sulfides (chalcocite pyrite, pyrrhotite and sphalerite), by reacting nano-Fe-rich forsterite

powder mixed with a potential catalyst in a $\text{NaH}^{13}\text{CO}_3$ solution at 200 bar, 200°C during 3 weeks. Significant quantities of methane were produced in the presence of sulfide minerals compared to oxide minerals, indicating that sulfides could be better catalysts than oxides. (Martinez et al., 2017). In this PhD, we aim to examine the catalytic potential of sphalerite (ZnS) and marcasite (FeS_2) essentially at the conditions similar to natural geological settings. This would allow to compare the catalytic potential of marcasite with that of sphalerite, as well as to revisit the experiment of Shipp et al. (2014), at conditions relevant to natural systems.

5.2 Materials and methods

5.2.1 Starting materials

Three iron-rich natural silicates were used for the *in-situ* production of hydrogen within the reactor via hydrothermal oxidation of Fe^{2+} (olivine, fayalite, and chamosite). Olivine from San Carlos (Arizona, USA) was obtained from Wards mineral company. The crystals were green, transparent to translucent and contained traces (~1%) of enstatite (MgSiO_3) and iron oxides, which were not removed during the sample preparation. The composition of olivine determined from electron probe micro analysis (EPMA) and XRD was $\text{Mg}_{1.8}\text{Fe}_{0.2}\text{SiO}_4$. Natural fayalite (Fe_2SiO_4) samples (Bellerberg, Germany) were obtained from Mikon mineral company, and these were gray color polycrystalline samples that contained abundant magnetite (Fe_3O_4) as an impurity. Magnetite contained in the sample was removed using a hand magnet during the preparation, Natural chamosite (iron end-member of the chlorite group (with a general endmember composition of $(\text{Fe}^{2+})_5\text{Al}(\text{AlSi}_3\text{O}_{10})(\text{OH})_8$) was obtained from Wards mineral company. Sphalerite (ZnS) was obtained from Vladivostok, Russia. The sphalerite samples were crushed and powdered using an agate mortar and pestle and sieved to obtain the <40 μm grain size fraction. Marcasite samples (Reims, France) was obtained from Wards mineral company. The samples were black color translucent to opaque crystals with fresh surfaces, and powder X-ray diffraction analysis confirmed the chemical composition to be FeS_2 .

The samples were crushed and powdered using a ball mill (FRITSCH Planetary Micro Mill PULVERISETTE 7 premium line) to obtain <20 μm grain size fraction, or using agate mortar and pestle when samples were present in small quantity (eg; fayalite). The chemical composition of the above minerals obtained by microprobe analysis and their specific surface areas (SSA), obtained by the Kr adsorption analysis Brunauer–Emmett–Teller (BET) method (Brunauer et al., 1938), are given in the Table 5-1.

Carbon was introduced in the form of a 0.64 mol/L $\text{NaHCO}_{3(\text{aq})}$ solution. The solution was prepared using analytical grade pure NaHCO_3 (99.9%, Sigma-Aldrich) powder dissolved in de-ionized water (18.2 $\text{M}\Omega\text{ cm}$), bubbled with nitrogen gas ($\text{N}_{2(\text{g})}$) for approximately 2 hours to eliminate most of the dissolved oxygen.

The starting materials were loaded into cylindrical gold capsules of 30 or 35 mm and outer diameter of 5 or 6 mm (wall thickness of 0.2 mm). The capsules were initially cleaned by dipping them into a 6 M hydrochloric (HCl) acid solution overnight followed by heating at

700 °C in a high temperature furnace for about 10 min to remove any contamination. The capsules were loaded with a Fe-bearing mineral (100 mg of olivine, fayalite or chlorite), a sulfide mineral (10 mg of sphalerite or marcasite) and a 0.64M NaHCO₃ (200 µL), and were then welded shut in an inert atmosphere (N₂). For each Fe-bearing mineral, three capsules were prepared: one with only the Fe-bearing mineral, the second with the Fe-bearing mineral and sphalerite, and the third with the Fe-bearing mineral and marcasite. The capsule without sphalerite or marcasite is the “blank”, used to compare the effect of the sulfide mineral on the hydrocarbon production. A summary of these experiments is given in Table 5-2. The capsules were welded using a Lampert PUK4.1 arc welding machine equipped with 0.5 mm Pt electrodes. Once the capsules were welded, they were kept in an oven at 60°C overnight to test for leaks by taking into account the mass difference before and after heating. The capsules were then used for the HP/HT experiments.

Another set of experiments were performed to quantify the background carbon levels, and the details are given in section 5.2.3.

5.2.2 High pressure and high temperature experiments

The high pressure and high temperature experiments were conducted in a non-stirred Parr[®] Hastelloy autoclave, of volume 75 ml, pressurized by water and argon (Ar). The capsules were loaded into the autoclaves (with space for up to ten capsules in one reactor). The reactor was then half-filled with water and pressurized with argon (Ar) up to about 15 MPa. The autoclave was heated up to 573 K. The pressure inside the reactor increased upon heating and a final pressure of 30 MPa was reached by pumping the required amount of argon. The experiments were conducted for 20 days. After quenching the experiments, the capsules were weighed to confirm that they did not leak during the run. Gas analysis was performed on these samples as described in section 5.2.4.

5.2.3 Gas extraction and analysis

The gases produced in the capsules were extracted and analyzed using a method similar to Malvoisin et al. (2013). However, for convenience, a glass tube with a piercer needle was adapted for the analysis instead of plastic syringe (chapter 2, Figure 2-20). The extracted gases were analyzed using gas chromatography (GC) using a Varian CP-3800 gas chromatograph equipped with two TCD detectors and one FID detector (TCD=thermal conductivity detector; FID=field ionization detector), at IFPEN, Rueil-Malmaison. The detailed protocol of the gas analysis is given in chapter 2, section 2.2.5.

Table 5-1. Electron microprobe analysis of Fe-bearing silicates and sulfides.

Fe-bearing silicate composition given in oxide wt.%																
	NaO	MgO	SiO ₂	Al ₂ O ₃	CaO	TiO ₂	Cr ₂ O ₃	FeO	MnO ₂	CoO	NiO	ZnO	CuO	S	Total	SSA (m ² /g)
Olivine	0.01	47.99	41.95	0.16	0.11	0.01	0.07	9.34	0.15	0.03	0.36	-	-	-	100.19	0.82
Chlorite	0.00	0.75	37.16	20.74	3.06	0.06	0.02	38.46	1.16	0.06	-0.01	-	-	-	101.48	1.36
Fayalite	-	-	-	-	-	-	-	-	-	-	-	-	-	-	-	-
Composition of sulfide minerals given in element wt.%																
	Fe	Zn	Na	Ni	Cu	S	Total	SSA (m ² /g)								
Sphalerite*	2.44	64.87	-	0.025	-	32.36	99.65	1.00								
Marcasite*	45.88	2.79E-03	3.38E-03	-	1.34E-03	52.64	98.58	1.83								

*The compositions of sphalerite and marcasite is given in element wt.%.

Table 5-2. Summary of experiments. All the experiments were conducted using a 0.64 M NaHCO₃ at 573 K and 30 MPa for 20 days.

Experiment no#	Fe-bearing silicate (100 mg)	Sulfide mineral (10 mg)	Abbreviation
69	olivine	marcasite	Ol+M
66	olivine	sphalerite	Ol+S
65 (blank)	olivine	-	Ol
70	fayalite	marcasite	Fa+M
71	fayalite	sphalerite	Fa+S
67 (blank)	fayalite	-	Fa
73	chlorite	marcasite	Chl+M
72	chlorite	sphalerite	Chl+S
68 (blank)	chlorite	-	Chl

Table 5-3. Carbon contamination by the starting minerals. Total carbon contained in C₁-C₄ alkanes that were released during the heating of olivine, sphalerite, chlorite, fayalite and marcasite in individual gold capsules at 300°C and 30 MPa were calculated. This value was used to define a background contamination level for our experiments. Gas composition was analyzed by gas chromatography.

Mineral Exp No.	Olivine (#77)	Sphalerite (#88)	Chlorite (#79)	Fayalite (#78)	Marcasite (#81)
Composition of gas phase (μmol)					
He	0.16±0.01	0.26±0.14	0.18±0.09	0.18±0.08	0.13±0.05
H ₂	0.04±0.02	nd	nd	nd	nd
CH ₄	0.04±0.00	0.02±0.00	0.03±0.00	0.03±0.00	nd
CO ₂	1.85±0.02	0.25±0.00	1.15±0.00	1.15±0.00	0.99±0.00
O ₂	3.69±0.00	1.00±0.03	2.92±0.07	2.93±0.07	1.06±0.02
N ₂	11.31±0.24	11.74±0.12	10.94±0.09	10.96±0.09	15.13±0.11
C ₂ H ₆	7.53E-03±0.06	nd	nd	nd	nd
C ₃ H ₈	1.18E-03±0.01	nd	nd	nd	nd
i-C ₄ H ₁₀	8.86E-04±0.08	nd	nd	nd	nd
C ₃ ?	nd	nd	1.30±0.00	nd	nd
Total C* (μmol)	0.06±0.00	0.02±0.00	0.03±0.00	0.03±0.00	nd
Total C* (mmol/L)	0.28±0.00	0.01±0.00	0.12±0.00	0.13±0.00	nd

*Total C= sum of carbon contained in the C₁-C₄ alkanes

Table 5-4. Carbon contamination in the mineral assemblages, calculated based on the GC data reported in Table 5-3.

Composition ^a	Ol	Ol+M	Ol+S	Fa	Fa+M	Fa+S	Chl	Chl+M	Chl+S
Total C (mmol/L)	0.28±0.00	0.28±0.00	0.29±0.00	0.13±0.00	0.13±0.00	0.14±0.00	0.12±0.00	0.12±0.00	0.13±0.00

^aabbreviations : Fa=fayalite, S=sphalerite, M=marcassite, Chl=chlorite, Ol=olivine (Fo90)

5.2.4 Estimation of carbon contamination

Carbon contamination by the starting minerals was estimated to define the background carbon contamination level in our experiments. Approximately, 1.0 g of Fe-bearing silicate (olivine, fayalite and marcasite), and 0.1 g of sulfide (sphalerite and marcasite) was individually reacted in gold capsules at 300°C and 30 MPa for approximately 4 hrs. Then, the gas phases of these capsules were analyzed using gas chromatography and the total carbon contained in the C₁-C₃ alkanes was obtained (Table 5-3). The quantity of total carbon that can be added by each mineral assemblage (olivine + sphalerite, olivine + marcasite, fayalite + sphalerite, fayalite + marcasite, chlorite + sphalerite, chlorite + marcasite) were also calculated (Table 5-4). These values were used as a threshold for background carbon introduced as part of the starting materials.

5.2.5 Schulz-Flory distribution

The Schulz-Flory distribution for the measured alkanes (C₁-C₄) in our experiments was tested. This distribution is used as a first order tool to determine the origin of HC's. The Schulz-Flory distribution is a molecular distribution of the hydrocarbon alkanes that is controlled by chain growth probability factor for abiotic stepwise polymerization where (C_(n+1)/C_n) is approximately constant (C_n is the concentration in mole units) (Etiope and Sherwood Lollar, 2013). A plot of the number of carbon atoms in the HC chain (1,2,3,...etc) versus the mole fraction of each hydrocarbons may be a good indication of FTT synthesis. It will give a linear correlation (straight line with a positive intercept), indicating a decrease of the mole fraction with increasing number of carbons in the hydrocarbons chain.

We calculated the Schulz-Flory correlation coefficient (r²), and the chain growth probability factor (α) for the plotted graphs. The r² is calculated from the linear regression of the experimental data. The origin of hydrocarbons is determined using this value, where thermogenic gas is typically characterized by r² < 0.9, while r² is > 0.9 for dominantly abiotic gas and > 0.99 for quasi-pure abiotic gas (Etiope and Sherwood Lollar, 2013). The hydrocarbon chain growth is predicted by the chain growth probability factor (α). Assuming that the chain growth probability is independent of the chain length, the polymerization is described by the Anderson-Schulz-Flory distribution:

$$P_n = \alpha^{n-1}(1 - \alpha) \quad [5-1]$$

where P_n is the probability of producing a hydrocarbon of length n (mole fraction). The distribution depends on α, which is the probability a chain will grow rather than desorb from the catalyst. αⁿ⁻¹ is the probability of adding (n-1) carbons, and (1-α) is the probability of not adding a carbon and therefore terminating chain growth. The expected chain length is given by:

$$\langle n \rangle = \sum n p_n = \frac{1}{(1-\alpha)}. \quad [5-2]$$

The weight fraction W_n = P_n (n/⟨n⟩) for each n is given by:

$$W_n = n\alpha^{n-1}(1 - \alpha)^2. \quad [5-3]$$

The maximum probability P_n with respect to α ($dP_n/d\alpha = 0$) occurs at $\alpha = (n-1)/(n+1)$ and is given by $P_n = 2/(n+1) \times (n-1/n+1)n-1$. A low value of α indicates a high probability of adding a carbon into the hydrocarbon chain.

5.2.6 Solid product analysis

X-ray diffraction analysis was performed on the recovered powder samples of these experiments (mostly from replicate experiments) after being oven-dried at 60°C. The acquisition was performed on an X'Pert PRO (PANalytical) X-ray diffractometer with a Cu anode (Cu K α = 1.5418 Å), operated under 45 kV and 40 mA. Then, the full powder patterns analysis were performed using XPert High ScorePlus software and the peak identification was done by peak-search-matching, using the available PDF database (Powder Diffraction File) of ICDD (International Center for Diffraction Data).

Scanning electron microscopy (SEM) was performed on a separate fraction of the reaction products, mounted on adhesive carbon-taped sample holders, gold (Au) coated and observed under “high vacuum” conventional SEM, EVO MA 10, Carl Zeiss SMT with a tungsten filament operated under 15 kV and 100 mA. A 150 pA beam was applied for secondary electron (SE) imaging to observe the surface topography with a high spatial resolution. The back scattered electron detector (BSE) was used to obtain images with atomic number contrast.

5.2.7 Liquid analysis

Replicate experiments were conducted using the same starting materials and following the methodology given in section 5.2.1 and section 5.2.2. The summary of these experiments was given in table 5-5.

The high performance liquid chromatography (HPLC) analysis was performed on the capsules of experiment #1, 2 and 3 (see Table 5-5). Instrumentation and analytical details of HPLC technique is given in chapter 2 (section 2.2.6.1). The analysis was performed at the Unité de Biologie Fonctionnelle et Adaptative (BFA), at University of Paris Diderot, using a Shimadzu HPLC system (Shimadzu, Kyoto, Japan), with a Supelco RP- C8 column (250 × 4.6 mm, 5 µm) (Sigma-Aldrich Corporation, Bellefonte, PA, USA), with a UV detector. After reacting at 300°C and 30 MPa, the capsules were recovered and opened using metal blades to extract the liquid. Each capsule was opened with a new blade cleaned with deionized water (DI water) to avoid contaminations. The liquid in the capsule (~200 µL) was extracted using a micropipette with changeable plastic tips. Then the extracted liquid was centrifuged and a 20 µL fraction of the centrifuged solution was injected into HPLC. The samples were injected at a pressure of 1-5 bar, which then passes through a column filled with a solid adsorbent material. Each component in the sample interacts slightly differently with the adsorbent material, causing different flow rates for the different components and leading to the separation of the components as they flow out the column.

Liquid state Nuclear magnetic resonance spectroscopy (NMR) analysis was performed on the capsules of experiment #4 (Table 5-5). Instrumentation and analytical details of NMR technique is given in chapter 2 (section 2.2.6.2). The analysis was performed at the department of Caractérisation matériaux, IFP Energies Nouvelles (IFPEN), Solaize. The liquid extraction from the capsules was performed using a new metal blade, similar to the method mentioned above. The extracted liquid was then dissolved in either water (D_2O) or chloroform ($CHCl_3$), a specific solvent used in NMR, which helps to locate the magnetic field homogeneously throughout the sample. Both 1H NMR and ^{13}C NMR analysis were performed on the samples.

Table 5-5. Summary of experiments conducted for the purpose of liquid analysis using HPLC and NMR methods. The capsules contained an iron rich mineral \pm catalyst (sphalerite or marcasite), reacted with water or 0.64 M NaHCO₃ solution at 573 K and 30 MPa for several days (as reported in Table 5-5).

Exp#	Composition ^a	Solution	t (days)
<u>Capsules used for HPLC analysis</u>			
<u>Experiment 1</u>			
1	Ol+M	DI water	5
2	Chl+M	DI water	5
3	Ol+S	DI water	5
4	Fa+S	DI water	5
5	Fa+M	DI water	5
6	Chl	DI water	5
7	Fa	DI water	5
8	Ol	DI water	5
-	Deionized water (blank)	-	-
<u>Experiment 2</u>			
20	Ol+M	0.64M NaHCO ₃	5
32	Chl+M	0.64M NaHCO ₃	5
36	Ol+S	0.64M NaHCO ₃	5
38	Fa+S	0.64M NaHCO ₃	5
40	Fa+M	0.64M NaHCO ₃	5
41	Chl	0.64M NaHCO ₃	5
43	Fa	0.64M NaHCO ₃	5
45	Ol	0.64M NaHCO ₃	5
<u>Experiment 3</u>			
47	Ol+S	0.64M NaHCO ₃	20
49	Chl+S	0.64M NaHCO ₃	20
51	Fa+S	0.64M NaHCO ₃	20
53	Ol+M	0.64M NaHCO ₃	20
56	Chl+M	0.64M NaHCO ₃	20
60	Ol	0.64M NaHCO ₃	20
61	Chl	0.64M NaHCO ₃	20
63	Fa	0.64M NaHCO ₃	20
-	Deionized water (blank)	-	-
<u>Capsules used for NMR analysis</u>			
<u>Experiment 4</u>			
75	Ol	0.64M NaHCO ₃	20
76	Ol+S	0.64M NaHCO ₃	20
77	Ol+S	0.64M NaHCO ₃	20

^aabbreviations : Fa=fayalite, S=sphalerite, M=marcassite, Chl=chlorite, Ol=olivine (Fo90)

DI water =deionized water.

5.2.8 Thermodynamic modeling

Thermodynamic modeling was performed using the CHESSE geochemical code (details are given in chapter 2, section 2.2.7). It was used to calculate the equilibrium concentration of organic species that could potentially form during the experiments. Using the CHESSE code we simulated the reactions taking place in each individual capsules. Input parameters similar to those used for the experiments were used: 200 mg of Fe-rich mineral (fayalite, olivine (Fo90) or chlorite), 10 mg of catalyst (sphalerite or marcasite), and 0.2 mL of NaHCO_3 solution (added as 0.64 mol/L Na^+ and HCO_3^{2-}). The reaction conditions were set to 573 K and at 30 MPa, and a closed system behavior (“batch”) was assumed. In this calculation, all the reactions between minerals and NaHCO_3 solution were enabled, including the two minerals sphalerite (ZnS) and marcasite (FeS_2). The calculations were performed using the eq36.tdb database that contains thermodynamic data of simple organic molecules. This calculation allows understanding (1) the equilibrium mineral assemblages, (2) the stability of sphalerite and marcasite at the reaction conditions in order to confirm if they chemically involved in the reaction (even though we observed these two minerals under XRD, we were unable to quantify them at the end of the experiment using XRD), (3) the types of organic molecules form at the equilibrium conditions (in order to compare with liquid analysis for dissolved organic compounds).

Several modifications in the database were needed to model the “exact” conditions of our experiments. The composition of olivine used in the experiment was Fo90 ($\text{Mg}_{1.8}\text{Fe}_{0.2}\text{SiO}_4$). The eq36.tdb database contained the thermodynamic data only for the end member compositions of olivine (forsterite and fayalite). As a result, the $\text{Mg}_{1.8}\text{Fe}_{0.2}\text{SiO}_4$ composition was reproduced by adding 90 mg of forsterite and 10 mg of fayalite (similar to the method of Milesi et al., (2015)). Thermodynamic data for marcasite (FeS_2) was not included in the default chess.tdb database. It was obtained from the GWB (geochemists’ workbench, Thermoddem_V1.10) database (LLNL), for the following dissolution reaction (5-4) and formatted according to chess.tdb format and included into the eq36.tdb as “pyrite2” (Table 5-6):

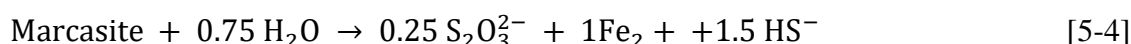


Table 5-6. Thermodynamic data of marcasite obtained from GWB (Geochemists’ Work Bench) (Thermoddem_V1.10) database.

T °C	0	25	60	100	150	200	250	300
logK	24.5977	22.8619	21.0557	19.6003	18.4280	17.8043	17.6647	18.0793
vol.weight = 5011.65 kg/m^3								

These modifications allowed us to reproduce the closed system of individual gold capsules and to run calculations successfully. The results were used to understand the reaction in the systems without an added catalyst (sphalerite or marcasite), and then how its presence could modify it.

5.3 Results

5.3.1 Production of gaseous hydrocarbons at 300°C and 30 MPa

The details of GC analysis (injection pressure, temperature, chromatogram number), the concentration of measured gases (H_2 , N_2 , CO_2 and alkanes C_1 - C_4), total organic carbon contained in measured alkanes, total carbon contained in starting minerals, and finally the conversion rate (in %) of inorganic carbon into organic carbon (conversion rate = [total organic C (mol)/total C introduced as $NaHCO_3$ (mol)]*100) are reported in Table 5-7. The C_1 - C_4 alkanes produced in the samples were plotted in Figure 5-1.

The gas samples produced by the olivine systems (#69, 66 and 65) were injected together with argon (Ar) at ~750 mbar. They were cooled down to -70 °C (to trap water) before injection, which apparently condensed part of the ethane, propane, butane and CO_2 . Methane remained as a gas since it has a higher saturation vapour pressure (chapter 2, section 2.2.5). No gas other than hydrogen was detected in capsule #65, which contained solely olivine. The other samples were injected into a vacuum, with injection pressures low as 25-100 mbar depending on the quantity of gas they produced. All the samples contained N_2 as a major phase, since the capsules were loaded and closed in a N_2 glove box, and the CO_2 in these samples coming from degassing of the $NaHCO_3$ solution.

Hydrogen has been produced in all the experiments and been consumed for the carbon reduction reactions. The measured hydrogen, thus represents the non-reacted hydrogen. The capsules with fayalite contained ~1 mmol/L and those with chlorite contained ~0.6 -10 mmol/L. The capsules with olivine (Fo90) contained ~1 mmol/L hydrogen. Lower amount of hydrogen was expected in the capsules those contained sulfide minerals, assuming that hydrogen is consumed for the production of hydrocarbons. Surprisingly, high quantities of hydrogen were present in those capsules containing sphalerite. For instance, the experiment with olivine+sphalerite produced 39.43 mmol/L of hydrogen (Table 5-7). Keep the sentence for discussion.

Methane was produced in all the experiments (except capsule #65) in approximately 0.20-0.45 mmol/L quantities. Ethane, propane and butane were produced in all the fayalite containing experiments, whereas in the other experiments, the heaviest of these alkanes were not detected (Table 5-5).

The total carbon contained in the measured C_1 - C_4 alkanes were calculated and reported in Table 5-7. The possible carbon contamination via starting materials were calculated and reported in Table 5-3 and 5-4. Comparison of the total carbon in measured alkanes and the background carbon contamination is given in Figure 5-2. The figure clearly shows that significant quantities of hydrocarbons were produced in the fayalite (Fa) experiments, well above the contamination level, whereas in chlorite, they fall in the same order of magnitude of the contamination. In olivine (Fo90) experiments, significant quantities of carbon have been introduced into the capsules via starting minerals (Figure 5-2). The experiment with fayalite, fayalite+marcasite and fayalite+sphalerite produced 1.5 mmol/L,

4.25 mmol/L and 2.38 mmol/L total organic carbon respectively while the background carbon levels were 0.13, 0.13 and 0.14 mmol/L respectively.

The Schulz-Flory distributions of measured hydrocarbons were plotted in Figure 5-3. The Schulz-Flory distribution coefficient (r^2), and chain growth probability (α), are also reported on the same plot. The calculated r^2 values of these plots are $r^2 < 0.9$ indicate a dominant thermogenic origin. Small α value were obtained for the fayalite alone (#67) and the fayalite+marcasite (#70) experiments (0.23 and 0.19 respectively), indicating a high probability of hydrocarbon chain growth. However, the α values of the other systems were ~ 0.6 indicating chain termination is more favored than chain growth.

Table 5-7. Concentration of H₂, N₂, CO₂, and hydrocarbons in gas phase extracted from gold capsules, analyzed by gas chromatography. All the experiments were conducted at 300 °C and 30 MPa.

Composition ^a :	Fa+ S	Fa + M	Fa	Chl+M	Chl+S	Chl	Ol+M	Ol+S	Ol
Exp no:	#70	#71	#67	#72	#73	#68	#69	#66	#65
Chromatogram#	GC09-16-1119	GC09-16-1121	GC09-16-1117	<u>Details of injection</u>		GC09-16-1159	GC09-16-728	GC09-16-731	GC09-16-721
P _{inj} (mbar) ^b	38.1	51.5	27.6	68.4	80.1	78	755	743.9	734.3
T (°C) ^c	25.2	25.0	25.0	24.6	26.3	26.3	26.0	25.7	26.1
<u>Concentration of gases (mmol/L)</u>									
H ₂	1.13±0.06	0.40±0.02	0.89±0.04	0.57±0.03	9.53±0.48	4.42±0.22	1.66±0.08	39.43±1.97	1.23±0.06
N ₂	63.79±2.11	29.09±0.96	46.01±1.52	74.54±2.46	50.66±1.67	43.71±1.44	63.61±2.10	40.86±1.35	nd
CO ₂	46.82±0.61	139.46±1.81	28.08±0.37	140.09±1.82	164.27±2.14	173.24±2.25	3.52±0.05	5.20±0.07	nd
CH ₄	0.35±0.00	0.45±0.00	0.30±0.00	0.28±0.00	0.33±0.00	0.28±0.00	0.20±0.00	0.15±0.00	nd
C ₂ H ₆	0.34±0.00	0.16±0.00	0.12±0.00	0.01±0.00	0.01±0.00	nd	0.02±0.00	nd	nd
C ₃ H ₈	0.17±0.00	0.48±0.01	0.17±0.00	0.01±0.00	nd	nd	0.01±0.00	nd	nd
i-C ₄ H ₁₀	0.13±0.00	0.44±0.01	0.07±0.00	0.01±0.00	nd	0.01±0.00	nd	nd	nd
n-C ₄ H ₁₀	0.08±0.00	0.07±0.00	0.05±0.00	nd ^f	nd	nd	0.01±0.00	nd	nd
Total C in C ₁ -C ₄ alkanes (mmol/L) ^d	2.38±0.00	4.25±0.01	1.53±0.00	0.37±0.00	0.35±0.00	0.32±0.00	0.31±0.00	0.15±0.00	nd
Total C(i) (mmol/L) ^e	0.14±0.00	0.13±0.00	0.13±0.00	0.12±0.00	0.13±0.00	0.12±0.00	0.28±0.00	0.29±0.00	0.28±0.00
%conversion ^g	0.17	0.25	0.11	0.05	0.05	0.05	0.04	0.02	0

^aabbreviations : Fa=fayalite, S=sphalerite, M=marcassite, Chl=chlorite, Ol=olivine (Fo90)^binjection pressure during the injection of sample into gas chromatogram^ctemperature in the room during the injection of sample into gas chromatogram^dsum of carbon in methane, ethane, propane and butane in our experiments as reported in this table^eCarbon contamination in the starting materials at same P/T to evaluate the amount of carbon introduced by background sources (also given in table 5-4).^fnd=not detected^gconversion rate (%) = [total organic C (mol)/total C introduced as NaHCO₃(mol)]*100

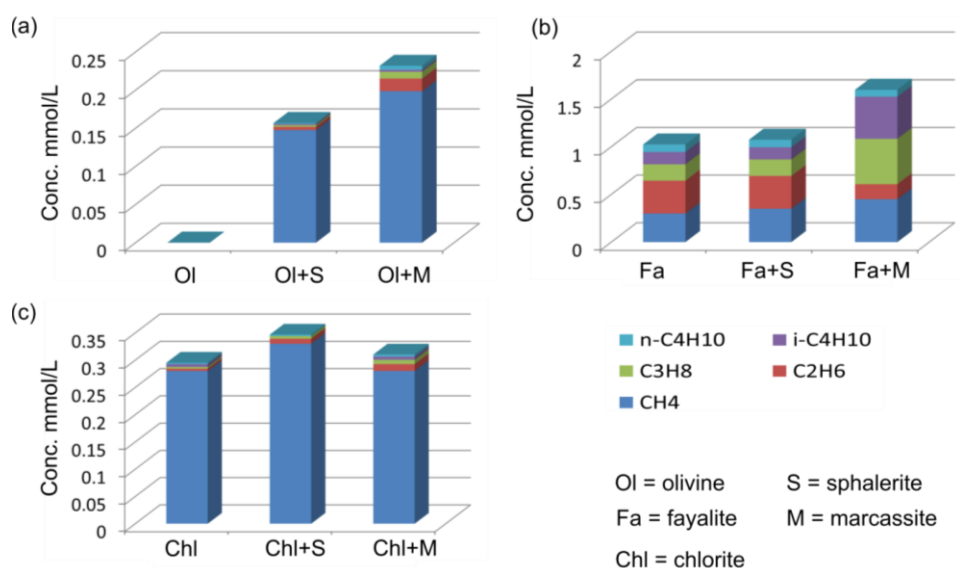


Figure 5-1. Comparison of hydrocarbon production with and without sphalerite, ZnS (S), or marcasite, FeS₂ (M), by reacting Fe-rich silicate: fayalite (Fa), chlorite (Chl) and olivine (Fo90), with 0.64 M NaHCO₃ solution at 300°C and 30 MPa.

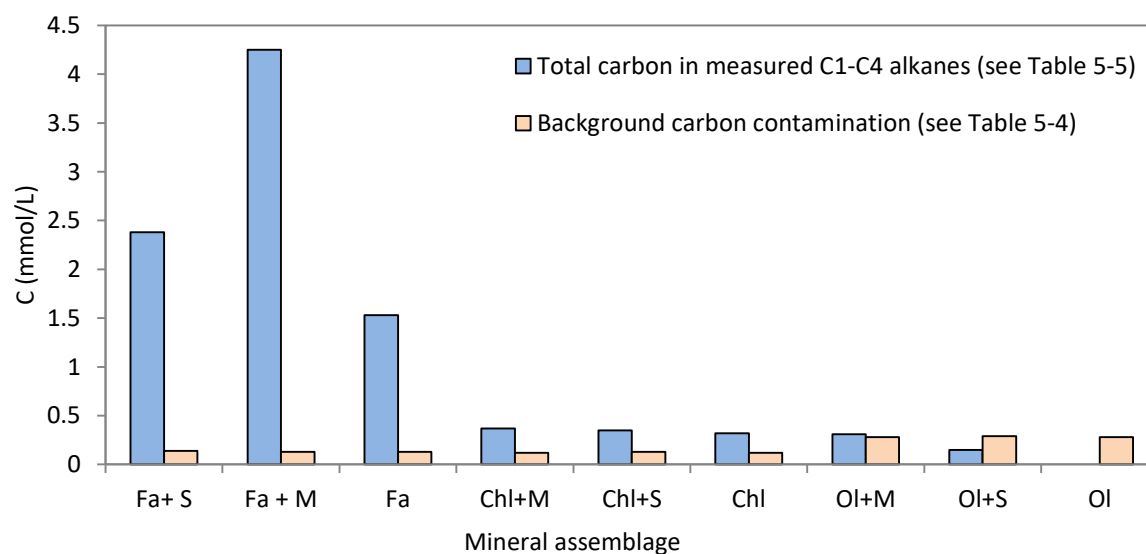


Figure 5-2. Comparison of total carbon contained in C₁-C₄ alkanes produced by the reaction (blue) (given in Table 5-5) and background carbon contamination (orange) (given in Table 5-4), showing that, significant quantities of hydrocarbons were produced in fayalite (Fa) experiments, well above the contamination level, whereas in chlorite, they fall in the same order of magnitude. In olivine (Fo90) experiments, significant quantities of carbon have been introduced to the capsules via starting minerals, but hydrocarbons were not detected in gas analysis. The uncertainty associated with Fa+M data (blue column) is 0.01 mmol/L and the error associated with the other data is 0.00.

Abbreviations: Fa= fayalite, S=sphalerite, M=marcasite, Chl=chlorite, Ol=olivine (Fo90)

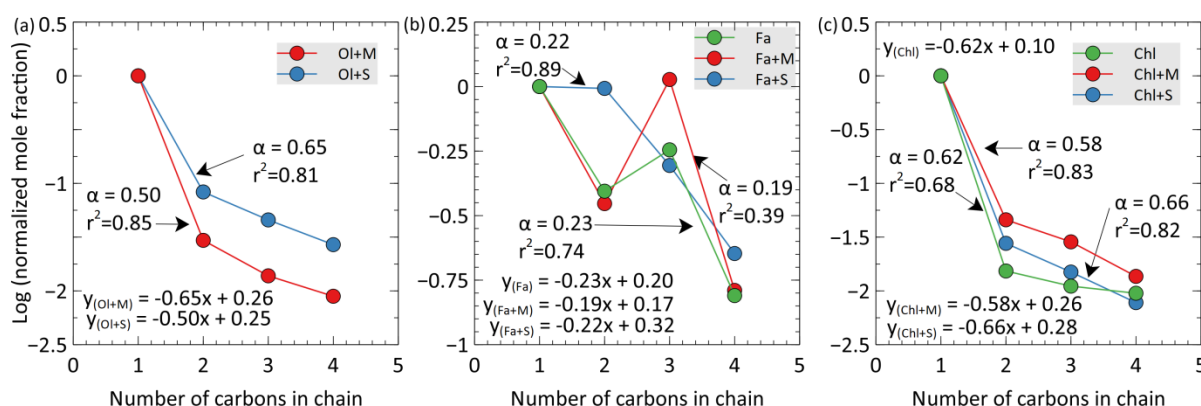


Figure 5-3. Schulz-Flory distribution of measured hydrocarbons of (a) olivine (Fo90), (b) fayalite and (c) chlorite, experiments. The Schulz-Flory distribution coefficient (r^2), and chain growth probability (α), for each curve is also indicated on the plot. Thermogenic gas is typically characterized by a correlation coefficient $r^2 < 0.9$, while r^2 is > 0.9 for dominantly abiotic gas and > 0.99 for quasi-pure abiotic gas. The calculated r^2 values of these plots are less than 0.9 ($r^2 < 0.9$) indicating that the hydrocarbons (C_1 - C_4 alkanes) were possibly formed by the thermal maturation of carbon, contaminated from the starting minerals.

Abbreviations: Fa= fayalite, S=sphalerite, M=marcasite, Chl=chlorite, Ol=olivine (Fo90)

5.3.2 Solid products

Olivine alteration: SEM images of run products of an experiment where olivine (Fo90) was reacted with 0.64M NaHCO_3 solution at 300°C and at 30 MPa in the presence of sphalerite (ZnS) are shown in Figure 5-4. These were obtained from two preliminary experiments (with olivine+sphalerite+ NaHCO_3), conducted for 11 days and 38 days. Both SEM and XRD analysis showed that the olivine in these experiments was partially reacted into serpentine (Figure 5-4 to 5-7). Brucite, magnetite and magnesite were observed only on the SEM images.

Fayalite alteration: The run product of the experiment containing synthetic fayalite+ NaHCO_3 , indicated that fayalite was slightly altered into magnetite (Figure 5-8). However, in the natural fayalite containing experiments, fayalite was completely altered into albite and magnetite (Figure 5-9 and 5-10).

Chlorite alteration: Chlorite in these samples was altered into almandine garnet and magnetite (Figure 5-11 and 5-12).

Sphalerite alteration: Sphalerite was observed in the three experiments that contained sphalerite (Figure 5-6, 5-9 and 5-11). However, sphalerite alteration into franklinite, a Fe-Zn oxide ($(\text{Zn}, \text{Mn}^{+2}, \text{Fe}^{+2}) (\text{Fe}^{+3}, \text{Mn}^{+3})_2 \text{O}_4$) was evidenced in the experiment with olivine+sphalerite+ NaHCO_3 (Figure 5-6).

Marcasite alteration: Marcasite has been completely transformed into pyrite in all the experiments (Figure 5-7, 5-10 and 5-12).

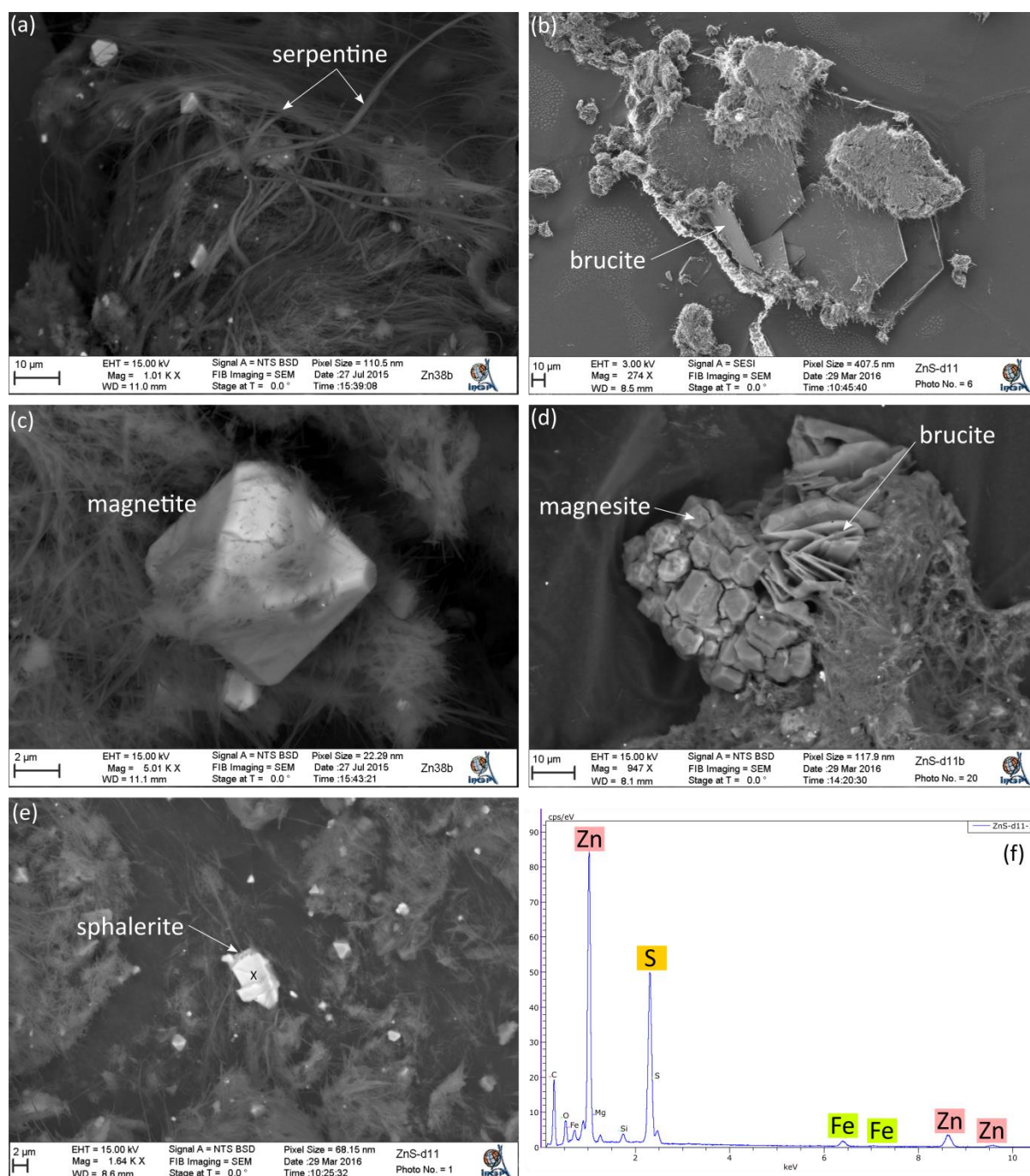


Figure 5-4. SEM images showing the products of serpentinization, magnesite produced from carbonation, and sphalerite in the recovered sample. (a) serpentine formed after 38 days (b) brucite after 11 days (c) magnetite formed after 38 days (d) magnesite formed after 11 days (e) sphalerite in the experiment run for 11 days (f) SEM-EDS of sphalerite. The SEM analysis was performed on the products of the two experiments with olivine (Fo90)+sphalerite+0.64M NaHCO_3 solution reacted at 300°C and at 30 MPa (for 11 days and 38 days).

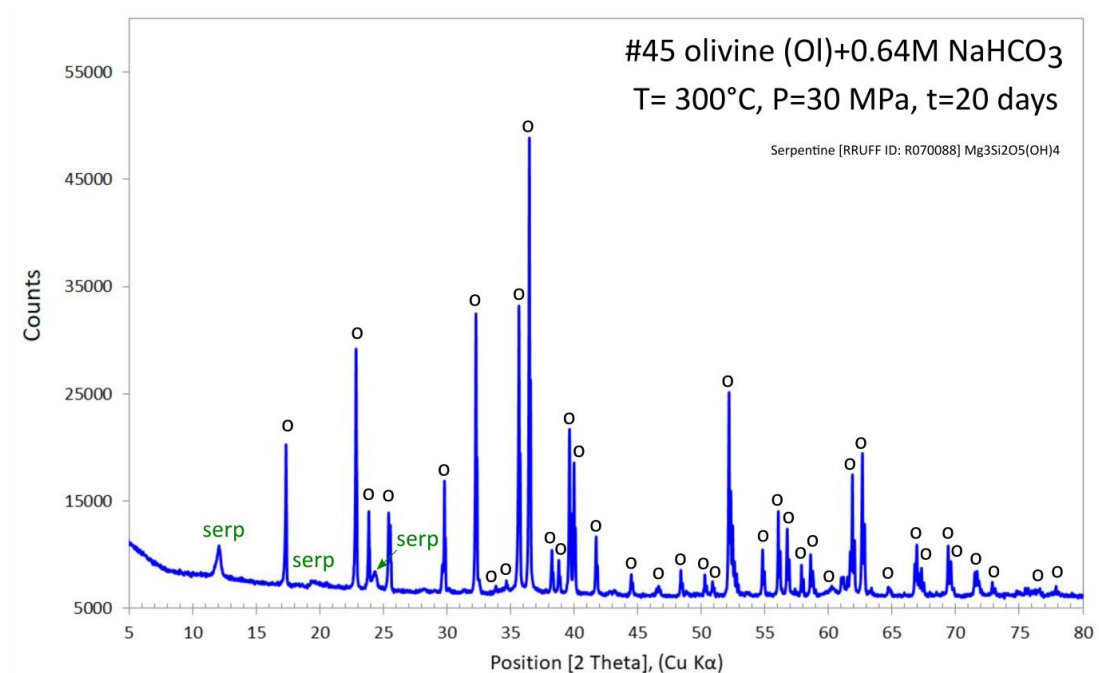


Figure 5-5. XRD pattern of an experiment with olivine+NaHCO₃, showing that the run product contained olivine (o) and small amount of serpentine (serp).

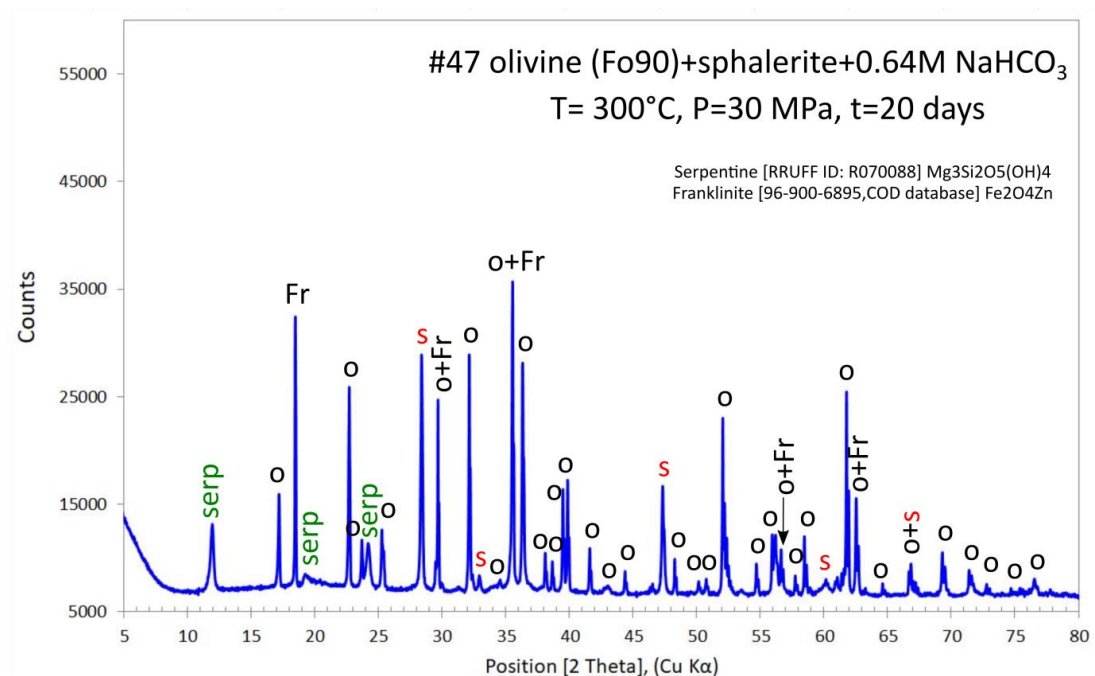


Figure 5-6. XRD pattern of an experiment with olivine+sphalerite+NaHCO₃(Ol+S) showing that the run product contained olivine (o), small amount of serpentine (serp), sphalerite (s) and franklinite (Fr).

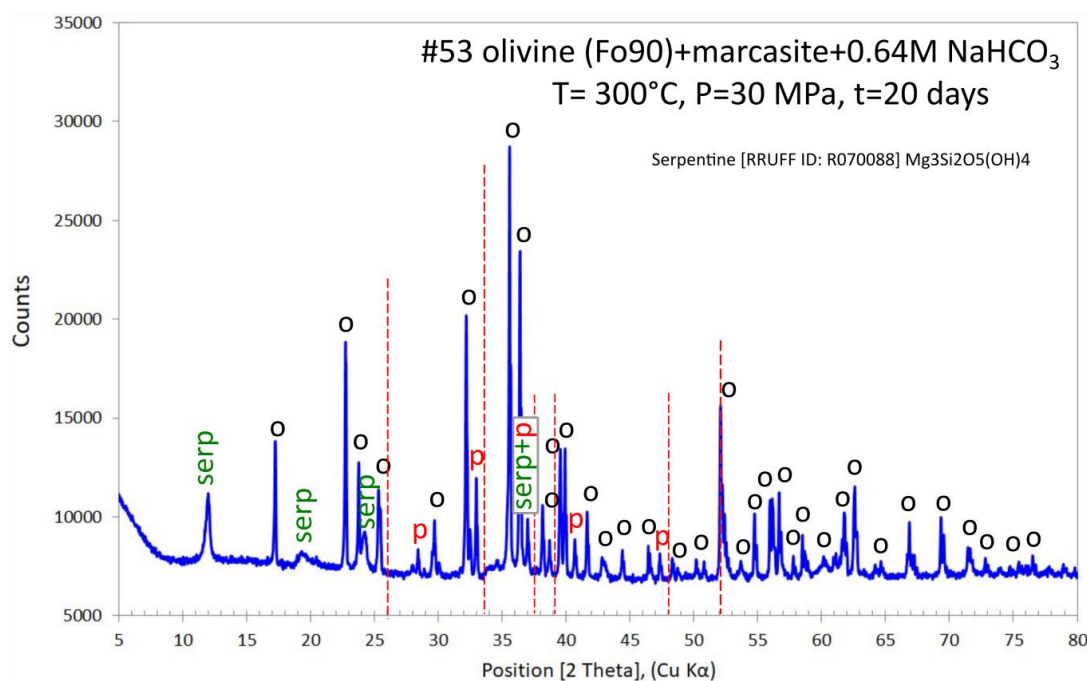


Figure 5-7. XRD pattern of an experiment with olivine+marcasite+NaHCO₃ (Ol+M) showing that the run product contained olivine (o), small amount of serpentine (serp) and pyrite (p). This pattern indicates that the initially introduced marcasite has been reacted to form pyrite. The characteristic peaks for marcasite obtained from RRUFF database (Ref. R060882.9) are shown in red-dashed lines, for comparison.

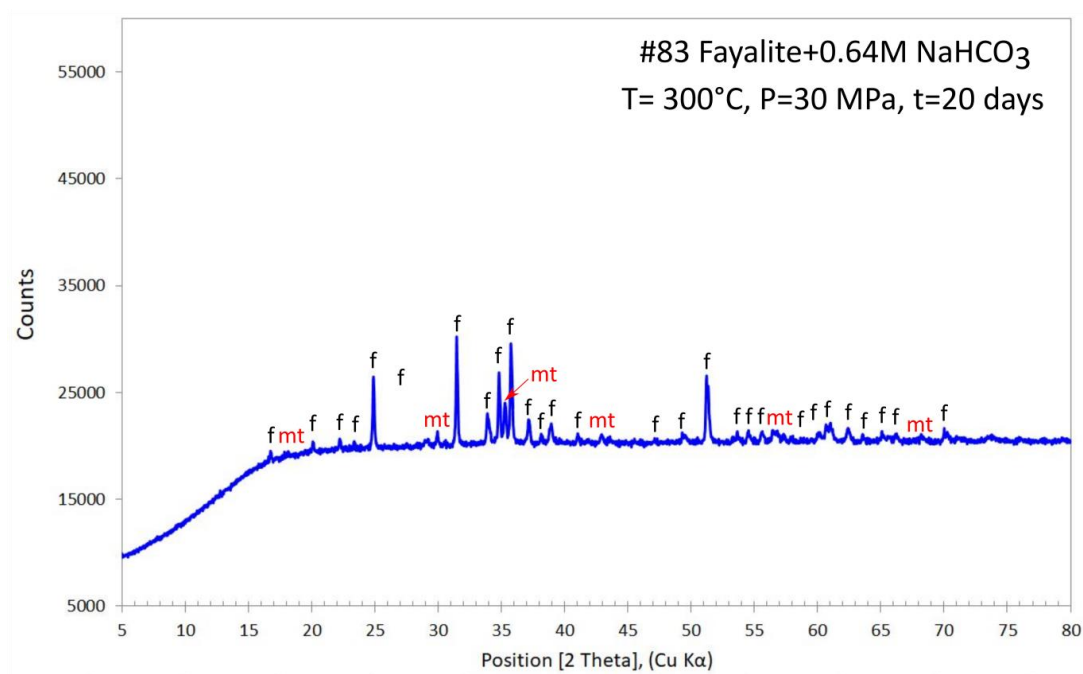


Figure 5-8. XRD pattern of an experiment with fayalite+NaHCO₃ (Fa) showing that the run product contained fayalite (f) and magnetite (mt). A synthetic fayalite sample was used in this experiment.

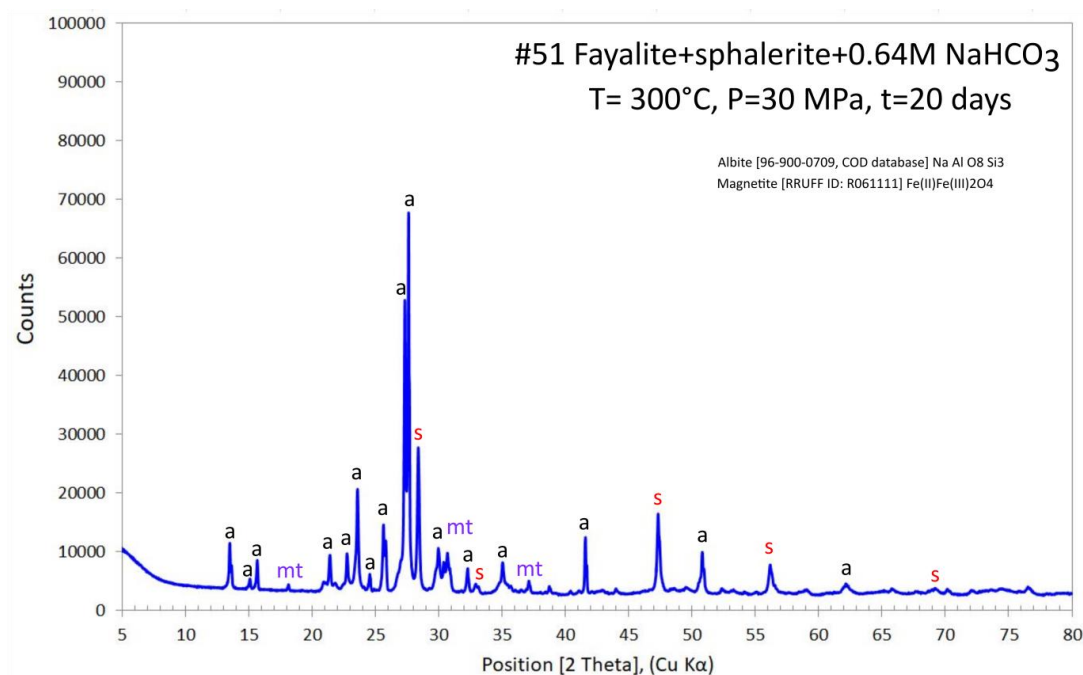


Figure 5-9. XRD pattern of an experiment with fayalite+sphalerite+NaHCO₃ (Fa+S) showing that the run product contained albite (a), magnetite (mt) and sphalerite. The XRD pattern indicates that fayalite has been completely dissolved. Albite was present in the natural fayalite sample.

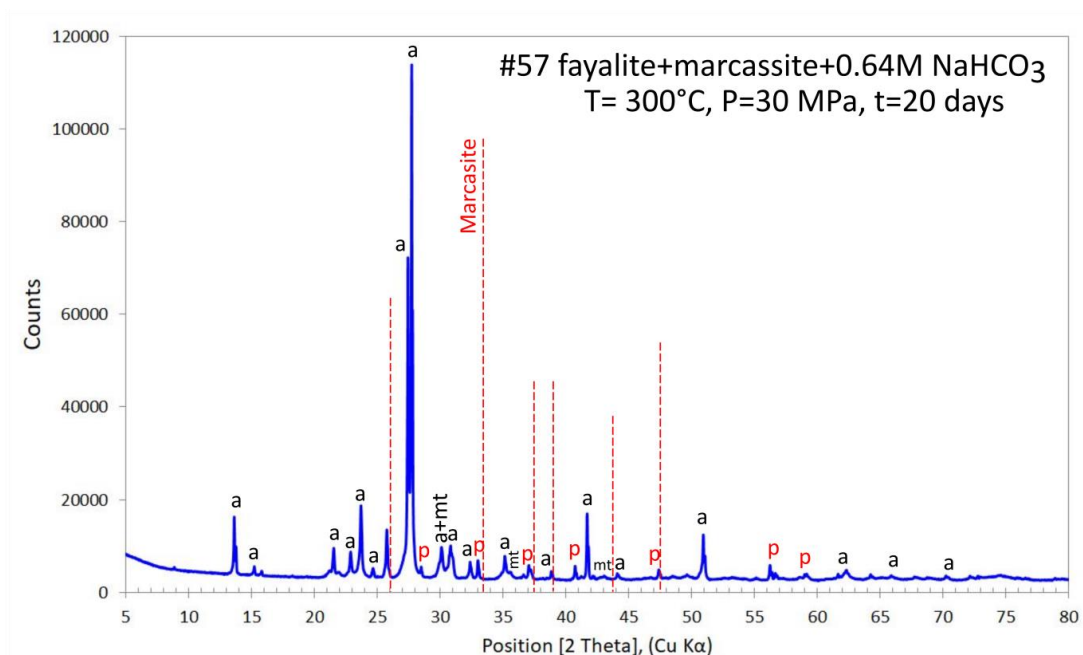


Figure 5-10. XRD pattern of an experiment with fayalite+marcasite+NaHCO₃ (Fa+M) showing that the run product contained albite (a), magnetite (mt) and pyrite (p). Albite was present in the natural fayalite sample. This pattern indicates that the initially introduced fayalite has been completely dissolved and marcasite has been reacted to form pyrite. The characteristic peaks for marcasite obtained from RRUFF database (Ref. R060882.9) are shown in dashed lines in red, for comparison (peak intensities are arbitrary).

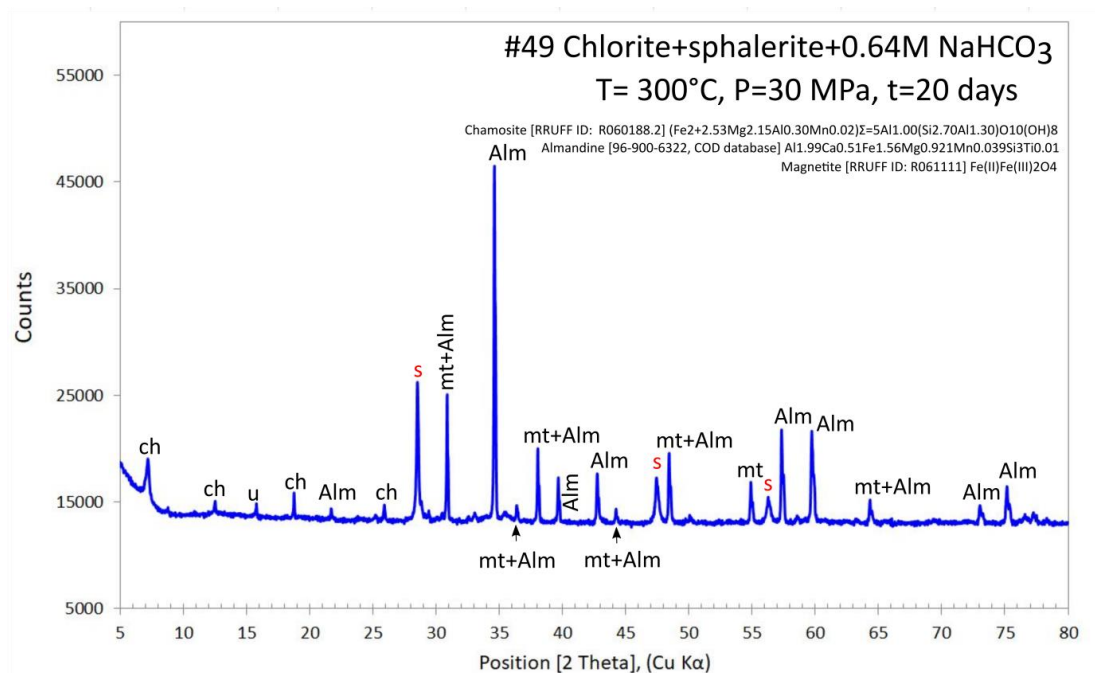


Figure 5-11. XRD pattern of an experiment with chlorite+sphalerite+NaHCO₃ (Chl+S) showing that the run product contained almandine (alm), chamosite (ch), magnetite (mt) and sphalerite (s). Initially introduced chamosite has been altered into almandine and magnetite.

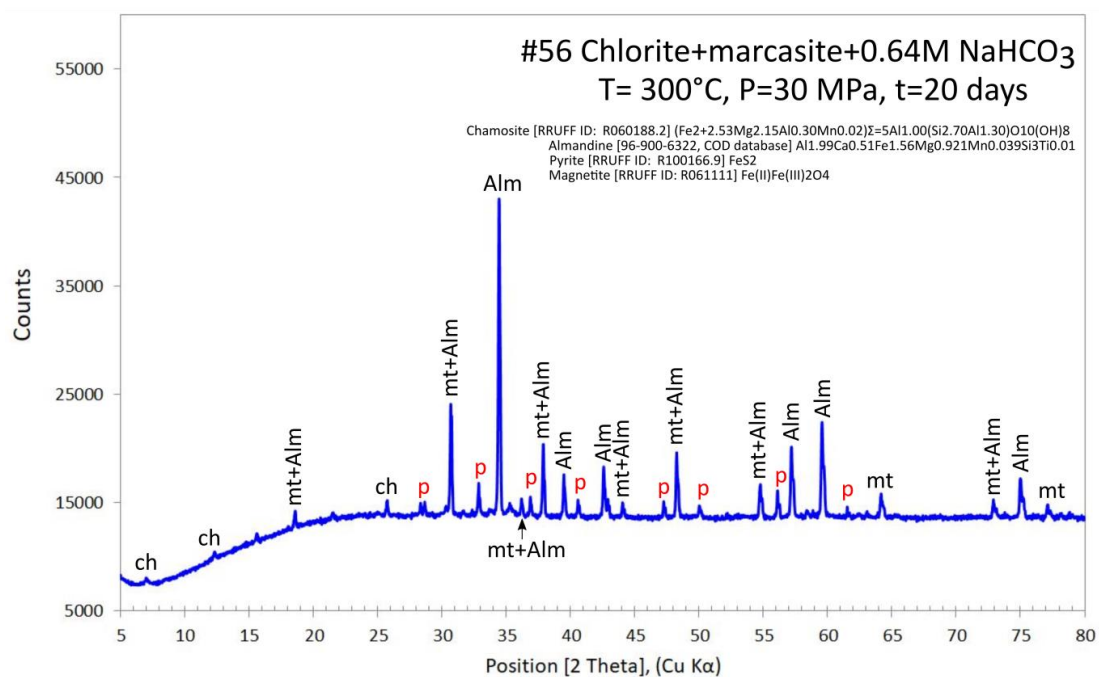


Figure 5-12. XRD pattern of an experiment with chlorite+marcasite+NaHCO₃ (Chl+M) showing that the run product contained almandine (alm), chamosite (ch), magnetite (mt) and sphalerite (s). Initially introduced chamosite has been altered into almandine and magnetite.

5.3.3 HPLC analysis for dissolved organic compounds

HPLC analysis was performed on liquids extracted from the capsules of experiment 1, 2 and 3 (see Table 5-5). Experiment 1 was performed in deionized water, providing a “carbon free” medium for the reaction. As a result, organic compounds were not expected in those with deionized water, unless the starting materials were carbon-contaminated. Experiment 2 and 3 were performed using a NaHCO_3 solution and therefore we anticipated to detect methane, formate, acetate and formic acid, according to those resulted from thermodynamic modeling. The only difference between experiment 2 and 3 was the reaction time (exp. 2= 5 days; exp. 3=20 days) in order to examine the evolution the dissolved organic compounds as a function of time.

HPLC analysis of liquids extracted from exp. 1 (5 days, C-free) (see table 5-5)

The HPLC spectra of these samples are shown in Figure 5-13. Unexpectedly we detected formic acid (characteristic peak at retention time $t=4.6\text{--}4.75$ min), acetic acid (characteristic peak at retention time $t=7.76$ min), and few unidentified compounds (detected at retention times 3.5 min and 4.0 min) in the liquids extracted from the capsules of experiment 1, in which all the reactions were mediated in deionized water. The presence of formic acid in the deionized water sample (the DI water used to prepare those capsules) indicates that it could possibly result from a contamination by DI water used in the laboratory, or later from the sample preparation for HPLC analysis. The concentration of formic acid in the samples was below the quantification limit of the analytical method used, but the acetic present in the sample were measurable and detected in 11-56 mmol/L. The unidentified compound with a peak at $t=3.5$ min, was detected only in the samples containing marcasite (#1, 2 and 5).

HPLC analysis of liquids extracted from exp. 2 (5 days) (see table 5-5)

The HPLC spectra of these samples are shown in Figure 5-14. These samples did not contain any of the expected organic compounds such as formate or formic acid. An unknown peak (at $t=3.7$) was resulted from the samples containing sphalerite and marcasite (#32, 20, 38, 36 and 40), and was not present in the deionized water indicating that it's a reaction product. The second unknown peak (at $t=\sim 4$ min) is present in almost all the samples except in the deionized water sample, indicating it's a reaction product as well. The third unknown peak (at $t=\sim 9.8$ min) is present in olivine+marcasite and olivine+sphalerite experiments (#20 and 36), which could also be a reaction product.

HPLC analysis of liquids extracted from exp. 3 (20 days) (see table 5-5)

The HPLC spectra of these samples are shown in Figure 5-15. These samples did not contain any of the expected organic compounds such as formate or formic acid. The first unknown peak (at $t=3.7$) observed in sphalerite and marcasite containing samples (#32, 20, 38, 36 and 40) of experiment 2 (5 days run), were present only two samples; olivine+sphalerite (#47) and olivine+marcasite (#53). The second unknown peak (at $t=\sim 4$ min) is present in almost all the samples except in the deionized water sample, indicating it is

a reaction product as well. The third unknown peak (at $t \sim 9.8$ min) is present only in olivine+sphalerite (#47) and olivine+marcasite (#53), similarly to what we observed in experiment 2 that was run for 5 days.

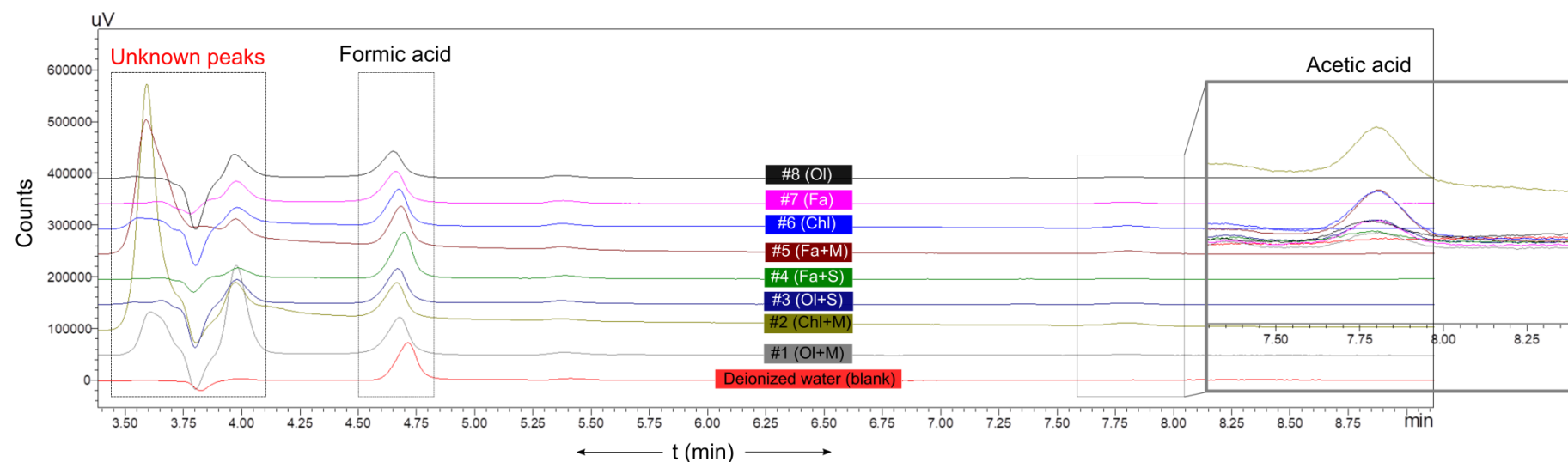


Figure 5-13. HPLC spectra of the solutions extracted from experiment 1, showing the presence of formic acid and acetic acid which were unexpected for this experiment. The formic acid is a contamination by deionized water, and the source for acetic acid is not known. The experiments were conducted by reacting Fe-rich minerals±catalyst (sphalerite or marcasite) with pure water at 573 K and 30 MPa for 5 days. (abbreviations : Fa=fayalite, S=sphalerite, M=marcasite, Chl=chlorite, Ol=olivine (Fo90)).

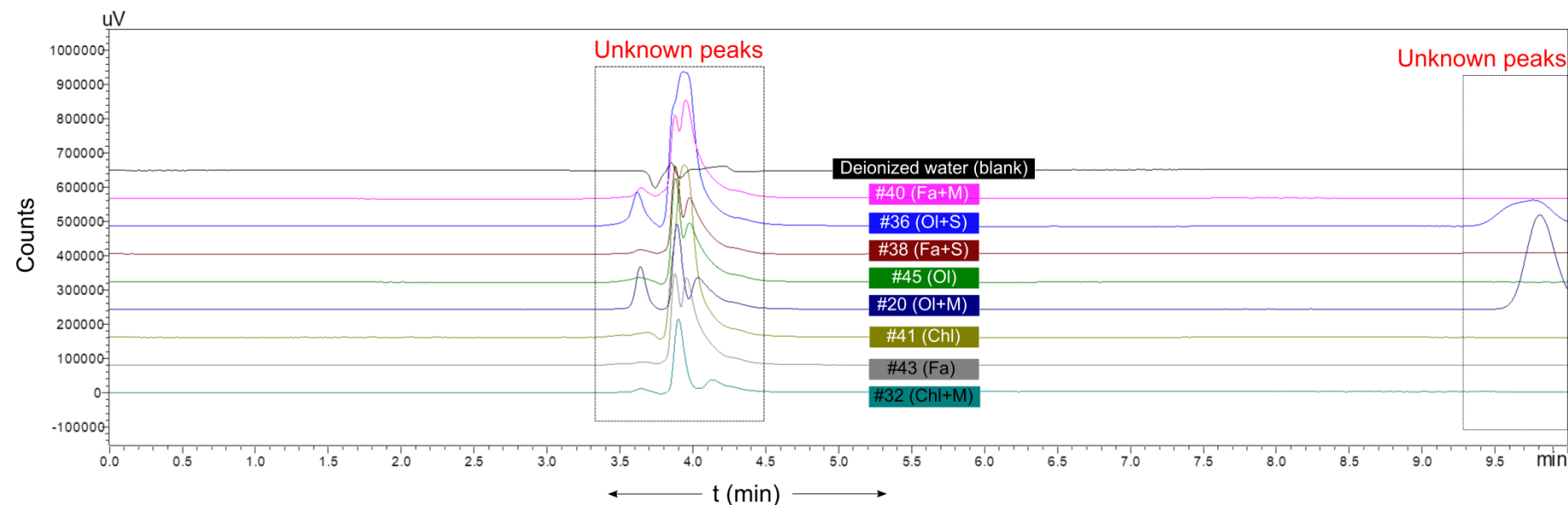


Figure 5-14. HPLC spectra of the solutions extracted from experiment 2, showing the presence of an unknown compound whose peak is $\sim t=3.5$ - 4.2 min in all the samples, but not in deionized water (blank). Therefore, it could possibly be a reaction product. Another unknown compound is present in the experiments where olivine is reacted with sphalerite and marcasite. These experiments were conducted by reacting Fe-rich minerals+catalyst (sphalerite or marcasite) with 0.64M NaHCO_3 at 573 K and 30 MPa for 5 days. (abbreviations : Fa=fayalite, S=sphalerite, M=marcasite, Chl=chlorite, Ol=olivine (Fo90)).

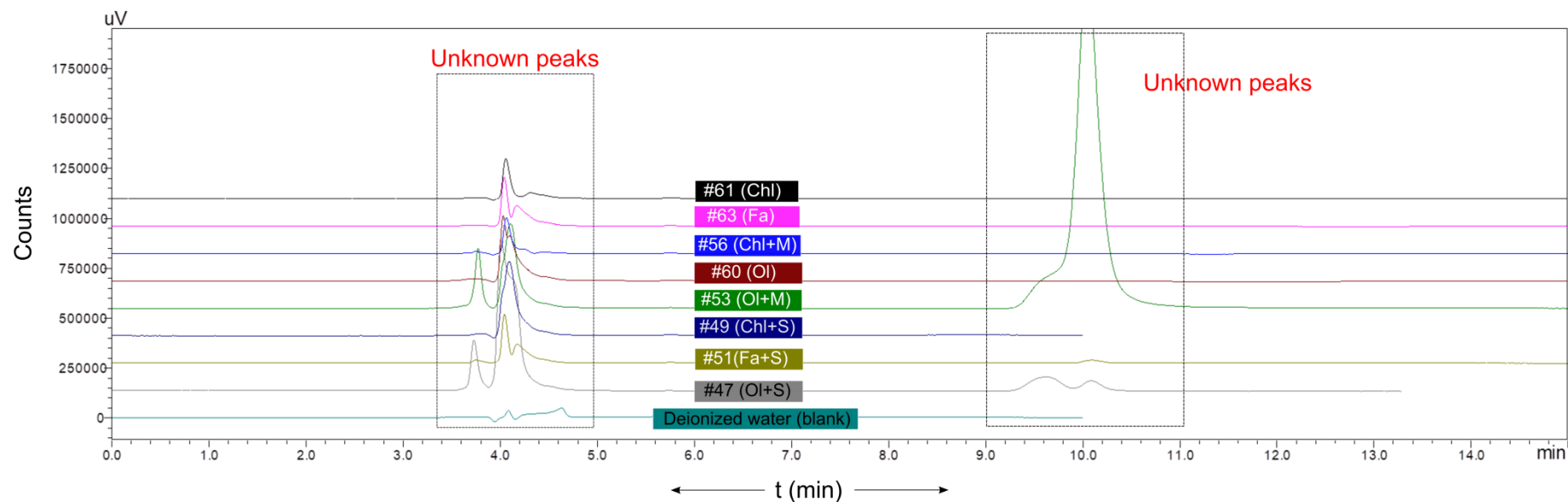


Figure 5-15. HPLC spectra of the solutions extracted from experiment 3, showing the presence of an unknown compound whose peak is $\sim t=3.5$ - 4.2 min in all the samples, but not in deionized water (blank), indicating that it could possibly be a reaction product. Another unknown compound is present in the experiments where olivine is reacted with sphalerite and marcasite. These experiments were conducted by reacting Fe-rich minerals \pm catalyst (sphalerite or marcasite) with 0.64M NaHCO_3 at 573 K and 30 MPa for 20 days. Compared to experiment 2, in which these experiments were run for 5 days, the peak intensity of the second peak of olivine+marcasite experiment has significantly increased. (abbreviations: Fa=fayalite, S=sphalerite, M=marcasite, Chl=chlorite, Ol=olivine (Fo90)).

5.3.4 NMR analysis for dissolved organic compounds

Results of ^{13}C NMR analysis

The ^{13}C NMR spectra of the two samples are shown in Figure 5-16. No peaks were observed in sample #75, and two peaks were observed for the sample #77, at 171 ppm and 175 ppm, which were identified as HCO_3^- or CO_3^{2-} and formic acid / formate, respectively.

Results of ^1H NMR analysis:

The ^1H NMR spectra of the two samples are shown in Figure 5-17. Both samples contain a peak at 4.8 ppm that is not identified. The peak at 8.2 ppm is present only in sample 77, and it could be a HCO_3^- or formic acid peak.

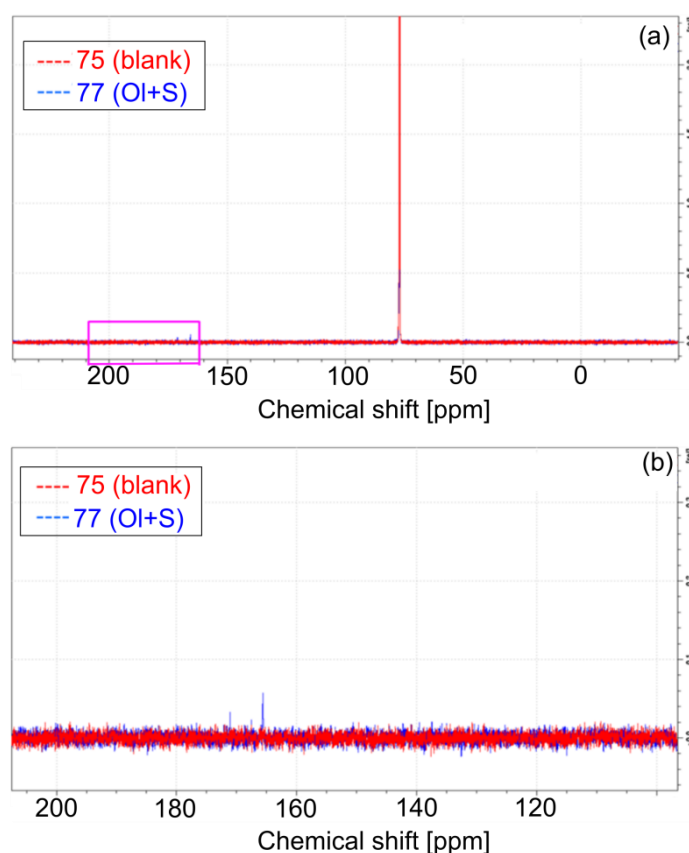


Figure 5-16. The ^{13}C NMR spectrum of solution extracted from a gold capsule containing olivine and NaHCO_3 (exp 75. blank) and olivine, sphalerite and NaHCO_3 (exp 77), reacted at 573 K and 30 MPa for 20 days plotted against signal intensity vs. chemical shift (a). The area marked in pink is enlarged and presented in figure (b), which shows two peaks at 171 and 175 ppm, possibly $\text{HCO}_3^-/\text{CO}_3$ and formic acid / formate.

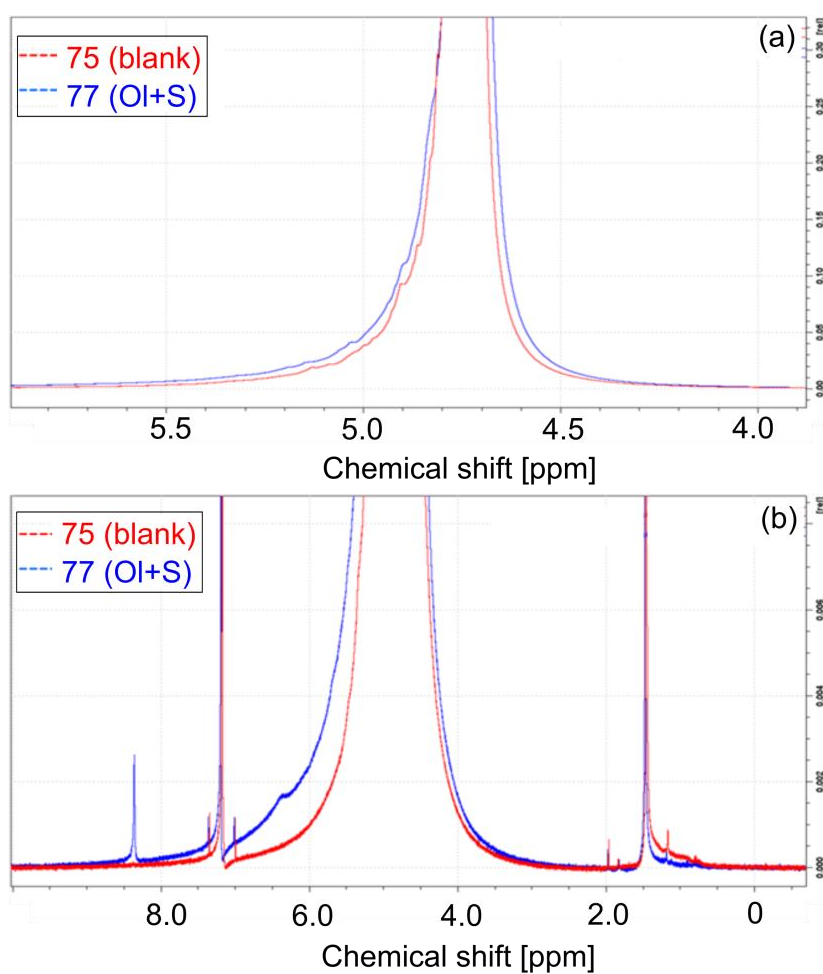


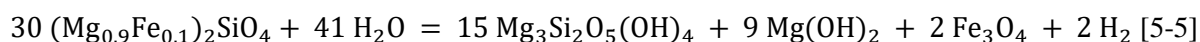
Figure 5-17. The ^1H NMR spectrum of experiment #75 containing olivine+ NaHCO_3 and experiment #77 containing olivine+sphalerite+ NaHCO_3 , reacted at 573 K and 30 MPa for 20 days. (a) Peak at 4.8 ppm was present in both the sample and blank (b) the peak at 8.2 is present only in the olivine, sphalerite+ NaHCO_3 (exp 77), the peak is possibly a HCO_3^- or formic acid.

5.4 Discussion

5.4.1 Reaction paths predicted by thermodynamic modeling

5.4.1.1 Olivine system

System 1, (Olivine): The reactions of olivine with 0.64 M NaHCO₃ at T in K and 30 MPa, and the effect of sphalerite / marcasite addition to the system on thermodynamic equilibrium was modeled. The resulting fluid composition and the minerals formed at the equilibrium were summarized in Table 5-8. The concentration of H₂, CO₂, H₂S and CH₄ in olivine, olivine+sphalerite and olivine+marcasite systems are plotted in Figure 5-18. A comparison between the amounts of organic compounds formed in each system is given Figure 5-19. At these hydrothermal conditions, all the added fayalite and forsterite (representing Fo90 composition) were completely reacted with the NaHCO₃ solution resulting in antigorite, magnetite, brucite and hydrogen in the system, via serpentinization.



In addition, magnesite (MgCO₃) and Na₂CO₃ were precipitated from the NaHCO₃ solution. Part of the NaHCO₃ dissociates into carbon dioxide. The solution reached thermodynamic equilibrium with respect to chrysotile, forsterite, hematite, wustite. A fraction of hydrogen produced in the system is involved in the reduction of HCO₃⁻ or CO_{2(aq)} into organic compounds. HCO₃⁻ was mainly reduced into methane (38 mmol/L) and formate (4.7 mmol/L) (Figure 5-19). Although our calculations show that the production of simple organic compounds (<C₃) are thermodynamically favorable, their quantities were several orders of magnitudes less than that of methane (CH₄). For instance, dissolved acetate and formic acid concentrations were 6 and 0.5 μmol/L respectively, while the concentrations of dissolved methanol and acetic acid in the solution were 7.7 and 5.6 nmol/L. Formaldehyde, ethanol and acetaldehyde were formed in traces which were <10⁻¹¹ mol/L (Figure 5-19). At equilibrium, 2.1 mmol/L of dissolved hydrogen H_{2(aq)}, 16 mmol/L of dissolved carbon dioxide CO_{2(aq)}, and 38 mmol/L methane remained in the solution (Figure 5-18).

Table 5-8. Summary of fluid composition and precipitated phases obtained thermodynamic modelling of the reaction of olivine (Fo90) \pm catalyst (sphalerite or marcasite) with NaHCO_3 at 573 K and 30 MPa, at equilibrium.

	System 1 (Olivine)	System 2 (Olivine+sphalerite)	System 3 (Olivine+marcasite)
<i><u>Dissolved species (mol/L)</u></i>			
H ₂	2.10E-03	2.10E-03	6.00E-04
CO ₂	0.016	0.016	0.016
CH ₄	3.80E-02	3.83E-02	2.55E-04
Formate	4.70E-03	4.60E-03	8.80E-05
H ₂ S	-	3.70E-07	4.00E-03
Acetate	6.0E-06	5.8E-06	2.6E-09
Formic acid	4.6E-07	4.6E-07	1.3E-07
Methanol	7.7E-09	7.7E-09	1.8E-10
Acetic acid	5.6E-09	5.6E-09	3.7E-11
Formaldehyde	4.1E-12	4.1E-12	3.4E-13
Ethanol	4.0E-12	4.0E-12	2.2E-15
Acetaldehyde	3.0E-13	3.0E-13	5.8E-16
<i><u>Solid phases in the system (mg)</u></i>			
Brucite	15.0	14.90	10.30
Magnesite	3.60	3.80	10.30
Na ₂ CO ₃	4.30	4.20	-
Magnetite	7.40	7.40	9.30
Antigorite	89.80	89.80	89.80
Sphalerite	-	9.70	-
Zincite	-	0.10	-
Pyrite	-	-	5.00
Troilite	-	-	1.30
<i><u>Phases near equilibrium (SI)</u></i>			
Chrysotile	-0.14	-0.15	-0.15
Forsterite	-0.35	-0.35	-0.35
Hematite	-0.67	-0.67	-0.49
FeO	-0.90	-0.90	-
Pyrrhotite	-	-	-0.07
Marcassite	-	-	-0.26

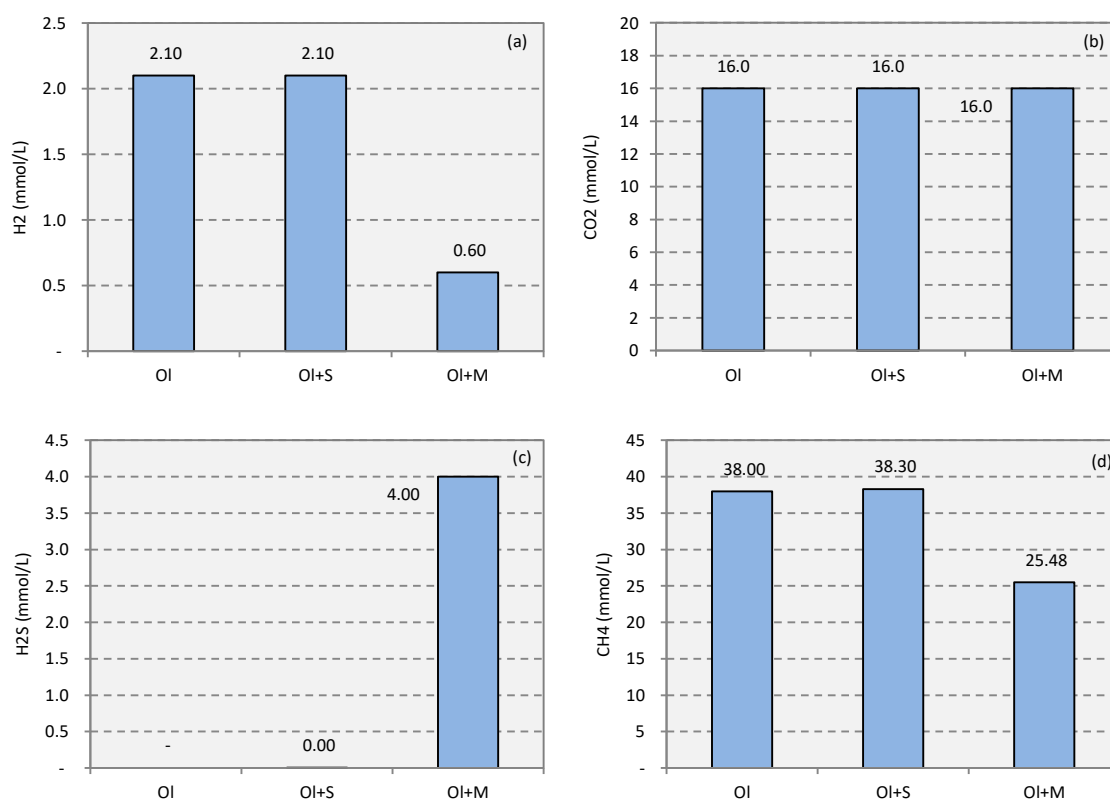


Figure 5-18. The equilibrium concentrations of dissolved (a) hydrogen (b) CO₂ (c) H₂S and (d) CH₄ in the solutions produced during the reactions of olivine (Fo90)±catalyst (sphalerite or marcassite) with NaHCO₃ solution at 573 K and 30 MPa. The presence of Marcassite releases important amounts of H₂S at equilibrium, while CH₄ production is inhibited. The concentrations were modeled by CHES geochemical code. (Abbreviations: Fa=fayalite, S=sphalerite, M=marcassite, Chl=chlorite, Ol=olivine (Fo90)).

System 2 (addition of 10 mg of sphalerite): Serpentinization produced approximately similar quantities of antigorite, magnetite, brucite and hydrogen compared to the olivine and NaHCO_3 system above (equation 5-5). Magnesite was also produced. The addition of sphalerite (ZnS) induced slight changes in the equilibrium compared to the System 1 above, due to the dissolution of sphalerite (~ 3.4 wt.%), precipitating zincite (ZnO). As a result of sphalerite dissolution, traces of $\text{H}_2\text{S}_{(\text{aq})}$ ($0.4 \mu\text{mol/L}$) are also formed (Figure 5-18c), following:



However, this does not affect the quantities of dissolved hydrocarbons in the solution. The solution reached thermodynamic equilibrium with respect to chrysotile, forsterite, hematite, and wustite. The equilibrium concentrations of $\text{H}_{2(\text{aq})}$, $\text{CO}_{2(\text{aq})}$ and $\text{CH}_{4(\text{aq})}$ were similar to those of system 1 (Figure 5-18).

System 3, (addition of 10 mg of marcasite): Serpentinization resulted in antigorite, magnetite, brucite formation, and liberating dihydrogen, similarly to Systems 1 and 2 (equation 5-5). In contrast to Systems 1 and 2 however, approximately three times more magnesite was deposited in this system. Although similar quantities of antigorite were formed, slightly lower amounts of brucite, but higher amounts of magnetite were produced, indicating significant changes upon addition of marcasite. The calculations indicate that marcasite could completely dissolve (saturation index of -0.26) at equilibrium, precipitating pyrite (FeS_2) and troilite (FeS) as given by the equation below:



Moreover, the quantity of H_2S formed in the presence of marcasite was four orders of magnitudes higher than that of in sphalerite introduced system (System 2) (Figure 5-18c). As a result of consumption of hydrogen for the formation of H_2S , the amount of dissolved hydrogen in the solution is lower than the one in Systems 1 and 2 described above. Likewise, formate and methane quantities decrease by two orders of magnitude in comparison to system 1 and 2 (Figure 5-18d and 5-19). The solution was in equilibrium with respect to chrysotile, forsterite and hematite and pyrrhotite. An overall decrease in concentrations of all the dissolved organic molecules is observed in comparison with system 1 and 2.

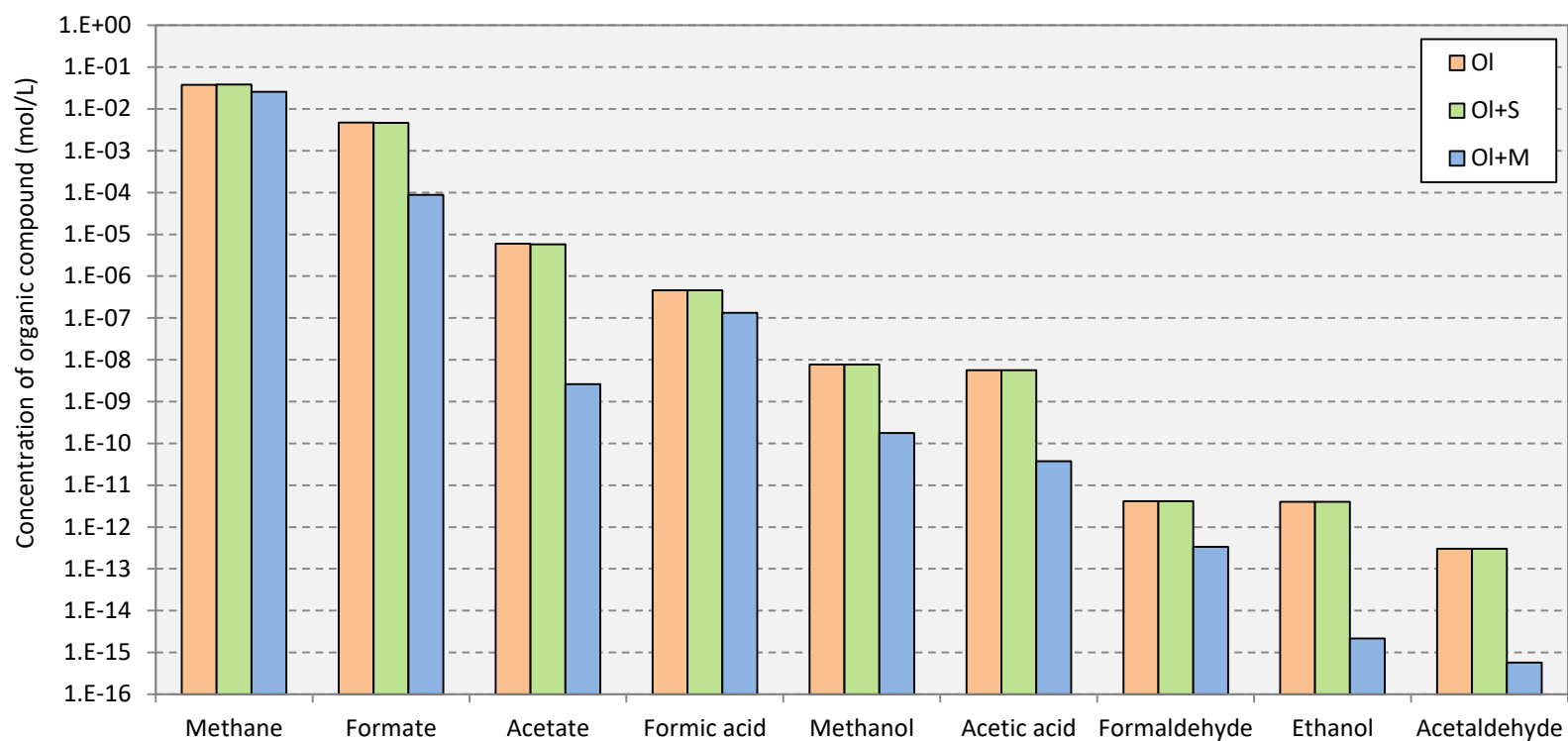
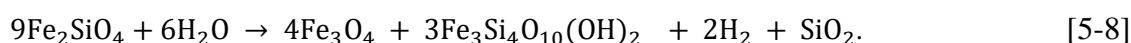


Figure 5-19. The equilibrium concentrations of dissolved organic compounds in the solutions produced during the reactions olivine (Fo90)±catalyst (sphalerite or marcasite) NaHCO_3 at 573 K and 30 MPa, calculated using by CHESSE geochemical code. Methane and formate are formed in mmol/L concentrations, while acetate and formic acid is formed in $\mu\text{mol/L}$ concentrations and other species formed in traces. (Abbreviations: Fa=fayalite, S=sphalerite, M=marcassite, Chl=chlorite, Ol=olivine (Fo90)).

5.4.1.2 Fayalite system.

System 4, (Fa): The reactions of fayalite with 0.64 MNaHCO₃ at 573 K and 30 MPa, and the effect of addition of sphalerite or marcasite to the system at thermodynamic equilibrium was modeled, and the resulting fluid composition, the minerals formed at the equilibrium were summarized in Table 5-9. The concentration of H₂, CO₂, H₂S and CH₄ in fayalite, fayalite+sphalerite and fayalite+marcasite systems are plotted in Figure 5-20. A comparison of amounts of organic compounds formed in each system is given Figure 5-21. At these hydrothermal conditions, fayalite completely reacted with NaHCO₃ resulting in iron-end member minnesotaite (Fe₃Si₄O₁₀(OH)₂), magnetite and H₂ given by the equation:



The iron-end member minnesotaite is a pyrophyllite-talc group mineral, which hosts Fe²⁺ whereas produced magnetite hosts Fe³⁺ resulted from iron oxidation producing hydrogen as shown above (equation 5-8). If the reaction reaches equilibrium, fayalite completely dissolves and the solution reaches near equilibrium with respect to fayalite (SI = -0.32). Hydrogen produced by the iron oxidation reacted with carbonate and/or CO_{2(aq)} producing simple organic molecules (<C3). The main dissolved organic species are methane (0.25 mol/L), formate (7.00 mmol/L), similarly to the previously discussed Systems 1, 2 and 3 (Figure 5-21). The concentrations of dissolved acetate (0.42 μmol/L) and formic acid (0.96 μmol/L) are approximately four orders of magnitude less than that of methane. Methanol and acetic acid concentrations are 0.3 and 0.5 nmol/L. The concentrations of formaldehyde, ethanol and acetaldehyde are extremely small and less than 10⁻¹¹ mol/L. The solution reaches near equilibrium with respect to quartz, ferrosilite (Fe,Mg)₂Si₂O₆) and chalcedony (SiO₂). The equilibrium solution contained 3 mmol/L of dissolved hydrogen H_{2(aq)}, 0.022 mol/L of dissolved carbon dioxide CO_{2(aq)} and 0.25 mol/L of methane remains in the solution (Figure 5-20).

System 5, (addition of 10 mg of sphalerite): The reaction between fayalite and NaHCO₃ produced minnesotaite, magnetite and hydrogen as given in equation [5-8]. Fayalite dissolves completely and the solution remained near equilibrium with respect to fayalite (SI = -0.32). Approximately 2.9 wt.% of sphalerite dissolved precipitating zincite (ZnO) and H₂S according to the equation given below:



The calculations show that 0.4 μmol/L of H₂S has formed. Nevertheless, the addition of sphalerite does not seem to change the thermodynamic equilibrium significantly and does not affect the formation of dissolved reduced organic compounds. The quantities of methane, formate and other organic species are in same order of magnitude compared to system 5 (Figure 5-21). The solution also reaches equilibrium with respect to quartz, ferrosilite and chalcedony. Finally, 24 μmol/L of CO_{2(aq)} and 3 μmol/L H_{2(aq)} and 0.25 mol/L methane remain in the equilibrium solution (Figure 5-20).

System 6, (addition of 10 mg of marcasite): The equilibrium calculations show that minnesotaite, magnetite and hydrogen are formed upon complete dissolution of added fayalite, similar to system 4 and 5 (equation 5-8). The added marcasite completely dissolved under these conditions precipitating troilite, and producing H₂S following:



The complete dissolution of marcasite seemed to affect the reaction products significantly. For instance, the amount of dissolved methane (0.13 mmol/L) and formate (3.7 μmol/L) in this system were half of that obtained for the two systems discussed above. Acetate formed in this system (250 μmol/L) is three orders of magnitudes less than those observed for systems 4 and 5. However, the formation of formic acid, methanol, acetic acid, formaldehyde and ethanol and acetaldehyde are not affected significantly by the addition of marcasite (Figure 5-21). The equilibrium solution contained 1.4 μmol/L of H_{2(aq)}, 0.31 μmol/L of CO_{2(aq)} and 0.13 mol/L methane (Figure 5-20).

Table 5-9. Summary of fluid composition and precipitated phases obtained thermodynamic modelling of the reaction of fayalite \pm catalyst (sphalerite or marcasite) with NaHCO_3 at 573 K and 30 MPa, at equilibrium.

	System 4 Fayalite	System 5 Fayalite+sphalerite	System 6 Fayalite+marcasite
<i>Dissolved species (mol/L)</i>			
H_2	3.00E-03	3.04E-03	1.36E-03
CO_2	2.20E-02	2.37E-02	3.08E-01
CH_4	2.50E-01	2.50E-01	1.32E-01
Formate	7.00E-03	7.41E-03	3.68E-03
H_2S	0.00E+00	3.67E-07	3.00E-03
Acetate	4.24E-05	4.3E-05	2.5E-08
Formic acid	9.56E-07	1.0E-06	5.8E-06
Methanol	3.40E-08	3.5E-08	4.1E-08
Acetic acid	5.15E-08	5.5E-08	3.8E-07
Formaldehyde	1.20E-11	1.3E-11	3.4E-11
Ethanol	7.89E-11	8.1E-11	1.1E-10
Acetaldehyde	4.08E-12	4.3E-12	1.3E-11
<i>Solid phases in the system (molal)</i>			
Magnetite	46.7	46.7	43.6
Minnesotaite	55.9	55.9	56.4
Troilite	-	-	10.4
Sphalerite	-	9.7	-
Na_2CO_3	3.8	3.8	-
Zincite	-	5.40E-02	-
<i>Phases near equilibrium (SI)</i>			
Quartz	-0.24	-0.23	-0.15
Ferrosilite	-0.3	-0.3	-
Fayalite	-0.32	-0.32	-0.46
Chalcedony	-0.37	-0.37	-
Pyrrhotite	-	-	-0.07

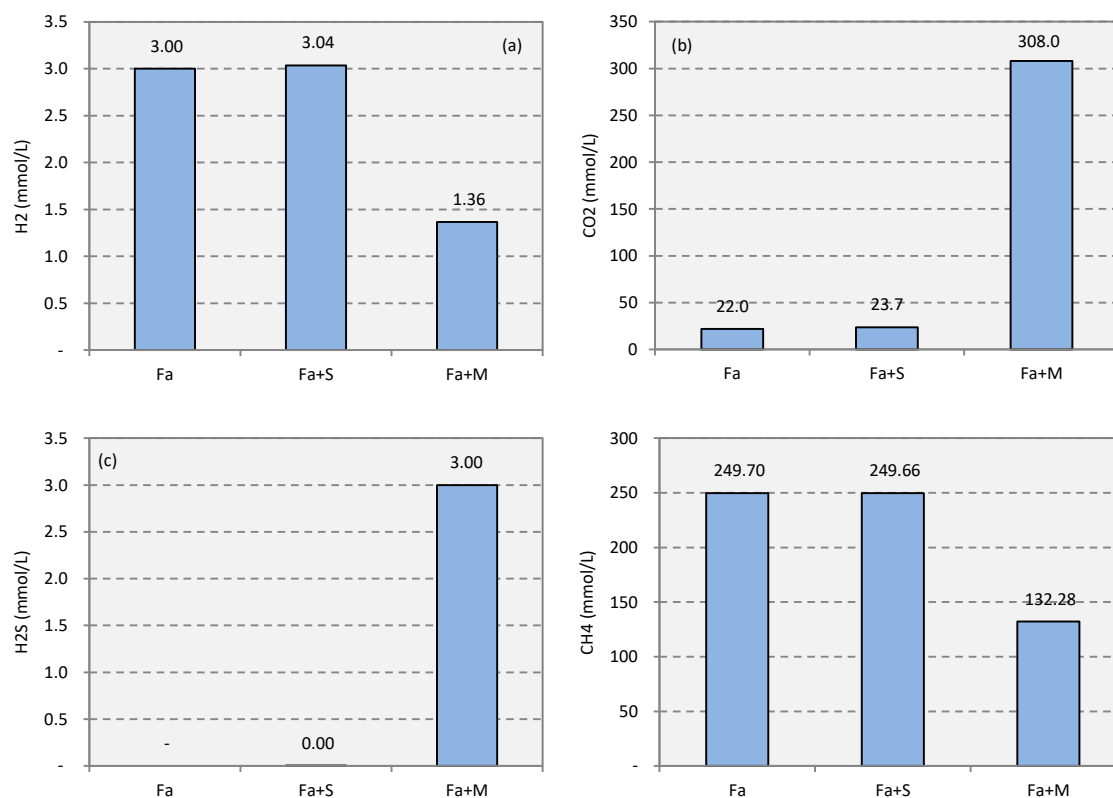


Figure 5-20. The equilibrium concentrations of dissolved (a) hydrogen (b) CO₂ (c) H₂S and (d) CH₄ in the solutions produced during the reactions of fayalite±catalyst (sphalerite or marcasite) with NaHCO₃ solution at 573 K and 30 MPa. The presence of Marcasite releases important amounts of H₂S at equilibrium, while CH₄ production is inhibited. The concentrations were modeled by CHESS geochemical code. (Abbreviations: Fa=fayalite, S=sphalerite, M=marcasite, Chl=chlorite, Ol=olivine (Fo90)).

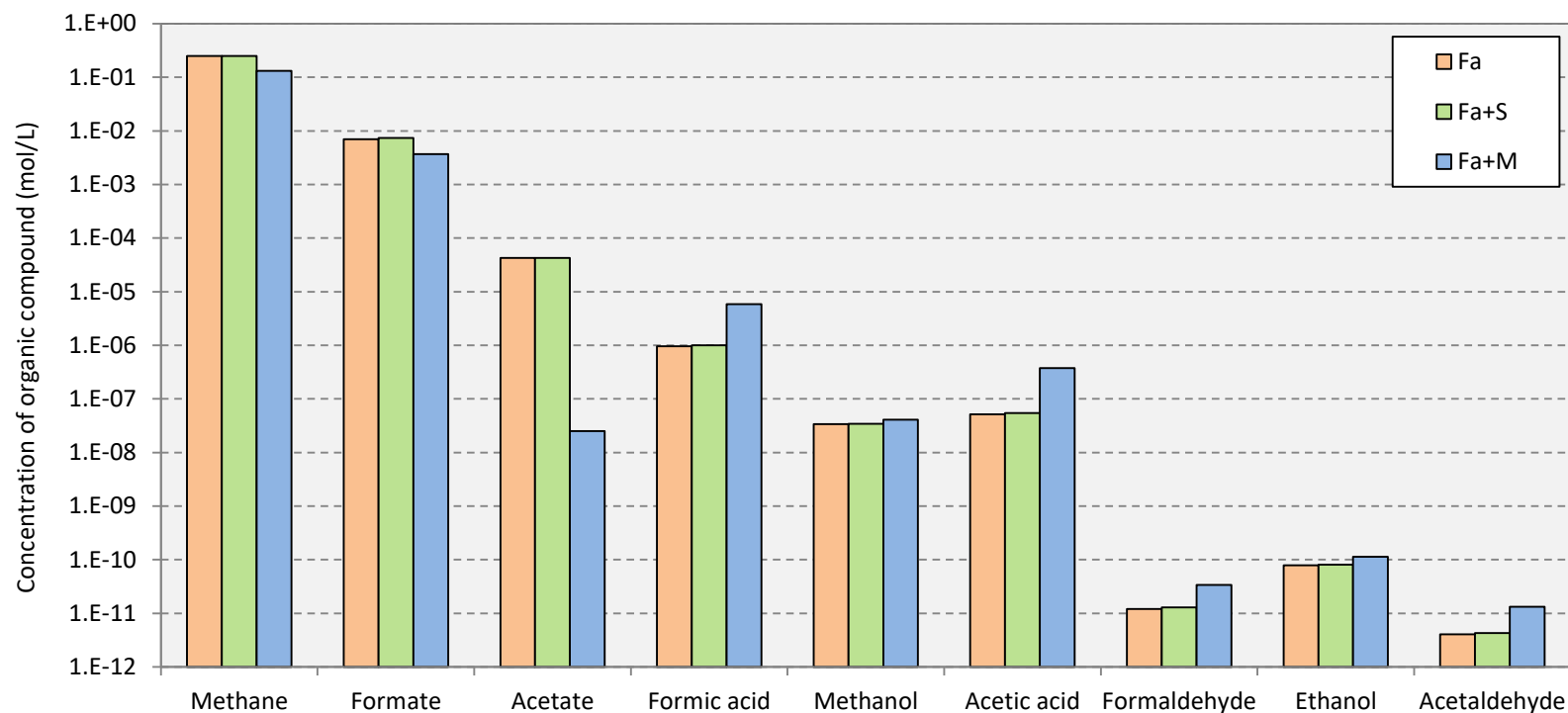
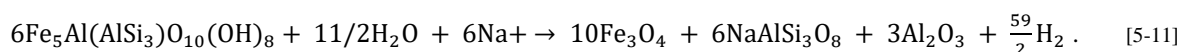


Figure 5-21. The equilibrium concentrations of dissolved organic compounds in the solutions produced during the reactions of fayalite±catalyst (sphalerite or marcasite) with NaHCO_3 at 300°C and 30 MPa, calculated using by CHES geochemical code. Methane and formate are formed in mmol/L concentrations, while acetate and formic acid is formed in $\mu\text{mol/L}$ concentrations and other species formed in traces. (Abbreviations: Fa=fayalite, S=sphalerite, M=marcasite, Chl=chlorite, Ol=olivine (Fo90)).

5.4.1.3 Chlorite system.

System 7, (Chl): The fluid composition and the minerals formed at the equilibrium in chlorite, chlorite+sphalerite and chlorite+marcasite systems were summarized in Table 5-10. The concentration of H₂, CO₂, H₂S and CH₄ are plotted in Figure 5-22. A comparison of the amounts of organic compounds formed in each system is given Figure 5-23. At equilibrium, chamosite, the iron-end member of the chlorite group, altered completely into magnetite, albite and corundum by reacting with NaHCO₃ solution at 573 K and 30 MPa. Oxidation of Fe²⁺ in chamosite into magnetite produced hydrogen in this system, following:



Hydrogen, produced by the oxidation of iron in chamosite into magnetite, created conditions reducing enough for the reduction of HCO₃²⁻ and/or CO_{2(aq)} into simple organic compounds. Dissolved methane (0.21 mol/L), and formate (3.5 mmol/L) are the main organic species in the solution followed by acetate (0.31 μmol/L), formic acid (5.1 μmol/L), methanol and acetic (0.05 μmol/L) acid (0.42 μmol/L) (Figure 5-23). Formaldehyde, ethanol and acetaldehyde concentrations are extremely small, <10⁻¹¹ mol/L. The solution reached equilibrium with high-, and low- albite (NaAlSi₃O₈), analcime (NaAlSi₂O₆·H₂O) and quartz. Dissolved hydrogen, CO_{2(aq)} and methane in the final equilibrium solution are 1.7 mmol/L, 0.22 and mol/L 0.21 mol/L (Figure 5-22).

System 8, (addition of 10 mg of sphalerite): The calculations show that chamosite was altered into magnetite, albite and corundum according to equation 5-11. Addition of sphalerite does not seem to affect the thermodynamic equilibrium of the system significantly. The initially added sphalerite slightly dissolved (2.9 wt.%), precipitating traces of zincite (equation 5-9). As a result of sphalerite dissolution, H₂S (0.37 μmol/L) is formed. However, the formation of traces of H₂S does not seem to affect the formation of organic compounds, since concentrations of methane, formate and other light hydrocarbons (<C3) were in the same order of magnitude compared to the system without any catalyst (System 7). Finally, the solution reaches equilibrium with high- and low-albite, analcime and quartz, similar to the chamosite and NaHCO₃ system. The concentrations of CO_{2(aq)}, H_{2(aq)}, and methane in the final solution were 0.22 mol/L, 1.2 mmol/L and 0.21 mol/L respectively (Figure 5-22).

System 9, (addition of 10 mg of marcasite): The equilibrium calculations show that chamosite dissolved completely precipitating magnetite, albite and corundum, and producing hydrogen (equation 5-11). However, the addition of marcasite imposed significant changes in the system equilibrium. The calculations show that marcasite completely dissolved (SI=-0.65) precipitating troilite (FeS) and producing H₂S (equation 5-7). Moreover, the quantity of H₂S formed in the presence of marcasite is four orders of magnitudes higher than the sphalerite-containing system (system 8). The equilibrium quantities of methane and formate quantities were half of those produced in Systems 7 and 8. However, there is no significant decrease in the concentration of other dissolved organic molecules (such as acetate, formic acid etc.) compared to Systems 7 and 8 (Figure 5-23). The solution reached equilibrium with respect to

pyrrhotite and minnesotaite. The equilibrium solution contained 0.43 mol/L $\text{CO}_{2(\text{aq})}$, 1.2 mmol/L of $\text{H}_{2(\text{aq})}$ and 0.15 mol/L of methane (Figure 5-22).

5.4.1.4 Summary of reaction paths predicted by thermodynamic modeling

The thermodynamic modeling of the nine systems concerned above leads to following conclusions:

- Hydrogen is produced in ~1-3 mmol/L quantities. However, in the marcasite added systems (olivine+marcasite; fayalite+marcasite; chlorite+marcasite), significant drop of hydrogen quantity was observed.
- H_2S is produced only in the marcasite added systems.
- Methane is produced in ~40-250 mmol/L quantities. However, in the marcasite added systems (olivine+marcasite; fayalite+marcasite; chlorite+marcasite), slightly lower amount of methane was formed.
- Formate was produced in ~1-7 mmol/L quantities. The other organic compounds were produced in traces, following the trend: formate>acetate>formic acid>methanol>acetic acid≈formaldehyde≈ethanol≈acetaldehyde

These calculations were based on the assumption that all the reactions occur at the thermodynamic equilibrium, and also that the sulfide minerals were reactants. Therefore, any difference between the model and the experimental results could arise due to the reactions occurring far from thermodynamic equilibrium conditions, and due to the catalytic activity of the added sulfide minerals.

Table 5-10. Summary of fluid composition and precipitated phases obtained thermodynamic modelling of the reaction of chlorite \pm catalyst (sphalerite or marcasite) with NaHCO_3 at 573 K and 30 MPa, at equilibrium.

	System 7 chlorite	System 8 Chlorite+sphalerite	System 9 Chlorite+marcassite
<i>Dissolved species (mol/L)</i>			
H_2	1.70E-03	1.67E-03	1.18E-03
CO_2	2.18E-01	2.18E-01	4.33E-01
CH_4	2.11E-01	2.11E-01	1.05E-01
Formate	3.50E-03	3.57E-03	1.64E-03
H_2S	-	3.67E-07	3.00E-03
Acetate	3.16E-05	3.2E-05	1.0E-05
Formic acid	5.06E-06	5.1E-06	7.1E-06
Methanol	5.30E-08	5.3E-08	3.7E-08
Acetic acid	4.20E-07	4.3E-07	4.2E-07
Formaldehyde	3.60E-11	3.6E-11	3.6E-11
Ethanol	1.90E-10	1.9E-11	9.5E-11
Acetaldehyde	1.80E-11	1.8E-11	1.3E-11
<i>Solid phases in the system (mg)</i>			
Corundum	24.3	24.3	24.3
Magnetite	44.1	44.1	38.4
Albite	24.9	24.9	24.9
Sphalerite	-	9.7	-
Troilite	-	-	13.7
Zincite	-	5.10E-04	-
<i>Phases near equilibrium (SI)</i>			
Albite(low)	-0.004	-0.004	-0.004
Analcime	-0.24	-0.24	-0.37
Quartz	-0.31	-0.31	-0.14
Albite(high)	-0.4	-0.4	-
Pyrrhotite	-	-	-0.06
Minnesotaite	-	-	-0.064

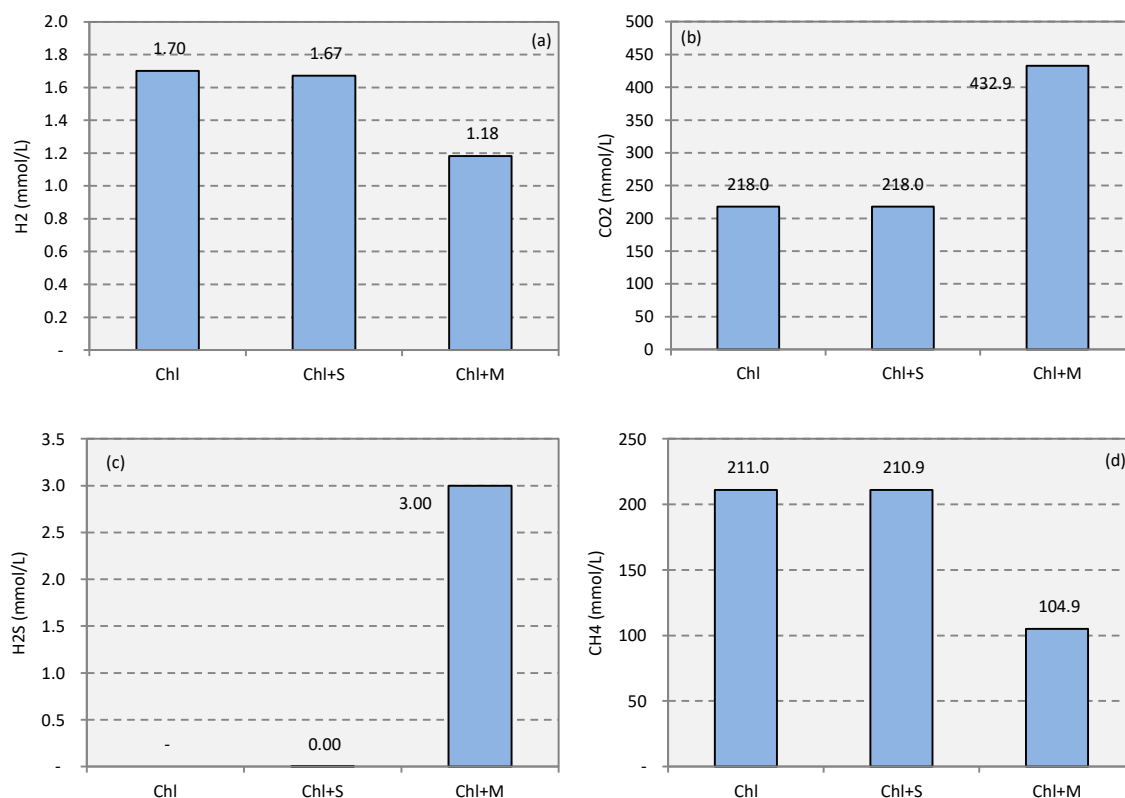


Figure 5-22. The equilibrium concentrations of dissolved (a) hydrogen (b) CO₂ (c) H₂S and (d) CH₄ in the solutions produced during the reactions of chlorite±catalyst (sphalerite or marcasite) with NaHCO₃ solution at 573 K and 30 MPa. The presence of marcasite releases important amounts of H₂S at equilibrium, while CH₄ production is inhibited. The concentrations were modeled by CHESS geochemical code. (Abbreviations: Fa=fayalite, S=sphalerite, M=marcassite, Chl=chlorite, Ol=olivine (Fo90)).

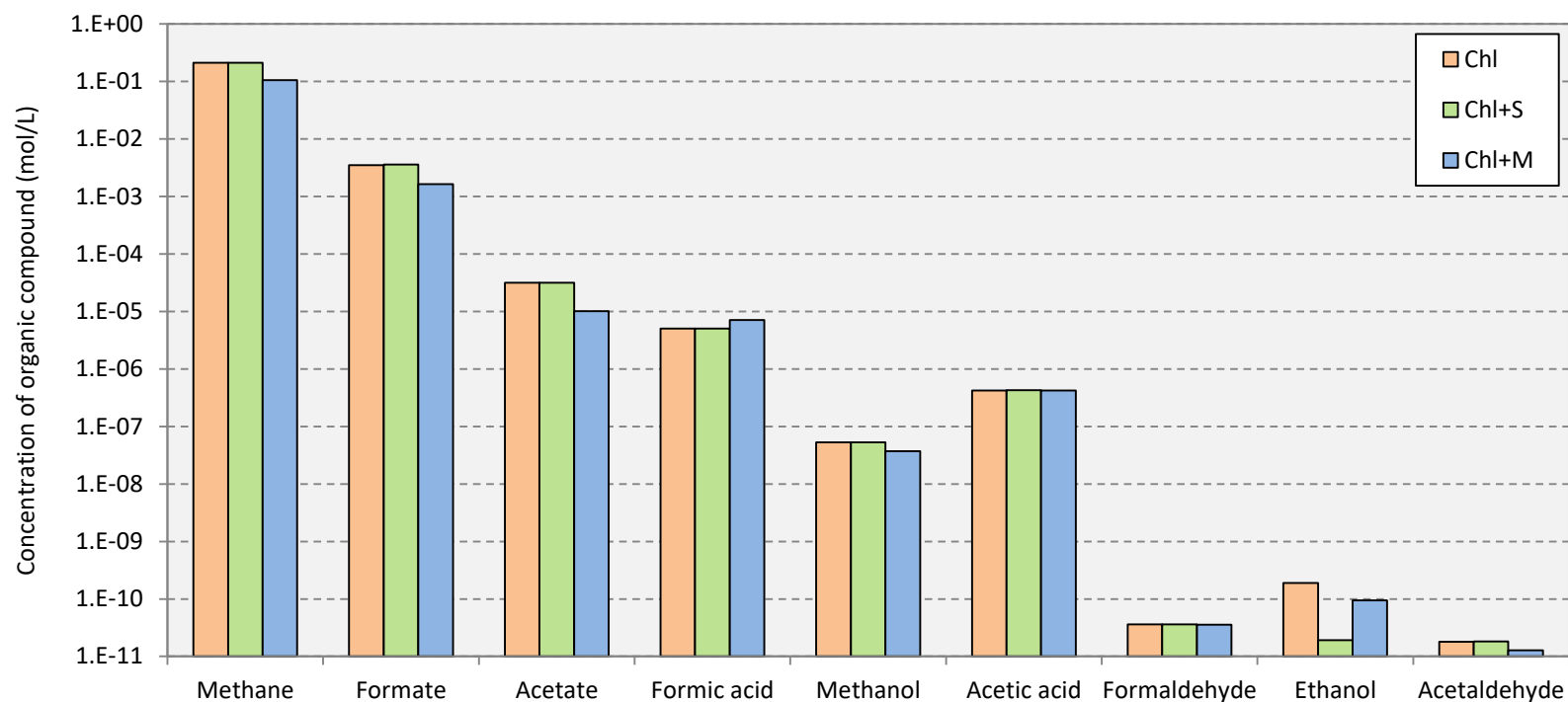


Figure 5-23. The equilibrium concentrations of dissolved organic compounds in the solutions produced during the reactions of chlorite±catalyst (sphalerite or marcasite) with NaHCO_3 at 300°C and 30 MPa, calculated using by CHES geochemical code. Methane and formate are formed in mmol/L concentrations, while acetate and formic acid is formed in $\mu\text{mol/L}$ concentrations and other species formed in traces. (Abbreviations: Fa=fayalite, S=sphalerite, M=marcassite, Chl=chlorite, Ol=olivine (Fo90)).

5.4.2 Summary of thermodynamic modelling and experimental data

5.4.2.1 Hydrogen production

Hydrogen produced via oxidation of Fe^{2+} in olivine (Fo90), fayalite and chlorite were obtained from: (1) the balanced equations 5-5, 5-8 and 5-11 assuming that the minerals were completely reacted; (2) the thermodynamic modelling (Table 5-8, 5-9 and 5-10); (3) the gas chromatography (GC) analysis that are reported in Table 5-11. The hydrogen concentration calculated via the balance equation was ~2 to 3 orders of magnitude higher than those obtained from CHESS calculation and GC measurement. Both methods (1) and (2) assume that the minerals were completely dissolved and all the Fe^{2+} was oxidized. Therefore, the difference in H_2 quantities between the methods (1) and (2) represents the consumption of hydrogen for the reduction of inorganic carbon, which has been taken into account by the CHESS equilibrium calculation. The CHESS calculation performed at equilibrium for this study does not take into account the kinetic laws of mineral dissolution, which could play an important role, especially in the experimental systems. For instance, the granulometry of the mineral powders (and thus their specific surface area) have a large impact on dissolution kinetics. Furthermore, it is interesting to notice that the equilibrium concentrations of hydrogen in olivine and fayalite systems measured with GC are slightly lower than the value modeled using CHESS. In contrast, the chlorite system produced slightly higher quantities of hydrogen than the modeled value. These observations indicate that the experiments might not have reached equilibrium at the time they were stopped.

Table 5-11. Hydrogen produced by Fe-rich minerals at 573 K and 30 MPa.

Mineral	H_2 (mol/L)		
	Theoretical ^(a)	CHESS model ^(b)	Measured in GC ^(c)
Olivine	0.7	0.0017	0.0012±0.0001
Fayalite	4.9	0.0030	0.0009±0.0000
Chlorite	3.5	0.0021	0.0044±0.0002

^(a) Hydrogen calculated according to the equation: $2\text{Fe}^{2+}_{(\text{aq})} + 2\text{H}_2\text{O}_{(\text{l})} = 2\text{Fe}^{3+}_{(\text{aq})} + 2\text{OH}^{-}_{(\text{aq})} + \text{H}_{2(\text{g})}$.

^(b) Equilibrium concentration of hydrogen calculated using CHESS geochemical code (given in table 5-8, 5-9 and 5-10).

^(c) Hydrogen measured in the gas phase using gas chromatography (GC), reported with 5% error associated with data (Table 5-7).

The results of the thermodynamic modelling demonstrated that the addition of marcasite imposes significant changes in the system: (1) H_2S production (2) low H_2 quantity (3) low methane quantity; compared to the system without marcasite. The results indicated that marcasite completely dissolved, producing H_2S . However, the amount of hydrogen in the produced H_2S does not compensate the amount of hydrogen in methane (i.e. ~1 to two orders of magnitudes lower than the amount of hydrogen in methane produced without a catalyst).

Therefore, the hydrogen mass balance in this system remains incomplete in gaseous form, and may have reacted to form dissolved organic compounds. In contrast, the dissolution of ~3wt% of sphalerite (according to CHESS modeling) does not seem to change the uncatalyzed system significantly. However, in the experiments, the capsules that contained sphalerite produced more hydrogen compared to those without sphalerite (Figure 5-25). Although it cannot be modeled using CHESS code, it is possible that sphalerite catalyzes production of hydrogen in these experiments. However, more experimental evidences are necessary to prove this hypothesis.

5.4.2.2 Far-from-equilibrium methane production

According to this thermodynamic calculation, the reaction path which leads to methane production takes a similar form than that described by Seewald et al. (2006). The equilibrium methane formation takes place through the stepwise reduction of dissolved CO₂, into formic acid \leftrightarrow formate, formaldehyde and methanol, in which formate is the most abundant dissolved organic species in the solution. In addition to these mono-carbon compounds, the formation of simple reduced carbon compounds up to C₄ is also thermodynamically favoured. However, the methane measured in the experimental samples were few orders of magnitude smaller than the methane produced at equilibrium (as calculated by CHESS code) indicating that methane formation occurred at far-from-equilibrium conditions (Figure 5-24). In addition, the liquid analysis of these experiments indicated that the concentration of dissolved intermediaries were below the detection limits of HPLC (formate/formic acid =2.08 mmol/L; acetate/acetic acid =1.67 mmol/L) and liquid state NMR analysis (detection limit).

5.4.2.3 Formation of carbon-rich solid phases

The mineral stability domains as a function of CO₂ and H₂ activities of the experimental and modeled fluids are shown in Figure 5-25 to 5-27. Let's consider the olivine system first (Figure 5-25). The activity of CO₂ and H₂ in both the experimental fluid and thermodynamically model fluid, fall within the magnetite stability field, close to the calculated CO₂-graphite equilibrium. The sphalerite-enhanced system, which produced the highest amount of hydrogen (compared to olivine alone, and olivine+marcasite experiments, Table 5-7 and Figure 5-29), is in the graphite stability field indicating the possibility of formation of solid graphite. Thermodynamically modeled fluid composition of the fayalite system remained at the CO₂-graphite equilibrium, whereas the experimentally observed fluid composition remained far from the graphite stability field (Figure 5-26). The modeled fluid composition of the chlorite system remained at the CO₂-graphite equilibrium, similar to modeled fluid of fayalite system. The fluid of marcasite-enhanced experimental system remained far from CO₂-graphite equilibrium, whereas those with chlorite alone and with added sphalerite lie well within the graphite stability field, indicating that marcasite is reacting in the system and potentially changing the redox conditions (-also observed by slight changes in calculated E_h values: [(Ol) and (Ol+S)=-0.85V; (Ol+M)=-0.69V; (Fa) and (Fa+S)=-0.85V; (Fa+M)=-0.70V; (Chl) and (Chl+S)=-0.72V; (Chl+M)=-0.65V]).

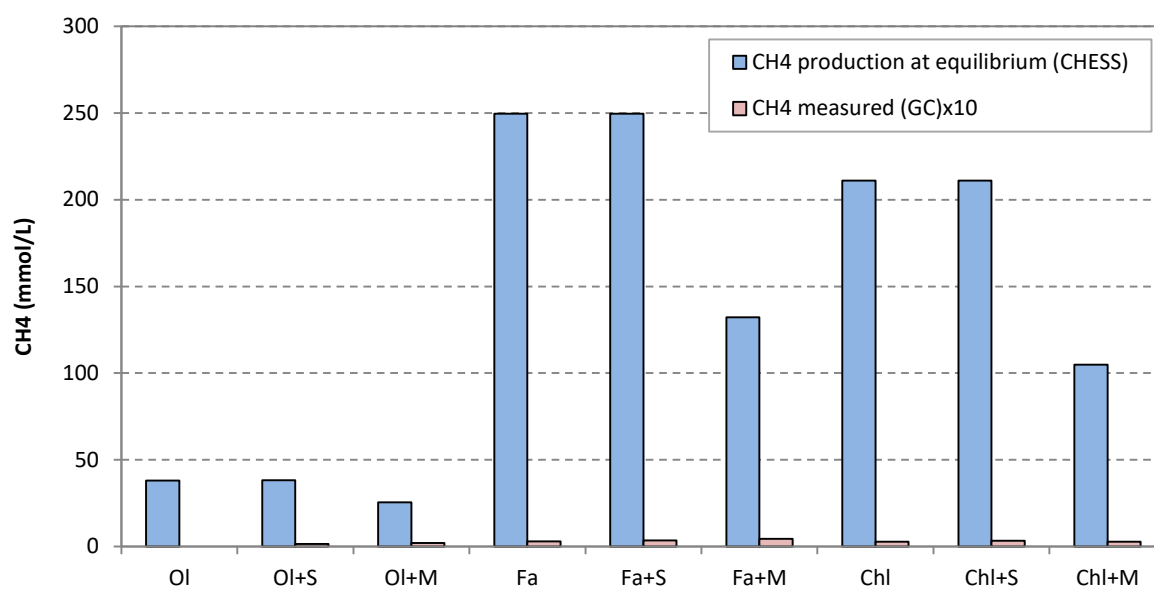


Figure 5-24. Measured methane concentrations are few orders of magnitude smaller than the methane anticipated at thermodynamic equilibrium.

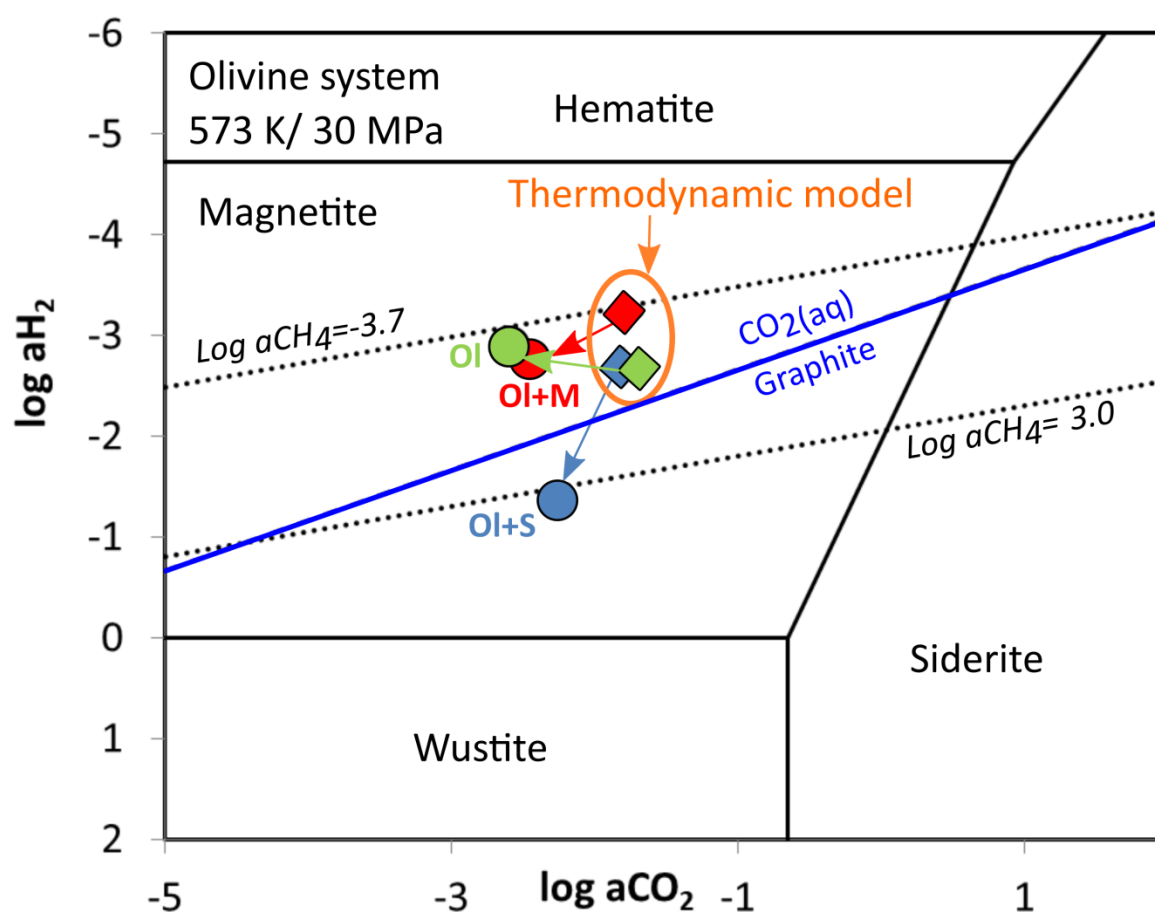


Figure 5-25. Mineral stability domains as a function of CO_2 and H_2 activities of olivine system at 573 K and 30 MPa. The black lines represent the thermodynamic equilibria between wustite, magnetite, hematite and siderite. The blue line represents the equilibria between CO_2 and solid graphite. The dotted lines represent the activity of methane in equilibrium with increasing H_2 in the system. The activity of CO_2 and H_2 in both the experimental fluids (circles) and thermodynamically model fluid (diamonds), fall in the magnetite stability field, close to the calculated CO_2 -graphite equilibrium. The sphalerite added system is in the graphite stability field, and H_2 activity is over one order of magnitude higher than in the other systems.

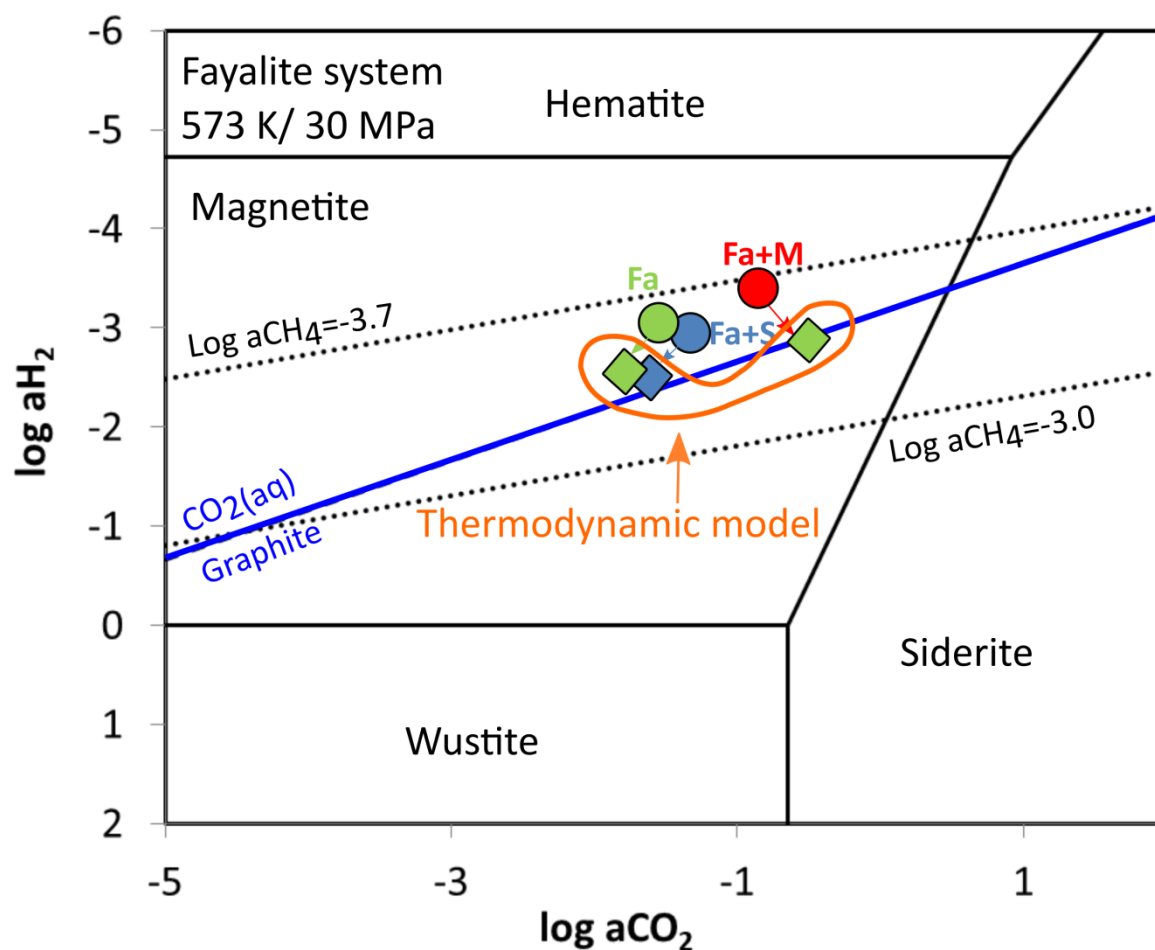


Figure 5-26. Mineral stability domains as a function of CO_2 and H_2 activities of fayalite system at 573 K and 30 MPa. The black lines represent the thermodynamic equilibria between wustite, magnetite, hematite and siderite. The blue line represents the equilibria between CO_2 and solid graphite. The dotted lines represent the activity of methane in equilibrium with increasing H_2 in the system. The activity of CO_2 and H_2 in both the experimental fluids (circles) and thermodynamically model fluid (diamonds), fall in the magnetite stability field. At equilibrium, the fluid reaches the CO_2 -graphite equilibrium, whereas the experimentally measured CO_2 and H_2 reach close to the CO_2 -graphite equilibrium.

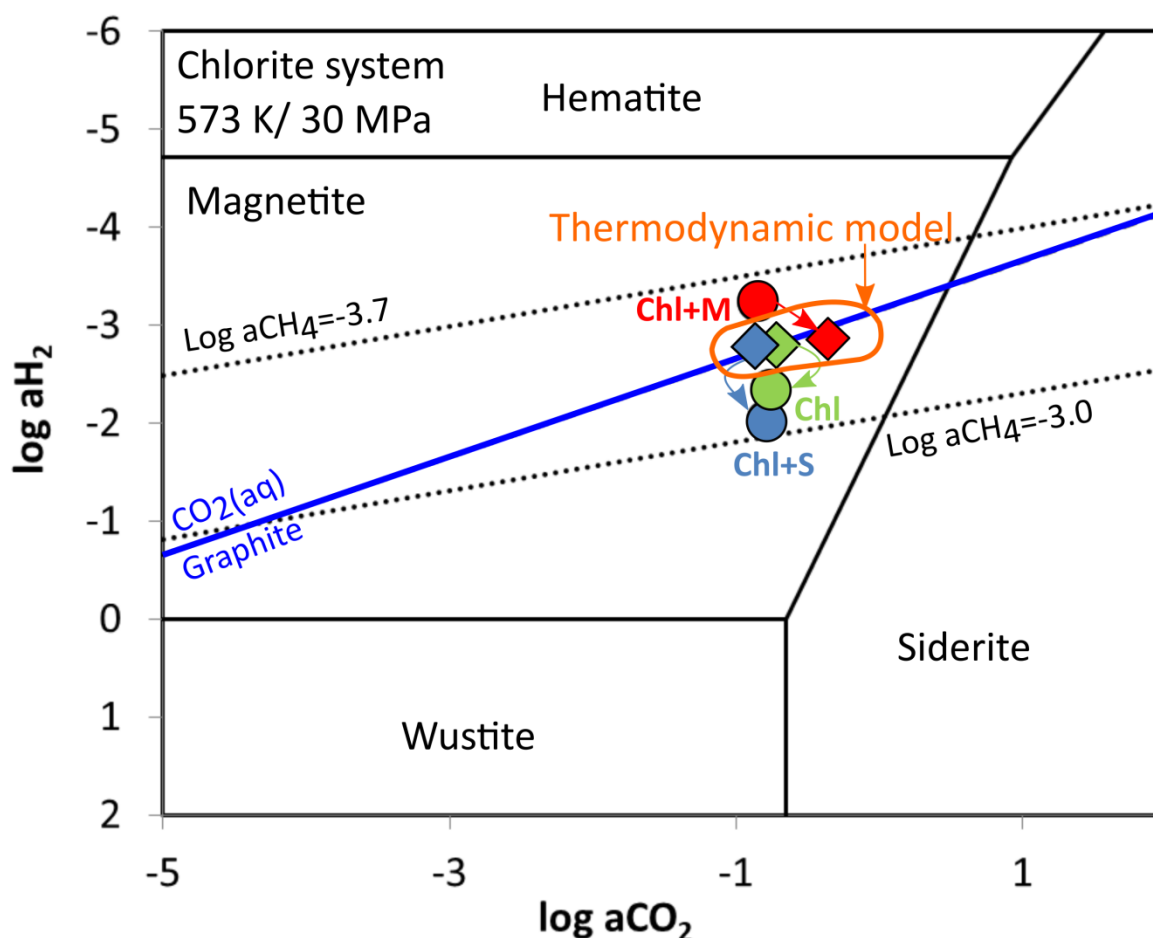


Figure 5-27. Mineral stability domains as a function of CO_2 and H_2 activities of chlorite system at 573 K and 30 MPa. The black lines represent the thermodynamic equilibria between wustite, magnetite, hematite and siderite. The blue line represents the equilibria between CO_2 and solid graphite. The dotted lines represent the activity of methane in equilibrium with increasing H_2 in the system. The activity of CO_2 and H_2 in both the experimental fluids (circles) and thermodynamically model fluid (diamonds), fall in the magnetite stability field. At equilibrium, the fluid reaches the CO_2 -graphite equilibrium, whereas the experimentally measured CO_2 and H_2 in the chl and chl+M experiments are in the graphite stability field.

5.4.3 Experimental production of C₁-C₄ hydrocarbons and catalysis by sphalerite and marcasite

The experiments conducted to determine the background carbon levels indicated that starting minerals could contain significant quantities of carbon. As they were natural samples, carbon could be present as surface contaminants, as well as in fluid inclusions (CO₂ fluid inclusions in mantle olivine (Créon et al., 2018)). The experiments conducted with fayalite resulted in significantly higher quantities of organic carbon compared to the background carbon levels (Figure 5-2). This indicates that, in the fayalite-containing experiments, there is a better conversion of introduced HCO₃⁻ into organic compounds, contrarily to the experiments with chlorite and olivine (Fo90), maybe because of a higher H₂ partial pressure due to a higher Fe content. The experiments with fayalite alone, fayalite+sphalerite, and fayalite+marcasite produced 0.30, 0.45 and 0.35 mmol/L of methane after 20 days of reaction, with a small conversion rate of 0.11, 0.25 and 0.17% respectively. A comparison between the quantities of methane produced in our fayalite experiments with those reported in literature, in which experiments were performed with various other catalysts, is presented Table 5-6. The amounts of methane in our experiments do not differ drastically from those previously reported. Higher quantities of methane were produced in our experiments compared to those reported by Berndt et al. (1996), Fu et al. (2007), Fu et al. (2008), Foustoukus and Seyfried (2004), and chalcocite, chromite and magnetite containing experiments of Martinez et al. (2017). However, they correspond to lower quantities than those produced in the presence of pyrite, pyrrhotite and chalcocite reported by Martinez et al. (2017). Overall, small quantities of methane and low conversion rates, confirm that methane synthesis is kinetically extremely sluggish, even at higher temperatures (300°C). Another reason for the observed small quantities of methane and low conversion rates could be the effect of reaction medium. As previously mentioned, the possibility of abiotic hydrocarbon production in the aqueous media has been experimentally demonstrated. However, a recent experimental study by McCollom (2016), showed that higher amounts of methane were formed in the vapour phase compared to those formed in aqueous phase, suggesting that the presence of a separate gas phase might be more favourable for abiotic synthesis of CH₄. Therefore, whether the abiotic hydrocarbon synthesis by FTT reactions takes place in liquid phase or in the vapour phase remains an open question.

Significant quantities of hydrocarbons were formed in our fayalite-containing experiments (essentially above background carbon levels), via the reduction of introduced HCO₃⁻ (Figure 5-2). Although the Schulz-Flory r^2 values of these experiments - 0.74 [Fa], 0.89 [Fa+S], 0.39 [Fa+M] - were all below 0.9, which is more characteristic of a thermal maturation of organic compounds than a FTT synthesis, the chain growth probability factors (α) of these experiments (0.23 [Fa], 0.22 [Fa+S], 0.39 [Fa+M]) indicate a high probability of chain growth. Therefore, the formation mechanism of hydrocarbons in the fayalite experiments remains unclear. One possibility could be that the gaseous compounds could form from maturation of a condensed C source, produced by reduction of inorganic C as shown by Milesi et al. (2015) for example.

Shipp et al. (2014) calculated the equilibrium concentration of Zn^{2+} that would be present as a result of dissolution of ZnS for their experimental conditions (300°C and 100 MPa) to be 4.4×10^{-6} mol/L. They also confirmed that the catalysis of C-H bond formation was not due to the aqueous Zn^{2+} . They pointed out that sulfide dissolution could be possible, and the aqueous sulfide species could have an effect on catalysis. Similarly in our experiments, we assume that both sphalerite and marcasite might slightly dissolve, but since our experimental set-up does not allow the quantification of dissolution, its significance remains unclear. Moreover, we were unable to examine the speciation and/or transformation of marcasite experimentally at 300°C and at 30 MPa conditions, which was transformed into pyrite in one of the experiments as indicated by Figure 5-6. Although preliminary results of thermodynamic modelling indicated that pyrite becomes stable at alkaline pH compared to marcasite, more experiments will be necessary to evaluate the stability of these minerals which might alter the nature of their surfaces and affect their catalytic ability (Kitchaev et al., 2016).

Our results are in agreement with those of Shipp et al. (2014), who demonstrated that sphalerite has the ability to activate C-H bond formation. In addition, the Fe-sulfide used in their experiment produced complex hydrocarbons compared to those expected, and at a lower conversion rate. In our study, marcasite-rich experiments resulted in higher quantities of total carbon, and higher conversions rates, compared to sphalerite-enhanced experiment. The chain growth probability (α) of these catalysts indicated that both of them promote the hydrocarbon chain growth ($\alpha = 0.22$ in Fa+S system; $\alpha = 0.17$ in Fa+S system).

The instability of marcasite in this system could arise due to the prevailing low H_2S fugacity or alkaline pH (induced through water reduction and H_2 production). Both the thermodynamic modeling (equation 5-7) and XRD showed that marcasite transformed into pyrite, during the reaction (Figure 5-7, 5-10 and 5-12). At higher H_2S fugacity, marcasite might be stable. However, in order to act as a catalyst, by definition, the catalyst mineral must be stable and 100% recoverable at the end of the reaction. In addition, it should not be involved in any chemical reaction in the system. From this point of view, sphalerite has higher catalytic ability than marcasite. In nature, however, in the fluids rich in H_2S , marcasite might be stable and could act as a catalyst for C-H bond formation.

In addition to hydrocarbon production, it is interesting to notice that larger amount of hydrogen was produced in the sphalerite-rich experiments, compared to those with marcasite or without catalyst (Figure 5-8). This might indicate a catalytic effect of sphalerite on water reduction and H_2 production. Such a property was already proposed for Zn-rich spinels by Mayhew et al. (2013)

Finally, judging from the results obtained in Martinez et al., 2017 (presented in Table 5-12 and Figure 5-28), it is apparent that sulphides are at least, more efficient than spinels to catalyse FTT synthesis. They also present a variability in efficiency depending on the metal bonded to sulphur; this warrants further investigation of sulfide phases present in nature samples in hydrothermal settings.

Table 5-12. Comparison of quantity of methane produced in the presence of various mineral catalysts. The P/T of the experiments, the Fe-rich minerals which involve in production of hydrogen, and the quantities of H₂ produced are also reported.

Fe rich mineral / solution	Catalyst	P/T	t (days)	H ₂ mmol/L	CH ₄ mmol/L	Reference
Fayalite	Sphalerite (ZnS)	300°C/ 30 MPa	20	1.13	0.35	This study
Fayalite	Marcasite (FeS ₂)	300°C/ 30 MPa	20	0.40	0.45	This study
Fayalite	Magnetite (Fe ₃ O ₄)	300°C/ 30 MPa	20	0.89	0.30	This study
Olivine	Magnetite (Fe ₃ O ₄)	300°C/ 50 MPa	69	158	0.08	Berndt et al., 1996
Formic acid	Magnetite (Fe ₃ O ₄)	400°C/ 50 MPa	42	150	0.32	Fu et al., 2007
Formic acid	Pentlandite ((Fe,Ni) ₉ S ₈)	400°C/ 50 MPa	38	13	0.01	Fu et al., 2008
H ₂ +formic acid	Fe,Ni alloy	300°C/ 50 MPa	5	222	11.53	Horita and Berndt, 1999
H ₂ +formic acid	Fe,Ni alloy	400°C/ 50 MPa	5	196	7.34	Horita and Berndt, 1999
Wustite	Chromite+Wustite(Cr ₂ O ₃)+FeO	390°C/ 40 MPa	44	192	0.12	Foustoukus and Seyfried., 2004
Wustite	Wustite (FeO)	390°C/ 40 MPa	120	121	0.20	Foustoukus and Seyfried., 2004
Olivine	Pyrite (FeS ₂)	200°C/20 MPa	21	56.32	0.53	Martinez et al., 2017
Olivine	Pyrrhotite (Fe ₇ S ₈)	200°C/20 MPa	21	68.55	0.56	Martinez et al., 2017
Olivine	Chalcocite(I) (Cu ₂ S)	200°C/20 MPa	21	85.32	0.17	Martinez et al., 2017
Olivine	Sphalerite (ZnS)	200°C/20 MPa	21	73.37	0.34	Martinez et al., 2017
Olivine	Chromite (Cr ₂ O ₃)	200°C/20 MPa	21	77.12	0.07	Martinez et al., 2017
Olivine	Magnetite (Fe ₃ O ₄)	200°C/20 MPa	21	122.21	0.04	Martinez et al., 2017
Fayalite	Chalcocite(II) (Cu ₂ S)	200°C/20 MPa	21	88.53	0.65	Martinez et al., 2017

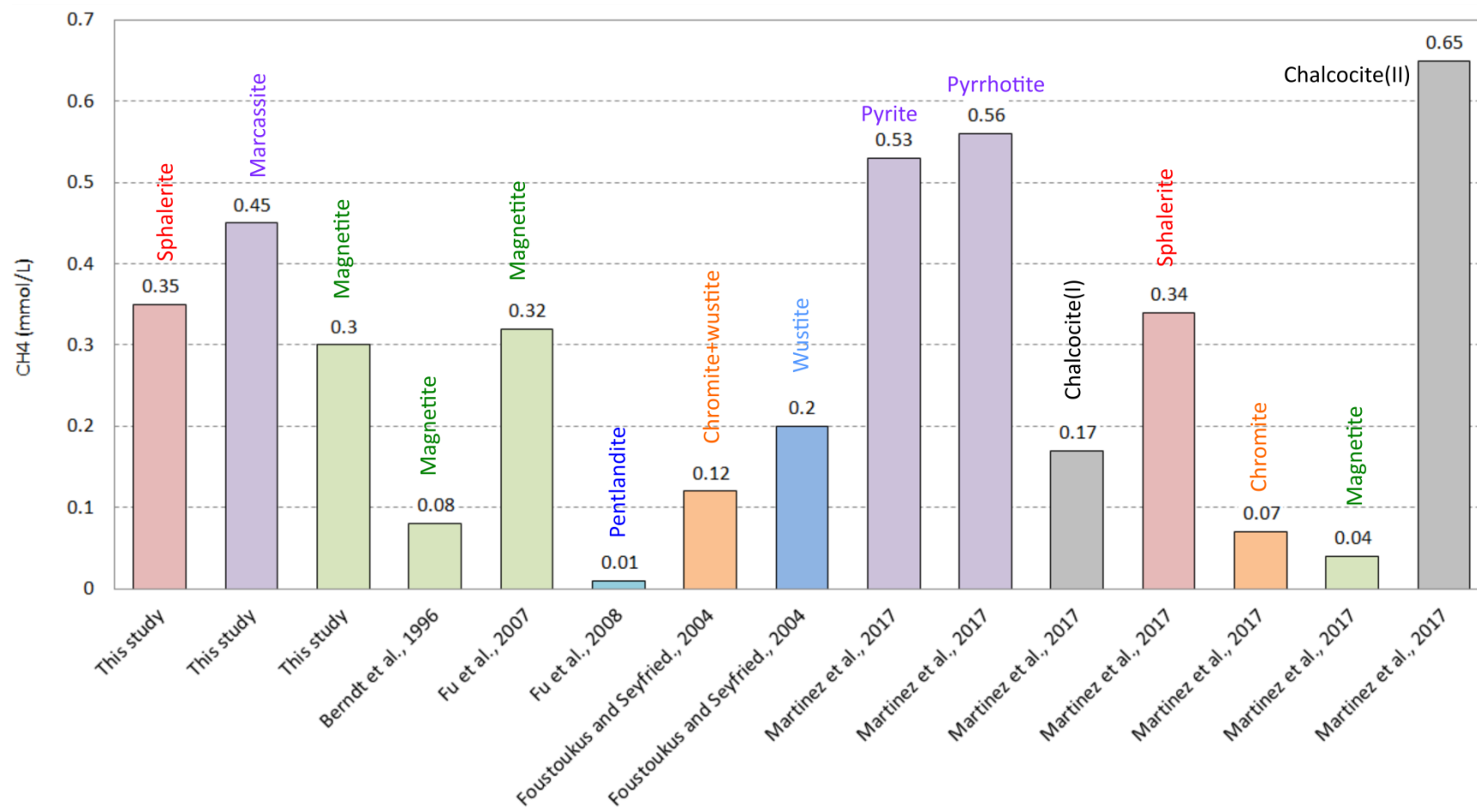


Figure 5-28. Comparison of quantity of methane produced in the presence of various mineral catalysts showing, except for pentlandite, sulphide based catalysts produce more methane compared to oxide catalysts such as magnetite and chromite (based on data are given in Table 5-12). Data of Horita and Berndt, 1999 were not included in the comparison since they were significantly higher than all these values.

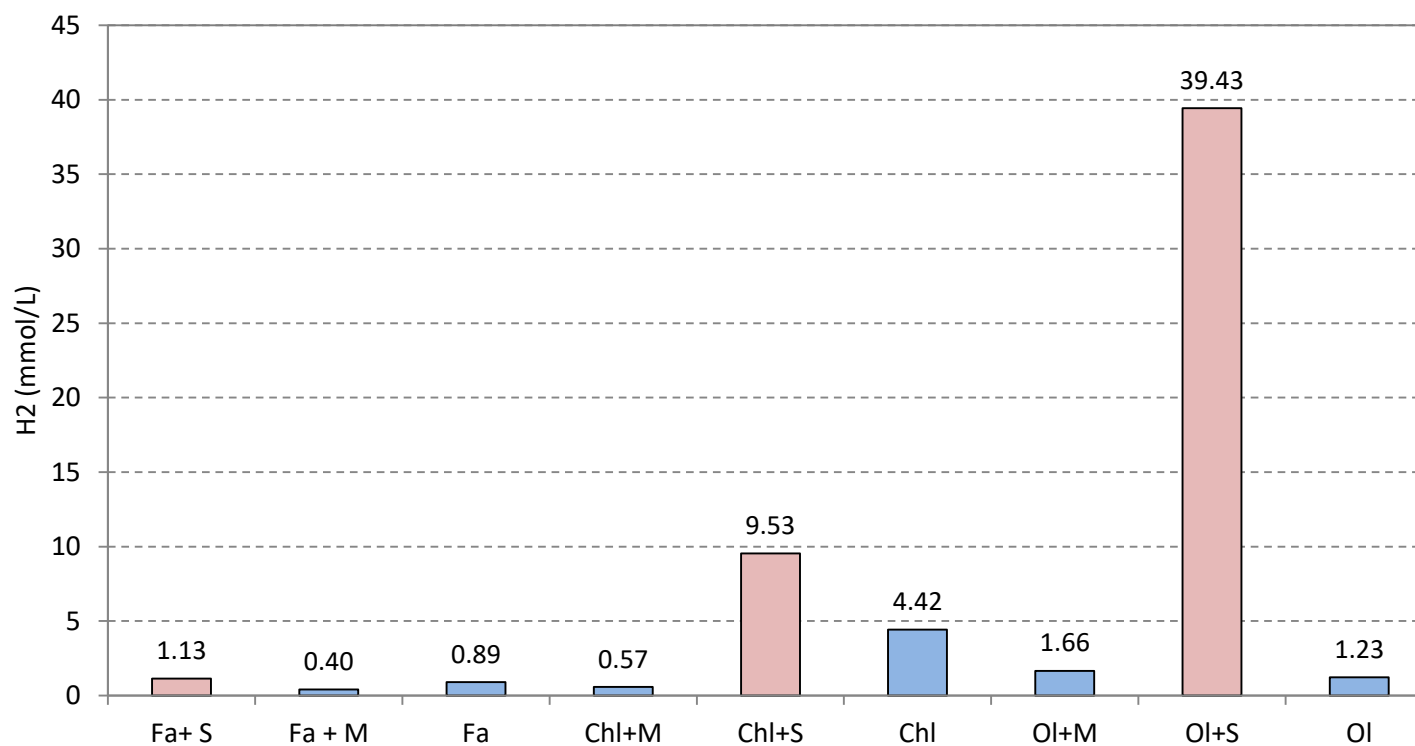


Figure 5-29. Higher amounts of hydrogen produced in the presence of sphalerite (ZnS) in our experiments conducted at 573 K, and at 30 MPa. H₂ productions in sphalerite containing experiments are indicated in red.
Abbreviations: Fa=fayalite, S=sphalerite, M=marcasite, Chl=chlorite, Ol=olivine (Fo90)

5.5 Conclusions

Laboratory simulation of abiotic hydrocarbons production via FTT synthesis were performed by reacting Fe-rich silicates with a 0.64M NaHCO₃ solution (pH~8) at 300°C and 30 MPa, adding marcasite and sphalerite as potential catalysts. The results of this study lead to following conclusions:

1. Natural samples contain carbon as contaminants as well as inclusions. Therefore, determination of background carbon level is crucial for the first order determination of carbon source.
2. In the experiments with chlorite and olivine (Fo90), background levels of carbon were measured approximatively in similar quantities as newly formed hydrocarbons. However, the experiments with fayalite clearly produced hydrocarbons above the background carbon levels, probably because higher H₂ concentrations were produced during the experiments.
3. There seems to be a slight catalytic effect of the sulfide minerals on methane formation when reacting fayalite. However, as the Schulz-Flory distribution is not indicative of a pure FTT synthesis, the hydrocarbon formation mechanism, though enhanced, remains unclear. The carbon source could come from the reduction of HCO₃⁻, or from the reaction of carbon compounds initially present in fayalite (but which did not show up in the blanks, and was converted to methane in the experiments because it reacted with the high amounts of H₂ produced). A last hypothesis could be that the gaseous compounds could form from maturation of a condensed and reduced C source, produced by reduction of inorganic C as shown by Milesi et al. (2015) and Martinez et al., 2017 for example.
4. The results agree with previous studies showing that formation of methane is kinetically sluggish even at higher temperatures such as 300°C.
5. Finally, it appears that sphalerite might have a catalytic effect on the generation of hydrogen, which is generated in quantities at least one order of magnitude larger than with the pure Fe-bearing silicates, or the mixture of Fe-silicate and marcasite. The question whether other sulfides may be able to serve as a catalyst for hydrogen production, remains open.

Chapter 6

Conclusions and perspectives

Conclusions

In the first part of this manuscript, the possibility of simultaneous ex-situ carbon dioxide (CO₂) storage and hydrogen (H₂) production using New Caledonian mine tailings have been investigated using various experimental and analytical apparatus at IFP energies nouvelles, Rueil Malmaison. The batch experiments conducted by reacting mine tailings with CO₂-saturated water, at 473 K - 573 K and under high pCO₂ of 15-30 MPa, at pH ~4, lead to the following conclusions.

[1] Those batch experiments have demonstrated the viability of using New Caledonian mine tailings in ex-situ carbonation process, while producing H₂ as a byproduct. The results indicate that mine tailings were altered into Fe-rich magnesite, (Mg,Fe)CO₃ and phyllosilicates when reacted with CO₂-saturated water at the above mentioned conditions. The competition between Mg and Fe incorporation among the secondary phases seems to control the quantities of magnesite precipitation and hydrogen production. The best conditions for the simultaneous ex-situ carbon dioxide (CO₂) storage and hydrogen (H₂) production are the temperatures between 523 K and 540 K at pCO₂=30 MPa, in order to maintain both carbonation and hydrogen production at optimum quantities.

[2] This work has suggested an application to treat New Caledonia's annual CO₂ emissions and energy demands cost-efficiently, by recycling the heat used in metal extraction (>1273 K), providing a novel valorization method for New Caledonian mine tailings. This approach could be globally applied to other mine tailings or industrial waste materials containing Ca, Mg, and Fe; however we believe that the optimum P/T conditions might vary depending on the mineral composition and textural features of individual material.

[3] Mine tailings can store significant quantities of CO₂ while producing significant amounts of H₂ by reacting with CO₂-saturated water at the conditions given above. However, the reactivity of mine tailings is lower compared its natural analogue, olivine. The glass, which amounts to 55 wt.% of the mine tailings has slower dissolution kinetics, subsequently limiting cation release, and thus carbonate precipitation and H₂ production.

[4] Based on the bulk analysis and nanometric scale analysis of the secondary products, three overall reactions were proposed. These reactions are qualitative, and do not take into account stoichiometric relations due to the complexity of clay mineral composition.

- The proposed overall reaction at 473 K/ 15 MPa is;

Mine tailings + water + CO₂ = (Fe, Mg)CO₃ (ferroan-magnesite) + Na_{0.3}Fe₂Si₄O₁₀(OH)₂·4H₂O (nontronite) + Mg_{0.7}(Mg, Fe³⁺, Al)₆(Si, Al)₈O₂₀(OH)_{4.8}H₂O (vermiculite) + SiO₂ (amorphous silica) + H₂ (hydrogen)

where, amorphous silica and vermiculite are present in traces. This reaction could also be an overall reaction consisting two steps; first, the serpentinization and then the carbonation of serpentinization products, as given below.

Mine tailings + water = (Mg,Fe,Al)₃Si₂O₅(OH) (serpentine) + (Mg,Fe)(OH)₂ (brucite) + Fe₃O₄ (magnetite) + H₂ (hydrogen)

(Mg,Fe,Al)₃Si₂O₅(OH) (serpentine) + Fe₃O₄ (magnetite) + O₂ + HCO₃⁻ = Na_{0.3}Fe₂Si₄O₁₀(OH)₂.4H₂O (nontronite) + Mg_{0.7}(Mg,Fe³⁺,Al)₆(Si,Al)₈O₂₀(OH)₄:8H₂O (vermiculite) + (Fe, Mg)CO₃ (ferroan-magnesite) + OH⁻ + H₂O

At high HCO₃⁻ activity and more oxidizing conditions, the latter reaction could completely mask the existence of serpentinization products depending on the reaction kinetics and thermodynamic stability of the phases.

- The proposed overall reaction at 523 K/ 30 MPa :

Mine tailings + water + CO₂ = (Fe, Mg)CO₃ (ferroan-magnesite) + Mg_{0.7}(Mg, Fe³⁺, Al)₆(Si,Al)₈O₂₀(OH)₄:8H₂O (vermiculite) + Fe oxide (Fe_xO_y) + chromite (Cr₂O₃) + H₂ (hydrogen)

where, iron oxide and chromite are present in traces.

- The proposed overall reaction at 573 K/ 30 MPa is:

Mine tailings + water + CO₂ = (Fe, Mg)CO₃ (ferroan-magnesite) + Na_{0.3}Fe₂Si₄O₁₀(OH)₂.4H₂O (nontronite) + proto-serpentine + Fe oxide (Fe_xO_y) + H₂ (hydrogen)

where proto-serpentine is present in traces.

[5] The secondary silicates formed by the reaction do not passivate the reactive surfaces.

In the second part of this manuscript, the ability of sulfides, and more particularly of sphalerite (ZnS) and marcasite (FeS₂) to catalyze the synthesis of abiotic hydrocarbon production via Fischer Tropsch Type (FTT) reactions were experimentally studied at 573 K/ 30 MPa. The following conclusions were drawn:

[1] The Fe-rich minerals dissolve at 573 K/ 30 MPa, in the 0.64 M NaHCO₃ solution (calculated pH~8) producing hydrogen. Inorganic carbon in the form of HCO₃⁻ reacts with hydrogen producing simple alkanes such as CH₄, C₂H₆, C₃H₈, and C₄H₁₀ (detectable in the gas phase). In addition, the carbon mass balance indicates the presence of reduced carbon in liquid solid form.

[2] Two techniques were used to detect dissolved reduced carbon species; the high performance liquid chromatography (HPLC) technique and the nuclear magnetic resonance (NMR) spectroscopy for liquid samples. The HPLC analysis indicated the presence of organic compounds which could not fit with the available standards. No organic compound was detected using the NMR analysis, suggesting the sulfides used are inefficient in catalyzing FTT reactions.

[3] The Schulz-Flory distribution suggests that these alkanes were not synthesized via FTT reaction. The Schulz-Flory R² values indicated that they were most probably formed by thermal decomposition of reduced carbon already present in the samples or formed during the reduction of inorganic C.

[4] Sphalerite seems however to catalyze the production of hydrogen when added to various Fe-rich silicates, in amounts at least one order of magnitude higher than it is with the presence of marcasite, or without any added minerals.

Perspectives

[1] The experimental results of carbon dioxide (CO₂) storage and hydrogen production from New Caledonian mine tailings presented in this study provide novel method of valorization of ultramafic mine tailings from New Caledonia. The study was focused on the quantities of CO₂ that can be stored while simultaneously producing hydrogen (H₂) (chapter 3), and the nature of water-rock interaction occur during these two simultaneous reactions (chapter 4). The results indicated that the reactivity of mine tailings is lower compared to olivine, due to the presence of glass, which is only a qualitative result. The effect of presence of glass on dissolution of mine tailings would be more interesting to study. Two additional experiments should be performed in order to obtain a quantitative result. Firstly, a flow-through experiment on mine tailings should be performed to determine the rate of dissolution of mine tailings at the P/T conditions of interest, keeping bulk solution far from thermodynamic equilibrium with any secondary phases. Secondly, a flow-through experiment on glass should be performed to determine the rate of dissolution of glass at the similar conditions. Glass can be separated from mine tailings using a suitable gravimetric method. A classical flow-through set-up or a batch micro-reactor coupled with in situ X-ray absorption spectroscopy (XAS) on synchrotron (Daval et al., 2010) could be used to perform the experiments.

[2] The experimental study on laboratory simulation of abiotic hydrocarbon production showed that marcasite and sphalerite do not explicitly catalyze the C-H bond formation at 573 K/ 30 MPa. This study was performed by using a commercially available NaHCO₃ as the carbon source, and therefore, the origin of the organic compounds could not be clearly traced. Few additional experimental studies should be performed by using a labeled carbon (¹³C) source such as NaH¹³CO₃. The idea would be to use a ¹³C enriched NaHCO₃ solution so that the resulting organic compounds would still be enriched in ¹³C even after isotopic fractionation during FTT synthesis. For instance, a NaHCO₃ solution with an isotopic composition $\delta^{13}\text{C} \sim 90\text{‰}$, would result methane with a $\delta^{13}\text{C} \sim 60\text{‰}$ assuming an isotopic fractionation of 30 ‰. Since natural carbon sources are depleted in ¹³C and have negative $\delta^{13}\text{C}$ values varying between $\delta^{13}\text{C} -14$ to -20‰ , such an experiment would allow to distinguish whether the source of carbon detected were the enriched ¹³C source or natural contamination carbon.

[3] As previous studies have suggested (McCollom, 2016), FTT synthesis of hydrocarbons in aqueous systems may only occur when H₂ is produced in amounts large enough that it saturates the aqueous phase and becomes present in gaseous form. A closer study of H₂ catalytic production through sulfides (such as sphalerite), could be the key to understanding abiotic reduction of inorganic carbon.

[4] The study of natural samples from environments where abiotic hydrocarbons have been reported remain a viable path to study these reaction pathways. Such samples could provide both insight into the conditions at which they form (using clumped isotopes of methane for instance), and an estimation of the amounts of associated oxides / sulfides capable of catalyzing those reactions.

References

- Abu-Jaber, N.S., 1991. Vein magnesite deposits on Margarita Island, Venezuela. North Carolina State University, Raleigh, NC.
- Abu-Jaber, N.S., Kimberley, M.M., 1992. Origin of ultramafic-hosted vein magnesite deposits. *Ore Geol. Rev.* 7, 155–191. doi:10.1016/0169-1368(92)90004-5.
- Abu-Jaber, N.S., Kimberley, M.M., 1992. Origin of ultramafic-hosted magnesite on Margarita Island, Venezuela. *Miner. Depos.* 27, 234–241. doi:10.1007/BF00202548.
- Ali-Bik, M.W., Taman, Z., El Kalioubi, B., Abdel Wahab, W., 2012. Serpentine-hosted talc-magnesite deposits of Wadi Barramiya area, Eastern Desert, Egypt: Characteristics, petrogenesis and evolution. *J. African Earth Sci.* 64, 77–89. doi:10.1016/j.jafrearsci.2011.11.002.
- Allen, D.E., Seyfried, W.E., 2003. Compositional controls on vent fluids from ultramafic-hosted hydrothermal systems at mid-ocean ridges: An experimental study at 400°C, 500 bars. *Geochim. Cosmochim. Acta* 67, 1531–1542. doi:10.1016/s0016-7037(02)01173-0.
- Anderson, R.B., 1984. The Fischer-Tropsch Reaction. Academic, London.
- Andreani, M., Daniel, I., Pollet-Villard, M., 2012. Aluminum speeds up the hydrothermal alteration of olivine. *Am. Mineral.* 98, 1738–1744. doi:10.2138/am.2013.4469.
- Andreani, M., Luquot, L., Gouze, P., Godard, M., Gibert, B., 2009. Experimental Study of Carbon Sequestration Reactions Controlled by the Percolation of CO₂-Rich Brine through Peridotites. *Environ. Sci. Technol.* 43, 1226–1231. doi:10.1021/es8018429.
- Assayag, N., Matter, J., Ader, M., Goldberg, D., Agrinier, P., 2009. Water–rock interactions during a CO₂ injection field-test: Implications on host rock dissolution and alteration effects. *Chem. Geol.* 265, 227–235. doi:10.1016/j.chemgeo.2009.02.007.
- Aston, J.G.; Messerly, G., 1940. The heat capacity and entropy, heats of fusion and vaporization and the vapor pressure of n-butane. *J. Am. Chem. Soc.* 62, 1917–1923.
- Atreya, S.K., Mahaffy, P.R., Wong, A.S., 2007. Methane and related trace species on Mars: Origin, loss, implications for life, and habitability. *Planet. Space Sci.* 55, 358–369. doi:10.1016/j.pss.2006.02.005.
- Balat, H., Kirtay, E., 2010. Hydrogen from biomass - Present scenario and future prospects. *Int.J. Hydrogen Energy.* doi:10.1016/j.ijhydene.2010.04.137.
- Barnes, C.S and Koretsky, M., 2004. Engineering and Chemical Thermodynamics. John Wiley and Sons.
- Barnes, C.S., 2007. ThermoSolver: an integrated educational thermodynamics software program.

Barnes, I., O'Neil, J.R., Trescases, J.J., 1978. Present day serpentinization in New Caledonia, Oman and Yugoslavia. *Geochim. Cosmochim. Acta* 42, 144–145. doi:10.1016/0016-7037(78)90225-9.

Barnola, J.M., Raynaud, D., Lorius, C. and Barkov, N.I., 2003. Historical CO₂ record from the Vostok ice core. In *Trends: A Compendium of Data on Global Change*. Carbon Dioxide Information Analysis Center. Oak Ridge, Tenn., USA Oak Ridge Natl. Lab. U.S. Dep. Energy.

Barthelemy, H., Weber, M., Barbier, F., 2017. Hydrogen storage: Recent improvements and industrial perspectives. *Int. J. HydrogenEnergy* 42, 7254–7262. doi:10.1016/j.ijhydene.2016.03.178.

Bearat, H., Mckelvy, M.J., Chizmeshya, A.V.G., Gormley, D., Nunez, R., Carpenter, R.W., Squires, K., Wolf, G.H., 2006. Carbon sequestration via aqueous olivine mineral carbonation: Role of passivating layer formation. *Environ. Sci. Technol.* 40, 4802–4808. doi:10.1021/es0523340

Behar, F., Beaumont, V., De B. Penteado, H.L., 2001. Rock-Eval 6 Technology: Performances and Developments. *Oil Gas Sci. Technol.* 56, 111–134. doi:10.2516/ogst:2001013.

Berndt, M.E., Allen, D.E., Seyfried, W.E., 1996. Reduction of CO₂ during serpentinization of olivine at 300°C and 500 bar. *Geology* 24, 351–354. doi:10.1130/0091-7613(1996)024<0351.

Bish, D.L., Howard, S.A., 1988. Quantitative phase analysis using the Rietveld method. *J. Appl. Crystallogr.* 21, 86–91. doi:10.1107/S0021889887009415.

Bish, D.L., Post, J.E., 1993. Quantitative mineralogical analysis using the Rietveld full-pattern fitting method. *Am. Mineral.*

Blum A, Lasaga A (1988) Role of surface speciation in the low-temperature dissolution of minerals. *Nature* 331:431-433.

Bobicki, E.R., Liu, Q., Xu, Z., Zeng, H., 2012. Carbon capture and storage using alkaline industrial wastes. *Prog. Energy Combust. Sci.* doi:10.1016/j.pecs.2011.11.002

Bobicki, E.R., Liu, Q., Xu, Z., 2014. Microwave heating of ultramafic nickel ores and mineralogical effects. *Miner. Eng.* 58, 22–25. doi:10.1016/j.mineng.2014.01.003.

Boden, T, Marland, G, and Andres, R., 2017. Global CO₂ Emissions from Fossil-Fuel Burning, Cement Manufacture, and Gas Flaring. Carbon Dioxide Inf. Anal. Center, Oak Ridge Natl. Lab. U.S. Dep. Energy, Oak Ridge, Tennessee, USA 1751–2014. doi 10.3334/CDIAC/00001_V2017.

Bodéan, F., Bourgeois, F., Petiot, C., Augé, T., Bonfils, B., Julcour-lebigue, C., Guyot, F., 2014. Ex situ mineral carbonation for CO₂ mitigation : Evaluation of mining waste resources,

aqueous carbonation processability and life cycle assessment (Carmex project) 59, 52–63. doi:10.1016/j.mineng.2014.01.011.

Bonin, B and Moyen, J., 2011. Magmatisme et roches magmatiques, 3rd ed. Dunod.

Brunauer, S., Emmett, P.H., Teller, E., 1938. Adsorption of Gases in Multimolecular Layer. J. Am. Chem. Soc. 60, 309–319. doi:citeulike-article-id:4074706.

Cannat, M., Bideau, D., & Bougault, H., 1992. Serpentinized peridotites and gabbros in the Mid-Atlantic Ridge axial valley at 15° 37' N and 16° 52' N. Earth and Planetary Science Letters, 109(1-2), 87-106. doi:10.1016/0012-821X(92)90076-8

Cannat, M., 1993. Emplacement of mantle rocks in the seafloor at mid-ocean ridges. J. Geophys. Res. doi:10.1029/92JB02221

Cannat, M., Fontaine, F., & Escartin, J., 2010. Serpentinization and associated hydrogen and methane fluxes at slow spreading ridges. In Diversity of hydrothermal systems on slow spreading ocean ridges (Vol. 188, pp. 241-264). American Geophysical Union Washington.

Capaccioni, B., Taran, Y., Tassi, F., Vaselli, O., Mangani, G., Macias, J.L., 2004. Source conditions and degradation processes of light hydrocarbons in volcanic gases: An example from El Chichón volcano (Chiapas State, Mexico). Chem. Geol. 206, 81–96. doi:10.1016/j.chemgeo.2004.01.011.

Carruth, G.F., Kobayashi, R., 1973. Vapor Pressure of Normal Paraffins Ethane Through n-Decane from Their Triple Points to About 10 Mm Hg. J. Chem. Eng. Data 18, 115–126. doi:10.1021/je60057a009.

Charlou, J.L., Donval, J.P., Fouquet, Y., Jean-baptiste, P., Holm, N., 2002. Geochemistry of high H₂ and CH₄ vent fluids issuing from ultramafic rocks at the Rainbow hydrothermal field (36° 14' N , MAR) 191, 345–359.

Charlou, J.L., Donval, J.P., Fouquet, Y., Jean-Baptiste, P., Holm, N., 2002. Geochemistry of high H₂ and CH₄ vent fluids issuing from ultramafic rocks at the Rainbow hydrothermal field (36°14'N,MAR). Chem. Geol. 191, 345–359. doi:10.1016/S0009-2541(02)00134-1.

Charlou, J.L., Donval, J.P., Konn, C., Ondréas, H., Fouquet, Y., Jean-Baptiste, P., Fourré, E., 2013. High Production and Fluxes of H₂ and CH₄ and Evidence of Abiotic Hydrocarbon Synthesis by Serpentinization in Ultramafic-Hosted Hydrothermal Systems on the Mid-Atlantic Ridge, in: Diversity of Hydrothermal Systems on Slow Spreading Ocean Ridges. pp. 265–296. doi:10.1029/2008GM000752.

Chen Y, Brantley SL (1998) Diopside and anthophyllite dissolution at 25° and 90 °C and acid pH. Chem Geol 147:233-248.

Chen, Y., Brantley, S.L., 2000. Dissolution of forsteritic olivine at 65°C and 2 < pH < 5. Chem. Geol. 165, 267–281. doi:10.1016/S0009-2541(99)00177-1.

- Chen, Z.Y., O'Connor, W.K., Gerdemann, S.J., 2006. Chemistry of aqueous mineral carbonation for carbon sequestration and explanation of experimental results. *Environ. Prog.* 25, 161–166. doi:10.1002/ep.10127.
- Chen, X., Shen, S., Guo, L., Mao, S.S., 2010. Semiconductor-based photocatalytic hydrogen generation. *Chem. Rev.* 110, 6503–6570. doi:10.1021/cr1001645.
- Crouzet, C., Brunet, F., Recham, N., Findling, N., Lanson, M., Guyot, F., Ferrasse, J.H., Goffé, B., 2017. Hydrogen production by hydrothermal oxidation of FeO under acidic conditions. *Int. J. Hydrogen Energy* 42, 795–806. doi:10.1016/j.ijhydene.2016.10.019.
- Cutler, A.J.B. and Morrison, J.A., 1965. Excess Thermodynamic Functions for Liquid Mixtures of Methane+Propane. *Trans. Faraday Soc.* 61, 429–442.
- Dabitzias, S.G., 1980. Petrology and genesis of the Vavdos cryptocrystalline magnesite deposits, Chalkidiki Peninsula, northern Greece. *Econ. Geol.* 75, 1138–1151.
- Das, T.R., Reed, C.O., Eubank, P.T., 1973. Pvt Surface and Thermodynamic Properties of N-Butane. *J. Chem. Eng. Data* 18, 244–253. doi:10.1021/je60058a002.
- Daval, D., Martinez, I., Corvisier, J., Findling, N., Goffé, B., Guyot, F., 2009a. Carbonation of Ca-bearing silicates, the case of wollastonite: Experimental investigations and kinetic modeling. *Chem. Geol.* 262, 262–277. doi:10.1016/j.chemgeo.2009.01.022.
- Daval, D., Martinez, I., Guigner, J. M., Hellmann, R., Corvisier, J., Findling, N., ... & Guyot, F. 2009b. Mechanism of wollastonite carbonation deduced from micro-to nanometer length scale observations. *American Mineralogist*, 94(11-12), 1707-1726.
- Daval, D., Sissmann, O., Menguy, N., Saldi, G.D., Guyot, F., Martinez, I., Corvisier, J., Garcia, B., Machouk, I., Knauss, K.G., Hellmann, R., 2011. Influence of amorphous silica layer formation on the dissolution rate of olivine at 90°C and elevated pCO₂. *Chem. Geol.* 284, 193–209. doi:10.1016/j.chemgeo.2011.02.021.
- Dry, M.E., 1981. *The Fischer-Tropsch Synthesis in Catalysis Sciences and Technology* (eds. Anderson, JR and Boudart, M). Springer-Verlag.
- Dufaud, F., Martinez, I., Shilobreeva, S., 2009. Experimental study of Mg-rich silicates carbonation at 400 and 500°C and 1 kbar. *Chem. Geol.* 262, 344–352. doi:10.1016/j.chemgeo.2009.01.026.
- Ece, Ö.I., Matsubaya, O., Çoban, F., 2005. Genesis of hydrothermal stockwork-type magnesite deposits associated with ophiolite complexes in the Kütahya-Eskişehir region, Turkey. *Neues Jahrb. für Mineral. - Abhandlungen* 181, 191–205. doi:10.1127/0077-7757/2005/0014.
- Edenhofer, O., Pichs-Madruga, R. Sokona, Y., Farahani, E., Kadner, S., Seyboth, K., Adler, A., Baum, I., Brunner, S., Eickemeier, P., Kriemann, B., Savolainen, J., Schlömer, S., von Stechow, C., Zwickel, T., Minx, J.C., 2014. IPCC, 2014: Summary for Policymakers,

Climate Change 2014: Mitigation of Climate Change. Contribution of Working Group III to the Fifth Assessment Report of the Intergovernmental Panel on Climate Change. doi:10.1007/s13398-014-0173-7.2

Eiler, J.M., 2013. The Isotopic Anatomies of Molecules and Minerals. *Annu. Rev. Earth Planet. Sci.* 41, 411–441. doi:10.1146/annurev-earth-042711-105348.

Eiler, J.M., 2007. “Clumped-isotope” geochemistry-The study of naturally-occurring, multiply-substituted isotopologues. *Earth Planet. Sci. Lett.* 262, 309–327. doi:10.1016/j.epsl.2007.08.020

Etiope, G., 2015. Natural Gas Seepage. doi:10.1007/978-3-319-14601-0.

Etiope, G., Oehler, D.Z., Allen, C.C., 2011. Methane emissions from Earths degassing: Implications for Mars. *Planet. Space Sci.* 59, 182–195. doi:10.1016/j.pss.2010.06.003

Etiope, G., Schoell, M., Hosgörmez, H., 2011. Abiotic methane flux from the Chimaera seep and Tekirova ophiolites (Turkey): Understanding gas exhalation from low temperature serpentinization and implications for Mars. *Earth Planet. Sci. Lett.* 310, 96–104. doi:10.1016/j.epsl.2011.08.001.

Etiope, G., Sherwood Lollar, B., 2013. Abiotic methane on earth. *Rev. Geophys.* 51, 276–299. doi:10.1002/rog.20011.

Fiebig, J., Woodland, A.B., Spangenberg, J., Oschmann, W., 2007. Natural evidence for rapid abiogenic hydrothermal generation of CH₄. *Geochim. Cosmochim. Acta* 71, 3028–3039. doi:10.1016/j.gca.2007.04.010.

Flory, P., 1936. Molecular Size Distribution in Linear Condensation Polymers. *J. Am. Chem. Soc.* 58, 1877–1885. doi:10.1021/ja01301a016.

Foustoukos, D. I., & Seyfried, W. E. (2004). Hydrocarbons in hydrothermal vent fluids: the role of chromium-bearing catalysts. *Science*, 304(5673), 1002–1005. doi:10.1126/science.1096033.

Früh-Green, G.L., Connolly, J.A.D., Plas, A., Kelley, D.S., Grobéty, B., 2004. Serpentinization of oceanic peridotites: Implications for geochemical cycles and biological activity, in: *Geophysical Monograph Series*. doi:10.1029/144GM08

Fu, Q., Foustoukos, D.I., Seyfried, W.E., 2008. Mineral catalyzed organic synthesis in hydrothermal systems: An experimental study using time-of-flight secondary ion mass spectrometry. *Geophys. Res. Lett.* 35, 1–5. doi:10.1029/2008GL033389.

Fu, Q., Sherwood Lollar, B., Horita, J., Lacrampe-Couloume, G., Seyfried, W.E., 2007. Abiotic formation of hydrocarbons under hydrothermal conditions: Constraints from chemical and isotope data. *Geochim. Cosmochim. Acta* 71, 1982–1998. doi:10.1016/j.gca.2007.01.022.

- Garcia, B., Beaumont, V., Perfetti, E., Rouchon, V., Blanchet, D., Oger, P., Dromart, G., Huc, A.Y., Haeseler, F., 2010. Experiments and geochemical modelling of CO₂ sequestration by olivine: Potential, quantification. *Appl. Geochemistry* 25, 1383–1396. doi:10.1016/j.apgeochem.2010.06.009.
- Gerdemann, S., Dahlin, D., O'Connor, W., 2004. Ex-situ and in-situ mineral carbonation as a means to sequester carbon dioxide. *Osti.Gov*.
- Gerdemann, S.J., O'Connor, W.K., Dahlin, D.C., Penner, L.R., Rush, H., 2007. Ex situ aqueous mineral carbonation. *Environ. Sci. Technol.* 41, 2587–2593. doi:10.1021/es0619253.
- Ghadimi, A., Amirilargani, M., Mohammadi, T., Kasiri, N., Sadatnia, B., 2014. Preparation of alloyed poly (ether block amide)/poly(ethylene glycol diacrylate) membranes for separation of CO₂/H₂(syngas application). *J. Memb. Sci.* 458, 14–26. doi:10.1016/j.memsci.2014.01.048.
- Ghoneim, M.F., Saleem, I.A., Hamdy, M.M., 2003. Origin of magnesite veins in serpentinites from Mount El-Rubshi and Mount El-Maiyit, Eastern Desert Egypt. *Arch. Mineral.* 2002, 41–63.
- Giammar, D.E., Bruant, R.G., Peters, C.A., 2005. Forsterite dissolution and magnesite precipitation at conditions relevant for deep saline aquifer storage and sequestration of carbon dioxide. *Chem. Geol.* 217, 257–276. doi:10.1016/j.chemgeo.2004.12.013.
- Gudbrandsson, S., Wolff-Boenisch, D., Gislason, S.R., Oelkers, E.H., 2011. An experimental study of crystalline basalt dissolution from 2pH11 and temperatures from 5 to 75°C. *Geochim. Cosmochim. Acta.* 75, 5496–5509. doi:10.1016/j.gca.2011.06.035
- Guyot, F., Daval, D., Dupraz, S., Martinez, I., Ménez, B., Sissmann, O., 2011a. CO₂geological storage: The environmental mineralogy perspective. *Comptes Rendus Geosci.* 343, 246–259. doi:10.1016/j.crte.2010.12.007.
- Han, S.B., Kang, T.B., Joo, O.S., Jung, K.D., 2007. Water splitting for hydrogen production with ferrites. *Sol. Energy* 81, 623–628. doi:10.1016/j.solener.2006.08.012.
- Hänchen, M., Prigiobbe, V., Storti, G., Seward, T.M., Mazzotti, M., 2006. Dissolution kinetics of fosteritic olivine at 90-150°C including effects of the presence of CO₂. *Geochim. Cosmochim. Acta* 70, 4403–4416. doi:10.1016/j.gca.2006.06.1560.
- Hansen, L.D., Dipple, G.M., Gordon, T.M., Kellett, D.A., 2005. Carbonated serpentinite (listwanite) at Atlin, British Columbia: A geological analogue to carbon dioxide sequestration. *Can. Mineral.* 43, 225–239. doi:10.2113/gscanmin.43.1.225.
- Harrison, A.L., Dipple, G.M., Power, I.M., Mayer, K.U., 2016. The impact of evolving mineral-water-gas interfacial areas on mineral-fluid reaction rates in unsaturated porous media. *Chem. Geol.* 421, 65–80. doi:10.1016/j.chemgeo.2015.12.005

- Harrison, A.L., Power, I.M., Dipple, G.M., 2013. Accelerated carbonation of brucite in mine tailings for carbon sequestration. *Environ. Sci. Technol.* 47, 126–134. doi:10.1021/es3012854
- Heaney, P.J., Vicenzi, E.P., Giannuzzi, L.A., Livi, K.J.T., 2001. Focused ion beam milling: A method of site-specific sample extraction for microanalysis of Earth and planetary materials. *Am. Mineral.* 86, 1094–1099.
- Hegleson, N.L., Sage, B.H., 1967. Latent Heat of Vaporization of Propane. *J. Chem. Eng. Data* 12, 47–49. doi:10.1021/je60032a015.
- Hellmann, R., Wirth, R., Daval, D., Barnes, J.P., Penisson, J.M., Tisserand, D., Epicier, T., Florin, B., Hervig, R.L., 2012. Unifying natural and laboratory chemical weathering with interfacial dissolution-reprecipitation: A study based on the nanometer-scale chemistry of fluid-silicate interfaces. *Chem. Geol.* 294–295, 203–216. doi:10.1016/j.chemgeo.2011.12.002.
- Hestermans, P., White, D., 1960. The vapor pressure, heat of vaporization and heat capacity of Methane from the boiling point to the critical temperature. *J. Phys. Chem.* 65, 362–365. doi:10.1021/j100820a044.
- Horita, J., Berndt, M.E., 1999. Abiogenic Methane Formation and Isotopic Fractionation Under Hydrothermal Conditions. *Science* (80). 285, 1055–1057. doi:10.1126/science.285.5430.1055.
- IEA (2015) Energy Technology Perspectives 2015 - Mobilising Innovation To Accelerate Climate Action. International Energy Agency, Paris, France.
- Ismail, A.A., Bahnemann, D.W., 2014. Photochemical splitting of water for hydrogen production by photocatalysis: A review. *Sol. Energy Mater. Sol. Cells.* doi:10.1016/j.solmat.2014.04.037.
- IPCC, Intergovernmental Panel on Climatic Change. Retrieved in 2016 from <http://www.ipcc.ch/>
- Janecky, D.R., Seyfried, W.E., 1986. Hydrothermal serpentinization of peridotite within the oceanic crust: Experimental investigations of mineralogy and major element chemistry. *Geochim. Cosmochim. Acta* 50, 1357–1378. doi:10.1016/0016-7037(86)90311-X.
- Jaques, A.L and Green, D., 1980. Anhydrous melting of peridotite at 0–15 Kb pressure and the genesis of tholeiitic basalts. *Contrib. to Mineral. Petrol.* 73, 287–310.
- Jarvis, K., Carpenter, R.W., Windman, T., Kim, Y., Nunez, R., Alawneh, F., 2009. Reaction mechanisms for enhancing mineral sequestration of CO₂. *Environ. Sci. Technol.* 43, 6314–6319. doi:10.1021/es8033507.
- Jenden, P.D., Kaplan, I.R., Hilton, D.R., Craig, H., 1993. Abiogenic hydrocarbons and mantle helium in oil and gas fields, in: *The Future of Energy Gases*. pp. 31–56. doi:OSTI ID: 7052010.

- Kaszuba, J., Yardley, B., Andreani, M., 2013. Experimental Perspectives of Mineral Dissolution and Precipitation due to Carbon Dioxide-Water-Rock Interactions. *Rev. Mineral. Geochemistry* 77, 153–188. doi:10.2138/rmg.2013.77.5.
- Katayama, I., Kurosaki, I., Hirauchi, K. ichi, 2010. Low silica activity for hydrogen generation during serpentinization: An example of natural serpentinites in the Mineoka ophiolite complex, central Japan. *Earth Planet. Sci. Lett.* 298, 199–204. doi:10.1016/j.epsl.2010.07.045
- Kelley, D.S., 1996. Methane-rich fluids in the oceanic crust. *J. Geophys. Res. Earth* 101, 2943–2962. doi:10.1029/95jb02252.
- Kemp, J.D., Egan, C.J., 1938. Hindered Rotation of the Methyl Groups in Propane. The Heat Capacity, Vapor Pressure, Heats of Fusion and Vaporization of Propane. Entropy and Density of the Gas. *J. Am. Chem. Soc.* 60, 1521–1525. doi:10.1021/ja01274a001.
- King, H.E., Plümper, O., Putnis, A., 2010. Effect of secondary phase formation on the carbonation of olivine. *Environ. Sci. Technol.* 44, 6503–6509. doi:10.1021/es9038193.
- Kitchaev, D. A., & Ceder, G. (2016). Evaluating structure selection in the hydrothermal growth of FeS 2 pyrite and marcasite. *Nature communications*, 7, 13799.
- Klein, F., Bach, W., Jöns, N., McCollom, T., Moskowitz, B., Berquó, T., 2009. Iron partitioning and hydrogen generation during serpentinization of abyssal peridotites from 15°N on the Mid-Atlantic Ridge. *Geochim. Cosmochim. Acta* 73, 6868–6893. doi:10.1016/j.gca.2009.08.021.
- Klein, F., Bach, W., McCollom, T.M., 2013. Compositional controls on hydrogen generation during serpentinization of ultramafic rocks. *Lithos* 178, 55–69. doi:10.1016/j.lithos.2013.03.008.
- Klein, F., Garrido, C.J., 2010. On Serpentinization and Mineral Carbonation of Serpentine. *Am. Geophys. Union*.
- Klein, F., McCollom, T.M., 2013. From serpentinization to carbonation: New insights from a CO₂ injection experiment. *Earth Planet. Sci. Lett.* 379, 137–145. doi:10.1016/j.epsl.2013.08.017.
- Konn, C., Charlou, J.L., Holm, N.G., Mousis, O., 2015. The production of methane, hydrogen, and organic compounds in ultramafic-hosted hydrothermal vents of the mid-atlantic ridge. *Astrobiology* 15, 381–399. doi:10.1089/ast.2014.1198.
- Konn, C., Charlou, J.L., Donval, J.P., Holm, N.G., Dehairs, F., Bouillon, S., 2009. Hydrocarbons and oxidized organic compounds in hydrothermal fluids from Rainbow and Lost City ultramafic-hosted vents. *Chem. Geol.* 258, 299–314. doi:10.1016/j.chemgeo.2008.10.034.

- Krasnopolsky, V.A., 2006. Some problems related to the origin of methane on Mars. *Icarus* 180, 359–367. doi:10.1016/j.icarus.2005.10.015.
- Krasnopolsky, V.A., Maillard, J.P., Owen, T.C., 2004. Detection of methane in the martian atmosphere: Evidence for life? *Icarus* 172, 537–547. doi:10.1016/j.icarus.2004.07.004.
- Kutcherov, V.G., Krayushkin, V.A., 2010. Deep-seated abiogenic origin of petroleum: From geological assessment to physical theory. *Rev. Geophys.* 48, 1–30. doi:10.1029/2008RG000270.
- Lackner, K. S. (2003). A guide to CO₂ sequestration. *Science*, 300(5626), 1677-1678. doi:10.1126/science.1079033.
- Lackner, K.S., Wendt, C.H., Butt, D.P., Joyce, E.L., Sharp, D.H., 1995. Carbon-dioxide disposal in carbonate minerals. *Energy* 20, 1153–1170. doi:10.1016/0360-5442(95)00071-n.
- Lafargue, E., Marquis, F., Pillot, D., 1998. Rock-Eval 6 Applications in Hydrocarbon Exploration, Production, and Soil Contamination Studies. *Oil Gas Sci. Technol.* 53, 421–437. doi:10.2516/ogst:1998036.
- Levin, G. V, Straat, P.A., 2009. Methane and life on Mars, in: *Instruments and Methods for Astrobiology and Planetary Missions XII*, SPIE Proceedings 7441. p. Paper No. 7441-10D. doi:10.1117/12.829183.
- Lollar, B.S., Lacrampe-Couloume, G., Voglesonger, K., Onstott, T.C., Pratt, L.M., Slater, G.F., 2008. Isotopic signatures of CH₄ and higher hydrocarbon gases from Precambrian Shield sites: A model for abiogenic polymerization of hydrocarbons. *Geochim. Cosmochim. Acta* 72, 4778–4795. doi:10.1016/j.gca.2008.07.004.
- Loomis, A.G., Walters, J.E., 1926. The vapor pressure of ethane near the normal boiling point. *J. Am. Chem. Soc.* 48, 2051–2055. doi:10.1021/ja01419a006.
- Lugli, S., Torres-Rutz, J., Garuti, G., Olmedo, F., 2000. Petrography and Geochemistry of the Eugui Magnesite Deposit (Western Pyrenees, Spain): Evidence for the Development of a Peculiar Zebra Banding by Dolomite Replacement. *Econ. Geol.* 95, 1775. doi:10.2113/gsecongeo.95.8.1775.
- Malvoisin, B., Brunet, F., Carlut, J., Montes-Hernandez, G., Findling, N., Lanson, M., Vidal, O., Bottero, J.Y., Goff, B., 2013. High-purity hydrogen gas from the reaction between BOF steel slag and water in the 473–673 K range. *Int. J. Hydrogen Energy* 38, 7382–7393. doi:10.1016/j.ijhydene.2013.03.163.
- Malvoisin, B., Brunet, F., Carlut, J., Rouméjon, S., Cannat, M., 2012a. Serpentinization of oceanic peridotites: 2. Kinetics and processes of San Carlos olivine hydrothermal alteration. *J. Geophys. Res. Solid Earth* 117, 1–13. doi:10.1029/2011JB008842.

- Malvoisin, B., Carlut, J., Brunet, F., 2012b. Serpentinization of oceanic peridotites: 1. A high-sensitivity method to monitor magnetite production in hydrothermal experiments. *J. Geophys. Res. Solid Earth* 117. doi:10.1029/2011JB008612.
- Manabe, S., Stouffer, R.J., 1993. Century-scale effects of increased atmospheric CO₂ on the ocean-atmosphere system. *Nature* 364, 215–218. doi:10.1038/364215a0.
- Manning, C.E., Shock, E.L., Sverjensky, D.A., 2013. The Chemistry of Carbon in Aqueous Fluids at Crustal and Upper-Mantle Conditions: Experimental and Theoretical Constraints. *Rev. Mineral. Geochemistry* 75, 109–148. doi:10.2138/rmg.2013.75.5.
- Marbán, G., Valdés-Solís, T., 2007. Towards the hydrogen economy? *Int. J. Hydrogen Energy* 32(12), 1625–1637. doi:10.1016/j.ijhydene.2006.12.017
- Marcaillou, C., Muñoz, M., Vidal, O., Parra, T., Harfouche, M., 2011. Mineralogical evidence for H₂ degassing during serpentinization at 300°C/300bar. *Earth Planet. Sci. Lett.* 303, 281–290. doi:10.1016/j.epsl.2011.01.006.
- Marini, L. (2006). Geological sequestration of carbon dioxide: thermodynamics, kinetics, and reaction path modeling (Vol. 11). Elsevier.
- Martinez I, Vacquand C, Kularatne K, Sissmann O, Milesi V & Bernard S, 2016. Formation of Reduced Carbon Compounds Using Natural Catalysts in Hydrothermal Experiments, *Goldschmidt abstracts*, 2017 2602.
- Mathez, E.A., 1984. Influence of degassing on oxidation states of basaltic magmas. *Nature* v. 310, 371–378. doi:10.1038/310371a0.
- Matsuoka, M., Kitano, M., Takeuchi, M., Tsujimaru, K., Anpo, M., Thomas, J.M., 2007. Photocatalysis for new energy production. Recent advances in photocatalytic water splitting reactions for hydrogen production. *Catal. Today* 122, 51–61. doi:10.1016/j.cattod.2007.01.042.
- Matter, J. M., Takahashi, T., & Goldberg, D. (2007). Experimental evaluation of in situ CO₂-water-rock reactions during CO₂ injection in basaltic rocks: Implications for geological CO₂ sequestration. *Geochemistry, Geophysics, Geosystems*, 8(2).
- Matter, J.M., Kelemen, P.B., 2009. Permanent storage of carbon dioxide in geological reservoirs by mineral carbonation. *Nat. Geosci.* 2, 837–841. doi:10.1038/ngeo683.
- Matter, J.M., Stute, M., Hall, J., Mesfin, K., Snæbjörnsdóttir, S., Gislason, S.R., Oelkers, E.H., Sigfusson, B., Gunnarsson, I., Aradóttir, E.S., Alfredsson, H.A., Gunnlaugsson, E., Broecker, W.S., 2014. Monitoring permanent CO₂ storage by in situ mineral carbonation using a reactive tracer technique, in: *Energy Procedia*. pp. 4180–4185. doi:10.1016/j.egypro.2014.11.450.

- McCollom, T.M., 2013. Laboratory Simulations of Abiotic Hydrocarbon Formation in Earth's Deep Subsurface. *Rev. Mineral. Geochemistry* 75, 467–494. doi:10.2138/rmg.2013.75.15.
- McCollom, T.M., Bach, W., 2009a. Thermodynamic constraints on hydrogen generation during serpentinization of ultramafic rocks. *Geochim. Cosmochim. Acta* 73, 856–875. doi:10.1016/j.gca.2008.10.032.
- McCollom, T.M., Klein, F., Robbins, M., Moskowitz, B., Berquó, T.S., Jöns, N., Bach, W., Templeton, A., 2016. Temperature trends for reaction rates, hydrogen generation, and partitioning of iron during experimental serpentinization of olivine. *Geochim. Cosmochim. Acta* 181, 175–200. doi:10.1016/j.gca.2016.03.002.
- McCollom, T.M., Ritter, G., Simoneit, B.R.T., 1999. Lipid synthesis under hydrothermal conditions by Fischer-Tropsch-type reactions. *Orig. Life Evol. Biosph.* 29, 153–166. doi:10.1023/A:1006592502746.
- McCollom, T.M., Seewald, J.S., 2007. Abiotic Synthesis of Organic Compounds in Deep-Sea Hydrothermal Environments on Abiotic Synthesis. *Nat. Geosci.* 382–401. doi:10.1021/cr0503660.
- McCollom, T.M., Seewald, J.S., 2006. Carbon isotope composition of organic compounds produced by abiotic synthesis under hydrothermal conditions. *Earth Planet. Sci. Lett.* 243, 74–84. doi:10.1016/j.epsl.2006.01.027.
- McCollom, T.M., Seewald, J.S., 2003. Experimental study of the hydrothermal reactivity of organic acids and acid anions: II. Acetic acid, acetate, and valeric acid. *Geochim. Cosmochim. Acta* 67, 3645–3664. doi:10.1016/S0016-7037(03)00135-2.
- McCollom, T.M., Seewald, J.S., 2001. A reassessment of the potential for reduction of dissolved CO₂ to hydrocarbons during serpentinization of olivine. *Geochim. Cosmochim. Acta* 65, 3769–3778. doi:10.1016/S0016-7037(01)00655-X.
- McCollom, T.M., Klein, F., Robbins, M., Moskowitz, B., Berquó, T.S., Jöns, N., Bach, W., Templeton, A., 2016. Temperature trends for reaction rates, hydrogen generation, and partitioning of iron during experimental serpentinization of olivine. *Geochim. Cosmochim. Acta* 181, 175–200. doi:10.1016/j.gca.2016.03.002.
- McCusker, L.B., Von Dreele, R.B., Cox, D.E., Louër, D., Scardi, P., 1999. Rietveld refinement guidelines. *J. Appl. Crystallogr.* 32, 36–50. doi:10.1107/S0021889898009856.
- McDermott, J.M., Seewald, J.S., German, C.R., Sylva, S.P., 2015. Pathways for abiotic organic synthesis at submarine hydrothermal fields. *Proc. Natl. Acad. Sci. U. S. A.* 112, 7668–72. doi:10.1073/pnas.1506295112.
- McMollom, T.M., Bach, W., 2008. Constraints on hydrogen generation during serpentinization of ultramafic rocks. *Geochim. Cosmochim. Acta* 72, A611.

McGrail, B. P., Schaef, H. T., Ho, A. M., Chien, Y. J., Dooley, J. J., & Davidson, C. L. (2006). Potential for carbon dioxide sequestration in flood basalts. *Journal of Geophysical Research: Solid Earth*, 111(B12).

Michel, R., Ammar, M.R., Poirier, J., Simon, P., 2013. Phase transformation characterization of olivine subjected to high temperature in air. *Ceram. Int.* 39, 5287–5294. doi:10.1016/j.ceramint.2012.12.031.

Milesi, V.M., 2015. Unconventional generation of hydrocarbon gases in the Solimoes sedimentary basin, Brazil: the role of the siderite-water interaction.

Milesi, V.M., Uyot, F.G., Runet, F.B., Ichard, L.R., 2015. Generation of condensed carbon from serpentinization fluids 2132.

Mousis, O., Lunine, J.I., Waite, J.H., Magee, B., Lewis, W.S., Mandt, K.E., Marquer, D., Cordier, D., 2009. Formation Conditions of Enceladus and Origin of Its Methane Reservoir. *Astrophys. J.* 701, L39–L42. doi:10.1088/0004-637X/701/1/L39.

Nann, T., Ibrahim, S.K., Woi, P.M., Xu, S., Ziegler, J., Pickett, C.J., 2010. Water splitting by visible light: A nanophotocathode for hydrogen production. *Angew. Chemie - Int. Ed.* 49, 1574–1577. doi:10.1002/anie.200906262.

NASA, 2016. retrieved from:

Http://data.giss.nasa.gov/gistemp/tabledata_v3/GLB.Ts+dSST.txt.

Nath, K., Das, D., 2003. Hydrogen from biomass. *Curr. Sci.* doi:10.1021/ef990034w.

New Caledonia Department of Energy, 2013. Bilan energetique de la nouvelle-caledonie-2013. Retrieved from:

https://maitriseenergie.nc/sites/default/files/documents/bilan_energetique_2013.pdf

Ni, M., Leung, D.Y.C., Leung, M.K.H., Sumathy, K., 2006. An overview of hydrogen production from biomass. *Fuel Process. Technol.* 87, 461–472. doi:10.1016/j.fuproc.2005.11.003.

NIST, 2017. NIST Chemistry WebBook, NIST Standard Reference Database Number 69. Eds. P.J. Linstrom W.G. Mallard. retrieved from <http://webbook.nist.gov/chemistry/>

NOAA 2016. retrieved from: <http://www.esrl.noaa.gov/gmd/ccgg/trends/>

O'Connor, W. K., Dahlin, D. C., Nilsen, D. N., Gerdemann, S. J., Rush, G. E., Penner, L. R., ... & Turner, P. C. (2002). Continuing Studies on Direct Aqueous Mineral Carbonation of CO₂ Sequestration (No. DOE/ARC-2002-003). Albany Research Center, OR (US).

Oelkers, E.H., 2005. Geochemical aspects of CO₂ sequestration. *Chem. Geol.* 217, 183–186. doi:10.1016/j.chemgeo.2004.12.006.

Oelkers, E.H., Cole, D.R., 2008. Carbon Dioxide Sequestration A Solution to a Global Problem. *Elements* 4, 305–310. doi:10.2113/gselements.4.5.305.

Oelkers, E.H., Gislason, S.R., Matter, J., 2008. Mineral carbonation of CO₂. *Elements* 4, 333–337. doi:10.2113/gselements.4.5.333.

OKFN, 2016. Retrieved from: <http://data.okfn.org/data/core/co2-ppm#resource-co2-annmean-mlo>

Oskierski, H.C., Dlugogorski, B.Z., Jacobsen, G., 2013. Sequestration of atmospheric CO₂ in a weathering-derived, serpentinite-hosted magnesite deposit: 14C tracing of carbon sources and age constraints for a refined genetic model. *Geochim. Cosmochim. Acta* 122, 226–246. doi:10.1016/j.gca.2013.08.029.

Palinkaš, L.A., Jurković, I., Garašić, V., Palinkaš, S.S., 2012. Genesis of vein-stockwork cryptocrystalline magnesite from the dinaride ophiolites. *Ofioliti* 37, 13–26.

Perkins, E. H., & Gunter, W. D. (1995). Aquifer disposal of CO₂-rich greenhouse gasses: modelling of water-rock reaction paths in a siliciclastic aquifer. In *Proceedings of the 8th international symposium on water–rock interaction* (pp. 895-898). Balkema Vladivostok.

Parthasarathy, P., Narayanan, K.S., 2014. Hydrogen production from steam gasification of biomass: Influence of process parameters on hydrogen yield - A review. *Renew. Energy*. doi:10.1016/j.renene.2013.12.025.

Petroleum, B., 2016. BP Statistical Review of World Energy. BP Stat. Rev. World Energy 1–48. doi:10.1016/j.egypro.2013.06.172.

Petrova, V.I., Kursheva, A. V., Litvinenko, I. V., Morgunova, I.P., Stepanova, T. V., Cherkashev, G.A., 2009. On genesis of organic matter in bottom sediments of hydrothermal field Ashadze-1, 13° N MAR. *Dokl. Earth Sci.* 429, 1583–1586. doi:10.1134/S1028334X09090360.

Pineau, F., Javoy, M., 1983. Carbon isotopes and concentrations in mid-oceanic ridge basalts. *Earth Planet. Sci. Lett.* 62, 239–257. doi:10.1016/0012-821X(83)90087-0.

Planetforlife (2017), retrieved from: <http://planetforlife.com/co2history/index.html>

Pohl, W., 1990. Genesis of magnesite deposits—models and trends. *Geol. Rundschau* 79, 291–299.

Power, I. M., Harrison, A. L., Dipple, G. M., Wilson, S. A., Kelemen, P. B., Hitch, M., & Southam, G. (2013). Carbon mineralization: from natural analogues to engineered systems. *Reviews in Mineralogy and Geochemistry*, 77(1), 305-360.

Power, I.M., Wilson, S.A., Dipple, G.M., 2013. Serpentinite carbonation for CO₂ sequestration. *Elements* 9, 115–121. doi:10.2113/gselements.9.2.115.

Prigibbe, V., Costa, G., Baciocchi, R., Hänchen, M., Mazzotti, M., 2009. The effect of CO₂ and salinity on olivine dissolution kinetics at 120°C. *Chem. Eng. Sci.* 64, 3510–3515. doi:10.1016/j.ces.2009.04.035.

- Prigobbe, V., Mazzotti, M., 2011. Dissolution of olivine in the presence of oxalate, citrate, and CO₂ at 90°C and 120°C. *Chem. Eng. Sci.* 66, 6544–6554. doi:10.1016/j.ces.2011.09.032.
- Pokrovsky OS, Schott J (2000) Kinetics and mechanism of forsterite dissolution at 25 °C and pH from 1 to 12. *Geochim Cosmochim Acta* 64(19):3313-3325.
- Proskurowski, G., Lilley, M.D., Seewald, J.S., Fru h-Green, G.L., Olson, E.J., Lupton, J.E., Sylva, S.P., Kelley, D.S., 2008. Abiogenic Hydrocarbon Production at Lost City Hydrothermal Field. *Science* (80-.). 319, 604–607. doi:10.1126/science.1151194.
- Prydz, R., Goodwin, R.D., 1972. Experimental melting and vapor pressures of methane. *J. Chem. Thermodyn.* 4, 127–133. doi:10.1016/S0021-9614(72)80016-8.
- Putnis, A., 2009. Mineral Replacement Reactions. *Rev. Mineral. Geochemistry* 70, 87–124. doi:10.2138/rmg.2009.70.3.
- Rabiee, H., Soltanieh, M., Mousavi, S.A., Ghadimi, A., 2014. Improvement in CO₂/H₂ separation by fabrication of poly(ether-b-amide6)/glycerol triacetate gel membranes. *J. Memb. Sci.* 469, 43–58. doi:10.1016/j.memsci.2014.06.026
- Regnier, J., 1972. Tension de Vapeur de L’Ethane Entre 80 et 135 K. *J. Chim. Phys.* 69, 942–944.
- Rimstidt, J.D., Brantley, S.L., Olsen, A.A., 2012. Systematic review of forsterite dissolution rate data. *Geochim. Cosmochim. Acta* 99, 159–178. doi:10.1016/j.gca.2012.09.019.
- Rips, S., 1963. On a Feasible Level of Filling in of Reservoirs by Liquid Hydrocarbons. *Khim. Prom. (Moscow)* 8, 610–613.
- Rosso JJ, Rimstidt JD (2000) A high resolution study of forsterite dissolution rates. *Geochim Cosmochim Acta* 64(5):797-811.
- Saldi, G.D., Daval, D., Morvan, G., Knauss, K.G., 2013. The role of Fe and redox conditions in olivine carbonation rates: An experimental study of the rate limiting reactions at 90 and 150°C in open and closed systems. *Geochim. Cosmochim. Acta* 118, 157–183. doi:10.1016/j.gca.2013.04.029
- Schmidt, K., Koschinsky, A., Garbe-Schonberg, D., de Carvalho, L.M., Seifert, R., 2007. Geochemistry of hydrothermal fluids from the ultramafic-hosted Logatchev hydrothermal field, 15°N on the Mid-Atlantic Ridge: Temporal and spatial investigation. *Chem. Geol.* 242, 1–21. doi:10.1016/j.chemgeo.2007.01.023.
- Schulz, H., 1999. Short history and present trends of Fischer–Tropsch synthesis. *Appl. Catal. A Gen.* 186, 3–12. doi:http://dx.doi.org/10.1016/S0926-860X(99)00160-X.
- Seewald, J.S., Zolotov, M.Y., McCollom, T., 2006. Experimental investigation of single carbon compounds under hydrothermal conditions. *Geochim. Cosmochim. Acta* 70, 446–460. doi:10.1016/j.gca.2005.09.002.

- Seifritz, W., 1990. CO₂ disposal by means of silicates. *Nature*. doi:10.1038/345486b0.
- Seyfried, W.E., Foustoukos, D.I., Fu, Q., 2007. Redox evolution and mass transfer during serpentinization: An experimental and theoretical study at 200°C, 500 bar with implications for ultramafic-hosted hydrothermal systems at Mid-Ocean Ridges. *Geochim. Cosmochim. Acta* 71, 3872–3886. doi:10.1016/j.gca.2007.05.015.
- Seyfried, W.E., Foustoukos, D.I., Fu, Q., 2007. Redox evolution and mass transfer during serpentinization: An experimental and theoretical study at 200°C, 500bar with implications for ultramafic-hosted hydrothermal systems at Mid-Ocean Ridges. *Geochim. Cosmochim. Acta* 71, 3872–3886. doi:10.1016/j.gca.2007.05.015.
- Shipp, J. a, Gould, I.R., Shock, E.L., Williams, L.B., Hartnett, H.E., 2014. Sphalerite is a geochemical catalyst for carbon-hydrogen bond activation. *Proc. Natl. Acad. Sci. U. S. A.* 2–5. doi:10.1073/pnas.1324222111.
- Shuai, Y., Etiope, G., Zhang, S., Douglas, P.M.J., Huang, L., Eiler, J.M., 2018. Methane clumped isotopes in the Songliao Basin (China): New insights into abiotic vs. biotic hydrocarbon formation. *Earth Planet. Sci. Lett.* 482, 213–221. doi:10.1016/j.epsl.2017.10.057.
- Sissmann, O., Brunet, F., Martinez, I., Guyot, F., Verlaquet, A., Piquier, Y., Daval, D., 2014. Enhanced olivine carbonation within a basalt as compared to single-phase experiments: Reevaluating the potential of CO₂ mineral sequestration. *Environ. Sci. Technol.* 48, 5512–5519. doi:10.1021/es405508a.
- Sissmann, O., Daval, D., Brunet, F., Guyot, F., Verlaquet, A., Piquier, Y., Findling, N., Martinez, I., 2013. The deleterious effect of secondary phases on olivine carbonation yield: Insight from time-resolved aqueous-fluid sampling and FIB-TEM characterization. *Chem. Geol.* 357, 186–202. doi:10.1016/j.chemgeo.2013.08.031.
- Snæbjörnsdóttir, S., Wiese, F., Fridriksson, T., Ármannsson, H., Einarsson, G.M., Gislason, S.R., 2014. CO₂ storage potential of basaltic rocks in Iceland and the oceanic Ridges. *Energy Procedia* 63, 4585–4600. doi:10.1016/j.egypro.2014.11.491.
- Snæbjörnsdóttir, S.Ó., Gislason, S.R., Galeczka, I.M., Oelkers, E.H., 2017. Reaction path modelling of in-situ mineralisation of CO₂ at the CarbFix site at Hellisheidi, SW-Iceland. *Geochim. Cosmochim. Acta*. doi:10.1016/j.gca.2017.09.053.
- Stolper, D.A., Sessions, A.L., Ferreira, A.A., Santos Neto, E. V., Schimmelmann, A., Shusta, S.S., Valentine, D.L., Eiler, J.M., 2014b. Combined ¹³C-D and D-D clumping in methane: Methods and preliminary results. *Geochim. Cosmochim. Acta* 126, 169–191. doi:10.1016/j.gca.2013.10.045.
- Szatmari, P., 1989. Petroleum formation by Fischer-Tropsch synthesis in plate tectonics. *Am. Assoc. Pet. Geol. Bull.* 73, 989–998.
- Tanksale, A., Beltramini, J.N., Lu, G.M., 2010. A review of catalytic hydrogen production

processes from biomass. *Renew. Sustain. Energy Rev.* 14, 166–182.
doi:10.1016/j.rser.2009.08.010.

Takahashi, E., 1986. Melting of a dry peridotite KLB-1 up to 14 GPa: Implications on the Origin of peridotitic upper mantle. *J. Geophys. Res.* 91, 9367–9382.
doi:10.1029/JB091iB09p09367.

Tissot, B.P., Welte, D.H., 1984. *Petroleum Formation and Occurrence, A New Approach to Oil and Gas Exploration*, Second Edition. Springer-Verlag Berlin Heidelberg. New York 1978 720.

Tobie, G., Lunine, J.I., Sotin, C., 2006. Episodic outgassing as the origin of atmospheric methane on Titan. *Nature* 440, 61–64. doi:10.1038/nature04497.

U.S. Geological Survey, 2017. *Mineral Commodity Summaries 2017*.

van der Lee, J and De Windt, L., 2002. *CHESSTutorial and Cookbook Updated for version 3.0*. Ecole des Mines de Paris, Fontainebleau, France.

Von Damm, K.L., 2001. Lost City found. *Nature* 412, 127–128. doi:10.1038/35084297.

Wacaster, S., 2013. *Minerals Yearbook New Caledonia (advance release)*. U.S. Geological survey.

Wang F, Giammar DE (2013) Forsterite dissolution in saline water at elevated temperature and high CO₂ pressure. *Environ Sci Technol* 47(1):168-173.

Webb, M.A., Miller, T.F., 2014. Position-specific and clumped stable isotope studies: Comparison of the urey and path-integral approaches for carbon dioxide, nitrous oxide, methane, and propane. *J. Phys. Chem. A* 118, 467–474. doi:10.1021/jp411134v.

Wetzel, L.R., Shock, E.L., 2002. Distinguishing ultramafic-from basalt-hosted submarine hydrothermal systems by comparing calculated vent fluid compositions. *J. Geophys. Res. Solid Earth*. doi:10.1029/1999jb900382.

Whiticar, M.J., 1999. Carbon and hydrogen isotope systematics of bacterial formation and oxidation of methane. *Chem. Geol.* 161, 291–314. doi:10.1016/S0009-2541(99)00092-3.

Wilson, S.A., Harrison, A.L., Dipple, G.M., Power, I.M., Barker, S.L.L., Ulrich Mayer, K., Fallon, S.J., Raudsepp, M., Southam, G., 2014. Offsetting of CO₂ emissions by air capture in mine tailings at the Mount Keith Nickel Mine, Western Australia: Rates, controls and prospects for carbon neutral mining. *Int. J. Greenh. Gas Control* 25, 121–140. doi:10.1016/j.ijggc.2014.04.002.

Wogelius RA, Walther JV (1991) Forsterite dissolution at 25 °C: Effects of pH, CO₂ and organic acids. *Geochim Cosmochim Acta* 55:943-954.

Wolff-Boenisch, D., Gislason, S.R., Oelkers, E.H., 2006. The effect of crystallinity on dissolution rates and CO₂ consumption capacity of silicates. *Geochim. Cosmochim. Acta* 70, 858–870. doi:10.1016/j.gca.2005.10.016.

Wolff-Boenisch, D., Gislason, S.R., Oelkers, E.H., Putnis, C. V., 2004. The dissolution rates of natural glasses as a function of their composition at pH 4 and 10.6, and temperatures from 25 to 74°C. *Geochim. Cosmochim. Acta* 68, 4843–4858. doi:10.1016/j.gca.2004.05.027.

Zedef, V., Russell, M.J., Fallick, A.E., Hall, A.J., 2000. Genesis of vein stockwork and sedimentary magnesite and hydromagnesite deposits in the ultramafic terranes of southwestern Turkey: A stable isotope study. *Econ. Geol.* 95, 429–445. doi:10.2113/gsecongeo.95.2.429.

Zhao, L., Sang, L., Jun, C., Ji, J., Teng, H.H., 2010. Aqueous carbonation of natural brucite: Relevance to CO₂ sequestration. *Environ. Sci. Technol.* 44, 406–411. doi:10.1021/es9017656.

Appendix 1

Protocol of quantification of gases from gas chromatography measurements

As discussed in section 1.4, these experiments were dedicated to study the valorization of New Caledonian mine tailings by simultaneous carbonation and hydrogen production. Experiments were conducted by reacting powdered mine tailings with carbon dioxide (CO₂) saturated water at hydrothermal conditions in batch reactors (section 2.1.4). All the results are presented in chapter 3, section 3.3. Here, we will discuss the procedure of calculating the concentration of gases in the gas phase of batch reactors.

The tables A1-A4 shows the gas compositions obtained by gas chromatography measurements.

Table A1: Composition of the gas phase of experiment conducted at 200°C and 15 MPa, measured by gas chromatography analysis. Gas compositions are given as a volume%. The date of analysis, chromatograph number and injection pressure P(inj) are also given.

	Date of analysis	Chromato: No	P(inj) bar	He	H2	CH4	CO2	O2	N2	C2H6	C3H8	i-C4H10	n-C4H10
MT1_01	12/17/2014	GC09-14-1696	2141.3	nd	0.00	nd	101.8	0.0	0.3	nd	nd	nd	nd
MT1_02	12/17/2014	GC09-14-1694	2094.4	nd	0.00	nd	97.0	1.0	4.0	nd	nd	nd	nd
MT1_03	12/3/2014	GC09-14-1568	1240.4	nd	0.00	nd	90.0	2.0	7.9	nd	nd	nd	nd
MT1_04	12/17/2014	GC09-14-1592	1691	nd	0.00	nd	98.2	nd	nd	nd	nd	nd	nd
MT1_05	12/3/2014	GC09-14-1574	1122.2	nd	0.01	nd	100.1	0.0	0.2	nd	nd	nd	nd
MT1_06	12/3/2014	GC09-14-1572	1145.5	nd	0.00	nd	100.2	nd	nd	nd	nd	nd	nd
MT1_07	12/17/2014	GC09-14-1690	1440.2	0.01	0.01	nd	101.8	nd	nd	nd	nd	nd	nd
MT1_08	12/16/2014	GC09-14-1674	1427.4	0.01	0.01	0.0001	100.6	nd	nd	nd	nd	nd	nd
MT1_09	12/16/2014	GC09-14-1672	1191.2	0.01	0.00	nd	100.5	nd	nd	nd	nd	nd	nd
MT1_10	12/16/2014	GC09-14-1670	1191.2	nd	0.00	0.0002	100.4	nd	nd	nd	nd	nd	nd
MT1_11	12/16/2014	GC09-14-1668	1191.2	0.01	0.01	0.0002	100.6	nd	nd	nd	nd	nd	nd
MT1_12	12/16/2014	GC09-14-1666	1191.2	nd	0.01	0.0002	100.0	nd	nd	nd	nd	nd	nd
MT1_13	1/23/2015	GC09-15-51	1154.2	nd	0.01	nd	100.4	nd	nd	nd	nd	nd	nd
MT1_14	1/23/2015	GC09-15-54	1940.6	nd	0.01	nd	100.8	nd	0.0	nd	nd	nd	nd

Appendix 1

Table A2: Composition of the gas phase of experiment conducted at 250°C and 30 MPa, measured by gas chromatography analysis. Gas compositions are given as a volume%. The date of analysis, chromatograph number and injection pressure P(inj) are also given.

	Date of analysis	Chromato: No	P(inj) bar	He	H2	CH4	CO2	O2	N2	C2H6	C3H8	i-C4H10	n-C4H10
MT2_1	3/4/2015	GC09-15-211	1711	0.02	nd	nd	99.83	0.01	0.07	nd	nd	nd	nd
MT2_2	3/5/2015	GC09-15-226	1600.6	0.07	nd	0.0002	99.92	nd	0.10	nd	nd	nd	nd
MT2_3	3/4/2015	GC09-15-208	1107.6	0.08	nd	0.0020	99.47	nd	0.09	nd	nd	nd	nd
MT2_4	3/5/2015	GC09-15-223	1615.1	0.04	nd	0.0001	99.64	nd	0.09	nd	nd	nd	nd
MT2_5	3/5/2015	GC09-15-219	1612.4	0.04	0.001	0.0001	99.47	nd	nd	nd	nd	nd	nd
MT2_6	3/5/2015	GC09-15-228	1613.2	0.03	0.001	0.0001	99.91	0.09	0.08	nd	nd	nd	nd
MT2_7	3/5/2015	GC09-15-216	1611.7	0.02	0.002	0.0002	99.45	0.01	0.14	nd	nd	nd	nd
MT2_8	3/5/2015	GC09-15-217	1616.6	0.02	0.002	0.0004	99.41	0.05	0.28	nd	nd	nd	nd
MT2_9	4/20/2015	GC09-15-438	1103.2	0.02	0.002	0.0002	102.48	0.02	0.21	nd	nd	nd	nd
MT2_10	4/21/2015	GC09-15-447	1099.5	0.02	0.002	0.0002	100.45	Nd	0.10	nd	nd	nd	nd
MT2_11	4/21/2015	GC09-15-449	1003.9	0.01	0.013	0.0014	99.70	nd	0.10	0.0002	0.0003	0.0002	0.0005
MT2_12	4/21/2015	GC09-15-451	1023.2	0.01	0.013	0.0035	96.28	0.616	2.74	0.0017	0.0008	0.0015	0.0009
MT2_13	4/21/2015	GC09-15-453	1101.4	0.01	0.010	0.0010	99.64	nd	0.10	nd	0.0002	0.0001	0.0003
MT2_14	4/21/2015	GC09-15-455	1059.3	0.01	0.014	0.0007	99.40	0.02	0.16	nd	0.0002	nd	0.0003
MT2_15	4/21/2015	GC09-15-457	1083.8	0.02	0.031	0.0016	99.40	0.03	0.25	nd	0.0002	0.0001	0.0004
MT2_16	3/26/2015	GC09-15-292	1129.2	0.01	0.015	0.0004	99.36	nd	nd	nd	nd	nd	nd
MT2_17	3/26/2015	GC09-15-290	1005.1	0.01	0.019	0.0005	98.93	nd	nd	nd	nd	nd	nd

Table A3: Composition of the gas phase of experiment conducted at 300°C and 30 MPa, measured by gas chromatography analysis. Gas compositions are given as a volume%. The date of analysis, chromatograph number and injection pressure P(inj) are also given.

	Date of analysis	Chromato: No	P(inj) bar	He	H2	CH4	CO2	O2	N2	C2H6	C3H8	i-C4H10	n-C4H10
MT4_1	3/6/2015	GC09-15-237	209.5	0.11	nd	0.0001	102.30	0.06	0.21	nd	nd	nd	nd
MT4_2	4/23/2015	GC09-15-491	194.9	0.08	0.063	0.0054	78.65	0.08	0.42	nd	0.0004	nd	0.0010
MT4_3	4/23/2015	GC09-15-493	212.5	0.10	0.056	0.0059	76.28	0.59	2.55	nd	0.0010	0.0005	0.0015
MT4_4	3/6/2015	GC09-15-239	73.5	0.72	nd	0.0002	100.72	0.24	1.24	nd	nd	nd	nd
MT4_5	4/23/2015	GC09-15-495	225.7	0.05	0.092	0.0130	67.76	nd	11.10	0.0018	0.0053	0.0029	0.0054
MT4_6	3/6/2015	GC09-15-241	205.3	0.22	nd	0.0009	100.13	0.45	1.78	nd	nd	nd	nd
MT4_7	3/10/2015	GC09-15-259	190.5	0.75	0.069	0.0008	102.66	nd	nd	nd	nd	nd	nd
MT4_8	3/10/2015	GC09-15-264	356.8	2.44	0.130	0.0006	103.00	nd	nd	nd	nd	nd	nd
MT4_9	4/23/2015	GC09-15-497	383.1	0.04	0.016	0.0038	102.46	0.07	0.62	0.0004	0.0009	0.0004	0.0013
MT4_10	4/23/2015	GC09-15-499	377.6	0.03	0.032	0.0026	103.24	0.01	0.09	nd	0.0002	0.0002	0.0006
MT4_11	4/23/2015	GC09-15-501	378.9	0.03	0.018	0.0020	103.67	0.003	0.06	nd	0.0002	0.0013	0.0003
MT4_12	4/23/2015	GC09-15-503	370.6	0.03	0.020	0.0023	103.10	0.004	0.07	nd	nd	0.0008	0.0003
MT4_13	3/26/2015	GC09-15-296	372.7	0.03	0.009	0.0008	98.77	nd	nd	nd	nd	nd	nd
MT4_15	4/30/2015	GC09-15-586	372.4	0.02	0.016	0.0094	94.97	0.046	0.19	0.00	0.01	0.00	0.01

Appendix 1

Table A4: Composition of the gas phase of blank experiments conducted at 250 and 300°C and 30 MPa, measured by gas chromatography analysis. Gas compositions are given as a volume%. The date of analysis, chromatograph number and injection pressure P(inj) are also given.

	Date of analysis	Chromato: No	P(inj) bar	He	H ₂	CH ₄	CO ₂	O ₂	N ₂	C ₂ H ₆	C ₃ H ₈	i-C ₄ H ₁₀	n-C ₄ H ₁₀
MT2b_1	4/20/2015	GC09-15-436	1104.9	0.001	0.009	0.0000	102.94	nd	0.04	nd	nd	nd	nd
MT2b_2	5/21/2015	GC09-15-739	1101.1	0.04	nd	0.0009	104.44	0.01	0.11	0.0009	0.0040	0.0044	0.0066
MT2b_3	5/21/2015	GC09-15-743	1096.7	0.05	nd	0.0013	104.37	0.01	0.11	0.0011	0.0044	0.0062	0.0090
MT4 - b1	4/20/2015	GC09-15-432	618.3	0.01	nd	0.0028	104.78	nd	nd	0.00	0.00	0.00	0.00
MT4 - b2	5/21/2015	GC09-15-741	366	0.02	nd	0.0043	103.99	0.09	0.18	0.00	0.01	0.02	0.03
MT4 - b3	5/21/2015	GC09-15-745	384.4	0.01	nd	0.0040	103.69	0.07	0.15	0.00	0.01	0.01	0.02

The gas compositions obtained in volume % were then converted into μmol s. Given below is the stepwise process showing the calculation of hydrogen composition as an example.

$$H_{2(\text{atomic}\%)} = H_{2(\text{vol}\%)} / 100 \quad [\text{Eq. A1}]$$

$$P_{H_2}(\text{MPa}) = H_{2(\text{atomic}\%)} * (P_{(\text{total, bar})} * 10^{-5}) \quad [\text{Eq. A2}]$$

$$nH_2(\text{mmol}) = [(P_{H_2}(\text{MPa}) * (V_{(\text{headspace})}) / (8.314 * T(\text{K}))] * 1000 \quad [\text{Eq. A3}]$$

$$nH_2(\mu\text{mol}) = nH_2(\text{mmol}) / 1000 \quad [\text{Eq. A4}]$$

$$nH_2(\mu\text{mol/g}) = nH_2(\mu\text{mol}) / (\text{wt of mine tailings(g)}) \quad [\text{Eq. A5}]$$

The gas headspace $V_{(\text{headspace})}$ necessary to calculate the number of mols of a particular gas (Eq.A3) was obtained as follows.

First, the initial volume of gaseous headspace in the batch reactor was calculated as shown below:

Volume of the batch reactor = 250 mL

Volume of water = 200 mL

Initial head space = 250 – 200 mL = 50 mL

Then we noted the volume of liquid sampled out ($V_{(\text{liq})}$) in order to calculate the moving total of the liquid sampled out. Finally, we calculated the gas headspace volume after each liquid sampling (table A5 to A8). The gas compositions in μmol s calculated according to Eq. A1 – A5 are shown in table A9 –A12.

Appendix 1

Table A5: Change in headspace volume during the experiment conducted at 200°C and 15 MPa.

Sample	t (hrs)	t (days)	V _(liq) (ml)	V _{(liq) moving total} (ml)	V _{(liq) moving total} (m ³)	V _(gas headspace) (m ³)
MT1_01	2.0	0.1	2.1026	2.1026	2.10E-06	0.00005
MT1_02	21.0	0.9	2.2969	4.3995	4.40E-06	0.00005
MT1_03	44.0	1.8	4.0689	8.4684	8.47E-06	0.00005
MT1_04	66.0	2.8	2.7004	11.1688	1.12E-05	0.00006
MT1_05	139.0	5.8	2.773	13.9418	1.39E-05	0.00006
MT1_06	187.0	7.8	3.1751	17.1169	1.71E-05	0.00006
MT1_07	212.0	8.8	2.8776	19.9945	2.00E-05	0.00007
MT1_08	235.0	9.8	2.9931	22.9876	2.30E-05	0.00007
MT1_09	312.0	13.0	3.6195	26.6071	2.66E-05	0.00007
MT1_10	330.0	13.8	3.2392	29.8463	2.98E-05	0.00008
MT1_11	384.0	16.0	3.0869	32.9332	3.29E-05	0.00008
MT1_12	480.0	20.0	2.6884	35.6216	3.56E-05	0.00008
MT1_13	547.0	22.8	2.8956	38.5172	3.85E-05	0.00009
MT1_14	570.0	23.8	3.4358	41.953	4.20E-05	0.00009

Table A6: Change in headspace volume during the experiment conducted at 250°C and 30 MPa.

Sample	t (hrs)	t (days)	V _(liq) (ml)	V _{(liq) moving total} (ml)	V _{(liq) moving total} (m ³)	V _(gas headspace) (m ³)
MT2_1	0.0	0.0	2.27	2.27E+00	2.27E-06	0.00008
MT2_2	16.5	0.7	2.5424	4.81E+00	4.81E-06	0.00008
MT2_3	23.2	1.0	2.6312	7.44E+00	7.44E-06	0.00008
MT2_4	41.2	1.7	2.6367	1.01E+01	1.01E-05	0.00009
MT2_5	47.0	2.0	2.1456	1.22E+01	1.22E-05	0.00009
MT2_6	112.3	4.7	2.5054	1.47E+01	1.47E-05	0.00009
MT2_7	141.0	5.9	2.1128	1.68E+01	1.68E-05	0.00009
MT2_8	160.3	6.7	2.6118	1.95E+01	1.95E-05	0.00010
MT2_9	185.3	7.7	1.7847	2.12E+01	2.12E-05	0.00010
MT2_10	214.0	8.9	2.2643	2.35E+01	2.35E-05	0.00010
MT2_11	281.0	11.7	2.4571	2.60E+01	2.60E-05	0.00010
MT2_12	329.0	13.7	2.4144	2.84E+01	2.84E-05	0.00011
MT2_13	353.0	14.7	2.604	3.10E+01	3.10E-05	0.00011
MT2_14	449.0	18.7	2.7197	3.37E+01	3.37E-05	0.00011
MT2_15	498.0	20.8	2.4442	3.61E+01	3.61E-05	0.00011
MT2_16	546.0	22.8	2.7589	3.89E+01	3.89E-05	0.00012
MT2_17	618.3	25.8	2.7752	4.17E+01	4.17E-05	0.00012

Appendix 1

Table A7: Change in headspace volume during the experiment conducted at 300°C and 30 MPa.

Sample	t (hrs)	t (days)	V _(liq) (ml)	V _{(liq) moving total} (ml)	V _{(liq) moving total} (m ³)	V _(gas headspace) (m ³)
MT4_1	0.0	0.0	3.0	3.0	2.95E-06	0.0000800
MT4_2	18.3	0.8	3.1	6.1	6.08E-06	0.0000830
MT4_3	27.0	1.1	2.5	8.6	8.56E-06	0.0000861
MT4_4	43.3	1.8	2.3	10.8	1.08E-05	0.0000886
MT4_5	68.3	2.8	1.8	12.6	1.26E-05	0.0000908
MT4_6	97.0	4.0	2.6	15.2	1.52E-05	0.0000926
MT4_7	164.0	6.8	2.9	18.1	1.81E-05	0.0000952
MT4_8	212.0	8.8	2.3	20.4	2.04E-05	0.0000981
MT4_9	237.0	9.9	2.6	23.1	2.31E-05	0.0001004
MT4_10	332.0	13.8	2.3	25.4	2.54E-05	0.0001031
MT4_11	381.0	15.9	2.6	28.0	2.80E-05	0.0001054
MT4_12	429.0	17.9	2.8	30.8	3.08E-05	0.0001080
MT4_13	501.0	20.9	2.8	33.6	3.36E-05	0.0001108
MT4_15	576.3	24.0	3.3	39.4	3.94E-05	0.0001161

Table A8: Change in headspace volume during the duplicates of experiments conducted at 250°C and 300°C and 30 MPa.

Sample	t (hrs)	t (days)	V _(liq) (ml)	V _{(liq) moving total} (ml)	V _{(liq) moving total} (m ³)	V _(gas headspace) (m ³)
MT2b_1	173.0	7.2	2.1	2.11E+00	2.11E-06	0.00012
MT2b_2	460.0	19.2	2.1	4.19E+00	4.19E-06	0.00008
MT2b_3	580.0	24.2	2.1	6.27E+00	6.27E-06	0.00008
MT4 - b1	173	7.2	2.12	2.12	2.12E-06	0.00012
MT4 - b2	460	19.2	1.79	3.91	3.91E-06	0.00008
MT4 - b3	580	24.2	2.12	6.03	6.03E-06	0.00008

Appendix 1

Table A9: Gas composition of the experiment conducted at 200°C and 15 MPa. H₂(atomic), PH₂(Pa) and n(H₂) values and similar parameters for CH₄, were obtained according to the equations A1-A5 above.

	H ₂ (atomic)	PH ₂ (Pa)	nH ₂ (mmols)	nH ₂ (μmols)	nH ₂ (μmols/g)	CH ₄ (atomic)	PCH ₄ (Pa)	nCH ₄ (mmols)	nCH ₄ (μmols)	nCH ₄ (μmols/g)	nH ₂ (mmol/g)
MT1_01	4.89E-05	733.53	0.009	9.32	4.5	0.00E+00	0.00	0.00	0.00000	0.000	4.54E-03
MT1_02	1.49E-05	223.54	0.003	2.96	1.4	0.00E+00	0.00	0.00	0.00000	0.000	1.44E-03
MT1_03	1.34E-05	200.46	0.003	2.77	1.4	0.00E+00	0.00	0.00	0.00000	0.000	1.35E-03
MT1_04	4.38E-05	656.45	0.010	9.76	4.8	0.00E+00	0.00	0.00	0.00000	0.000	4.76E-03
MT1_05	5.82E-05	872.86	0.014	13.57	6.6	0.00E+00	0.00	0.00	0.00000	0.000	6.62E-03
MT1_06	5.00E-05	749.90	0.012	12.19	5.9	0.00E+00	0.00	0.00	0.00000	0.000	5.94E-03
MT1_07	6.75E-05	1011.96	0.017	17.27	8.4	0.00E+00	0.00	0.00	0.00000	0.000	8.42E-03
MT1_08	6.15E-05	922.97	0.016	16.42	8.0	1.29E-06	19.32	0.00	0.34377	0.168	8.01E-03
MT1_09	1.52E-06	22.85	0.000	0.42	0.2	0.00E+00	0.00	0.00	0.00000	0.000	2.07E-04
MT1_10	4.29E-05	643.88	0.013	12.54	6.1	1.71E-06	25.69	0.00	0.50030	0.244	6.11E-03
MT1_11	1.14E-04	1710.56	0.035	34.72	16.9	1.56E-06	23.47	0.00	0.47629	0.232	1.69E-02
MT1_12	9.86E-05	1479.28	0.031	31.19	15.2	1.74E-06	26.04	0.00	0.54906	0.268	1.52E-02
MT1_13	1.12E-04	1683.95	0.037	36.65	17.9	0.00E+00	0.00	0.00	0.00000	0.000	1.79E-02
MT1_14	1.21E-04	1822.43	0.041	41.01	20.0	0.00E+00	0.00	0.00	0.00000	0.000	2.00E-02

Appendix 1

Table A10: Gas composition of the experiment conducted at 250°C and 30 MPa. H2(atomic), PH2(Pa) and n(H2) values and similar parameters for CH4, were obtained according to the equations A1-A5 above.

	H2 (atomic)	PH2 (Pa)	nH2 (mmols)	nH2 (μmols)	nH2 (μmols/g)	CH4 (atomic)	PCH4 (Pa)	nCH4 (mmols)	nCH4 (μmols)	nCH4 (μmols/g)	nH2 (μmol/g)*0,83	nCH4 (μmol/g)*0,83
MT2_1	0.00E+00	0.00	0.00	0.00	0.0	0.00E+00	0.00	0.00	0.00	0.00	0.0	0.00
MT2_2	0.00E+00	0.00	0.00	0.00	0.0	1.55E-06	46.39	0.00	0.88	0.52	0.0	0.43
MT2_3	0.00E+00	0.00	0.00	0.00	0.0	2.00E-05	599.78	0.01	11.70	6.88	0.0	5.71
MT2_4	0.00E+00	0.00	0.00	0.00	0.0	1.49E-06	44.59	0.00	0.90	0.53	0.0	0.44
MT2_5	1.15E-05	344.45	0.01	7.13	4.2	7.07E-07	21.22	0.00	0.44	0.26	3.5	0.21
MT2_6	8.99E-06	269.84	0.01	5.72	3.4	6.99E-07	20.97	0.00	0.44	0.26	2.8	0.22
MT2_7	1.77E-05	530.86	0.01	11.56	6.8	2.02E-06	60.75	0.00	1.32	0.78	5.6	0.65
MT2_8	2.35E-05	705.67	0.02	15.71	9.2	4.41E-06	132.29	0.00	2.95	1.73	7.7	1.44
MT2_9	1.95E-05	583.59	0.01	13.34	7.8	2.27E-06	68.05	0.00	1.56	0.92	6.5	0.76
MT2_10	2.46E-05	736.85	0.02	17.15	10.1	2.21E-06	66.40	0.00	1.55	0.91	8.4	0.75
MT2_11	1.25E-04	3758.93	0.09	89.45	52.6	1.38E-05	414.88	0.01	9.87	5.81	43.7	4.82
MT2_12	1.34E-04	4014.68	0.10	97.80	57.5	3.46E-05	1036.51	0.03	25.25	14.85	47.8	12.33
MT2_13	1.03E-04	3080.76	0.08	76.76	45.2	9.84E-06	295.28	0.01	7.36	4.33	37.5	3.59
MT2_14	1.44E-04	4318.43	0.11	110.19	64.8	6.85E-06	205.46	0.01	5.24	3.08	53.8	2.56
MT2_15	3.07E-04	9211.88	0.24	240.80	141.6	1.55E-05	465.49	0.01	12.17	7.16	117.6	5.94
MT2_16	1.50E-04	4486.73	0.12	119.81	70.5	3.60E-06	107.99	0.00	2.88	1.70	58.5	1.41
MT2_17	1.92E-04	5745.79	0.16	157.07	92.4	5.01E-06	150.21	0.00	4.11	2.42	76.7	2.00

Appendix 1

Table A11: Gas composition of the experiment conducted at 300°C and 30 MPa. H₂(atomic), PH₂(Pa) and n(H₂) values and similar parameters for CH₄, were obtained according to the equations A1-A5 above.

	H ₂ (atomic)	PH ₂ (Pa)	nH ₂ (mmols)	nH ₂ (μmols)	nH ₂ (μmols/g)	CH ₄ (atomic)	PCH ₄ (Pa)	nCH ₄ (mmols)	nCH ₄ (μmols)	nCH ₄ (μmols/g)	nH ₂ (μmol/g)*0,6	nCH ₄ (μmol/g)*0,6
MT4_1	0.00E+00	0.00	0.0000	0.00	0.0	5.77E-07	17.31	0.00	0.29	0.17	0.0	0.10
MT4_2	6.30E-04	18907.71	0.3291	329.14	193.6	5.39E-05	1617.01	0.03	28.15	16.56	116.2	9.93
MT4_3	5.58E-04	16746.96	0.3025	302.51	177.9	5.92E-05	1775.82	0.03	32.08	18.87	106.8	11.32
MT4_4	0.00E+00	0.00	0.0000	0.00	0.0	2.38E-06	71.28	0.00	1.32	0.78	0.0	0.47
MT4_5	9.23E-04	27693.85	0.5278	527.83	310.5	1.30E-04	3893.02	0.07	74.20	43.65	186.3	26.19
MT4_6	0.00E+00	0.00	0.0000	0.00	0.0	8.53E-06	255.83	0.00	4.97	2.93	0.0	1.76
MT4_7	6.86E-04	20565.45	0.4110	411.01	241.8	8.20E-06	245.92	0.00	4.91	2.89	145.1	1.73
MT4_8	1.30E-03	38998.47	0.8032	803.25	472.5	5.61E-06	168.30	0.00	3.47	2.04	283.5	1.22
MT4_9	1.61E-04	4835.14	0.1019	101.91	59.9	3.79E-05	1138.00	0.02	23.99	14.11	36.0	8.47
MT4_10	3.22E-04	9663.70	0.2090	209.05	123.0	2.55E-05	765.59	0.02	16.56	9.74	73.8	5.85
MT4_11	1.78E-04	5349.42	0.1183	118.32	69.6	2.02E-05	604.50	0.01	13.37	7.87	41.8	4.72
MT4_12	2.01E-04	6021.43	0.1365	136.48	80.3	2.29E-05	686.52	0.02	15.56	9.15	48.2	5.49
MT4_13	8.91E-05	2673.77	0.0622	62.17	36.6	7.63E-06	228.81	0.01	5.32	3.13	21.9	1.88
MT4_15	1.60E-04	4789.19	0.1167	116.68	68.6	9.36E-05	2807.55	0.07	68.40	40.24	41.2	24.14

Appendix 1

Table A12: Gas composition of the blank experiments conducted at 250°C and 300°C and at 30 MPa. H₂(atomic), PH₂(Pa) and n(H₂) values and similar parameters for CH₄, were obtained according to the equations A1-A5 above.

	H₂ (atomic)	PH₂ (Pa)	nH₂ (mmols)	nH₂ (μmols)	nH₂ (μmols/g)	CH₄ (atomic)	PCH₄ (Pa)	nCH₄ (mmols)	nCH₄ (μmols)	nCH₄ (μmols/g)	nH₂ (μmol/g)	nCH₄ (μmol/g)
MT2b_1	9.13E-05	2739.23	0.08	76.63	45.1	3.60E-07	10.79	0.00	0.30	0.18	37.41	0.15
MT2b_2	0.00E+00	0.00	0.00	0.00	0.0	8.75E-06	262.41	0.00	4.95	2.91	0.00	2.42
MT2b_3	0.00E+00	0.00	0.00	0.00	0.0	1.35E-05	403.57	0.01	7.81	4.60	0.00	3.81
MT4 - b1	0.00E+00	0.00	0.0000	0.00	0.0	2.80E-05	840.92	0.02	21.07	12.39	0.00	7.44
MT4 - b2	0.00E+00	0.00	0.0000	0.00	0.0	4.26E-05	1276.55	0.02	22.00	12.94	0.00	7.76
MT4 - b3	0.00E+00	0.00	0.0000	0.00	0.0	4.02E-05	1205.84	0.02	21.23	12.49	0.00	7.49

As shown in table A10 and A11, the final values of nH_2 and nCH_4 at 250°C and 300°C experiments were obtained by multiplying the nH_2 and nCH_4 in μmol s by a factor of 0.83 and 0.6 respectively. This correction was conducted as a correction to the partial pressure of each gas considering the effect of water vapor in the gas headspace.

Correction for the partial pressure of H_2 and CH_4

Initially, the gas phase of the batch reactor consisted of CO_2 and traces of oxygen. However, during the course of the experiments conducted at $200\text{ }^\circ\text{C} < T < 300\text{ }^\circ\text{C}$, $15\text{ MPa} < p_{CO_2} < 30\text{ MPa}$, $t \sim 25$ days, water vapor is added to the gas phase due to partial evaporation of water in the reactor and hydrogen is added by the redox reaction of water and Fe^{2+} from mine tailings.

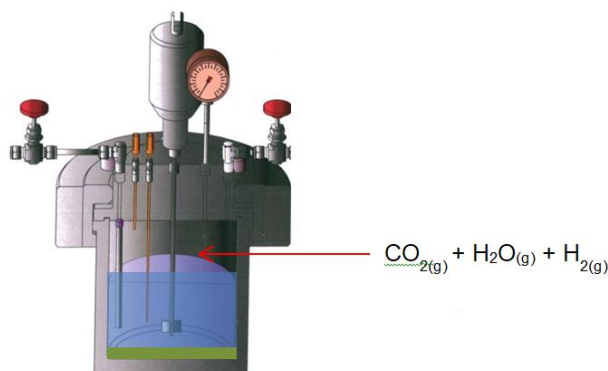


Figure A1. Batch reactor operating at hydrothermal conditions contains carbon dioxide, hydrogen and water vapor in the gas phase.

Maintaining a constant carbon dioxide partial pressure (p_{CO_2}) is one of the major aspects of this experiment. If the gas phase is entirely composed of CO_2 , then the total pressure of the reactor is equal to the p_{CO_2} . Since, the gas phase is a mixture of three gases the total pressure of the reactor is the addition of partial pressures of these three gases as given below:

$$P_{\text{total}} = p_{CO_2} + p_{H_2O} + p_{H_2}$$

From the trial experiments, we observed that only a trace of hydrogen is produced in contrary to water vapor. Therefore, first we calculated the mole fractions of $CO_{2(g)}$ and $H_{2O(g)}$ at temperature ranging from 100-300°C, using the Peng-Robinson Equation of state (EOS) (Søreide and Whitson, 1996) incorporated in the Thermosolver software, to understand whether the amount of water vapor in the gas phase is significant. The Peng-Robinson Equation of state used for this calculation is given below:

Appendix 1

$$P = \frac{RT}{v - b} - \frac{a \propto}{v^2 + 2bv - b^2}$$

P= pressure

R= ideal gas constant

T=absolute temperature

a,b = substance specific constants at critical point

$\alpha = (1 + K \cdot [1 - (T_r)^{1/2}])$, where $T_r = T/T_c$

v = volume

$K = 0.37464 + 1.54226 \cdot \omega - 0.26992 \cdot \omega^2$, where $\omega = p_{\text{sat}}/p_c$

The results showed that the mole fraction of water vapor ($X_{\text{H}_2\text{O}}$) increases as a function of temperature, whereas the mole fraction of carbon dioxide (X_{CO_2}) decreases with increasing temperature (Figure A2).

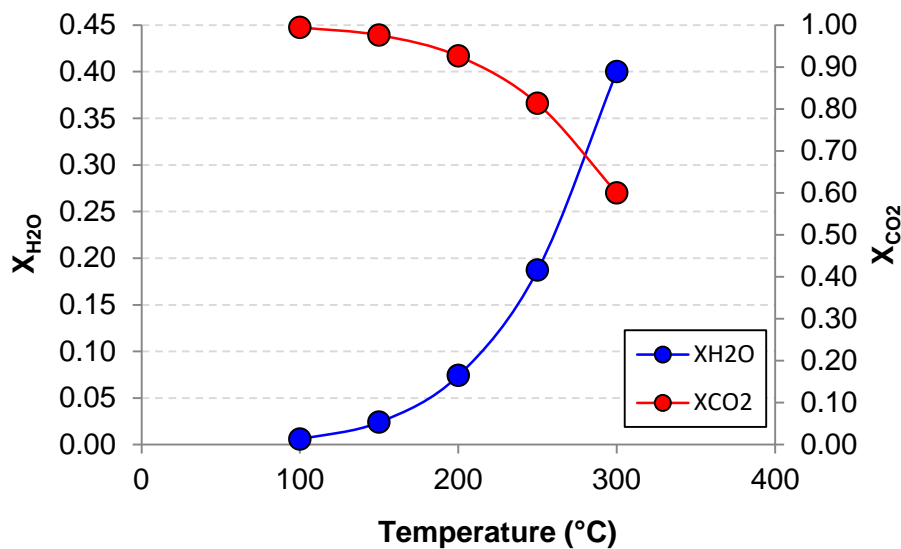


Figure A2. Variation of mole fraction of water vapor ($X_{\text{H}_2\text{O}}$) and mole fraction of carbon dioxide (X_{CO_2}) as a function of temperature.

According to this calculation, it is evident that the total pressure in the batch reactor significantly decreases due to the partial pressure of water vapor in the gas phase. Therefore, a correction factor of 0.87, 0.83 and 0.60 is necessary to correct the pressure or to obtain the accurate $p\text{CO}_2$ of the system at 200°C, 250°C and 300°C (Table A13). The correction factor was obtained by the following equation:

$$\text{Correction factor} = [\text{Desired } p\text{CO}_2 \text{ (MPa)}] / [\text{Actual } p\text{CO}_2 \text{ (MPa)}] \quad [\text{Eq. A6}]$$

Appendix 1

Table A13. Mole fraction of CO₂ and H₂O in the gas phase of batch reactors operated at 200, 250 and 300 °C, calculated based on the Peng-Robinson EOS (Søreide and Whitson, 1996), and the partial pressure of CO₂ at each temperature. Not that the desired p_{CO_2} has been significantly lowered by the presence of water vapor.

T (°C)	X _{CO2}	X _{H2O}	Desired P _{CO2} (MPa)	Actual P _{CO2} (MPa)	Correction factor
200	0.87	0.13	15	13.1	0.87
250	0.81	0.19	30	24.3	0.83
300	0.60	0.40	30	18.0	0.60

Appendix 2

Supplementary material for Chapter 3

Gas phase data

S1. The composition of gas phase of MT1 experiment conducted at 473 K and 15 MPa.

Duration (days)	H2 ($\mu\text{mol}/\text{g}$)	CH4 ($\mu\text{mol}/\text{g}$)	CO2 (mmol/g)	N2 (mmol/g)	O2 (mmol/g)
0.1	4.54	-	94.6	0.24	0.04
0.9	1.44	-	94.0	3.84	0.99
1.8	1.35	-	91.0	7.98	2.02
2.8	4.76	-	106.8	-	-
5.8	6.62	-	113.8	0.24	0.04
7.8	5.94	-	119.1	-	-
8.8	8.42	-	127.0	-	-
9.8	8.01	0.17	130.9	-	-
13.0	0.21	-	136.4	-	-
13.8	6.11	0.24	143.0	-	-
16.0	16.92	0.23	149.3	-	-
20.0	15.20	0.27	154.1	-	-
22.8	17.87	-	159.8	-	-
23.8	19.99	-	165.9	0.05	-

S2. The composition of gas phase of MT2 experiment conducted at 523 K and 30 MPa.

Duration (days)	H2 ($\mu\text{mol}/\text{g}$)	CH4 ($\mu\text{mol}/\text{g}$)	CO2 (mmol/g)	N2 (mmol/g)	O2 (mmol/g)	C2H6 ($\mu\text{mol}/\text{g}$)	C3H8 ($\mu\text{mol}/\text{g}$)	iC4H10 ($\mu\text{mol}/\text{g}$)	nC4H11 ($\mu\text{mol}/\text{g}$)
0.00	0.00	0.00	179.13	0.13	0.02	-	-	-	-
0.69	0.00	0.43	184.38	0.18	-	-	-	-	-
0.96	0.00	5.71	189.23	0.18	-	-	-	-	-
1.71	0.00	0.44	195.42	0.18	-	-	-	-	-
1.96	3.48	0.21	200.97	-	-	-	-	-	-
4.68	2.79	0.22	206.68	0.17	0.19	-	-	-	-
5.88	5.64	0.65	211.31	0.29	0.03	-	-	-	-
6.68	7.67	1.44	215.93	0.61	0.11	-	-	-	-
7.72	6.52	0.76	228.60	0.46	0.04	-	-	-	-
8.92	8.37	0.75	228.11	0.23	-	-	-	-	-
11.71	43.67	4.82	231.46	0.24	-	0.41	0.59	0.04	1.27
13.71	47.75	12.33	228.82	6.52	1.46	4.01	1.93	0.36	2.23
14.71	37.48	3.59	242.22	0.25	-	-	0.38	0.03	0.72
18.71	53.80	2.56	247.42	0.40	0.04	-	0.42	-	0.67
20.75	117.57	5.94	253.49	0.64	0.09	-	0.58	0.03	0.99
22.75	58.49	1.41	258.83	-	-	-	-	-	-
25.76	76.69	2.00	263.83	-	-	-	-	-	-

S3. The composition of gas phase of MT4 experiment conducted at 573 K and 30 MPa.

Duration (days)	H2 ($\mu\text{mol}/\text{g}$)	CH4 ($\mu\text{mol}/\text{g}$)	CO2 (mmol/g)	N2 (mmol/g)	O2 (mmol/g)	C2H6 ($\mu\text{mol}/\text{g}$)	C3H8 ($\mu\text{mol}/\text{g}$)	iC4H10 ($\mu\text{mol}/\text{g}$)	nC4H11 ($\mu\text{mol}/\text{g}$)
0	0.00	0.10	183.56	0.38	0.10	-	-	-	-
0.76	116.17	9.93	146.34	0.78	0.15	-	0.82	-	1.89
1.13	106.77	11.32	147.27	4.92	1.14	-	1.95	0.09	2.89
1.80	0.00	0.47	200.07	2.47	0.47	-	-	-	-
2.85	186.29	26.19	138.04	22.60	-	3.70	10.72	0.60	11.08
4.04	0.00	1.76	208.04	3.71	0.93	-	-	-	-
6.83	145.06	1.73	219.28	-	-	-	-	-	-
8.83	283.50	1.22	226.74	-	-	-	-	-	-
9.88	35.97	8.47	230.83	1.40	0.17	0.79	2.12	0.10	2.87
13.83	73.78	5.85	238.71	0.20	0.02	-	0.45	0.04	1.40
15.88	41.76	4.72	245.09	0.15	0.01	-	0.37	0.30	0.73
17.88	48.17	5.49	249.76	0.16	0.01	-	-	0.19	0.71
20.88	21.94	1.88	245.44	-	-	-	-	-	-
24.01	41.18	24.14	247.30	0.50	0.12	8.16	16.95	0.74	14.76

S4. The composition of gas phase of MT2b experiment conducted at 523 K and 30 MPa. This is a blank experiment conducted at similar PT conditions in comparison with MT2, without introducing mine tailings in the reactor (due to technical difficulties, CO2 was not readjusted after the first sampling).

Duration (days)	H2 ($\mu\text{mol}/\text{g}$)	CH4 ($\mu\text{mol}/\text{g}$)	CO2 (mmol/g)	N2 (mmol/g)	O2 (mmol/g)	C2H6 ($\mu\text{mol}/\text{g}$)	C3H8 ($\mu\text{mol}/\text{g}$)	iC4H10 ($\mu\text{mol}/\text{g}$)	nC4H11 ($\mu\text{mol}/\text{g}$)
7.21	-	0.15	280.94	0.10	-	-	-	-	-
19.17	-	2.42	192.34	0.19	0.03	1.67	7.28	0.81	12.16
24.17	-	3.81	197.10	0.20	0.02	2.05	8.37	1.17	16.95

S5. The composition of gas phase of MT4b experiment conducted at 573 K and 30 MPa. This is a blank experiment without reactants in order to monitor H2 and CH4 concentrations. It was conducted at similar PT conditions in comparison with MT4, without introducing mine tailings in the reactor (due to technical difficulties, CO2 was not readjusted after the first sampling).

MT4b									
Duration (days)	H2 ($\mu\text{mol}/\text{g}$)	CH4 ($\mu\text{mol}/\text{g}$)	CO2 (mmol/g)	N2 (mmol/g)	O2 (mmol/g)	C2H6 ($\mu\text{mol}/\text{g}$)	C3H8 ($\mu\text{mol}/\text{g}$)	iC4H10 ($\mu\text{mol}/\text{g}$)	nC4H11 ($\mu\text{mol}/\text{g}$)
7.21	-	7.44	280.58	-	-	2.51	6.02	0.30	7.30
19.17	-	7.76	191.52	0.33	0.16	6.72	26.92	3.55	52.42
24.17	-	7.49	195.13	0.29	0.13	4.29	13.39	1.84	28.87

Quantification of secondary phases

S6. Calculation of carbonate yield

The quantification of carbonate phases using Rock-Eval 6 (Behar et al., 2001) involves pyrolysis and oxidation of ~40 mg of sample in an inert gas flow above 400 °C and oxidation at temperatures between 650°C–850°C. The gaseous CO₂ produced during the pyrolysis and oxidation cycles is analyzed by an infra-red analyzer (eg; S3' peak and S5 peak respectively) in online mode and the peak areas of S3' and S5 peaks are used to calculate the percent weight of carbonate according to the equations,

$$\text{PyroMinC (wt.\%)} = [(S3' \times 12/44) + (S3'CO/2) \times 12/28]/10$$

$$\text{OxiMinC (wt.\%)} = [S5 \times 12/44]/10$$

The amount of total mineral carbon (MinC) in the sample is obtained by the addition of weight percent (wt.%) of mineral carbon produced from pyrolysis cycle (PyroMinC) and oxidation cycle (OxyMinC) as below,

$$\text{MinC (wt.\%)} = \text{PyroMinC} + \text{OxyMinC}$$

$\text{wt\% Carbonate} = \text{MinC} \times (M_{\text{carbonate}} / M_{\text{carbon}})$, where the molar mass of carbon is 12 g/mol the molar mass of carbonates is :

- for MT1 $M((\text{Mg}_{0.92}\text{Fe}_{0.08})\text{CO}_3) = 86.8 \text{ g/mol}$
- for MT2 $M((\text{Mg}_{0.58}\text{Fe}_{0.42})\text{CO}_3) = 97.53 \text{ g/mol}$
- for MT4 $M((\text{Mg}_{0.83}\text{Fe}_{0.17})\text{CO}_3) = 89.7 \text{ g/mol}$

	MinC	$M_{\text{carbonate}} \text{ g/mol}$	wt% Carbonate	$m_{\text{Carbonate}} \text{ g/kg}$	$n_{\text{Carbonate}} \text{ mol/kg}$	$n_{\text{CO}_2} \text{ mol/kg}$	$m_{\text{CO}_2} \text{ g/kg}$
MT1	2.8	86.8	20.3%	225.7	2.60	2.60	114.4
MT2	6.62	97.5	53.8%	710.5	7.28	7.28	320.5
MT4	2.89	89.7	21.6%	241.6	2.69	2.69	118.5

Calculations for the amount of CO₂ trapped can be performed as follows:

$$m_{\text{CO}_2 \text{ trapped}} = \frac{M_{\text{CO}_2}}{M_{\text{carbonate}}} \times m_{\text{carbonate}}$$

$$m_{\text{CO}_2 \text{ trapped}} = \frac{M_{\text{CO}_2}}{M_{\text{carbonate}}} \times (\text{wt\%}_{\text{carbonate}} \times m_{\text{run products}})$$

$$m_{\text{CO}_2 \text{ trapped}} = \frac{M_{\text{CO}_2}}{M_{\text{carbonate}}} \times \text{wt\%}_{\text{carbonate}} \times (m_0 \text{ mine tailings} + m_{\text{CO}_2 \text{ trapped}})$$

$$\text{e.g. for MT2 : } m_{\text{CO}_2 \text{ trapped}} = \frac{44}{97.53} \times 53.8 \% \times (2 \text{ g} + m_{\text{CO}_2 \text{ trapped}})$$

$$m_{\text{CO}_2 \text{ trapped}} = 0.485 \text{ g} + (0.243 \times m_{\text{CO}_2 \text{ trapped}})$$

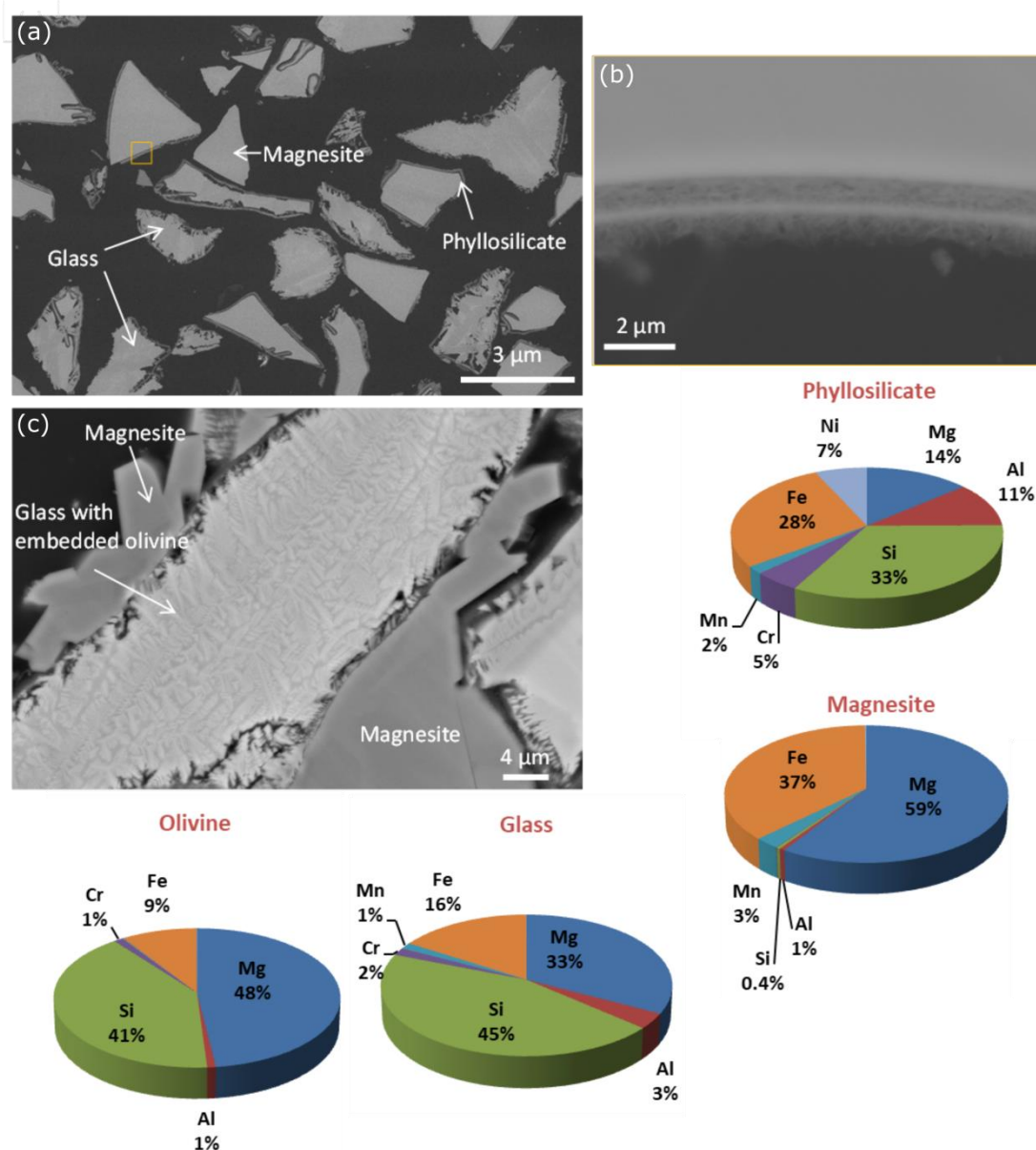
$$m_{\text{CO}_2 \text{ trapped}} = 0.485 \text{ g} + (0.243 \times m_{\text{CO}_2 \text{ trapped}})$$

$$m_{\text{CO}_2 \text{ trapped}} = 0.641 \text{ g for 2 g of mine tailings}$$

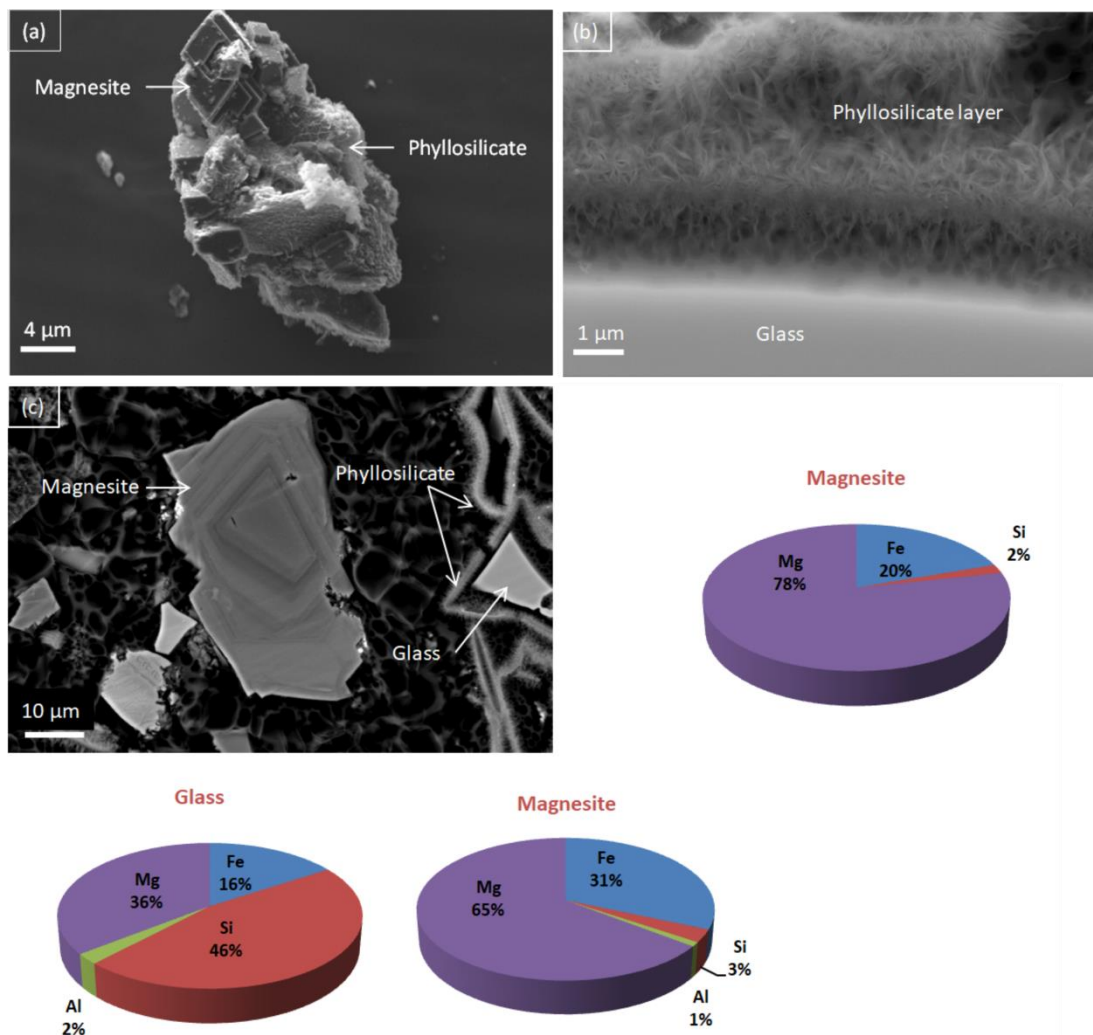
$$m_{\text{CO}_2 \text{ trapped}} = 320 \text{ g for 1 kg of mine tailings}$$

SEM analysis on reaction products

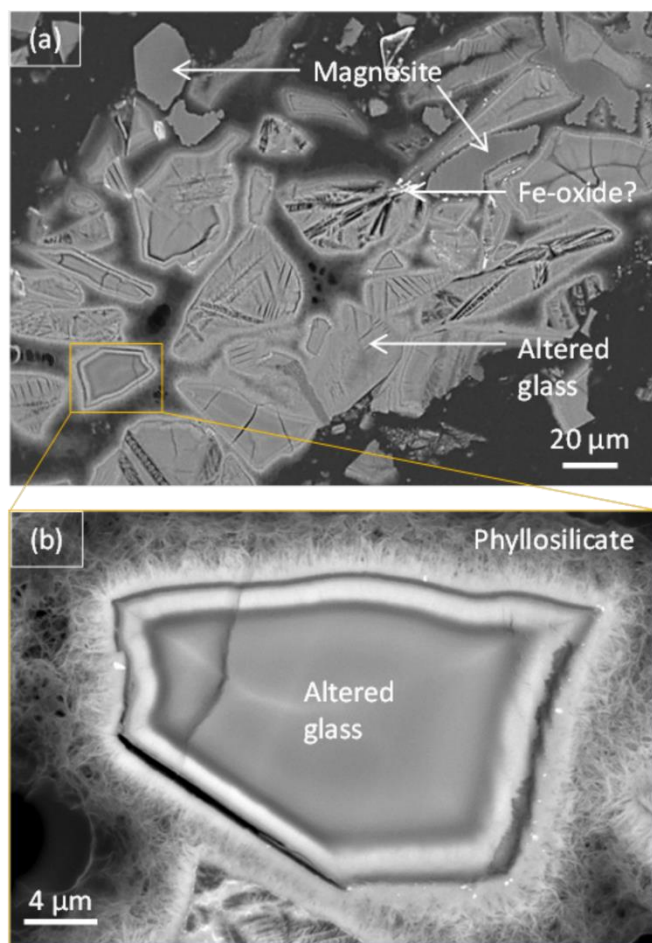
S7. SEM images of the ionically polished sections of experimental run product at $T = 473$ K and $P = 15$ MPa showing large anhedral magnesite crystals grown around glass (gl) and olivine (ol). Secondary phyllosilicates (phy) layers around glass. (b) magnified image of yellow square marked on (a); (c) glass altered into magnesite; The chemical composition of phyllosilicate, magnesite, olivine and glass analyzed by SEM-EDX are shown in the pie charts.



S8. SEM images of the ionically polished sections of experimental run product at $T = 523$ K and $P = 30$ MPa showing euhedral magnesite crystals and secondary phyllosilicates. (b) a magnified view of phyllosilicate (c) SEM image of a polished section of the run products showing magnesite with zoning. The chemical composition obtained by SEM EDX analysis is shown in pie charts.



S9. SEM images of the ionically polished sections of experimental run product at $T = 573$ K and $P = 30$ MPa, showing anhedral magnesite formed around glass, and heavily altered glass with thick layers of phyllosilicate.



S10. FIB –TEM analysis

Ultra-thin, electron transparent (<200 nm) sections of each solid reaction product was prepared by performing FIB milling at IPGP and also at Institute of Electronics, Microelectronics and Nanotechnology (IEMN), Lille using a gallium (Ga) beam. These sections which are thinned down to electron transparency (<200 nm) were then analyzed using transmission electron microscopy (TEM).

11. Calculation of maximum carbonation of mine tailings

Fo88	molar mass		
(Mg _{1.76} ,Fe _{0.24}) ₂ SiO ₄	148.21 g/mol		
MgO _{1.76} + FeO _{0.24}	88.16		
Mg(0.8)Fe _{0.2} CO ₃	87.43 g/mol		
CO ₂	44 g/mol		<u>45 wt.% Fo88</u>
MgO _{1.76} + FeO _{0.24} +2CO ₂	176.16		79.272
Olivine + 2CO ₂	236.21 g/mol		106.2954
Ratio max carbonation	74.58%		74.58%
glass			
(Mg _{1.50} ,Fe _{0.50}) ₂ SiO ₃	126.45 g/mol		
MgO _{1.50} + FeO _{0.50}	82.4		
Mg(0.75)Fe _{0.25} CO ₃	92.125 g/mol		<u>55 wt.% glass</u>
CO ₂	44 g/mol		93.72
(Mg _{1.50} ,Fe _{0.50}) ₂ SiO ₃ +CO ₂	170.4		117.9475
GLASS + CO ₂	214.45 g/mol		79.46%
Ratio max carbonation	79.46%		
		Fo88+glass	<u>Average</u>
		MT composit	172.992
			224.2429
		Ratio max ca	<u>77.14%</u>

Appendix 3

Figure A1. Variation of Na, Ca, K, Fe, Al in the solutions sampled from the on going batch experiments reacting CO₂-saturated water and mine tailings.

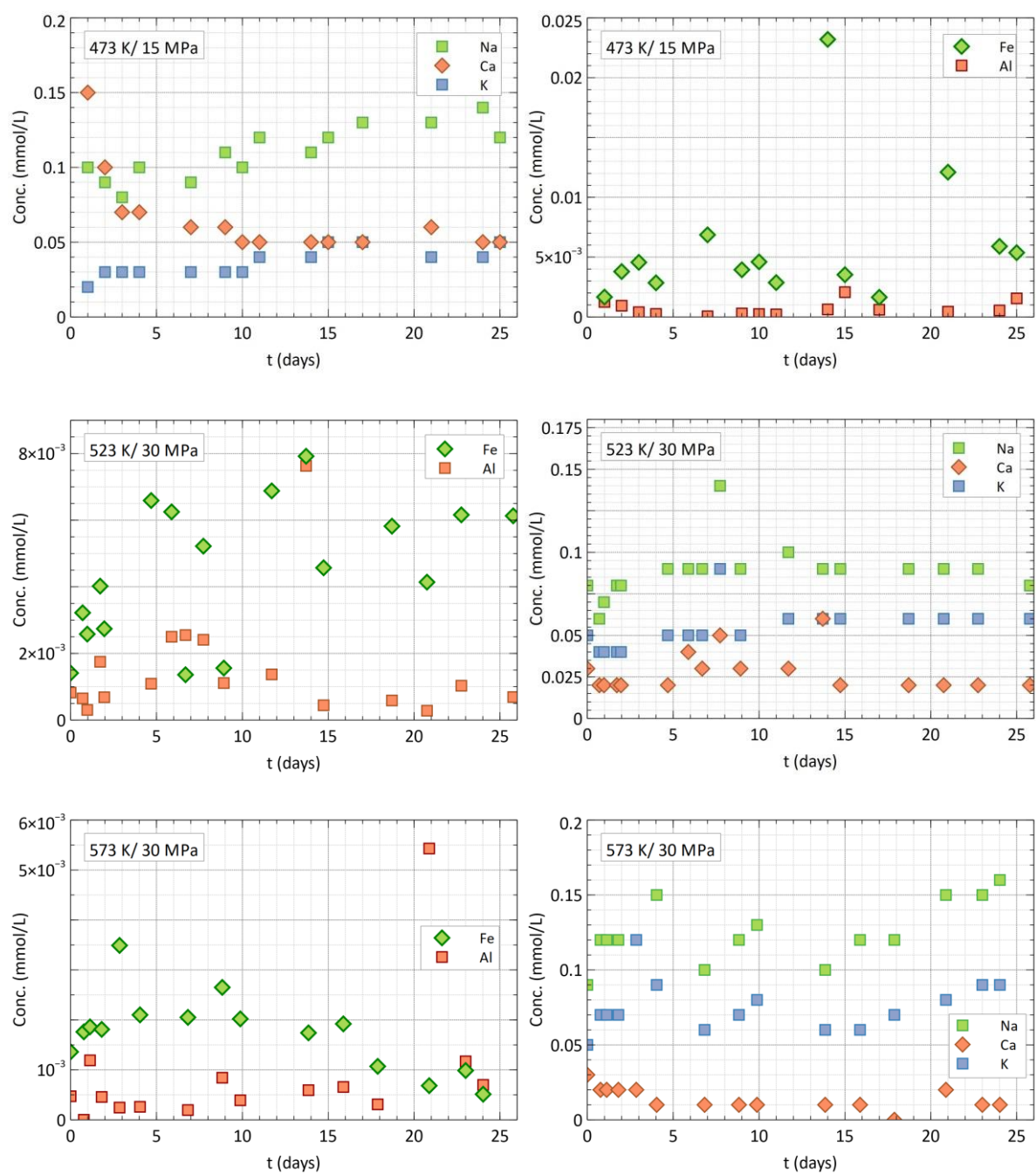


Figure A2. Variation of Si and Mg in the solutions sampled from the on going batch experiments showing the incongruent dissolution of mine tailings.

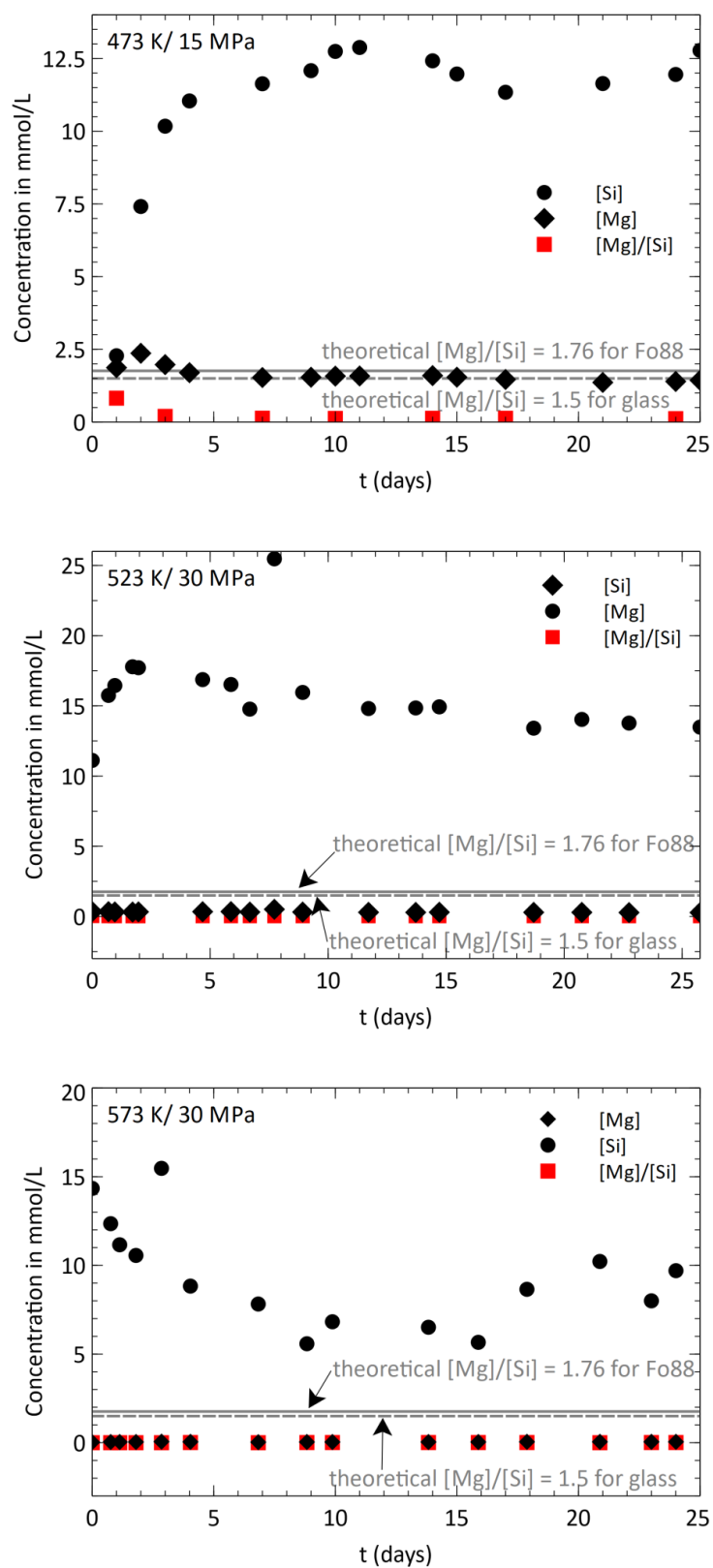


Figure A3. The composition of aqueous solutions (red circles) in the batch experiments reacting CO₂-saturated water and mine tailings. The simplified three component system MgO, SiO₂ and H₂O, reaches the sepiolite-antigorite stability field, whereas the run products contained Fe, Mg, Al-bearing phyllosilicates, indicating the effect of Al,Fe on the precipitation of secondary ilicates.

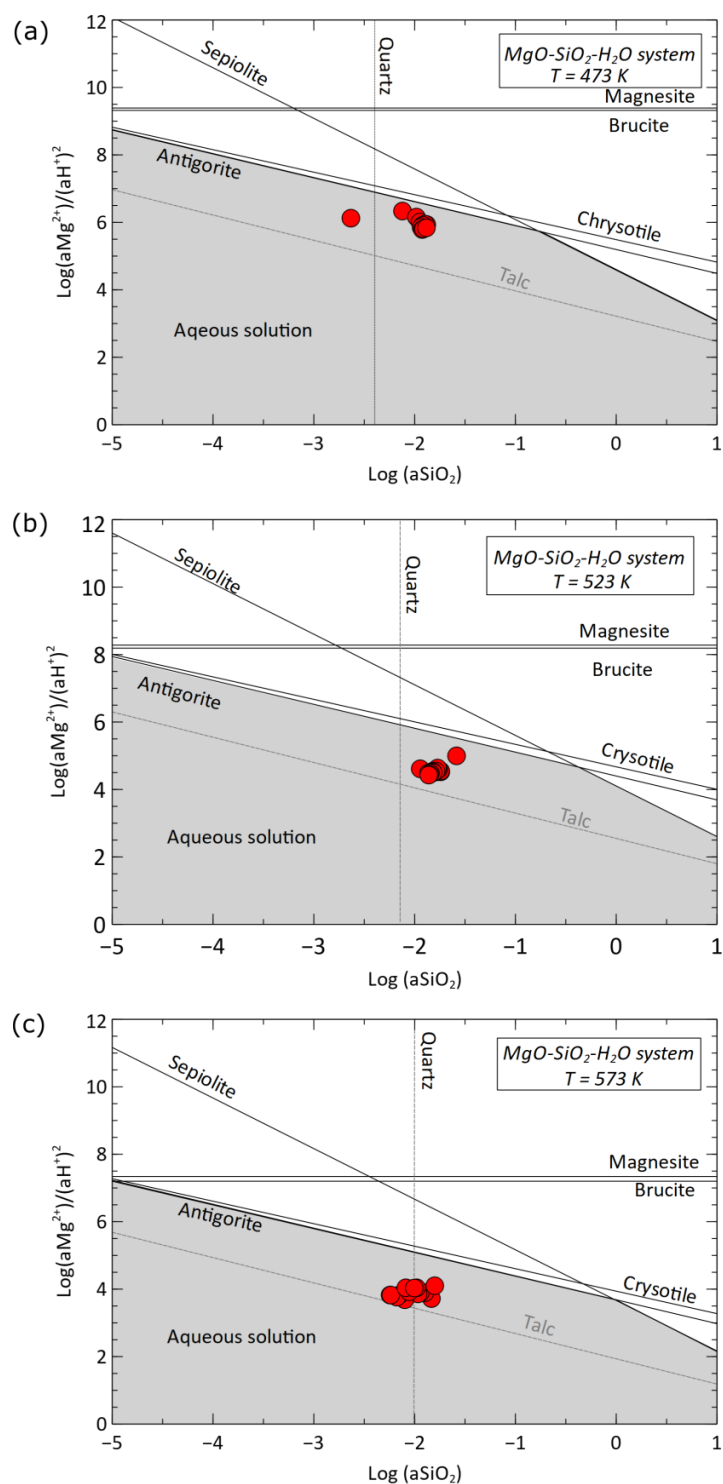
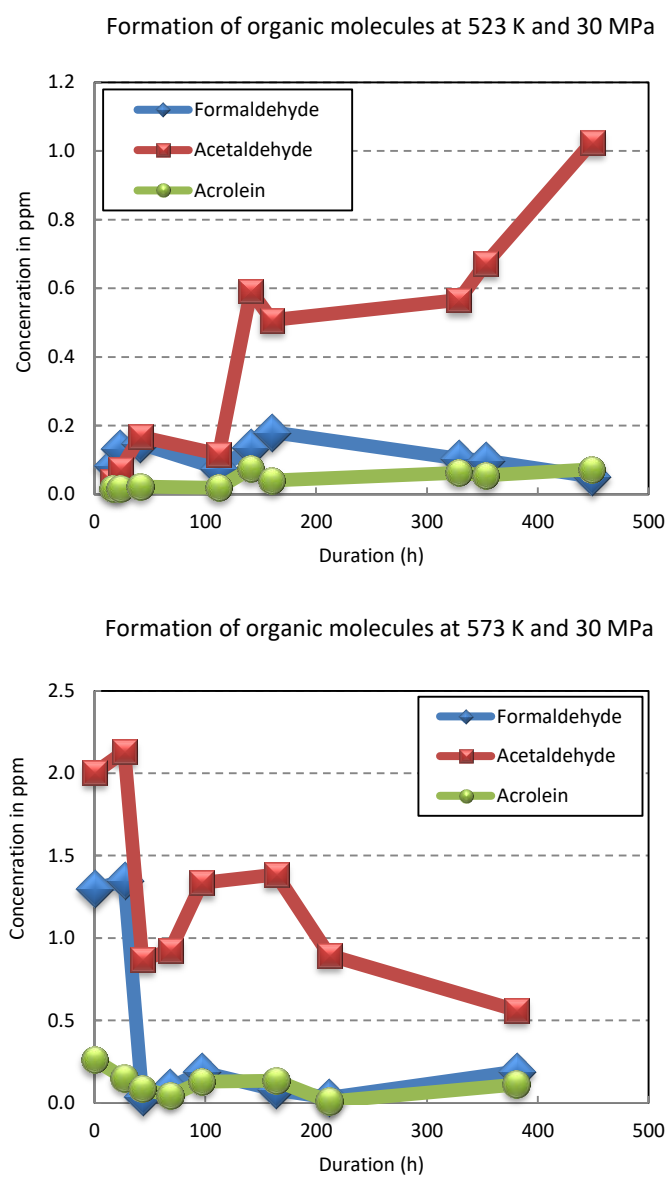


Figure A4. Variation of dissolved formaldehyde, acetaldehyde and acrolein (an aldehyde with a double bond, $\text{H}_2\text{C}=\text{CH}-\text{CHO}$), measured using HPLC method on the liquids sampled from the on going experiments reacting CO_2 -saturated water and mine tailings.



Appendix 4



Simultaneous ex-situ CO₂ mineral sequestration and hydrogen production from olivine-bearing mine tailings

Kanchana Kularatne^{a,b,*}, Olivier Sissmann^a, Eric Kohler^a, Michel Chardin^a, Sonia Noirez^a, Isabelle Martinez^b

^a IFP Energies Nouvelles, 1-4 Avenue du Bois Préau, 92852, Reuil-Malmaison, France

^b Institut de Physique du Globe de Paris, Sorbonne Paris Cité, Université Paris Diderot, UMR 7154 CNRS, 1 rue Jussieu, F-75005, Paris, France

ARTICLE INFO

Handling Editor: Michael Kersten

Keywords:

New Caledonia
Nickel
Carbonation
Hydrogen
Hydrothermal
Olivine
Glass

ABSTRACT

Hydrothermal alteration batch experiments were conducted on olivine bearing mine tailings in order to investigate two potential valorization methods: the ex-situ CO₂ sequestration and hydrogen production. The originality of this work lies in the simultaneous investigation of these two processes. We reacted powdered mine tailings with CO₂-saturated water at three different sets of P/T conditions, 473 K/15 MPa, 523 K/30 MPa and 573 K/30 MPa. After 25 days of reaction, CO₂ was sequestered in the form of Fe-bearing magnesite, (Mg,Fe)CO₃ in all the experiments. Maximum carbonation yield was achieved at 523 K and 30 MPa, which was 53.8 wt.% of product, equivalent to the trapping of 320.5 g of CO₂ per kg of mine tailings. Hydrogen gas was produced via the oxidation of Fe²⁺ in olivine. The highest quantity of hydrogen (H₂) was produced at 573 K/30 MPa which was 0.57 g of H₂ per kg of mine tailings. It suggests that the temperatures between 523 K and 540 K at pCO₂ = 30 MPa are favorable for simultaneous ex-situ CO₂ mineral sequestration and hydrogen production from New Caledonian mine tailings.

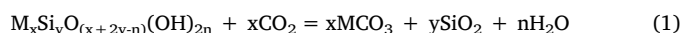
The combined method of ex-situ CO₂ storage and hydrogen production proposed by this study offsets 90% of New Caledonia's annual CO₂ emissions while compensating ~10% of New Caledonia's annual energy demand. More globally, it has implications for cost effective disposal of industrial CO₂ emissions and production of hydrogen gas (clean energy) at a large scale; those two processes could be combined using the residual heat provided by a third one such as the high temperature smelting of ore.

1. Introduction

Since the industrial revolution, the atmospheric carbon dioxide (CO₂) level has been substantially increased up to its present day value of ~407 ppm (NOAA, 2016), eventually causing enormous climatic changes such as global warming, ocean acidification, and glacial melting (Manabe and Stouffer, 1993; Kondo et al., 2018; Zhang et al., 2017; Caesar et al., 2018; Marzeion et al., 2018). Up to 65% of the global CO₂ emissions were attributed to fossil fuel combustion (Edenhofer et al., 2014), directing the CO₂ mitigation measures essentially towards CO₂ sequestration mechanisms and introduction of alternate energy sources to fossil fuels.

Scientists have considered the CO₂ sequestration in minerals as the so-called permanent method to capture and store industrial emissions of CO₂. This method was first suggested by Seifritz (1990), based on the natural phenomena of silicate weathering into carbonates (Abu-Jaber and Kimberley, 1992; Ece et al., 2005; Lugli et al., 2000; Oskierski

et al., 2013; Palinkaš et al., 2012; Zedef et al., 2000), during which CO₂ reacts with silicates precipitating thermodynamically stable solid carbonates as given by the generalized equation below:



where (M²⁺) represents a divalent cation such as, Fe²⁺, Mg²⁺ and Ca²⁺ in a silicate mineral, and MCO₃ thus represents the carbonate incorporating the element M. Once CO₂ is converted into a carbonate following reaction (1), it will not be released into the atmosphere over geological time scales.

For the last three decades various aspects of CO₂ mineral sequestration have been experimentally investigated, on several mafic minerals such as olivine, serpentine, and pyroxenes (Johnson et al., 2014; Béarat et al., 2006; King et al., 2010; Sissmann et al., 2013; Daval et al., 2009a; Wolff-Boenisch et al., 2006; Park et al., 2003). Among the minerals which consist of divalent Ca, Mg or Fe in their structure, olivine

* Corresponding author. Present address: Institut de Physique du Globe de Paris, 1 rue Jussieu, F-75005, Paris, France.

E-mail addresses: kularatne@ipgp.fr (K. Kularatne), olivier.sissmann@ifpen.fr (O. Sissmann), eric.kohler@ifpen.fr (E. Kohler), michel.chardin@ifp.fr (M. Chardin), sonia.noirez@ifp.fr (S. Noirez), martinez@ipgp.fr (I. Martinez).

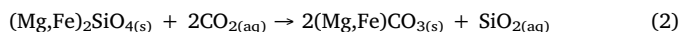
<https://doi.org/10.1016/j.apgeochem.2018.05.020>

Received 24 November 2017; Received in revised form 23 May 2018; Accepted 23 May 2018

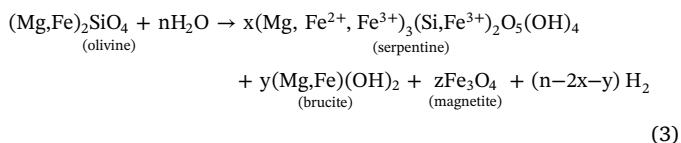
Available online 30 May 2018

0883-2927/ © 2018 Elsevier Ltd. All rights reserved.

((Mg,Fe)₂SiO₄) is considered the most favorable for carbonation due to several reasons. Firstly, olivine is abundant in nature in mafic and ultramafic environments (e.g. basalt, peridotites, and dunites). Secondly, it's one of the fastest dissolving silicates (Guthrie, 2001; Brantley, 2003; Golubev et al., 2005; Wolff-Boenisch et al., 2006). Olivine, which contains both Fe and Mg, may form Fe-bearing magnesite ((Mg,Fe)CO₃) during the carbonation process, according to equation (2):



Gerdemann et al. (2007), who conducted carbonation experiments on olivine under a wide range of temperature (298 K < T < 523 K) and CO₂ partial pressure (1 MPa < pCO₂ < 25 MPa), have shown that olivine (< 75 μm) could be carbonated efficiently, with ca. 85% completion of reaction within an extremely short period of time (around 6 h), by reacting with a solution of 0.64 M NaHCO₃ + 1 M NaCl, at T = 458 K and pCO₂ = 15 MPa. This study also demonstrated that the extent of olivine carbonation is directly proportional to the CO₂ partial pressure in the system (pCO₂). In addition, the authors showed that, at a given pCO₂, the extent of carbonation was negligible at lower temperatures (< 363 K), while a decrease in the extent of reaction was observed at high temperatures (> 458 K). It indicated that at low temperatures, the carbonation reaction is kinetically not favorable due to slow mineral dissolution, whereas if the temperature is too high, although mineral dissolution is kinetically favorable, the extent of carbonation nevertheless decreases. This is due to the formation of Mg-rich phyllosilicates during the competing reaction of serpentinization, in which extensive oxidation of Fe²⁺ also occurs, producing hydrogen, as shown by:



The stoichiometric parameters n, x, y and z in this equation strongly depend on how iron is partitioned among the reaction products (McCollom et al., 2016). Large quantities of hydrogen are added to the deep sea floor by this reaction which takes place at the mid oceanic ridge hydrothermal systems. A number of studies reported the temperature, thermodynamic, and compositional controls on serpentinization (Janecky and Seyfried, 1986; Klein et al., 2013, 2009; Klein and Garrido, 2010; McCollom et al., 2016; McCollom and Bach, 2009a; Seyfried et al., 2007). Two important information from these studies indicate that high temperatures (~573 K) favor large quantities of hydrogen due to (i) an increase of overall reaction rate of serpentinization, and (ii) an increased partitioning of Fe into brucite (Mg(OH)₂), rather than into magnetite (Fe₃O₄). In addition to the hydrothermal alteration of olivine, pure iron or iron-rich materials have also been experimentally studied for hydrogen production (Crouzet et al., 2017; Malvoisin et al., 2013).

Olivine, which contains both Mg and Fe, could therefore be favorable for simultaneous CO₂ mineral sequestration and hydrogen production, when reacting within a specific range of pressure, temperature and pH conditions, under which carbonation and serpentinization

reactions will not inhibit one another. Therefore, this method is a clear improvement on current CO₂ mitigation methods, as it proposes reduction of CO₂ emissions by mineral storage, and also hydrogen production which is a green energy source. Compared to Fe-Mg-bearing pure minerals or rocks, mine tailings serve as an alternative source of mineral alkalinity that are readily and cheaply available (Bobicki et al., 2012), and can be valorized by the above method (Bobicki et al., 2012; Harrison et al., 2016, 2013; Power et al., 2013; Wilson et al., 2014; Malvoisin et al., 2013). However, these previous studies on mine tailings have only focused on either CO₂ storage or H₂ production separately. The present study aims to investigate the potential of combining the strategy of CO₂ mineral storage with hydrogen production by reacting olivine-bearing mine waste material obtained from nickel (Ni) extraction mines in New Caledonia. In order to maintain both of these reactions, the mine tailings were reacted with CO₂-saturated water at P/T range slightly inferior to the conditions previously identified as optimum for ex-situ carbonation (Gerdemann et al., 2007), and close to optimum hydrogen production in hydrothermal systems (McCollom et al., 2016; McCollom and Bach, 2009a; McMollom and Bach, 2008; Tutolo et al., 2018; Mayhew et al., 2018). We present the quantities of CO₂ that can be stored in mine tailings, and the quantities of H₂ that can be produced by this method. Based on these experimental values, we estimated the CO₂ offset and compensation of energy demand of New Caledonia. Although the application of this process is centered on New Caledonian mine tailings, it could be translated to other industrial sites where Mg and Fe remain major components of the wastes after ore processing.

2. Materials and methods

2.1. Starting materials

All the experiments were performed on olivine bearing mine tailings from industrial nickel (Ni) extraction sites in New Caledonia, where Ni is extracted from laterite and saprolite ores (Wacaster, 2013). The hand specimens of mine tailings consisted of light- to dark-green irregular shaped grains with sizes ranging from few millimeters to < 1 cm. The X-ray diffraction (XRD) analysis performed on a finely powdered sample indicated the presence of olivine, traces of enstatite and an amorphous phase (glass). The amount of glass was quantified by XRD Rietveld analysis performed on the diffraction pattern of a mixture of powdered mine tailings and alumina (20 wt.%) where alumina serves as the internal standard (Bish and Howard, 1988; Bish and Post, 1993; McCusker et al., 1999). According to this analysis the sample was composed of 55 wt.% of glass and 45 wt.% of crystalline olivine. The chemical composition of mine tailings was obtained by electron probe micro analysis (EPMA) operated at 15 keV and 40 nA, on few randomly selected macroscopic grains mounted on epoxy resin. The analysis was performed on multiple points on glass and olivine, which appeared texturally different under SEM, and the average compositions were reported in Table 1. This is in good agreement with the composition reported by Bodénan et al. (2014), who used the same material for CO₂ sequestration experiments. The magnesium numbers (Mg# = Mg/(Mg + Fe)) of the glass and crystalline olivine were 0.75 and 0.88

Table 1

The chemical composition of New Caledonian mine tailings, determined by electron probe micro analysis (EPMA) performed on crystalline olivine and glass, expressed in weight percent (wt.%) of corresponding oxide.

	Na ₂ O	MgO	SiO ₂	Al ₂ O ₃	K ₂ O	CaO	TiO ₂	Cr ₂ O ₃	FeO	MnO	CoO	NiO	Total	Mg# ^a
Olivine	0.05	47.27	40.88	0.07	0.01	0.11	0.04	0.02	11.67	0.12	0.05	0.38	100.68	0.88
Glass	0.04	23.94	55.22	3.81	0.01	0.48	0.06	1.68	14.23	0.9	0.01	0.01	100.39	0.75
Avg ^b	0.05	35.61	48.05	1.94	0.01	0.30	0.05	0.85	12.95	0.51	0.03	0.20	100.54	0.82

^a The magnesium number; Mg# = Mg/(Mg + Fe).

^b Average composition of mine tailings.

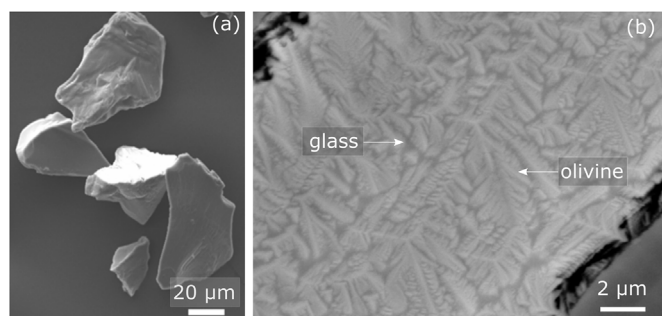


Fig. 1. Powdered mine tailings observed under SEM (a) secondary electron image of powdered and cleaned sample used for the experiments. The grain surfaces are free of any adhered particles (b) angle selective back scattered image of a polished section of mine tailings showing the olivine crystals (white), embedded in glass (gray matrix) resulting a dendritic texture.

respectively, and were calculated on molar basis using the average oxide wt.%.

Mine tailings were crushed in a ball mill to obtain 40–63 μm size fraction. This size fraction was chosen in order to maintain rapid dissolution kinetics, as well as to facilitate microscopic observations. Furthermore, those grain sizes are in the same range than those used in the few previous studies on hydrogen generation (Malvoisin et al., 2013, 2012a, 2012b), thus making the comparison easier. Even though the choice of nano-scale particles could have provided a considerably faster reaction, the mineral surfaces available for microscopic studies of the products would have been limited. Finally, for industrial purposes, grinding large quantities of solid down to the nanometer scale would largely increase the cost of the process.

The selected sieve fraction was subsequently ultrasonically cleaned in ethanol for 8–10 min to remove the fine particles adhered to the surface. This process was repeated until the supernatant became clear. The powder was dried in oven at 343 K overnight after cleaning with ultra-pure de-ionized water (electrical conductivity = 18.2 MΩ cm). Very few fine particles remained adhering to the grain surfaces of the above dried powder, when observed under SEM (Fig. 1a). The specific surface area (SSA) of the cleaned starting powder was determined by Kr adsorption analysis, according to the Brunauer–Emmett–Teller (BET) method (Brunauer et al., 1938), yielding a value of 0.23 m²/g.

Scanning electron microscopic (SEM) analysis performed on a polished section of mine tailings indicate that it consists of inclusion of free and textured glass with embedded olivine crystals, resulting in a “dendritic texture” or a “quench texture” (Fig. 1b). The glass and dendritic texture were assumed to be the result of two steps in the ore processing. The first is the “calcination” performed by pre heating the ore at > 1173 K for moisture removal and first phase of metal oxide reduction. The second is the “fusion reduction” by which the ore is

melted using an electrode operated at < 1973 K, separating Ni from the residue or mine tailings. We assume that these conditions reached the “dry” melting-point of peridotite (~approximate composition for the ophiolite) under atmospheric pressure (Takahashi, 1986), where olivine can coexist with pyroxene melt up to about 2023 K at 1 atm during the eutectic melting of peridotite, which could probably explain the quench texture in mine tailings.

2.2. High pressure and high temperature experiments

Three batch experiments were conducted at different P/T conditions, in order to investigate the most favorable conditions for simultaneous CO₂ sequestration and H₂ production. All the experiments were performed in 250 ml volume Parr® hastelloy stirring-type batch reactors (impeller speed, 100 r.p.m), with a TiO₂ inner lining. Powdered mine tailings and deionized water (1:100 mass ratio) were added to the batch reactors and pressurized with CO₂ (99.9% purity).

The first experiment (MT1) was conducted at 473 K/15 MPa, which was slightly above the known optimum temperature reported for the CO₂ mineral sequestration, i.e. 453 K/15 MPa, using a solution of 0.64 M NaHCO₃/1 M NaCl. The second and third experiments were conducted at P/T conditions more favorable for H₂ production by serpentinization, such as 473 K and 673 K and 30–50 MPa (Allen and Seyfried, 2003; Andreani et al., 2012; Berndt et al., 1996; Janecky and Seyfried, 1986; Malvoisin et al., 2012a; McCollom and Bach, 2009b; McCollom and Seewald, 2001). These conditions are known to accelerate the serpentinization rate while producing large amounts of H₂. The second experiment (MT2) was thus conducted at 523 K/30 MPa, both temperature and pressure being slightly above MT1. The third experiment (MT4) was performed at 573 K/30 MPa. Two more experiments were conducted as blank runs (MT2b, and MT4b) to determine possible contaminations in gas phase. They were conducted under similar conditions (-in terms of amount of water, pCO₂, T) to those of MT2 and MT4, but without any solid phases added in the reactor. Details of these experiments are reported in Table 2. The run duration of all the experiments was approximately 25 days. The pCO₂ of the experiments drops intermittently (0.1–0.5 MPa) during the run due to; (i) CO₂ consumption by carbonation reaction, and (ii) sampling out aliquots of gas from the batch reactor. The pressure was re-adjusted to the initial pressure by pumping CO₂ gas back to the batch reactor. At the end of the 25-days run, the experiments were quenched rapidly to ambient conditions by cooling the reactor cell in a water bath for ~20–30 min. The autoclaves were then opened right after releasing the pressurized CO₂ inside the reactor, minimizing the potential formation of secondary products at this stage. The solid products were recovered and oven-dried at 333 K overnight, then used for further analysis, as described below.

At these P/T conditions, most of the CO₂ pumped into the reactor exists as CO_{2(aq)} with a smaller amount of HCO_{3(aq)}[−] and traces of

Table 2

Summary of experimental conditions, pH of the solutions, carbonate yields, measured hydrogen and methane in each batch experiment.

	P(total) (MPa)	P(CO ₂) ^a (MPa)	T (K)	t (days)	Mine tailings (g)	Pure water (g)	water/rock ratio ^b	Initial pH ^c	CO ₂ storage ^d (g/kg)	Hydrogen(max) measured by GC (g/kg) ^e	Methane(max) (g/kg) ^e
MT1	15	13.1	473	25	2.0	201	100	3.55	114.4	0.04	nd
MT2	30	26.4	523	25	1.7	170	100	3.65	320.5	0.24	0.02
MT4	30	28.2	573	24	1.7	170	100	3.94	118.5	0.57	0.05
MT2b (blank)	30	26.4	523	24	–	170	–	–	nd	nd	0.01
MT4b (blank)	30	28.2	573	24	–	170	–	–	nd	nd	0.06

nd = not detected in the gas chromatography analysis.

^a Calculated for the given temperature and P(total) using the thermosolver software (Barnes and Koretsky, 2004).

^b Water/rock ratio = mass of water(g)/mass of mine tailings(g).

^c pH at experimental conditions calculated using the CHESSE geochemical code (van der Lee and De Windt, 2002).

^d Grams of molecular CO₂ trapped in 1 kg of mine tailings.

^e Grams of hydrogen (H₂), or methane (CH₄) produced per 1 kg of mine tailings.

$\text{CO}_3(\text{aq})^{-2}$, which can therefore be summed up to a binary mixture of CO_2 - H_2O that has not reached critical condition. The initial pH at P/T relevant to experimental conditions was calculated by the CHES geochemical code (van der Lee and De Windt, 2002) for each reaction temperature, creating a closed system with water and CO_2 ($f\text{CO}_2$ at each P/T conditions) was calculated using the Thermosolver program (Barnes and Koretsky, 2004). The experimental conditions and the calculated initial pH of the solutions are reported in Table 2.

2.3. Sampling and analytical methods

2.3.1. Gas sampling and analysis

The gas phase in the head space of the batch reactor was sampled every 2–3 days during the reaction, by connecting a gas-sampling tube to the batch reactor. Before sampling, a vacuum of 10^{-5} bars was created along the tubings of the batch reactor and also in the sampling tube. The vacuum was held for about 10–15 min. This procedure ensures the absence of any leak and contaminations in the tubings. Collected gas samples were then analyzed with a Varian CP-3800 gas chromatograph (GC) to identify and quantify the gaseous products of the reaction. For this purpose, two standards were first analyzed: one with an atmospheric composition, and the other being a mixture of H_2 , He, N_2 , CO_2 and alkanes up to four carbons (C_1 – C_4). The samples and the standards were injected to the GC at ~ 1200 mbar at room temperature. Before analyzing a standard or a sample, a blank measurement was carried out by injecting N_2 . Finally, the percentages (%) of each gas in the analyzed samples were calculated using the response factors (k) obtained. The uncertainty on H_2 , CO_2 , CH_4 and other simple alkanes abundances (C_2 – C_4) measured by GC were 5.4%, 1.3%, 0.6% and $\sim 1.2\%$ respectively.

2.3.2. Solid product analysis

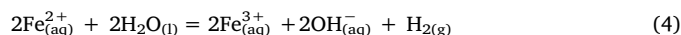
The mineralogical composition of bulk solid products was obtained through XRD analysis performed on finely powdered reaction products, using a X'Pert PRO (PANalytical) x-ray diffractometer with a Cu anode (Cu $K\alpha = 1.5418 \text{ \AA}$), operated under 45 kV and 40 mA. The detection limit of XRD is $\sim 1\%$. Rock-Eval 6 analysis was performed for better detection and quantification of carbonate. The quantification limit of Rock-Eval 6 is ~ 0.02 wt.% C, which corresponds to ~ 0.15 wt.% MgCO_3 ; this method is one order of magnitude more sensitive than the phase quantification by XRD. More details on sample preparation, instrumentation and analysis of the Rock-Eval 6 technique can be found in Behar et al. (2001) and Lafargue et al. (1998). The analytical details and the calculation of carbonates are reported in supporting information S6. Energy dispersive X-ray analysis in transmission electron microscope (TEM-EDX) was performed on ultra-thin sections prepared by focused ion beam milling (FIB), in order to obtain the composition of magnesite: more details are given in supporting information S10.

A separate fraction of the reaction products was mounted on adhesive carbon-taped sample holders, gold (Au) coated and observed under “high vacuum” conventional SEM, EVO MA 10, Carl Zeiss SMT with a tungsten filament operated under 15 kV and 100 mA. A 150 pA beam was applied for secondary electron (SE) imaging to observe the surface topography with a high spatial resolution, while the back scattered electron detector (BSE) was used to obtain images with atomic number contrast. Qualitative chemical analyses were performed by energy dispersive X-ray analysis (EDX), with a probe current at 700–750 pA (Oxford). The silicon drift detector is calibrated on cobalt (Co) for quantitative analyzes during 10 s at 10–15 keV with a dead time of about 15 s. In addition, SEM element mapping was performed on the reaction products mounted on epoxy resin, finely polished by ion beam milling.

2.3.3. Fe(III)/Fe(II) analysis

The amounts of Fe^{2+} and total iron in the non-reacted mine tailings, and the three experimental products were analyzed at the Centre de

Recherches Pétrographiques et Géochimiques (CRPG), Nancy, France. The samples were boiled in $\text{HF}/\text{H}_2\text{SO}_4$ to release Fe^{2+} which was then quantified by volumetric titration with $\text{K}_2\text{Cr}_2\text{O}_7$. Another fraction of the sample was then heated with LiBO_2 at 1223 K and acid digested (4 vol. % HNO_3) to convert all species of iron (e.g. Fe^0 and Fe^{2+}) contained in the sample into Fe_2O_3 (Fe^{3+}). The resulting ferric iron was measured by atomic absorption spectrophotometer (AAS). The amount of Fe^{3+} in the non-reacted mine tailings sample was calculated by subtracting the Fe^{2+} molar amount measured in the FeO analysis from the ($\text{Fe}^{2+} + \text{Fe}^{3+}$) amount measured in the Fe_2O_3 analysis. The value being close to 0 suggests there is little to no oxidized iron in the initial material. The quantities of H_2 measured by GC at the end of the experiments were compared to the amounts calculated from the loss of Fe^{2+} (through oxidation and simultaneous H_2 production) in the products. In order to estimate the amount of Fe^{3+} formed during the experiments, the amount of Fe^{2+} measured in the products were subtracted from the one measured in the initial non-reacted mine tailings; the quantity of H_2 produced was then extrapolated from the oxidized iron (Fe^{3+}) according to:



where, the stoichiometric proportion of Fe^{2+} : H_2 is 2:1.

3. Results

3.1. Secondary products

XRD pattern of non-reacted mine tailings and the reaction products of three experiments are shown in Fig. 2c. The non-reacted mine tailings sample primarily consisted of olivine. The peaks of corundum (Fig. 2c), in this diffraction pattern are due to pure corundum which was added to mine tailings as the internal standard for quantification of glass. The products consisted of Fe-rich magnesite as the major phase, small quantities of phyllosilicates and traces of non-reacted olivine (Fig. 2c). Fe-bearing magnesite was identified by the characteristic reflections at $2\theta = 35.9^\circ$ and 50° (Giammar et al., 2005; Garcia et al., 2010). SEM element mapping performed on a polished section of MT2 sample showed the presence of abundant magnesite compared to other phases such as olivine, glass, and phyllosilicate, and therefore is well in agreement with the XRD results (Fig. 2a). The SEM analysis performed on a carbon-coated reaction product of the same sample indicates the growth of rhombohedral magnesite containing both Fe and Mg, as confirmed by the EDX spectra collected on SEM (Fig. 2b). Fig. 3 shows the SEM analysis performed on polished sections of solid products of the three experiments, each mounted on epoxy resin. At 473 K/15 MPa, mine tailings have been altered, precipitating anhedral magnesite, and thin layers of phyllosilicate (Fig. 3a). Magnesites precipitated along a grain of textured mine tailings are shown on Fig. 3b. At 523 K/30 MPa, the product contained thick phyllosilicate layers around mine tailings and subhedral magnesite with Fe and Mg compositional zoning (Fig. 3c). At 573 K/30 MPa, the products contained anhedral magnesites and mine tailings heavily covered by a thick fibrous phyllosilicate layer (Fig. 3c). More SEM images with EDX analysis on these samples are given in supplementary S7–S9. The chemical composition of magnesites analyzed by TEM-EDX yielded $\text{Mg}_{0.92}\text{Fe}_{0.08}\text{CO}_3$, $\text{Mg}_{0.58}\text{Fe}_{0.42}\text{CO}_3$ and $\text{Mg}_{0.83}\text{Fe}_{0.17}\text{CO}_3$ at 473 K/15 MPa, 523 K/30 MPa and 573 K/30 MPa respectively, showing different concentrations of iron further discussed in section 4.2. The details of TEM analysis is given in supplementary information S10.

Compared to the diffraction pattern of the non-reacted sample, the peak intensity of olivine gradually decreases with the increasing temperature of the experiments, indicating olivine dissolution has mostly increased along with temperature. The semi-quantitative phase analysis on the collected diffraction patterns indicated that approximately 23.3 wt.%, 9.4 wt.% and 12.2 wt.% of olivine were still remaining in the

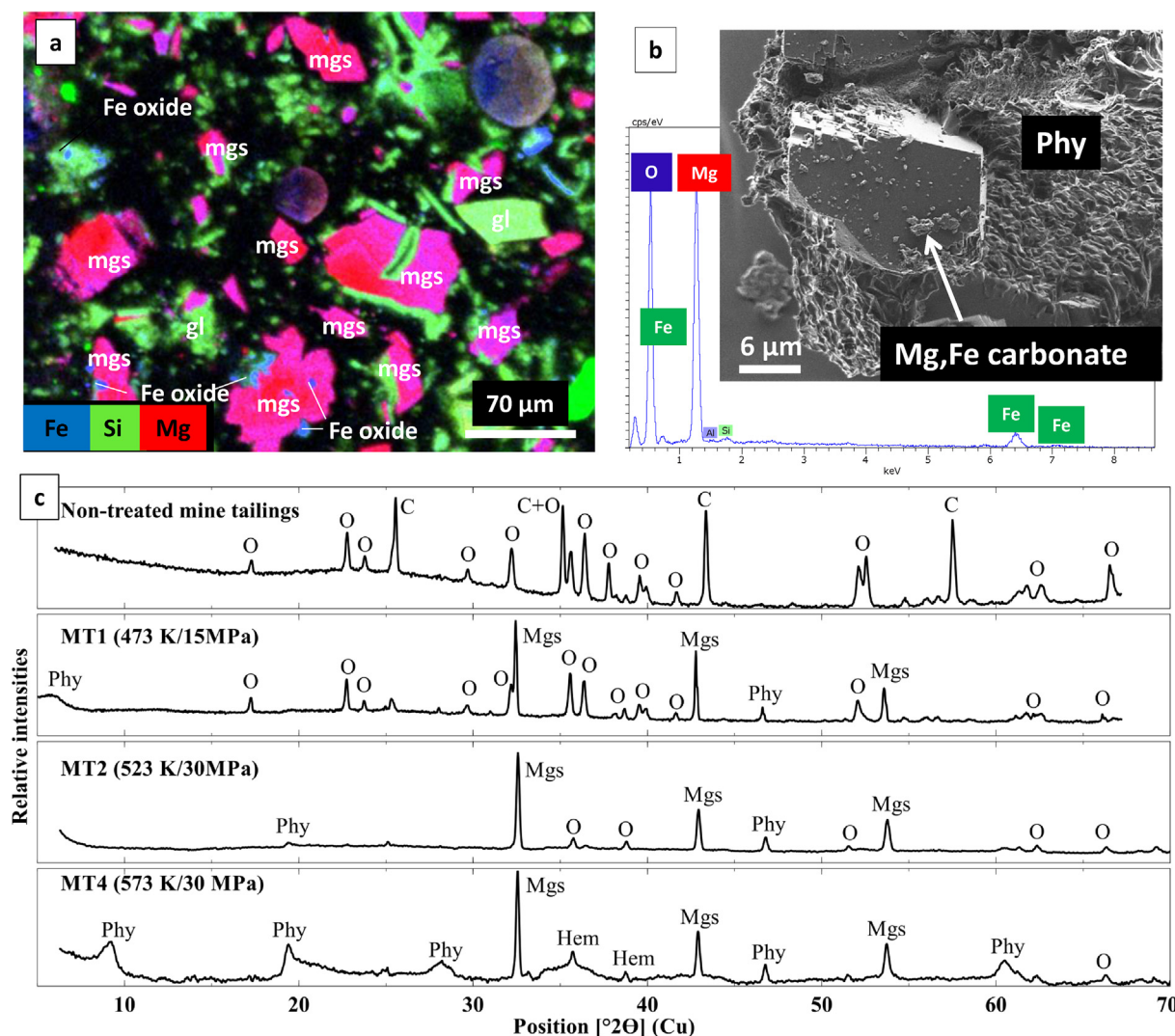


Fig. 2. Mineralogical analysis of experimental run products (a) Element mapping (SEM) performed on a polished section the run product of experiment MT2 ($T = 523$ K and $P = 30$ MPa), showing formation of magnesite in large quantities (color coded by blue (Fe), green (Si) and red (Mg)). Magnesite crystals are shown in pink and initial silicate glass and traces of phyllosilicate is shown in green. A very small amount of iron oxide phases (not detectable through XRD) was observed only in this region of the sample and is marked in blue. (b) SEM secondary electron (In-lens detector) image of the same experimental run product taken on carbon coated powder showing euhedral grain of Fe-bearing magnesite (-as shown in SEM-EDX spectra) embedded in phyllosilicate. (c) X ray powder diffraction pattern of non-treated mine tailings sample and the run products of the three batch experiments, showing the progressive disappearance of olivine (O) peaks and the formation of magnesite (Mgs) during the reaction at high pressure and high temperature. The other secondary phases were phyllosilicates (Phy), and hematite (Hem). The peaks labeled (C) in the non-treated sample are the reflections of corundum which was added to the sample as the internal standard to quantify the fraction of glass (amorphous) in the initial non-reacted main tailings. (For interpretation of the references to color in this figure legend, the reader is referred to the Web version of this article.)

reaction products of 473 K/15 MPa, 523 K/30 MPa and 573 K/30 MPa experiments respectively. The peaks for phyllosilicates are broad and less intense in all experiments, and the number of phyllosilicate peaks visible on the diffractogram increased with temperature, indicating more phyllosilicates formed with higher temperature. A preliminary identification of these phyllosilicates was obtained by applying a treatment with ethylene glycol to verify their expansion properties, which suggested that they were smectite clay minerals. However, due to the inherent limitations of the equipment, the amount of phyllosilicate and remaining glass could not be quantified separately.

3.2. Carbonate yield

The presence of carbonates and their precise quantification were further confirmed using the Rock-Eval 6 technique. The only carbonate phase produced in all the experiments were Fe-bearing magnesites,

(Mg,Fe)CO₃, in accordance with the results of XRD analysis. Carbonate quantification by Rock-Eval 6 resulted in 20.3%, 44.9% and 21.6% at 473 K/15 MPa, 523 K/30 MPa and 573 K/30 MPa respectively (the calculation is given in S6); those carbonation yields are averages of duplicate experiments. These yields suggest that 1.00 kg of mine tailings could capture 115 g, 321 g and 119 g of gaseous CO₂ by a reaction with pure water at 473 K/15 MPa, 523 K/30 MPa and 573 K/30 MPa, respectively (Table 2 and Table S6).

3.3. Hydrogen production

As the starting mine tailings material is iron-rich (average of 10.9 wt.%), its reaction with water at high pressure and high temperature leads to the production of H₂, as a result of iron oxidation through water reduction (also written for the serpentinization reaction given by eq. (3)). However, the produced hydrogen in all the

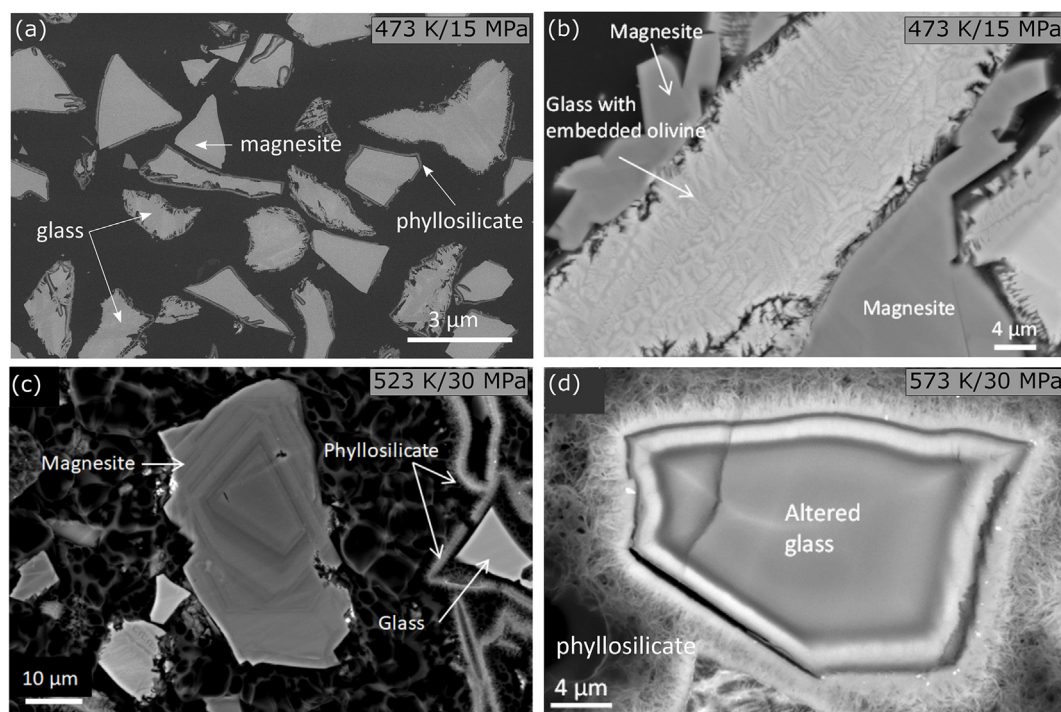


Fig. 3. (a) SE image of the experimental run product at 473 K/15 MPa, showing some remaining glass, thin phyllosilicate layer formed around mine tailings and newly formed magnesite crystals; (b) a grain of mine tailing with olivine embedded in glass, which reacted to form anhedral magnesite crystals; (c) large magnesite crystals formed at 523 K/30 MPa showing Fe, Mg compositional zoning, and phyllosilicates which apparently detached from the original grains; (d) glass altered at 573 K/30 MPa forming a thick phyllosilicate layer.

experiments is approximately three orders of magnitude lower than the CO_2 in the gas phase, since CO_2 was injected to reach a total pressure of either 15 or 30 MPa. The variations in gas phase composition in each experiment are given below.

At 473 K and 15 MPa: Fig. 4a, illustrates the cumulative production of hydrogen as a function of time for MT1. Hydrogen was produced gradually reaching a maximum of $20.0 \mu\text{mol/g}$ of mine tailings after 25 days of reaction, which indicates that the reaction is still in progress. The maximum hydrogen production of $20.0 \mu\text{mol/g}$ is equivalent to producing around 0.04 g of H_2 for 1.0 kg of mine tailings. Hydrogen was produced at a rate of approximately $0.7 \mu\text{mol/g/day}$, obtained by the gradient fitted through the data. Traces of methane ($< 0.30 \mu\text{mol/g}$) were detected in the gas phase after 9.8 days of reaction, but other light hydrocarbons ($\text{C}_2\text{--C}_4$) were not detected (S 1).

At 523 K and 30 MPa: The cumulative hydrogen production as a function of reaction time of MT2 experiment is shown in Fig. 4b. Hydrogen continues to be produced at a rate of $1 \mu\text{mol/g/day}$ until ~ 9 days, as the reaction proceeds. After 9 days, hydrogen production increases abruptly and then continues to increase at a rate of $3.2 \mu\text{mol/g/day}$. The maximum amount of gaseous hydrogen measured in this experiment was $117.6 \mu\text{mol/g}$ or 0.24 g/kg of mine tailings, which is approximately 5 times more than in MT1. No hydrogen was detected in the gas phase of an experimental blank (MT2b) conducted under the same without adding mine tailings confirming that hydrogen was produced only by reaction between pure water and mine tailings (Fig. 4b). Light hydrocarbons such as CH_4 , C_2H_6 , C_3H_8 and C_4H_{10} were also observed in the gas phases of both the experiment and experimental blank, but in trace quantities (S2 and S4).

At 573 K and 30 MPa: Cumulative hydrogen production of MT4 experiment is shown in Fig. 4c. At the initial stage, hydrogen was produced at a rate of $21 \mu\text{mol/g/day}$ ($0 < t < 8.8$ days), reaching a maximum of $283.5 \mu\text{mol/g}$ or 0.57 g/kg . This is the highest quantity of hydrogen produced among all three experiments, and is confirmed by the H_2 production inferred from iron (III) measured at the end of the experiments ($265 \mu\text{mol/g}$, see Table 2). Then, the amount of hydrogen

decreased drastically, reaching a plateau with an average of $41 \mu\text{mol/g}$ (Fig. 4c). Similarly to MT2, hydrogen was not detected in the gas phase of an experimental blank (MT4b) conducted at the same P/T conditions, which confirmed there was no contamination of hydrogen in the experiment (Fig. 4c and Fig. S3). This decrease in cumulative hydrogen could be explained by the formation of short-chained organic molecules through its interaction with CO_2 , as discussed by Seewald et al. (2006). In addition, CH_4 , C_2H_6 , C_3H_8 and C_4H_{10} were detected in the gas phase, in which the detected methane was above the 10% uncertainty of the concentration detected in the experimental blank (S5).

3.4. H_2 production estimated by Fe(III)/Fe(II) analysis

As previously stated, hydrogen is produced via the oxidation of Fe^{2+} in the starting material according to equation (4) (section 2.3.3). Therefore, the difference between the amounts of FeO measured in the starting material and the reaction products quantifies the Fe^{2+} that has been oxidized at high pressure and high temperature.

The analysis shows that the starting mine tailings sample contained, 1.3 mmol/g of FeO, whereas the reaction products of MT1, MT2 and MT4 experiments contained 1.3 , 1.1 and 0.8 mmol/g of FeO, respectively. According to this result, the initial mine tailings and the MT1 experiment contained the same amount of FeO, meaning that no Fe^{2+} oxidation took place. However, $20 \mu\text{mol/g}$ of hydrogen was detected in the gas chromatography analysis of this experiment. This could possibly suggest an analytical error in detecting such a low level of FeO quantity due to the detection limit of the method used. The H_2 production estimated from the stoichiometric ratio with Fe^{3+} (given in eq. (4)) are reported in Table 3 for the three experimental runs. Except for MT1, the estimated values of hydrogen are in good agreement with those observed in gas chromatography analysis.

Moreover, if all the Fe^{2+} in initial mine tailings (i.e. 1.3 mmol/g) was to completely oxidize into Fe^{3+} , then following equation (4) (1 mol of H_2 produced for 2 mol of Fe^{2+} oxidized), it could produce $655 \mu\text{mol}$ of H_2 per one gram of mine tailings. This value can be used to calculate

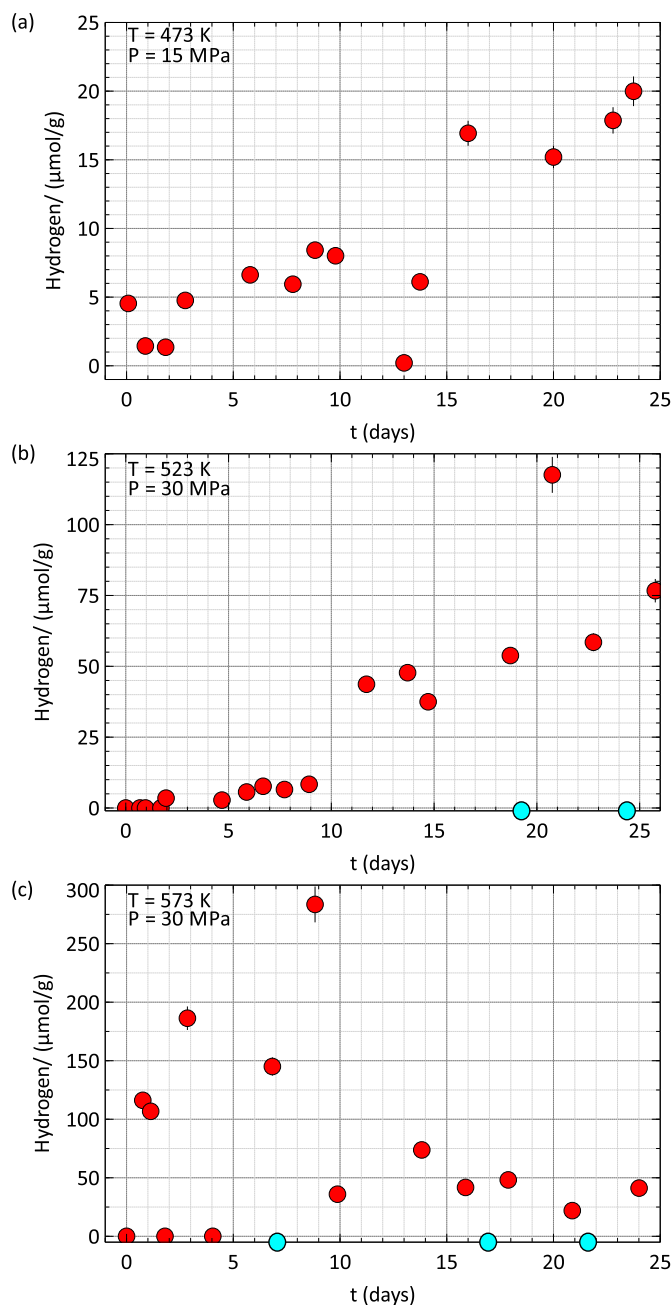


Fig. 4. Variations in the production of H_2 , measured in the gas phase as a function of time (red points). The blue points represent blank experiments, which didn't yield any measurable concentrations of hydrogen. The error bars around the data points (smaller than the marker for most of them) represent a 5% uncertainty associated with the concentration measurements of hydrogen (H_2) by gas chromatography. (For interpretation of the references to color in this figure legend, the reader is referred to the Web version of this article.)

the reaction progress with respect to Fe oxidation in the system. Although the value for MT1, as mentioned earlier, is too low and thus unreliable to be properly exploited, the estimation shows that MT2 and MT4 reach 17.6% and 40.5% completion of reaction respectively (see Table 3).

Table 3

Production of hydrogen in each experiment estimated from FeO analysis. Reaction progress calculated based on the hydrogen production is also reported (Rx%).

Exp.	Wt (g)	T (K)	FeO wt%	FeO (mmol/g)	Δ FeO (mmol/g) ^a	Eq. H_2 (μmol/g) ^b	Eq. H_2 (g/kg)	Rx%
MT ^c	2	–	9.39	1.31	0	no		
MT1	2	473	9.65 ^d	1.34	–0.03	–15	–0.03	–2.3
MT2	2	523	7.74	1.08	0.23	115	0.23	17.6
MT4	2	573	5.61	0.78	0.53	265	0.53	40.5

^a Δ FeO = FeO wt.% in non-reacted mine tailings (MT) – FeO wt.% of reacted mine tailings.

^b Equivalent hydrogen.

^c MT refers to non-treated mine tailings.

^d This is an analytical error (see text), causing the successive negative values.

4. Discussion

4.1. Preferential dissolution of olivine within mine tailings at 473–573 K and 15–30 MPa

The suitability of geological material as carbon sequestration and hydrogen production feedstocks depends primarily on their reactivity and chemical composition (Power et al., 2013). Mafic and ultramafic rocks are rich in Ca^{2+} , Mg^{2+} and Fe^{2+} , and therefore, are the ideal sources for this purpose. New Caledonian mine tailings contained abundant Mg^{2+} and Fe^{2+} , and thus their chemical composition and reactivity favored CO_2 sequestration and hydrogen production. Mineral dissolution, is essentially the first step that makes Mg^{2+} and Fe^{2+} available for both carbonation and hydrogen production reactions, and is a function of crystal chemistry, particle size of reacting mineral, pH, and temperature. As shown in Fig. 2, olivine dissolved gradually with increasing temperature of our experiments, indicating that for our grain sizes and pH, increasing temperatures were favoring the dissolution of olivine. Inevitably, XRD pattern does not indicate the dissolution of glass due to its lack of crystallinity. In acidic to neutral pH, the dissolution kinetics of olivine have been reported to be faster than that of basaltic glass, which is an approximation that can be made for mine tailings (Gudbrandsson et al., 2011; Wolff-Boenisch et al., 2006, 2011). These two previous studies suggest that, under acidic conditions such as those of our study, the constituent minerals of crystalline basalt dissolve faster than basaltic glass by more than one order of magnitude (olivine, a nesosilicate with a Q_0 structure, has all silicate tetrahedrons disconnected from each other, as opposed to glass, and thus faster dissolution kinetics). This indicates that olivine is the major contributor to the Mg^{2+} and Fe^{2+} cations in the solution.

4.2. Reaction path and formation of secondary Mg-silicates

The XRD patterns of the products indicated that the reaction of mine tailings with CO_2 -saturated water, resulted in Fe-rich magnesite, and small quantity of phyllosilicates. Hydrogen is the gaseous product of this reaction. Hematite (Fe_2O_3) was observed only in MT4 (573 K/30 MPa) experiment. Although, we anticipated the production of hydrogen through serpentinization reaction, our result showed that the products of the reaction after 25 days consisted of smectites. However, formation of proto-serpentine-like phase using New Caledonian mine tailings was reported by Bodénan et al. (2014), in an experimental work where 1-day reactions took place either in water or in a 0.43 M NaCl/0.27 M $NaHCO_3$ solution at 453 K at a pCO_2 of 1–9 MPa.

The difference between the reaction products of those two sets of experiments cannot be explained by different pH conditions, as Bodénan et al. (2014) run experiments both in bicarbonate solution (which has the buffer ability to remain neutral under pCO_2 pressure),

and in deionized water (which becomes acidic). The temperature, though lower in Bodénan et al.'s study (453 K), remains close to our study's conditions (473–573 K), and grain size (which influences specific surface area) should not have a critical influence on thermodynamic equilibrium. With respect to these parameters, the two studies are comparable, while their reaction products differ. One possible explanation could very well lie in the duration of the experiments. A study investigating the genesis of ultramafic hosted magnesite vein deposits by Abu-Jaber and Kimberley (1992) has reported, within natural samples, on the reaction of serpentine, magnetite and bicarbonate into (Fe-) nontronite (smectite) and magnesite. Furthermore, a recent experimental study describes various pathways for the conversion of serpentine to smectite under hydrothermal conditions, during which Al^{3+} substitutes to Si^{4+} . They suggest that solid-state transformation is the main mechanism involved. Since this is a process is kinetically limited, the difference in the experiments duration (1 day for Bodénan et al. vs 25 days for this study) could explain the different reaction product. Serpentine would therefore only be an intermediate phase.

4.3. Fe-rich magnesite precipitation and hydrogen production

Fe-rich magnesite was the only carbonate precipitated in our experiments as confirmed by XRD and Rock-Eval 6 analysis. Theoretically, mine tailings could precipitate a maximum of 77 wt.% of magnesite, assuming 100% dissolution of mine tailings (S11). The quantities of Fe-rich magnesite precipitated at 473 K/15 MPa, 523 K/30 MPa and 573 K/30 MPa were 20.3, 44.9 and 21.6 wt.%, respectively. If the reaction completion (Rx) with respect to carbonate precipitation is given by the ratio between the observed carbonate wt.% versus the calculated maximum carbonate wt.%, then 26.4%, 58.3% and 28.1% of reaction completion were achieved respectively during the experiments. Interestingly, the iron content in magnesite followed the same trend as reaction completion, with 0.08, 0.58 and 0.17 mol of iron in one mole of magnesite at 473 K/15 MPa, 523 K/30 MPa and 573 K/30 MPa respectively. This would indicate that the lower temperature and low pCO_2 in MT1 (473 K/15 MPa) slowed down kinetics of the dissolution and precipitation reactions resulting in low quantities of magnesite with small quantity of iron, compared to the other two experiments. The MT2 and MT4 experiments, which were conducted at same pCO_2 (30 MPa), revealed that almost all the olivine dissolved at increasing temperature up to 573 K. But, the precipitated magnesite at 523 K was twice higher than at 573 K. As Mg is the major element in magnesite, this result clearly indicates the competition of Mg incorporation into magnesite vs. secondary Mg-silicates in the 523–573 K temperature range. In addition, the quantity of iron incorporated in magnesite at 523 K is twice as high than at 573 K, indicating that temperatures between 523 and 573 K favored the incorporation of iron into other phases than magnesite. As shown by Andreani et al. (2012), the fast precipitation of Al-Fe-rich serpentines indeed competes with magnetite nucleation and may indeed inhibit it altogether. Nevertheless, magnetite formation is enhanced with increasing temperature, as shown by Malvoisin et al. (2012a, 2012b); those studies thus support the present observations and findings on Fe(III) incorporation into secondary phases. Total iron (II + III) incorporation into secondary phases and its correlation with hydrogen production is also worth mentioning because it demonstrates the competition between two other reactions in the system: the iron incorporation into magnesite versus secondary Mg-silicates (\pm iron oxides). As the temperature increased from 523 K to 573 K, hydrogen production was approximately doubled, producing more Fe^{3+} . At 523 K, the most likely secondary phase to host Fe^{3+} was secondary phyllosilicate, whereas at 573 K, it could possibly be incorporated into phyllosilicate and into iron (III) oxides as well. Although, ferric-hydrate complexes could host Fe^{3+} ions, we assumed their quantities to be negligible. Magnesite structure accommodates only Fe^{2+} . Therefore, the results clearly indicate that temperatures between 523 and 573 K favor iron oxidation, whereas temperatures

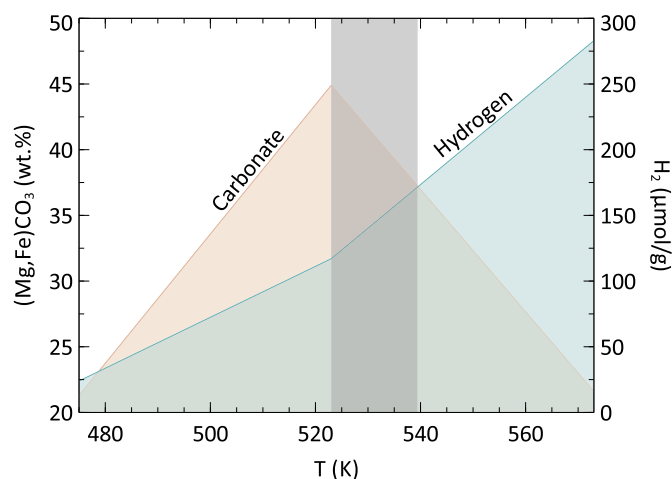


Fig. 5. Quantities of magnesite precipitation and hydrogen production, obtained during the reaction of New Caledonian mine tailings, with CO_2 -saturated water and as a function of temperature. The diagram emphasizes the competition between the two reactions. The shaded area indicates the temperature range at 30 MPa, recognized as the best conditions for the simultaneous carbonation and hydrogen production from mine tailings.

between 473 K and 523 K favor the iron incorporation into magnesite. The competition between Mg and Fe incorporation among the secondary phases seems to control the quantities of magnesite precipitation and hydrogen production. Moreover, Fig. 5, which shows the magnesite production (in wt.%) versus hydrogen production clearly demonstrates that temperatures between 523 K and 540 K at $\text{pCO}_2 = 30$ MPa (shown by shaded area) would be the most favorable conditions for reacting mine tailings in order to maintain both carbonation and hydrogen production in significant quantities. Although the P/T conditions of maximum carbonation in our experiments differ slightly from those of Gerdemann et al. (2007), it can be argued that this discrepancy arises from the different solutions used in two studies; a CO_2 -saturated water here compared with a 0.64 M NaHCO_3 , 1 M NaCl solution in Gerdemann et al. (2007). Furthermore, Andreani et al. (2012) and Sissmann et al. (2013) mention the effect of aluminum on dissolution kinetics of olivine dissolution kinetics. Its presence in the associated glass phase of the mine tailings could also slightly change not only those dissolution kinetics but also the precipitation kinetics of carbonates.

The analysis of FeO in the starting material and the products were used to evaluate the amount of iron oxidation, and to further confirm the hydrogen amounts measured by gas chromatography. As mentioned in section 3.4, the Fe(III)/Fe(II) analysis of non-reacted mine tailings confirmed that the starting material does not contain any Fe^{3+} that could have resulted from ore processing. Assuming the mine tailings have been well homogenized after crushing and sieving, the Fe^{2+} measured in the experimental products was expected to be lower than in the initial sample, due to the oxidation of Fe^{2+} during the experiment. However, the amount of Fe^{2+} measured for MT1 is slightly above the value measured for the initial non-reacted sample. Such an inconsistency could be explained by potential inhomogeneities caused by a sampling bias of the starting material or the products, or due to detection limit for low Fe concentrations in this sample. Nevertheless, the estimated hydrogen production from MT2 and MT4 experiments are in good agreement with the measured hydrogen quantities using gas chromatography (Table 3).

The variation of hydrogen production as a function of reaction time (Fig. 4) indicates that the hydrogen production at 473 K/15 MPa and 523 K/30 MPa continued to increase steadily until the end of the experiment, whereas at 573 K/30 MPa, it suddenly decreased after 9 days of reaction, reaching a plateau. This result suggests that at the lower

Table 4Comparison of ex-situ CO₂ sequestration at 573 K < T > 423 K and P < 30 MPa.

Composition	d (μm)	P (MPa)	T (K)	t (h)	Solution	CO ₂ (g/kg) ^a	Reference
chrysotile (OK)	425–1000	12.4	428	1	1 M NaCl, 0.64 M NaHCO ₃	183.0	Bobicki et al., 2015
chrysotile (Pipe)	425–1000	12.4	428	1	1 M NaCl, 0.64 M NaHCO ₃	157.0	Bobicki et al., 2015
Olivine	20–80	15	423	336	supercritical CO ₂	261.0	Garcia et al., 2010
Olivine	40–63	15	473	600	CO ₂ -saturated water	114.4	This study_MT1
Olivine	40–63	30	523	600	CO ₂ -saturated water	320.5	This study_MT2
Olivine	40–63	30	573	576	CO ₂ -saturated water	118.5	This study_MT4

^a Grams of molecular CO₂ captured by one kg of starting material.

temperatures, the production on of H₂ is not buffered by new secondary phases (no phyllosilicates passivating the surface of mine tailings). However, at 573 K, it appears that hydrogen production is being buffered. A possible explanation would be the limitation of Fe²⁺ supply, and thus of further water reduction and H₂ production. Nevertheless, the sharp decrease in H₂ concentration followed by a plateau could indicate that a steady state has been reached, and that H₂ is being consumed to form light organic compounds dissolved within the system (not quantified in this study) through a reaction with CO₂.

4.4. Carbonation and hydrogen production from mine tailings vs. other slags

First our results on CO₂ sequestration were compared with two experimental studies by Bobicki et al. (2015) and Garcia et al. (2010), who conducted experiments at T ~ 423 K and PCO₂ ~ 15 MPa. Bobicki et al. (2015) used chrysotile from two nickel (Ni) mines (Okanogan nickel deposit in Washington State, USA (OK ore) and Thompson Nickel Belt in Manitoba, Canada, (Pipe ore), respectively) (Table 4). The ores contained 6.0 and 7.8 wt.% of MgO, with approximately < 7 wt.% of CaO + FeO. In contrast, Garcia et al. (2010) used pure olivine (Fo91), with 55.5 wt.% of MgO (theoretical), which is also close to the average MgO content of this study (53.6 wt.%), but containing nearly half of the iron compared to mine tailings in this study (12.95 wt.%). Our results on carbonation yields lie within the same order of magnitude compared to the two studies considered here. However, despite the large granulometry of the starting materials, Bobicki et al. (2015) was able to store CO₂ at a higher rate (~200 g/kg CO₂ within one hour) than the other two studies. They reacted olivine (formed from the reversion of heat-treated chrysotile) at the conditions previously suggested by Gerdemann et al. (2007), making solution salinity and bicarbonate concentration the main differences with the other two studies. This suggests that the rate of CO₂ storage in our experiments could have been enhanced if such high concentrations had been used. However, even though the rate was slower, MT2 experiment stored more CO₂ compared to Bobicki et al. (2015) and Garcia et al. (2010).

It is highly probable that the higher temperature range presumably limits carbonation, while the lower range limits H₂ production. The higher temperatures increase dissolution kinetics, leading to a larger amount of silica in solution. As that silica precipitates, they form secondary phyllosilicates that scavenge the divalent cations (equation (3)). In contrast, the lower temperatures create lower silica supersaturation, and the cations enter carbonate phases leaving less iron available for oxidation and hydrogen production (equation (2)). Nevertheless, this study proves that intermediate conditions can be set to make both processes work simultaneously.

The amounts of hydrogen produced in our experiments were compared with two similar studies (Crouzet et al., 2017; Malvoisin et al., 2013), who attempted to produce hydrogen by using pure wüstite (FeO) and Fe-rich steel slag (Table 5). For the sake of comparison, hydrogen produced at 473 K or 573 K, and 30 MPa after ca. 69 or 160 h of each study were used. The study by Malvoisin et al. (2013) used a carbonated basic oxygen furnace (CARBOF) containing 2.7 wt.% Fe(O), 20.58 wt.% FeO and 3.16 wt.% Fe₂O₃. The grain size of original steel slag used for carbonation was 1–50 μm. The second study (Crouzet

Table 5

Comparison of hydrogen production by experiments conducted at 473 and 573 K.

Reference	Material	Solution	pH	T	t (h)	^b (H ₂ g/kg)
Malvoisin et al., 2013	CARBOF ^a	water	6.9	473	69.2	0.01
Crouzet et al., 2017	FeO	0.05M acetic	3	473	72	5.34
This study	mine tailings	CO ₂ + water	3.6	473	66	0.07
Malvoisin et al., 2013	CARBOF	water	6.9	573	141	1.38
Crouzet et al., 2017	FeO	water	6	573	144	2.18
This study	mine tailings	CO ₂ + water	3.9	573	164	2.26

^a CARBOF = carbonated basic oxygen furnace steel slag.^b grams of H₂ produced by 1 kg of FeO.

et al., 2017) is a follow-up study of Malvoisin et al. (2013) that investigates the hydrogen production under acidic pH conditions using 50–100 μm size pure wüstite (FeO). Because the chemical composition of steel slag, wüstite and New Caledonian mine tailings largely differ from each other, we calculated the hydrogen production per mass unit of FeO of each material. In our study, the hydrogen measured by gas chromatography, and average FeO in mine tailings (12.95 wt.%) were used for this calculation.

As shown in Table 5, H₂ production seems to be correlated with pH: the lower it is, the higher the amount of H₂ generated. This can be explained by the fact that low pH promotes mineral dissolution and thus Fe²⁺ release. Thus, at a similar temperature (573 K), this study (pH 3.9) generates more H₂ than Crouzet (pH 6.0), which generates more than Malvoisin (pH 6.9). However, the pH effect is not the only way to increase H₂ production. As shown by Crouzet et al. (2017), the addition of organic ligands (such as acetic acid) can increase H₂ generation even further by promoting mineral dissolution.

4.5. Implications for CO₂ sequestration and hydrogen production in New Caledonian mining sites and other Ni mining sites

New Caledonia is the 11th largest Ni producer in the world, preceded by the United states, Australia, Brazil, Canada, China, Columbia, Cuba, Guatemala, Indonesia and Madagascar (U.S. Geological Survey, 2017). When scaled to land area, however, its production of Nickel is in the top 3, implying a high environmental fingerprint. In 2013, New Caledonia produced 127,027 metric tons (t) of nickel from 7.8 million metric tons (Mt) of saprolite ore and 36,839 t of nickel from 4.2 Mt of laterite ore, resulting approximately in 12 million metric tons (Mt) of mine tailings per year (Wacaster, 2013). The management of mine tailings such as collection, storage and re-usage are costly to process. Currently these mine tailings are used for geo-technical aspects such as building roads, dams, and land filling. Compared to the traditional valorization methods, those proposed by this study are novel and might be used to contribute to today's always-increasing energy demands, by producing an energy source through waste recycling. In addition, implementing a simultaneous ex-situ CO₂ storage and hydrogen production plant in the vicinity of mining sites provides a safe and permanent

disposal of CO₂ emitted by the nickel industry. Although the chemical looping processes have been documented for carbon capture and storage (Bui et al., 2018; Cormos, 2011), the idea of energy looping does not appear prominently in literature. It is nevertheless our belief that inspiration could be drawn from chemical looping: the energy needed for heating the material could be obtained passively by locating this plant near high temperature furnaces used for ore-processing.

The annual CO₂ emission of New Caledonia is about 4.3 Mt/y (Boden et al., 2017). Our experiments having shown that at 523 K and 30 MPa, mine tailings can trap at least 320 g of CO₂ per kg of mine tailings (supporting information S6), it follows that the annual mine tailings production could potentially trap 3.8 Mt/y of CO₂, which represents about 90% of New Caledonia's annual emissions.

The annual electrical consumption of New Caledonia is approximately 2400 GWh; (New Caledonia Department of Energy, 2013). The maximum hydrogen production in our experiments was 0.57 g hydrogen per kg of mine tailings at 573 K and 30 MPa. According to this value, the annual mine tailings produced in New Caledonia is able to produce 6840 tons of hydrogen per year, which is equivalent of generating 229 GWh/y (with H₂ combustion generating around 120.5 MJ/kg or 33.5 kWh/kg). It represents around 10% of New Caledonia's annual electrical consumption. Furthermore, assuming an average family consumes 3400 kWh/y (New Caledonia Department of Energy, 2013), the energy produced would be sufficient to sustain around 67,350 families.

One limiting factor regarding this method is the separation of small quantities of hydrogen from CO₂ in the reactor. Separating CO₂ and H₂ from industrially important gas mixtures (synthesis gas or natural gas) are widely performed using membrane methods (Korelskiy et al., 2015). These membranes could be either made from polymers (Ghadimi et al., 2014; Rabiee et al., 2014), or ceramic (Korelskiy et al., 2015), and they provide cost effective means of separating gases in large scale. In our opinion, a membrane method would be suitable to separate hydrogen from CO₂ in this process.

We believe that the simultaneous application of ex-situ CO₂ sequestration and hydrogen production using New Caledonian mine tailings could be easily applied to various mining industries of mafic rocks, which presumably produce mine wastes of similar compositional and mineralogical characteristics. By using the residual heat provided by a third process such as the high temperature smelting of ore, those two processes could be translated into a high-value, cost-effective industrial way of storing wastes and generating clean energy.

5. Conclusions

Batch experiments conducted between 473 K and 573 K under high pCO₂ of 15–30 MPa have demonstrated the viability of using New Caledonian mine tailings in ex-situ carbonation process, while producing H₂ as a byproduct. The results suggest that mine tailings were altered into Fe-rich magnesite and phyllosilicates when reacted with CO₂-saturated water at the above mentioned conditions. We have outlined that the competition between Mg and Fe incorporation among the secondary phases seems to control the quantities of magnesite precipitation and hydrogen production. Taken together, these results suggest that the temperatures between 523 K and 540 K at pCO₂ = 30 MPa would be the most favorable conditions for reacting mine tailings in order to maintain both carbonation and hydrogen production in significant quantities.

This work suggest a method to treat New Caledonia's annual CO₂ emissions and energy demands cost-efficiently by recycling the heat used in metal extraction (> 1273 K), providing a novel valorization method for New Caledonian mine tailings. This approach can be globally applied to nickel (Ni) mine tailings as well as other industrial waste materials containing Ca, Mg, and Fe; however we believe that the optimum P/T conditions might vary depending on the mineral composition and textural features of individual material.

Acknowledgments

We thank Joel Lopes-Azvedo, Fanny Lutz, Julien Labaume for their support in mineralogical analysis. We also thank Daniel Pillot for his support in Rock-Eval 6 analysis. Virgile Rouchon, François Guyot and Valerie Beaumont are warmly acknowledged for their constructive comments and discussions. Finally, the thorough review and constructive comments of the executive editor Prof. Michael Kersten and the two anonymous reviewers are greatly appreciated.

Appendix A. Supplementary data

Supplementary data related to this article can be found at <http://dx.doi.org/10.1016/j.apgeochem.2018.05.020>.

References

- Abu-Jaber, N.S., Kimberley, M.M., 1992. Origin of ultramafic-hosted vein magnesite deposits. *Ore Geol. Rev.* 7, 155–191. [http://dx.doi.org/10.1016/0169-1368\(92\)90004-5](http://dx.doi.org/10.1016/0169-1368(92)90004-5).
- Allen, D.E., Seyfried, W.E., 2003. Compositional controls on vent fluids from ultramafic-hosted hydrothermal systems at mid-ocean ridges: an experimental study at 400° C, 500 bars. *Geochim. Cosmochim. Acta* 67, 1531–1542. [http://dx.doi.org/10.1016/s0016-7037\(02\)01173-0](http://dx.doi.org/10.1016/s0016-7037(02)01173-0).
- Andreani, M., Daniel, I., Pollet-Villard, M., 2012. Aluminum speeds up the hydrothermal alteration of olivine. *Am. Mineral.* 98, 1738–1744. <http://dx.doi.org/10.2138/am.2013.4469>.
- Barnes, C.S., Koretsky, M., 2004. In *Engineering and Chemical thermodynamics*. John Wiley and Sons.
- Béarat, H., McKelvy, M.J., Chizmeshya, A.V., Gormley, D., Nunez, R., Carpenter, R.W., et al., 2006. Carbon sequestration via aqueous olivine mineral carbonation: role of passivating layer formation. *Environ. Sci. Technol.* 40 (15), 4802–4808.
- Behar, F., Beaumont, V. De B., Penteado, H.L., 2001. Rock-Eval 6 technology: performances and developments. *Oil Gas Sci. Technol.* 56, 111–134. <http://dx.doi.org/10.2516/ogst:2001013>.
- Berndt, M.E., Allen, D.E., Seyfried, W.E., 1996. Reduction of CO₂ during serpentinization of olivine at 300°C and 500 bar. *Geology* 24, 351–354. [http://dx.doi.org/10.1130/0091-7613\(1996\)024<0351:ROCDSD>2.3.CO](http://dx.doi.org/10.1130/0091-7613(1996)024<0351:ROCDSD>2.3.CO).
- Bish, D.L., Howard, S.A., 1988. Quantitative phase analysis using the Rietveld method. *J. Appl. Crystallogr.* 21, 86–91. <http://dx.doi.org/10.1107/S0021889887009415>.
- Bish, D.L., Post, J.E., 1993. Quantitative mineralogical analysis using the Rietveld full-pattern fitting method. *Am. Mineral.* 78 (9–10), 932–940.
- Bobicki, E.R., Liu, Q., Xu, Z., Zeng, H., 2012. Carbon capture and storage using alkaline industrial wastes. *Prog. Energy Combust. Sci.* <http://dx.doi.org/10.1016/j.pecs.2011.11.002>.
- Bobicki, E.R., Liu, Q., Xu, Z., 2015. Mineral carbon storage in pre-treated ultramafic ores. *Miner. Eng.* 70, 43–54.
- Boden, T., Marland, G., Andres, R., 2017. Global, Regional, and National Fossil-Fuel CO₂ Emissions. Oak Ridge 3 National Laboratory, U.S. Department of Energy, Oak Ridge, Tenn., U.S.A.
- Bodénan, F., Bourgeois, F., Petiot, C., Augé, T., Bonfils, B., Joulcour-lebigue, C., Guyot, F., 2014. Ex situ mineral carbonation for CO₂ mitigation: evaluation of mining waste resources, aqueous carbonation processability and life cycle assessment (Carmex project). 59, 52–63. <http://dx.doi.org/10.1016/j.mineng.2014.01.011>.
- Brantley, S.L., 2003. Reaction kinetics of primary rock-forming minerals under ambient conditions. *Treatise Geochem.* 5, 605.
- Brunauer, S., Emmett, P.H., Teller, E., 1938. Adsorption of gases in multimolecular layer. *J. Am. Chem. Soc.* 60, 309–319 doi:citeulike-article-id:4074706.
- Bui, M., Adjiman, C.S., Bardow, A., Anthony, E.J., Boston, A., Brown, S., et al., 2018. Carbon capture and storage (CCS): the way forward. *Energy Environ. Sci.* 11, 1062–1176 ISSN 1754-5692.
- Caesar, L., Rahmstorf, S., Robinson, A., Feulner, G., Saba, V., 2018. Observed fingerprint of a weakening Atlantic Ocean overturning circulation. *Nature* 556 (7700), 191.
- Cormos, C.C., 2011. Hydrogen production from fossil fuels with carbon capture and storage based on chemical looping systems. *Int. J. Hydrogen Energy* 36 (10), 5960–5971.
- Crouzet, C., Brunet, F., Recham, N., Findling, N., Lanson, M., Guyot, F., Ferrasse, J.H., Goffé, B., 2017. Hydrogen production by hydrothermal oxidation of FeO under acidic conditions. *Int. J. Hydrogen Energy* 42, 795–806. <http://dx.doi.org/10.1016/j.ijhydene.2016.10.019>.
- Daval, D., Martinez, I., Corvisier, J., Findling, N., Goffé, B., Guyot, F., 2009a. Carbonation of Ca-bearing silicates, the case of wollastonite: experimental investigations and kinetic modeling. *Chem. Geol.* 262, 262–277. <http://dx.doi.org/10.1016/j.chemgeo.2009.01.022>.
- Ece, Ö.I., Matsubaya, O., Çoban, F., 2005. Genesis of hydrothermal stockwork-type magnesite deposits associated with ophiolite complexes in the Kütahta-Eskişehir region, Turkey. *Neues Jahrb. Mineral. Abhand.* 181, 191–205. <http://dx.doi.org/10.1127/0077-7757/2005/0014>.
- Edenhofer, O., Pichs-Madruga, R., Sokona, Y., Farahani, E., Kadner, S., Seyboth, K., Adler, A., Baum, I., Brunner, S., Eickemeier, P., Kriemann, B., Savolainen, J., Schlömer, S.,

- von Stechow, C., Zwickel, T., Minx, J.C., 2014. IPCC, 2014. Summary for policy-makers, climate change 2014: mitigation of climate change. In: Contribution of Working Group iii to the Fifth Assessment Report of the Intergovernmental Panel on Climate Change, <http://dx.doi.org/10.1007/s13398-014-0173-7-2>.
- Garcia, B., Beaumont, V., Perfetti, E., Rouchon, V., Blanchet, D., Oger, P., Dromart, G., Huc, A.Y., Haeseler, F., 2010. Experiments and geochemical modelling of CO₂ sequestration by olivine: potential, quantification. *Appl. Geochem.* 25, 1383–1396. <http://dx.doi.org/10.1016/j.apgeochem.2010.06.009>.
- Gerdemann, S.J., O'Connor, W.K., Dahlin, D.C., Penner, L.R., Rush, H., 2007. Ex situ aqueous mineral carbonation. *Environ. Sci. Technol.* 41, 2587–2593. <http://dx.doi.org/10.1021/es0619253>.
- Ghadimi, A., Amirilargani, M., Mohammadi, T., Kasiri, N., Sadatnia, B., 2014. Preparation of alloyed poly(ether block amide)/poly(ethylene glycol diacrylate) membranes for separation of CO₂/H₂ (syngas application). *J. Membr. Sci.* 458, 14–26. <http://dx.doi.org/10.1016/j.memsci.2014.01.048>.
- Giammar, D.E., Bruant Jr., R.G., Peters, C.A., 2005. Forsterite dissolution and magnesite precipitation at conditions relevant for deep saline aquifer storage and sequestration of carbon dioxide. *Chem. Geol.* 217 (3–4), 257–276.
- Golubev, S.V., Pokrovsky, O.S., Schott, J., 2005. Experimental determination of the effect of dissolved CO₂ on the dissolution kinetics of Mg and Ca silicates at 25 °C. *Chem. Geol.* 217 (3–4), 227–238.
- Gudbrandsson, S., Wolff-Boenisch, D., Gislason, S.R., Oelkers, E.H., 2011. An experimental study of crystalline basalt dissolution from 2pH11 and temperatures from 5 to 75 °C. *Geochim. Cosmochim. Acta* 75, 5496–5509. <http://dx.doi.org/10.1016/j.gca.2011.06.035>.
- Guthrie, G., 2001. *Geochemical Aspects of the Carbonation of Magnesium Silicates in an Aqueous Medium* (No. LA-UR-01-1429). Los Alamos National Lab., NM (US).
- Harrison, A.L., Dipple, G.M., Power, I.M., Mayer, K.U., 2016. The impact of evolving mineral-water interfacial areas on mineral-fluid reaction rates in unsaturated porous media. *Chem. Geol.* 421, 65–80. <http://dx.doi.org/10.1016/j.chemgeo.2015.12.005>.
- Harrison, A.L., Power, I.M., Dipple, G.M., 2013. Accelerated carbonation of brucite in mine tailings for carbon sequestration. *Environ. Sci. Technol.* 47, 126–134. <http://dx.doi.org/10.1021/es3012854>.
- Janecky, D.R., Seyfried, W.E., 1986. Hydrothermal serpentinization of peridotite within the oceanic crust: experimental investigations of mineralogy and major element chemistry. *Geochim. Cosmochim. Acta* 50, 1357–1378. [http://dx.doi.org/10.1016/0016-7037\(86\)90311-X](http://dx.doi.org/10.1016/0016-7037(86)90311-X).
- Johnson, N.C., Thomas, B., Maher, K., Rosenbauer, R.J., Bird, D., Brown Jr., G.E., 2014. Olivine dissolution and carbonation under conditions relevant for in situ carbon storage. *Chem. Geol.* 373, 93–105.
- King, H.E., Plümper, O., Putnis, A., 2010. Effect of secondary phase formation on the carbonation of olivine. *Environ. Sci. Technol.* 44 (16), 6503–6509.
- Klein, F., Bach, W., Jöns, N., McCollom, T., Moskowit, B., Berquó, T., 2009. Iron partitioning and hydrogen generation during serpentinization of abyssal peridotites from 15°N on the Mid-Atlantic Ridge. *Geochim. Cosmochim. Acta* 73, 6868–6893. <http://dx.doi.org/10.1016/j.gca.2009.08.021>.
- Klein, F., Bach, W., McCollom, T.M., 2013. Compositional controls on hydrogen generation during serpentinization of ultramafic rocks. *Lithos* 178, 55–69. <http://dx.doi.org/10.1016/j.lithos.2013.03.008>.
- Klein, F., Garrido, C.J., 2010. On serpentinization and mineral carbonation of serpentine. In: AGU Fall Meeting Abstracts, Am. Geophys. Union.
- Kondo, M., Ichii, K., Patra, P.K., Canadell, J.G., Poulter, B., Sitch, S., et al., 2018. Land use change and El Niño-Southern Oscillation drive decadal carbon balance shifts in Southeast Asia. *Nat. Commun.* 9.
- Korelskiy, D., Ye, P., Fouladvand, S., Karimi, S., Sjöberg, E., Hedlund, J., 2015. Efficient ceramic zeolite membranes for CO₂/H₂ separation. *J. Mater. Chem. A* 3 (23), 12500–12506.
- Lafargue, E., Marquis, F., Pillot, D., 1998. Rock-Eval 6 applications in hydrocarbon exploration, production, and soil contamination studies. *Oil Gas Sci. Technol.* 53, 421–437. <http://dx.doi.org/10.2516/ogst:1998036>.
- Lugli, S., Torres-Rutz, J., Garuti, G., Olmedo, F., 2000. Petrography and geochemistry of the Eugui magnesite deposit (Western Pyrenees, Spain): evidence for the development of a peculiar zebra banding by dolomite replacement. *Econ. Geol.* 95 (8), 1775–1791. <http://dx.doi.org/10.2113/gsecongeo.95.8.1775>.
- Malvoisin, B., Brunet, F., Carlut, J., Montes-Hernandez, G., Findling, N., Lanson, M., Vidal, O., Bottero, J.Y., Goff, B., 2013. High-purity hydrogen gas from the reaction between BOF steel slag and water in the 473–673 K range. *Int. J. Hydrogen Energy* 38, 7382–7393. <http://dx.doi.org/10.1016/j.ijhydene.2013.03.163>.
- Malvoisin, B., Brunet, F., Carlut, J., Rouméjon, S., Cannat, M., 2012a. Serpentinization of oceanic peridotites: 2. Kinetics and processes of San Carlos olivine hydrothermal alteration. *J. Geophys. Res. Solid Earth* 117, 1–13. <http://dx.doi.org/10.1029/2011JB008842>.
- Malvoisin, B., Carlut, J., Brunet, F., 2012b. Serpentinization of oceanic peridotites: 1. A high-sensitivity method to monitor magnetite production in hydrothermal experiments. *J. Geophys. Res. Solid Earth* 117. <http://dx.doi.org/10.1029/2011JB008612>.
- Manabe, S., Stouffer, R.J., 1993. Century-scale effects of increased atmospheric CO₂ on the ocean-atmosphere system. *Nature* 364, 215–218. <http://dx.doi.org/10.1038/364215a0>.
- Marzeion, B., Kaser, G., Maussion, F., Champollion, N., 2018. Limited influence of climate change mitigation on short-term glacier mass loss. *Nat. Clim. Change* 8 (4), 305.
- Mayhew, L.E., Ellison, E.T., Miller, H.M., Kelemen, P.B., Templeton, A.S., 2018. Iron transformations during low temperature alteration of variably serpentinized rocks from the Samail ophiolite, Oman. *Geochim. Cosmochim. Acta* 222, 704–728.
- McCollom, T.M., Bach, W., 2009a. Thermodynamic constraints on hydrogen generation during serpentinization of ultramafic rocks. *Geochim. Cosmochim. Acta* 73, 856–875. <http://dx.doi.org/10.1016/j.gca.2008.10.032>.
- McCollom, T.M., Bach, W., 2009b. Thermodynamic constraints on hydrogen generation during serpentinization of ultramafic rocks. *Geochim. Cosmochim. Acta* 73, 856–875. <http://dx.doi.org/10.1016/j.gca.2008.10.032>.
- McCollom, T.M., Klein, F., Robbins, M., Moskowit, B., Berquó, T.S., Jöns, N., Bach, W., Templeton, A., 2016. Temperature trends for reaction rates, hydrogen generation, and partitioning of iron during experimental serpentinization of olivine. *Geochim. Cosmochim. Acta* 181, 175–200. <http://dx.doi.org/10.1016/j.gca.2016.03.002>.
- McCollom, T.M., Seewald, J.S., 2001. A reassessment of the potential for reduction of dissolved CO₂ to hydrocarbons during serpentinization of olivine. *Geochim. Cosmochim. Acta* 65, 3769–3778. [http://dx.doi.org/10.1016/S0016-7037\(01\)00655-X](http://dx.doi.org/10.1016/S0016-7037(01)00655-X).
- McCusker, L.B., Von Dreele, R.B., Cox, D.E., Louër, D., Scardi, P., 1999. Rietveld refinement guidelines. *J. Appl. Crystallogr.* 32, 36–50. <http://dx.doi.org/10.1107/S0021889898009856>.
- McMollom, T.M., Bach, W., 2008. Constraints on hydrogen generation during serpentinization of ultramafic rocks. *Geochim. Cosmochim. Acta* 72, A611.
- New Caledonia Department of Energy, 2013. Bilan énergétique de la nouvelle-caledonie-2013. Retrieved from: https://maitrise-energie.nc/sites/default/files/documents/bilan_energetique_2013.pdf.
- NOAA, 2016. Trends in Atmospheric Carbon Dioxide. Retrieved from: <http://www.esrl.noaa.gov/gmd/ccgg/trends/>.
- Oskierski, H.C., Dlugogorski, B.Z., Jacobsen, G., 2013. Sequestration of atmospheric CO₂ in a weathering-derived, serpentinite-hosted magnesite deposit: ¹⁴C tracing of carbon sources and age constraints for a refined genetic model. *Geochim. Cosmochim. Acta* 122, 226–246. <http://dx.doi.org/10.1016/j.gca.2013.08.029>.
- Palinkas, L.A., Jurković, I., Garašić, V., Palinkas, S.S., 2012. Genesis of vein-stockwork cryptocrystalline magnesite from the dinaride ophiolites. *Ophiolite* 37, 13–26.
- Park, A.H.A., Jadhav, R., Fan, L.S., 2003. CO₂ mineral sequestration: chemically enhanced aqueous carbonation of serpentine. *Can. J. Chem. Eng.* 81 (3–4), 885–890.
- Power, I.M., Harrison, A.L., Dipple, G.M., Wilson, S.A., Kelemen, P.B., Hitch, M., Southam, G., 2013. Carbon mineralization: from natural analogues to engineered systems. *Rev. Mineral. Geochem.* 77, 305–360. <http://dx.doi.org/10.2138/rmg.2013.77.9>.
- Rabiee, H., Soltanieh, M., Mousavi, S.A., Ghadimi, A., 2014. Improvement in CO₂/H₂ separation by fabrication of poly(ether-b-amide6)/glycerol triacetate gel membranes. *J. Membr. Sci.* 469, 43–58. <http://dx.doi.org/10.1016/j.memsci.2014.06.026>.
- Seewald, J.S., Zolotov, M.Y., McCollom, T., 2006. Experimental investigation of single carbon compounds under hydrothermal conditions. *Geochim. Cosmochim. Acta* 70 (2), 446–460.
- Seifritz, W., 1990. CO₂ disposal by means of silicates. *Nature* 345 (6275), 486. <http://dx.doi.org/10.1038/345486b0>.
- Seyfried, W.E., Foustoukos, D.I., Fu, Q., 2007. Redox evolution and mass transfer during serpentinization: an experimental and theoretical study at 200 °C, 500 bar with implications for ultramafic-hosted hydrothermal systems at Mid-Ocean Ridges. *Geochim. Cosmochim. Acta* 71, 3872–3886. <http://dx.doi.org/10.1016/j.gca.2007.05.015>.
- Sissmann, O., Daval, D., Brunet, F., Guyot, F., Verlaquet, A., Pinquier, Y., Findling, N., Martinez, I., 2013. The deleterious effect of secondary phases on olivine carbonation yield: insight from time-resolved aqueous-fluid sampling and FIB-TEM characterization. *Chem. Geol.* 357, 186–202. <http://dx.doi.org/10.1016/j.chemgeo.2013.08.031>.
- Takahashi, E., 1986. Melting of a dry peridotite KLB-1 up to 14 GPa: implications on the Origin of peridotitic upper mantle. *J. Geophys. Res.* 91, 9367–9382. <http://dx.doi.org/10.1029/JB091iB09p09367>.
- Tutolo, B.M., Luhmann, A.J., Tosca, N.J., Seyfried, W.E., 2018. Serpentinization as a reactive transport process: The brucite silicification reaction. *Earth Planet Sci. Lett.* 484, 385–395.
- U.S. Geological Survey, 2017. Mineral Commodity Summaries 2017.
- van der Lee, J., De Windt, L., 2002. CHESS Tutorial and Cookbook Updated for Version 3.0. Ecole des Mines de Paris, Fontainebleau, France.
- Wacaster, S., 2013. Minerals Yearbook New Caledonia (Advance Release). U.S. Geological Survey.
- Wilson, S.A., Harrison, A.L., Dipple, G.M., Power, I.M., Barker, S.L.L., Ulrich Mayer, K., Fallon, S.J., Raudsepp, M., Southam, G., 2014. Offsetting of CO₂ emissions by air capture in mine tailings at the Mount Keith Nickel Mine, Western Australia: rates, controls and prospects for carbon neutral mining. *Int. J. Greenh. Gas Contr.* 25, 121–140. <http://dx.doi.org/10.1016/j.ijggc.2014.04.002>.
- Wolff-Boenisch, D., Gislason, S.R., Oelkers, E.H., 2006. The effect of crystallinity on dissolution rates and CO₂ consumption capacity of silicates. *Geochim. Cosmochim. Acta* 70 (4), 858–870.
- Wolff-Boenisch, D., Wenau, S., Gislason, S.R., Oelkers, E.H., 2011. Dissolution of basalts and peridotite in seawater, in the presence of ligands, and CO₂: implications for mineral sequestration of carbon dioxide. *Geochim. Cosmochim. Acta* 75 (19), 5510–5525.
- Zhang, X., Knorr, G., Lohmann, G., Barker, S., 2017. Abrupt North Atlantic circulation changes in response to gradual CO₂ forcing in a glacial climate state. *Nat. Geosci.* 10 (7), 518.
- Zedef, V., Russell, M.J., Fallick, A.E., Hall, A.J., 2000. Genesis of vein stockwork and sedimentary magnesite and hydromagnesite deposits in the ultramafic terranes of southwestern Turkey: a stable isotope study. *Econ. Geol.* 95, 429–445. <http://dx.doi.org/10.2113/gsecongeo.95.2.429>.



CO₂ Valorization by Mineral Storage and Abiotic Hydrocarbons Generation

Par

Kanchana Kularatne

Abstract

This study examined hydrogen production, CO₂ storage and abiotic hydrocarbon generation during gas-water-rock interactions by conducting hydrothermal experiments. The first part of this manuscript presents the simultaneous CO₂ sequestration and hydrogen production by reacting New Caledonian mine tailings with CO₂ saturated water at 473 K <T< 573 K and 15 MPa <PCO₂< 30 MPa. The results showed that the best conditions for both these reactions were 523 K <T<540 K at 30 MPa, capturing 320.5 g of CO₂ in the form of iron-rich magnesite ((Mg,Fe)CO₃), and producing 0.57 g of H₂ per 1 kg of mine tailings. In addition, considering the annual mine tailings production and the annual CO₂ emission in New Caledonia, the proposed method could potentially capture ~90 % of New Caledonia's CO₂ emissions. In addition, the H₂ produced by this method could offset ~10 % of New-Caledonia's annual electrical consumption. Further investigation of secondary products and their mineral-water interfaces at nanometer scale indicated that the reactions were taken place by dissolving mine tailings followed by precipitation of iron rich magnesite, smectite group clay minerals (nontronite, vermiculite), traces of iron oxides and amorphous silica. Although, the phyllosilicates and amorphous silica could potentially act as passivating layers, slowing down the dissolution kinetics and consequently limiting the CO₂ storage and H₂ production capacities, our experiments demonstrated that the reactivity of New Caledonian mine tailings could also be lowered by the presence of glass. The second part of this manuscript presents the interaction of dissolved CO₂ and H₂ during the synthesis of "abiotic" hydrocarbons, via Fischer-Tropsch type (FTT) synthesis in the presence of two potential catalysts found in natural systems; sphalerite (ZnS) and marcasite (FeS₂). The experiments were conducted at 573 K and 30 MPa in gold capsules heated and pressurize in autoclaves. Hydrogen necessary for the reaction was provided by Fe²⁺ oxidation of minerals such as olivine (Mg_{1.80}Fe_{0.2}SiO₄), fayalite (Fe₂SiO₄) and Fe-rich chlorite or chamosite (6Fe₅Al(AlSi₃)O₁₀(OH)₈). Methane (CH₄) produced in our experiments was one order of magnitude higher than those reported in previous studies when magnetite and iron oxide-chromite were used as catalysts for CH₄ production, and in the same order of magnitude as pentlandite and Fe-Ni alloy catalysts. However, the small conversion rates of inorganic carbon into organic carbon as well as the Schulz-Flory distribution of C1-C4 alkanes demonstrated that sphalerite and marcasite do not explicitly catalyze the FTT synthesis of hydrocarbons under the conditions of these experiments.

Key words: CO₂ sequestration, hydrogen, methane, water-rock interactions, New Caledonian mine tailings